

FINAL REPORT

Phase II: Field Load Testing of Shallow Foundations in Florida Limestone

FDOT Contract No: BDV31-977-124

UF Project No: P0147823



Submitted to:

Rodrigo Herrera, P.E.

David Horhota, Ph.D., P.E.

Project Managers

Florida Department of Transportation

Principal Investigators:

Michael B. Rodgers, Ph.D., P.E. (PI)

Michael C. McVay, Ph.D. (Co-PI)

Scott Wasman, Ph.D. (Co-PI)

Khiem Tran, Ph.D. (Co-PI)

Graduate Assistant:

Kunyu Yang

December 2022

University of Florida

Department of Civil and Coastal Engineering

DISCLAIMER

The opinions, findings, and conclusions expressed in this publication are those of the authors and not necessarily those of the Florida Department of Transportation.

SI (MODERN METRIC) CONVERSION FACTORS (from FHWA)

APPROXIMATE CONVERSIONS TO SI UNITS

SYMBOL	WHEN YOU KNOW	MULTIPLY BY	TO FIND	SYMBOL
LENGTH				
in	inches	25.4	millimeters	mm
ft	feet	0.305	meters	m
yd	yards	0.914	meters	m
mi	miles	1.61	kilometers	km

SYMBOL	WHEN YOU KNOW	MULTIPLY BY	TO FIND	SYMBOL
AREA				
in²	square inches	645.2	square millimeters	mm ²
ft²	square feet	0.093	square meters	m ²
yd²	square yard	0.836	square meters	m ²
ac	acres	0.405	hectares	ha
mi²	square miles	2.59	square kilometers	km ²

SYMBOL	WHEN YOU KNOW	MULTIPLY BY	TO FIND	SYMBOL
VOLUME				
fl oz	fluid ounces	29.57	milliliters	mL
gal	gallons	3.785	liters	L
ft³	cubic feet	0.028	cubic meters	m ³
yd³	cubic yards	0.765	cubic meters	m ³

NOTE: volumes greater than 1000 L shall be shown in m³

SYMBOL	WHEN YOU KNOW	MULTIPLY BY	TO FIND	SYMBOL
MASS				
oz	ounces	28.35	grams	g
lb	pounds	0.454	kilograms	kg
T	short tons (2000 lb)	0.907	megagrams (or "metric ton")	Mg (or "t")

SYMBOL	WHEN YOU KNOW	MULTIPLY BY	TO FIND	SYMBOL
TEMPERATURE (exact degrees)				
°F	Fahrenheit	5 (F-32)/9 or (F-32)/1.8	Celsius	°C

SYMBOL	WHEN YOU KNOW	MULTIPLY BY	TO FIND	SYMBOL
ILLUMINATION				
fc	foot-candles	10.76	lux	lx
fl	foot-Lamberts	3.426	candela/m ²	cd/m ²

SYMBOL	WHEN YOU KNOW	MULTIPLY BY	TO FIND	SYMBOL
FORCE and PRESSURE or STRESS				
Lbf[*]	poundforce	4.45	newtons	N
kip	kip force	1000	pounds	lbf
lbf/in² (psi)	poundforce per square inch	6.89	kilopascals	kPa
ksf	kips per square foot	0.04788	Megapascals	Mpa
tsf	tons per square foot	0.09576	Megapascals	Mpa

APPROXIMATE CONVERSIONS TO SI UNITS

SYMBOL	WHEN YOU KNOW	MULTIPLY BY	TO FIND	SYMBOL
LENGTH				
mm	millimeters	0.039	inches	in
m	meters	3.28	feet	ft
m	meters	1.09	yards	yd
km	kilometers	0.621	miles	mi

SYMBOL	WHEN YOU KNOW	MULTIPLY BY	TO FIND	SYMBOL
AREA				
mm²	square millimeters	0.0016	square inches	in ²
m²	square meters	10.764	square feet	ft ²
m²	square meters	1.195	square yards	yd ²
ha	hectares	2.47	acres	ac
km²	square kilometers	0.386	square miles	mi ²

SYMBOL	WHEN YOU KNOW	MULTIPLY BY	TO FIND	SYMBOL
VOLUME				
mL	milliliters	0.034	fluid ounces	fl oz
L	liters	0.264	gallons	gal
m³	cubic meters	35.314	cubic feet	ft ³
m³	cubic meters	1.307	cubic yards	yd ³

SYMBOL	WHEN YOU KNOW	MULTIPLY BY	TO FIND	SYMBOL
MASS				
g	grams	0.035	ounces	oz
kg	kilograms	2.202	pounds	lb
Mg (or "t")	megagrams (or "metric ton")	1.103	short tons (2000 lb)	T

SYMBOL	WHEN YOU KNOW	MULTIPLY BY	TO FIND	SYMBOL
TEMPERATURE (exact degrees)				
°C	Celsius	1.8C+32	Fahrenheit	°F

SYMBOL	WHEN YOU KNOW	MULTIPLY BY	TO FIND	SYMBOL
ILLUMINATION				
lx	lux	0.0929	foot-candles	fc
cd/m²	candela/m ²	0.2919	foot-Lamberts	fl

SYMBOL	WHEN YOU KNOW	MULTIPLY BY	TO FIND	SYMBOL
FORCE and PRESSURE or STRESS				
N	newtons	0.225	poundforce	lbf
kPa	kilopascals	0.145	poundforce per square inch	lbf/in ²

*SI is the symbol for International System of Units. Appropriate rounding should be made to comply with Section 4 of ASTM E380. (Revised March 2003)

TECHNICAL REPORT DOCUMENTATION PAGE

1. Report No.	2. Government Accession No.	3. Recipient's Catalog No.	
4. Title and Subtitle Phase II: Field Load Testing of Shallow Foundations in Florida Limestone		5. Report Date Dec. 2022	
		6. Performing Organization Code	
7. Author(s) Michael Rodgers, Michael McVay, Scott Wasman, Khiem Tran, Kunyu Yang		8. Performing Organization Report No.	
9. Performing Organization Name and Address University of Florida – Dept. of Civil and Coastal Engineering Engineering School of Sustainable Infrastructure and Environment 365 Weil Hall – P.O. Box 116580 Gainesville, FL 32611-6580		10. Work Unit No. (TRAIS)	
		11. Contract or Grant No. BDV31-977-124	
12. Sponsoring Agency Name and Address Florida Department of Transportation 605 Suwannee Street, MS 30 Tallahassee, FL 32399		13. Type of Report and Period Covered Final Report 11/2019 – 12/2022	
		14. Sponsoring Agency Code	
15. Supplementary Notes			
<p>16. Abstract: Three full-scale shallow foundation load tests (900 tons) were performed at Miami, Fort Lauderdale, and Bell, Florida, to validate the Florida Bearing Capacity equations (Phase I – FDOT BDV31-977-51) as well develop and verify load-settlement response for service limit state. Rock coring, Standard penetration test (SPT), and seismic shear tests were performed at each site; the split tension, unconfined compression, and triaxial compression tests were performed on the recovered cores to establish strength envelope and moduli of the rock. Exact footing location at each site was selected based on the limit of load test frames and the strength envelope, which was established as a function of dry unit weight and formation. The seismic shear tests representing a larger volume of rock beneath the footing were found to characterize the mass dry unit weight of each site (validated by the cores). The subsurface information (in-situ testing), construction of load test, and the load test setup and measured results as well as predicted behavior are presented in the report.</p> <p>The Florida Bearing Capacity equations were validated in all three load tests for different formations and boundaries (single rock layer and rock over sand). The load-settlement response of a single layer was shown to be predicted with Fenton and Griffiths method. For the rock-over-sand case, the Burmister method and/or Equivalent Modulus (Winkler model) method are recommended to characteristic the bilinear load-settlement response. A parametric study between the Burmister method, Winkler model, and finite element method was conducted for different footing widths, shapes, embedment depths, rock dry unit weights, and rock layer thicknesses as well as the sand modulus. Good agreement was achieved between both.</p>			
17. Key Words Shallow Foundation, Bearing Capacity, Load-settlement response, Load Tests, Winkler model		18. Distribution Statement No restrictions.	
19. Security Classif. (of this report) Unclassified	20. Security Classif. (of this page) Unclassified	21. No. of Pages 251	22. Price

ACKNOWLEDGEMENTS

The researchers would like to thank the Florida Department of Transportation (FDOT) for the financial support to carry out this research; CEMEX for Miami site access; PSI and HR Engineering for drilling at the CEMEX and SR-84 sites; State material office (SMO) for laboratory testing of all samples (3 sites) and field work at the Bell site; and District 2 maintenance for assistance with excavation at the Bell site. Special thanks to H2R for installation of micropiles at CEMEX site and RW Harris for fabrication and installation of the reaction drilled shafts at both the SR-84 and Bell sites.

EXECUTIVE SUMMARY

Most of the existing bridges and overpasses in Florida are supported by deep foundations. The Florida Department of Transportation (FDOT) is planning to use shallow foundations for support of bridge piers or bents in areas of shallow competent limestone (South Florida). Although the geological age of Florida limestone is very young (average 2 million years, FDOT BDV31-977-51, referred to as Phase I hereafter), much of it has already been exposed to the weathering process. In addition, due to varying degrees of submersion in the past, shallow Florida limestone formations are by nature highly heterogeneous (dry unit weights from 85 pcf to 140 pcf), porous (median porosity 37%), and ductile.

The design of any shallow foundation requires the assessment of bearing capacity (ultimate strength) and its load-settlement response (service limit state). In Phase I, researchers investigated the strength envelope of several Florida limestone formations as well as existing bearing capacity equations for shallow foundation design. Due to the porous nature of Florida limestone, the research revealed that the strength envelope of the rock is not linear but bilinear or curved (concave downward). Similarly, both the unconfined compression and triaxial compression results of limestone showed linear stress vs. strain response up to failure and then constant (i.e., bilinear) under further strain (ductile case). Using the stress vs. strain response, and strength envelope, bearing capacity equations for shallow foundations for both heterogeneous rock and for rock-over-sand scenarios were developed based on finite element numerical analyses.

This research (Phase II) focused on validation of Phase I bearing equations as well as developing methods for estimating footing settlements under service and ultimate load states, i.e., bearing failure (e.g., single and two-layer: rock over sand). For the validation, three shallow

foundation load tests at different locations under different boundary conditions (homogeneous and rock over sand) as well as different strengths and formations (Miami and Ocala) were undertaken. Each footing test was sized to fit the load frame (FDOT 900 tons-SMO) using laboratory-assessed rock strength at each site. The first test was carried out in downtown Miami (Cemex Mine) and involved a 42 in x 42 in footing embedded 3 ft below the water table in the Miami limestone. The second test occurred on a 60 in x 72 in footing adjacent to SR-84 (Davie-Fort Lauderdale) on a 10-ft-thick layer of Miami limestone overlying sand. The third and final test involved a 60 in x 60 in footing in a strong Ocala limestone layer (5 ft thick) over a weathered limestone mixed with loose sand and soft clay inclusions.

For each field test, a series of unconfined compression tests, split tension tests, and triaxial compression tests (50 psi, 130 psi, and 600 psi confining stress) were performed on cores recovered on each site to assess stress-strain and the strength envelope of rock near the footing. The strength envelope for Miami limestone found in Phase I was found the same as the rock strengths at Cemex and SR-84 sites. The strength envelope of Ocala limestone was found more linear due to the reduced crushing of rock under increased confining stress. The seismic shear testing was performed at each site along multiple lines to identify mean mass dry unit weight as well as variability of rock vertically and horizontally. At the Ocala site, the seismic shear test and measuring while drilling (MWD) testing revealed the presence of a thin (2 ft) weathered rock layer mixed with soil beneath the loaded 5-ft-thick upper bearing rock layer.

The Florida bearing capacity equations (Phase I) were found to be in good agreement with measured field response at all three sites. The CEMEX site underwent general shear failure (rotation), and the other 2 sites exhibited punching shear or yielding of the upper rock layer with appreciable settlement of the lower layer.

Using the laboratory stress-strain response of the rock (q_u or 50 psi confining stress triaxial tests), an initial linear Young's modulus (E_i) up to yield/failure may be used to predict settlements up to bearing failure (CEMEX). In the case of rock over sand (SR-84 & Bell), a bilinear secant Young's model of rock was established: initial modulus, E_i (settlement up to punching shear), and secant, E_s , based on 2% strain for settlement beyond. The Young's modulus of the sand was assessed based on SPT N values of the layer. In the validation of bearing capacity or development of load-settlement response, the mass effect cannot be neglected, appropriate (rock core adjusted-recovery) $REC_{adjusted}$ need to be assessed and care has to be taken in measuring the index properties of the rock (total unit weight, moisture content). It is strongly recommended that at least 20 to 25 testable samples (e.g., 10 q_u , 10 q_t and 5 triaxial tests) within the influence zone be obtained for parameter assessment (strength, moduli, and layering). Based on measured field response, the load-settlement behavior of single layer can be predicted by the nonlinear finite element method or both mean and differential settlement can be characterized with Fenton and Griffiths method; in the case of rock over sand (SR-84 & Bell), the load vs. deformation can be predicted by the nonlinear Finite Element method, Burmister method, and/or the Equivalent Modulus method (stress dependent weighted harmonic mean).

The proposed Winkler model uses the Florida bearing capacity equations coupled with Fenton and Griffiths median modulus for a layer and the equivalent stress dependent weighted harmonic mean modulus in the case of multiple layers. A parametric study involving 64 simulations was performed for different footing widths, shapes, embedment depths, rock dry densities, and layer thicknesses, as well as sand moduli for a comparison between Burmister, finite element method, and the Winkler model. Good agreement was achieved between the three methods, and the Winkler model was proposed for Phase III due to its simplicity and generality.

TABLE OF CONTENTS

DISCLAIMER.....	i
SI (MODERN METRIC) CONVERSION FACTORS (from FHWA).....	ii
TECHNICAL REPORT DOCUMENTATION PAGE	iv
ACKNOWLEDGEMENTS	v
EXECUTIVE SUMMARY	vi
LIST OF TABLES	xii
LIST OF FIGURES	xiv
Chapter 1 Introduction.....	1
Chapter 2 Bearing Capacity of Shallow Foundation on Florida Limestone	4
2.1. Stress-strain Behavior and Volumetric Response	4
2.1.1. Stress-strain Behavior.....	4
2.1.2. Volumetric Response and Poisson’s Ratio	7
2.2. Strength Envelope and Bearing Capacity Equations	11
2.2.1. Intact Rock Strength Envelope and Bearing Capacity Equations	11
2.2.2. Rock Mass Strength Envelope	16
2.2.3. Comparison of Phase I Bearing Capacity vs. Carter-Kulhawy Method.....	18
Chapter 3 Load-settlement Response of a Shallow Foundation on Florida Limestone.....	20
3.1. Load-settlement Response of Shallow Foundation on Rock	20
3.2. Load-settlement Response of a Footing on a Heterogeneous Single Rock Layer.....	24
3.3. Load-settlement Response of a Footing on two-layer heterogeneous System.....	27
Chapter 4 Seismic Testing.....	31
4.1. Introduction.....	31
4.2. Cemex Site	32
4.2.1. 2D Full Waveform Inversion of SH-wave Data.....	33
4.2.2. 3D Full Waveform Inversion of PSV-wave Data	38
4.3. SR-84 Site.....	46
4.3.1. 2D Full Waveform Inversion of SH-wave Data.....	47
4.3.2. 3D Full Waveform Inversion of PSV-wave Data	52
4.4. Bell Site	59
4.5. Conclusion	69
Chapter 5 Load Test at Cemex	71

5.1. Site Investigation	71
5.2. Construction of Load Test.....	76
5.2.1. Micropiles Installation	76
5.2.2. Construction of the Load Test Frame	83
5.3. Bearing Capacity.....	92
5.4. Load-settlement Response.....	99
5.4.1. Finite Element Modeling	101
5.4.2. Fenton and Griffith Method.....	107
Chapter 6 Load Test at SR-84	112
6.1. Site Investigation	112
6.2. Construction of Load Test.....	122
6.2.1. Construction of the Drilled Shaft	122
6.2.2. Construction of the Load Test Frame	136
6.3. Bearing Capacity.....	147
6.4. Load-settlement Response.....	158
6.4.1 Finite Element Modeling	158
6.4.2. Burmister Method.....	164
6.4.3. Proposed FB-Multiplier Settlement of Two-layer System.....	165
Chapter 7 Load Test at Bell	168
7.1. Site Investigation	168
7.2. Construction of Load Test.....	178
7.2.1. Construction of the Drilled Shaft	178
7.2.2. Construction of the Load Test Frame	187
7.3. Bearing Capacity.....	193
7.4. Load-settlement Response.....	198
7.4.1. Finite Element Modeling	198
7.4.2. Burmister Method.....	202
7.4.3. Proposed FB-Multiplier (Winkler Model) Settlement of a Two-layer System.....	203
Chapter 8 Comparison of FEM, Burmister, and Winkler Model Settlement Predictions for Shallow Foundations in Florida Limestone.....	206
8.1. Introduction.....	206
8.2. Parametric Studies.....	206
8.3. Results of Parametric Studies	209

Chapter 9 Worked Examples: Bearing Capacity and Load-settlement response.....	213
9.1. Two Cases in Parametric Study.....	213
9.2. Worked Examples: Single Layer and Rock-over-sand Cases.....	220
9.2.1. Single Layer Case.....	220
9.2.2. Rock-over-sand Case	232
Chapter 10 Conclusions and Recommendations.....	242
LIST OF REFERENCES	247
Appendix A Load Test Design.....	250
Appendix B SPT and Rock Cores for Miami Limestone.....	253
Appendix C Resistivity Test, MWD Profile and SPT Log at Bell Site	265

LIST OF TABLES

Table 2-1 Approximate behavior type table of Florida limestone (reproduced from Phase I)	5
Table 2-2 Strength parameters and bearing pressure of a 15 ft by 15 ft footing for different formation and dry unit weight	15
Table 2-3 Hoek Brown with GSI values versus $REC_{adjusted}$ and Florida bearing capacity equations	19
Table 4-1 Cemex site: soil and rock properties at the footing location	46
Table 4-2 SR-84 site: soil/rock properties at the test footing	58
Table 4-3 Soil properties at the footing location	68
Table 5-1 Summary of compression tests for cement grout	78
Table 5-2 Statistical summary at boring location (RC-2)	98
Table 5-3 Mass strength properties for Cemex site bearing capacity prediction	98
Table 5-4 Bearing capacity calculations for Cemex load test	99
Table 5-5 Strength and stiffness parameters of different layers	105
Table 5-6 Elastic modulus of unconfined compression strength test from Cemex and SR-84 site ..	106
Table 5-7 Stress state, Young's modulus, and Poisson's ratio of different layers in each loading stage	107
Table 5-8 Stress-dependent weighted harmonic mean calculation	108
Table 5-9 Load-settlement prediction calculation: $\gamma(B, T)$ calculation	109
Table 6-1 Summary of bulk dry unit weight of Miami limestone, 3 ft to 13 ft depth	117
Table 6-2 Measured range of properties of bentonite slurry for East shaft	128
Table 6-3 Measured compressive strength of concrete specimens for East shaft	128
Table 6-4 Measured properties of concrete for East shaft	128
Table 6-5 Measured properties of the bentonite slurry for the West shaft	134
Table 6-6 Measured compressive strength of concrete specimens for West shaft	134
Table 6-7 Dry unit weight and modulus profile (B-3)	153
Table 6-8 Summary statistics for B-3 and sand layer	153
Table 6-9 Mass strength properties for SR-84 site bearing capacity prediction	153
Table 6-10 Bearing capacity calculation at SR-84 site	154
Table 6-11 Bearing pressure comparison of the nearest bridge pier spread footings	157
Table 6-12 Material properties of SR-84 finite element model	160
Table 6-13 Stiffness and stress state in each loading step for Miami limestone layer	162
Table 6-14 Burmister calculations for rock-over-sand case	165
Table 6-15 Winkler model calculations for rock-over-sand case	166
Table 7-1. Initial modulus for Ocala limestone (without correction, reproduced of Figure 3-1)	177
Table 7-2. Measured range of properties of bentonite slurry for West shaft	183
Table 7-3. Measured compressive strength of concrete specimens for West shaft	183
Table 7-4. Measured properties of concrete for West shaft	184
Table 7-5. Measured range of properties of bentonite slurry for East shaft	187
Table 7-6. Measured compressive strength of concrete specimens for East shaft	187
Table 7-7. Measured properties of concrete for East shaft	187
Table 7-8 Intact and mass strength envelope conversion	196
Table 7-9 Intact strength versus mass strength properties	196
Table 7-10 Bearing capacity calculation at Bell site	197

Table 7-11. Layering and parameters used in FEM	200
Table 7-12 Burmister’s calculations for rock over sand case (Bell)	203
Table 7-13 Winkler model calculations for rock-over-sand case (Bell)	204
Table 8-1 Variables for parametric study	207
Table 8-2 Rock properties for parametric study: (a) 100 pcf and (b) 110 pcf	208
Table 8-3 Sand properties for parametric study	209
Table 8-4 Rock thickness versus model depth	209
Table 8-5 The settlement ratio of footings with L/B =2 to 1 (square)	209
Table 9-1 Bearing capacities for case a	215
Table 9-2 Burmister solution for case a	216
Table 9-3 Winkler model for case a	217
Table 9-4 Bearing capacities for case c	218
Table 9-5 Burmister solution for case c	219
Table 9-6 Winkler model for case c	220
Table 9-7 Dry unit weight and Modulus profile	223
Table 9-8 Summary statistics	224
Table 9-9 Intact and mass strength envelope conversion	225
Table 9-10 Intact strength versus mass strength properties	225
Table 9-11 Bearing capacity calculations	226
Table 9-12 Layering, modulus, and additional stress	227
Table 9-13 Load-settlement prediction calculation: $\gamma(B, T)$ calculation	229
Table 9-14 Dry unit weight and modulus profile	234
Table 9-15 Summary statistics: rock-over-sand case	234
Table 9-16 Intact and mass strength envelope conversion	235
Table 9-17 Intact strength versus mass strength properties	236
Table 9-18 Bearing capacity for rock-over-sand case	237
Table 9-19 Burmister calculations for rock-over-sand case	239
Table 9-20 Winkler model calculations for rock-over-sand case	240
Table B-1 Adjusted-recovery at the Cemex site	258
Table B-2 B-1 SPT log for Cemex site	262
Table B-3 B-2 SPT log for Cemex site	263
Table B-4 SPT log for SR-84 site	264
Table C-1 Resistivity of different soil types	266

LIST OF FIGURES

Figure 2-1 Measured and predicted stress-strain response for (a) Miami limestone, (b) Ocala limestone and (c) Key Largo (Phase I) limestone under 50-psi confining stress	7
Figure 2-2 Load-settlement response for (a) single layer and (b) rock-over-sand case	7
Figure 2-3 Volume strain versus vertical strain for Ocala, Miami, Key Largo limestone under 50-psi confining stress	9
Figure 2-4 Poisson's ratio versus vertical strain for Ocala, Miami, Key Largo limestone under 50-psi confining stress	10
Figure 2-5 Examples of stress paths (Lambe and Whitman, 1969)	10
Figure 2-6 Volumetric strain versus dry unit weight for isotropic loading	11
Figure 2-7 Intact rock strength envelopes of Miami limestone and Ocala limestone	14
Figure 2-8 Bilinear strength envelope for rock mass from intact rock (Phase I)	18
Figure 3-1 Initial modulus versus dry unit weight: (a) Miami limestone and (b) Ocala and Key Largo limestone (limited data)	23
Figure 3-2 Coefficient of variation (COV or CV) of settlement with varying $\theta_{\ln E}/W_f$ (correlation length/footing width) for single soil layer profile (Fenton & Griffiths, 2002)	24
Figure 3-3 Log-normal distribution of mass modulus	24
Figure 3-4 Random field representation of a single footing	27
Figure 3-5 Burmister solution (Burmister, 1958) deflection factor versus the modulus ratio and rock thickness for rigid footing	29
Figure 3-6 Maximum relative error between equivalent modulus methods (Pantelidis, 2019)	30
Figure 3-7 Vertical interface stress (Fox, 1948)	30
Figure 4-1 Testing setup at the Cemex site in Miami	33
Figure 4-2 Acquisition geometry used for 2D SH-source at the Cemex site. The blue box is the planned foundation location (middle of test array)	34
Figure 4-3 (a) spectral image of measured data from the first shot, (b) initial model based on the spectral analysis, (c) final inverted result of V_s and density, and (d) shear and Young's modulus calculated based on inverted result	36
Figure 4-4 Waveform comparison of a sample shot for observed and estimated data at the end of inversion	37
Figure 4-5 Equation to estimate the relationship between density and S-wave velocity	38
Figure 4-6 Detail of the acquisition geometry used to gather data for the 3D FWI analysis, The blue box is the foundation location.	39
Figure 4-7 Propelled energy generator (PEG) source	40
Figure 4-8 Distribution of V_s and V_p (m/s) for (a) the initial model and (b) final inverted result	41
Figure 4-9 Waveform comparison for a sample shot for observed and estimated data at the end of inversion	42
Figure 4-10 3D rendering of the final inverted result for (a) V_s and (b) V_p with transparent features	43
Figure 4-11 Distribution of (a) density, (b) shear modulus, and (c) the Young's modulus for the analyzed medium	44
Figure 4-12 Testing setup at SR-84 site in Miami	47
Figure 4-13 Acquisition geometry used for SR-84 site	48
Figure 4-14 The shear-beam pressed by the hydraulic jack	48

Figure 4-15 Spectral image of measured data from the first shot and first line of receivers	49
Figure 4-16 Waveform comparison of observed data and estimated data from the final inverted model	51
Figure 4-17 SR-84 site: (a) Density and V_s profiles and (b) shear and Young's moduli.....	51
Figure 4-18 SR-84 site: Equation to estimate the relationship between S-wave velocity and density	52
Figure 4-19 The acquisition geometry used to gather data for the 3D FWI analysis	53
Figure 4-20 SR-84 site: V_s and V_p (m/s) for (a) the initial model (b) the final inverted result	54
Figure 4-21 SR-84 site: 3D rendering of the final inverted result for (a) V_s and (b) V_p with transparent features.....	55
Figure 4-22 SR-84 site: waveform comparison for a sample shot for the observed and estimated data at the end of inversion	55
Figure 4-23 SR-84 site: (a) density, (b) shear modulus, and (c) Young's modulus	57
Figure 4-24 Testing setup at Bell site	59
Figure 4-25 SH-wave testing setup at Bell site	60
Figure 4-26 Acquisition geometry	60
Figure 4-27 The shear-beam pressed by the vehicle wheel	61
Figure 4-28 Spectral image of measured data from the first shot and first line of receivers	62
Figure 4-29 Waveform comparison of observed and estimated data from the final inverted model: (a) line 1 and (b) line 2	63
Figure 4-30 Density and V_s profile for (a) line 1, (b) line 2, (c) line 3, (d) line 4, (e) line 5, and (f) line 6. The blue box in (e) denotes the test foundation location.	65
Figure 4-31 Shear and Young moduli calculated from inverted results for (a) line 1, (b) line 2, (c) line 3, (d) line 4, (e) line 5, and (f) line 6.....	66
Figure 4-32 Bell site: relationship between S-wave velocity and density for data from all six seismic lines.....	67
Figure 5-1 Dimension of planned Cemex site	73
Figure 5-2 Locations of SPT and rock coring tests	73
Figure 5-3 Frequency distribution of bulk dry unit weight at Cemex site.....	74
Figure 5-4 Direct tension strength values versus depth at Cemex site	74
Figure 5-5 Unconfined compression strength values versus depth at Cemex site.....	74
Figure 5-6 Mass strength envelope of Miami limestone at Cemex site	75
Figure 5-7 Variogram for Miami limestone.....	75
Figure 5-8 Tricone drill bit.....	77
Figure 5-9 6 in casing used for drilling	77
Figure 5-10 S5Z WIL-X hydraulic expansive cement	77
Figure 5-11 Schematic of typical fracture patterns (ASTM C39/C39M-20)	79
Figure 5-12 Broken specimens, type "III"	79
Figure 5-13 Drilling process with threaded rods nearby.....	80
Figure 5-14 Placement of 36-ft- and 20-ft-long threaded rods with centralizers	81
Figure 5-15 Grouting process (the grout mixed with ASTM C494 Type D retarder admixture and the ASTM C494 Type F superplasticizer admixture).....	82
Figure 5-16 (a) Drill with clear water-loose holes; (b) drill with polymer mud-tight holes; (c) polymer mud.....	82
Figure 5-17 Eight micropiles after installation.....	83

Figure 5-18 Excavation of tested Pit: (a) bucket teeth of the excavator; (b) pit; (c) excavated rocks (deeper rocks are closer to the screen)	85
Figure 5-19 Water pump	86
Figure 5-20 Pictures of rock pieces from tested pit during excavation: high variability with low (middle) and high (left) porosity of Miami limestone	86
Figure 5-21 D-rings welded on the plates and the new load spreader	88
Figure 5-22 Twelve bricks under support systems at each end of girders	88
Figure 5-23 Bubble level on the two wide flange beams	89
Figure 5-24 Pyramid load spreader	89
Figure 5-25 Hydraulic jack and load cell setup	90
Figure 5-26 (a) locations of tape measures and measuring frame; (b) total station	91
Figure 5-27 Completed construction of load test at Cemex site	92
Figure 5-28 Measured bearing capacity versus displacement curve and predicted bearing capacity	95
Figure 5-29 Inclination of the loading jack and load cell	96
Figure 5-30 Depth versus dry unit weight at RC-2	97
Figure 5-31 Adjusted-recovery ($REC_{adjusted}$) versus E_m/E_i	101
Figure 5-32 Differential settlement	103
Figure 5-33 Different elastic modulus of Miami limestone with different bulk dry unit weights	103
Figure 5-34 Different elastic modulus of Miami limestone under the different confining pressure	104
Figure 5-35 Yielded zone and motion field under different load: (a) 4.52 tsf; (b) 7.0 tsf; (c) 8.5 tsf (Lambe and Whitman, 1969)	104
Figure 5-36 Finite element model	105
Figure 5-37 Finite element vs. measured results	106
Figure 5-38 Measured and predicated Bearing stress versus Displacement Curve	111
Figure 6-1 SR-84 site picture and test layout	113
Figure 6-2 Locations of rock coring and SPT tests	114
Figure 6-3 Subsurface layering system at SR-84 Site	115
Figure 6-4 Distribution of (a) density, (b) shear modulus, and (c) the Young's Modulus for the SR-84 site (reproduced of Figure 4-23)	116
Figure 6-5 Unconfined compression strength versus depth at SR-84 site	118
Figure 6-6 Direct tension strength versus depth at SR-84 site	119
Figure 6-7 Mass strength envelopes of 109 pcf and 145 pcf, Miami limestone, SR-84 ($REC_{adjusted} = 78\%$)	119
Figure 6-8 Mass strength envelope of 129 pcf and 137 pcf, Fort Thompson limestone, SR-84 ($REC_{adjusted} = 78\%$)	120
Figure 6-9 Comparison of mass strength envelope at 109 pcf, 110 pcf, 115 pcf, and 145 pcf, for Miami limestone ($REC_{adjusted} = 78\%$)	120
Figure 6-10 Coefficient of variation of settlement with varying θ_{lnE}/W_f for a two soil layers profile. θ_{lnE}: scale of fluctuation; W_f: footing width. (Kuo, et al., 2004)	121
Figure 6-11 Design of the drilled shaft at SR-84 site	123
Figure 6-12 Picture of steel rebar cages: (a) templates position: top, middle, bottom; (b) William threaded rods with templates secured by the nuts; (c) 8 of No. 10 rebars; (d) rebar cages at the site; (e) unloading the rebar cages at the site	124
Figure 6-13 Miami limestone layer: (a) excavated down to 15 in; (b) excavated down to 3 ft.	125

Figure 6-14 First attempt to install the west shaft	126
Figure 6-15 Drilling for the East shaft: (a), (b), and (c): 42-in rock auger bit; (d): 42-in temporary casing.....	129
Figure 6-16 Change to the 36-in rock auger bit	130
Figure 6-17 Bailing bucket	130
Figure 6-18 (a) Placement of the rebar cage (b) spacer installation.....	131
Figure 6-19 Measure the depth of the top of the threaded rods (2 ft from the ground surface) and align the drilled shafts	132
Figure 6-20 (a) mounted boom concrete pump truck and concrete truck; (b) delivery pipe and end hose.....	132
Figure 6-21 Temporary casing pull out and concrete overflow	133
Figure 6-22 Picture of the east drilled shaft after two days of installation	133
Figure 6-23 (a) drilling for the West shaft; (b-c) placement of the steel rebar cage; (d) spacers installation; (e) extension bar for alignment; (f) alignment and elevation measurement.....	135
Figure 6-24 (a-b) concrete pumping; (c) overflow	136
Figure 6-25 Stands to support the girders	138
Figure 6-26 Fast setting concrete placement	139
Figure 6-27 Bricks and wood spacers on top of shafts beneath test stands	139
Figure 6-28 (a) stands on the top of bricks; (b-d) stands are leveled in both directions.....	140
Figure 6-29 Placement of girders: (a-b) girders lifted by the crane; (c) using forks to against the girders; (d) ratchet straps around the girders.....	142
Figure 6-30 Installation of two sets of C channels and plates	143
Figure 6-31 Eight steel plates representing the footing. (a): lower 4 steel plates, top to down: 4 ft by 4 ft, 4 ft by 4 ft, 4 ft by 6 ft and 5 ft by 6 ft; (b): upper 4 steel plates, top to bottom: 28 in by 28 in, 28 in by 28 in, 36 in by 36 in and 42 in by 42 in.....	144
Figure 6-32 Measuring system. (a): from a ground surface view; (b): bricks used to make the scaffolding base plate fully contact with the footing (5 ft by 6 ft steel plate).....	145
Figure 6-33 Completed construction of the load test at SR-84	146
Figure 6-34 Load versus loading time curve	148
Figure 6-35 Load versus settlement curve	148
Figure 6-36 (a) picture of 28 in by 28 in steel plate before test; (b) picture of 28 in by 28 in steel plate after test; (c) picture of 48 in by 48 in steel plate after test with settlements at each location	150
Figure 6-37 (a) experimental setup for footing residing on a sand layer overlying soft clay; (b) stress-settlement relationships for sand over clay. (Kenny et al., 1997).....	151
Figure 6-38 Bearing capacity predictions and load versus settlement curve.....	155
Figure 6-39 Boring and pier locations at the SR-84 site (I-75 express lanes segment E).....	156
Figure 6-40 Effective friction angle and SPT N-value (Peck et al., 1974)	158
Figure 6-41 Geometry of finite element modeling.....	160
Figure 6-42 Numerical results of SR-84 finite element model	161
Figure 6-43 Shear failure plane in Miami limestone layer under 23-tsf load	162
Figure 6-44 Photos of the failure mechanism observed in the plate load tests (a) $H/D = 0.25$; (b) $H/D = 1$. H = thickness of top strong layer: D = footing width (plate load tests on cemented soil layers overlying weaker soil, (Consoli et al., 2009))	163
Figure 6-45 Measured vs. Winkler model vs. Burmister’s solution: load-settlement response	167

Figure 7-1. (a) Site investigation zone and boring location at Bell site and (b) top rock surface depth based on 200 hand auger holes at Bell site.....	172
Figure 7-2. Subsurface layering at Bell site	173
Figure 7-3. Distribution of density and shear velocity for (a) seismic line 5 and (b) seismic line 6 (reproduced of Figure 4-31)	174
Figure 7-4. Unconfined compression strength versus depth at the Bell site	175
Figure 7-5. Direct tension strength versus depth at Bell site.....	175
Figure 7-6. Comparison of intact strength envelopes between Miami limestone and Ocala limestone from 85 pcf to 105 pcf (reproduced of Figure 2-7).....	176
Figure 7-7. Measured vs. FEM stress-strain relationship for 50-psi confining stress triaxial tests (reproduced of Figure 2-1b).....	177
Figure 7-8. Design of the drilled shaft at Bell site	179
Figure 7-9. Picture of steel rebar cages: (a) templates position: top, middle, bottom and (b) William threaded rods with templates secured by the nuts and (c) 8 of No. 10 rebars.....	180
Figure 7-10. Construction of West shaft: (a) casing placement; (b) bailing bucket to clean the hole; (c) rebar cage installation; (d) installation of spacers for rebar cage and (e) concrete pumping	183
Figure 7-11. Sinkholes that opened during the East shaft construction: (a) 12” chimney sinkhole opened at 45ft depth near the East shaft; (b) filling the east shaft with asphalt waste (rap) to plug the chimney sinkhole alongside the shaft and (c) another sinkhole at 15’ depth in wall of the East shaft.....	186
Figure 7-12. Completed construction of the East shaft: (a) cage spacer installations and (b) leveling both shafts.....	186
Figure 7-13. Footing location excavation (circles identify soil-filled voids).....	189
Figure 7-14. One in concrete leveling pad for placement of the steel foundation elements	190
Figure 7-15. Construction of the load test: (a) excavation of 5 ft of overlying topsoil and placement of stands with threaded rods and (b) placement of steel plates, steel box sections, jack, and load cell	191
Figure 7-16. Measuring system: (a) auto-level to measure vertical deformations of the foundation and (b) four corner and center vertical scales to measure vertical deformations: 1, front left (FL); 2, front right (FR); 3, hydraulic jack, middle (courtesy of AFT); 4, rear left (RL); 6, rear right (RR)	192
Figure 7-17. Measured load test results and bearing capacity at Bell site.....	195
Figure 7-18. Measured results at SR-84 site, second load test	195
Figure 7-19 Tension cracks after load test.....	198
Figure 7-20. Finite element modeling for Bell load test.....	200
Figure 7-21. Measured vs. predicted load-settlement response	201
Figure 7-22. Relative shear stress contour at the bearing stress of 14.8 tsf.....	201
Figure 7-23. Measured vs. Winkler model vs. Burmister’s solution: load settlement response (Bell)	205
Figure 8-1 Representative cases: (a) 3 ft rock thickness, 110 pcf, B = 6 ft, square footing, no embedment, loose sand; (b) 16 ft rock thickness, 110 pcf, B = 16 ft, square footing, 8 ft embedment, loose sand; (c) 3 ft rock thickness, 100 pcf, B = 6 ft, L/B = 2, 3 ft embedment, loose sand; (d) 6 ft rock thickness, 100 pcf, B = 6 ft, L/B = 2, 3 ft embedment, dense sand	211
Figure 8-2 Parametric study between Burmister, Winkler, and Finite element models (settlement up to rock failure)	212

Figure 9-1 Dry unit weight versus depth: single layer case	222
Figure 9-2 100 pcf intact and mass strength envelope	224
Figure 9-3 Boussinesq stress chart, interpolated between the strip and square footings (Lambe and Whitman, 1969)	228
Figure 9-4 Load-settlement prediction of single layer case	231
Figure 9-5 Limestone dry unit weight versus depth (3 ft to 13 ft)	233
Figure 9-6 Sand layer SPT N versus depth (13 ft to 33 ft)	233
Figure 9-7 105 pcf intact strength envelope and mass strength envelope	235
Figure 9-8 Load-settlement prediction for rock over sand case	241
Figure A-1 Load test design for Cemex site	250
Figure A-2 Load test design at SR-84 site	251
Figure A-3 Load test design at Bell site	252
Figure B-1 RC 1 run 1 and run 2	253
Figure B-2 RC 1 run 3 and run 4	254
Figure B-3 RC 1 run 5 and run 6	255
Figure B-4 RC 2 run 1 and run 2	256
Figure B-5 RC 2 run 3 and run 4	257
Figure B-6 RC 2 run 5 and run 6	258
Figure B-7 Pictures of rock cores for B-1. (a): 3 ft – 13 ft; (b): 33 ft – 43 ft; (c): 68 ft – 73 ft	259
Figure B-8 Pictures of rock cores for B-2. (a):3 ft – 13 ft; (b): 33 ft – 43 ft; (c): 43 ft – 53 ft	260
Figure B-9 Pictures of rock cores for B-3. (a): 3 ft – 13 ft; (b): 33 ft – 43 ft; (c): 43 ft – 53 ft	261
Figure C-1 Resistivity test	265
Figure C-2 MWD profile: q_u versus depth	266
Figure C-3 SPT log of boring B2 and B3	267

Chapter 1 Introduction

The FDOT is investigating the use of shallow foundations to replace deep foundations (piles, drilled shafts, etc.) for support of bridge piers when limestone is near the ground surface (e.g., south Florida). FDOT research project BDV31-977-51 investigated the strength envelope of several Florida limestone formations as well the bearing capacity of shallow foundations residing on limestone. Due to the porous nature of Florida limestone, the research revealed that the strength envelope of the rock is curved (concave downward), but appreciable bearing resistance is available depending on unit weight (strength) of the limestone. FDOT BDV31-977-51 recommended that a phase II “Field Testing of Shallow Foundation on Rock” be undertaken to verify the developed bearing capacity equations as well as provide much needed load vs. settlement response for footing settlement analyses for service design as well as Phase III “Implementation of Shallow Foundation Design in Florida Limestone for FB-MultiPier”.

The objective of this research (Phase II) is to validate the bearing capacity equations developed in FDOT research project BDV31-977-51, as well as obtain load vs. settlement data and verify and develop methods for predicting shallow foundation settlements. The results of Phase I (FDOT BDV31-977-51) and this project will be used for implementation (Phase III) in FB-MultiPier for the design of shallow foundations beneath bridge piers. Besides load vs. settlement and bearing capacity, the project will look at newer seismic methods for assessing mass properties (Shear modulus G , Young’s modulus, E , and density/unit weight, γ) of rock beneath the foundation necessary for design.

To address these objectives, this report is organized as follows:

- Chapter 2: Overview of Florida limestone stress-strain relationship, volumetric response under triaxial conditions. Review of Florida limestone strength envelope and Bearing capacity equations. Emphasis of mass effect.
- Chapter 3: Overview of load-settlement response for general shear failure and punching shear failure. Emphasis of high variability of Florida limestone.
- Chapter 4: The newer seismic testing at each site and corresponding results.
- Chapter 5 to Chapter 7: Three load tests on single limestone layer (Chapter 5), rock over sand (Chapter 6) and strong rock over weak rock (Chapter 7). The site investigation, validation of Bearing capacity equations and development of load-settlement response prediction are discussed in each chapter.
- Chapter 8: Parametric study between the developed load-settlement response prediction, Burmister method and the nonlinear Finite Element method.
- Chapter 9: Worked examples with detailed procedures.
- Chapter 10: Summary, Conclusions and Recommendations.

The study highlights the following key findings: i) Three load tests were conducted and the Florida Bearing Capacity Equations were validated; ii) The load-settlement response prediction for single layer and rock over sand case were developed based on the bi-linear stress-strain relationship (initial modulus and secant modulus at 2% strain); iii) The influence of high variability of Florida limestone cannot be neglected, and it may result in larger differential settlements depending on the size of the footings; iv) At least 20 to 25 tested cores within the footing influence zone are recommended in order to obtain representative strength and modulus parameters (e.g., geomean) as well as layering; v) Seismic shear testing should be considered as alternative to obtain mass dry unit weight, variability, and layering; vi) The high porosity and

voids of Florida limestone reveals that mass properties of rock are different than the intact specimen and may be accounted for (strength and modulus) based on the adjusted-recovery; and vii) adjusted-recovery should be assigned based on testable (q_u , q_t , and triaxial) samples with smaller pieces used to assess dry unit weights within core run: and viii) proper rock sample storage and index measurement is required (i.e., porosity or dry unit weight measurements).

Chapter 2

Bearing Capacity of Shallow Foundation on Florida Limestone

2.1. Stress-strain Behavior and Volumetric Response

2.1.1. Stress-strain Behavior

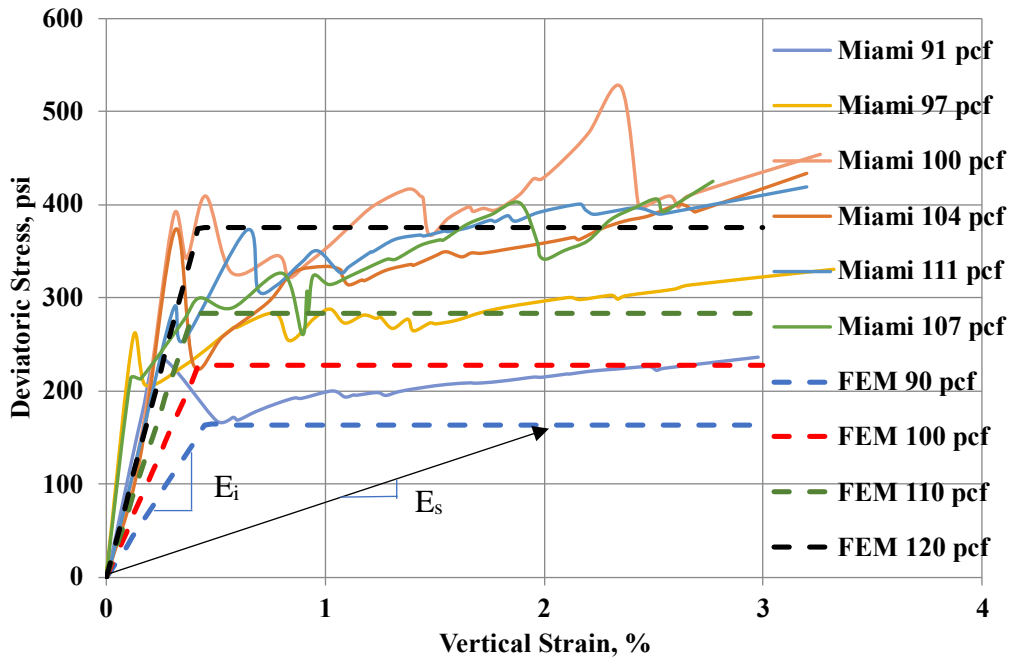
Generally, the stress-strain behavior of Florida limestone can be separated into two groups: brittle and ductile based on the dry unit weight and confining stress, Table 2-1. However, at shallower depths (i.e., within the 15 ft from the ground surface), the dry unit weight of limestone is commonly less than 110 pcf and most of rock is either ductile or in transition phase (Table 2-1) depending on confining stress. The confining stress under footing is a function of the bearing pressure and the Poisson's Ratio of the rock, which will be discussed in the next section.

In this section, the ductile stress-strain behavior of Florida limestone from the triaxial tests (50 psi confining stress – typical field lateral stress at bearing) is presented in Figure 2-1, which is a function of formation (Miami, Anastasia, Ocala, etc.) and dry unit weight of rock. The ductile stress-strain behavior (i.e., loading to large strains) can be approximated as bi-linear curve: linear up to yielding then a flat line. The modulus of linear portion is defined as the initial modulus (E_i) and the modulus from the origin to any points on the flat line is defined as the secant modulus (E_s). It is noted that the secant modulus is a function of the strain level, which for a footing depends on the size of the footing, settlement, and the thickness of bearing rock layer. Given the constant E_i of the rock to yield/failure, it is believed that the load-settlement response of shallow foundation on a homogeneous layer can be approximated as a linear line up to rock yield/failure, then a constant resistance with large settlements, Figure 2-2a. In the case of the rock over sand, a bi-linear load-settlement response, Figure 2-2b is expected. Note, even though the rock has undergone punching shear, the sand will undergo increased resistance due to its

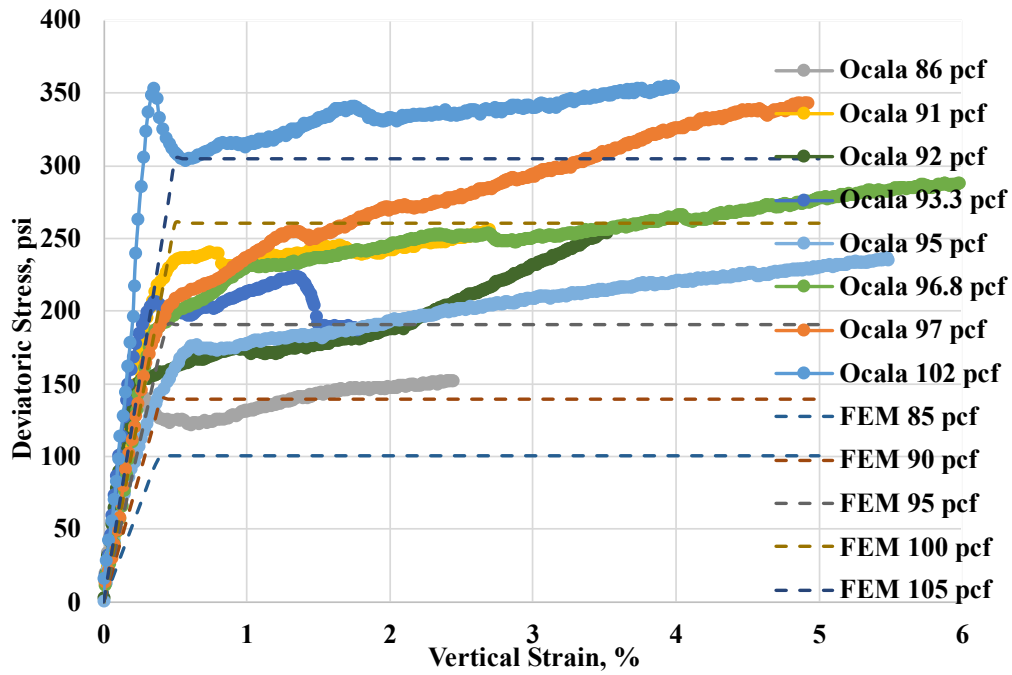
confined (rock above) behavior. For stresses less than bearing, a linear response (initial Young's modulus, E_i of the rock and soil) are employed. However, after punching shear failure of the rock (bearing capacity of rock), the second line of the load-settlement response is predicted by using the secant shear modulus, E_s of the rock at 2% strain as discussed in Chapter 8 is employed. The 2% strain is based on the Canadian Foundation Engineering Manual which recommends design bearing pressure for Service Limit states not to exceed 1 in of settlement for foundations on rock (Canadian Geotechnical Society, 2006). For instance, a 5 ft thick rock layer beneath a footing at 2% strain would yield 1.2 in of settlement. Also note the E_i and E_{sand} will be used to obtain the bearing pressure for the rock over sand required for the Florida Bearing Capacity equations, which are used in all load vs. deformation predictions (Figure 2-2 a & b) and settlement models (Burmister, Winkler Model, etc.) discussed in Chapter 8.

Table 2-1 Approximate behavior type table of Florida limestone (reproduced from Phase I)

σ_3 (MPa)	σ_3 (psi)	Bulk Dry Unit Weight Range (pcf)					
		60-65	66-85	86-110	111-120	121-130	130-135
0.1	15	Transition	Transition	Brittle	Brittle	Brittle	Brittle
0.3	50	Ductile	Transition	Transition	Brittle	Brittle	Brittle
0.9	130	Ductile	Ductile	Transition	Transition	Brittle	Brittle
1.4	200	Ductile	Ductile	Ductile	Transition	Transition	Brittle
2.1	300	Ductile	Ductile	Ductile	Ductile	Transition	Transition
4.1-6.9	600-1,000	Ductile	Ductile	Ductile	Ductile	Ductile	Transition
6.9-20.7	1,000-3,000	Ductile	Ductile	Ductile	Ductile	Ductile	Ductile

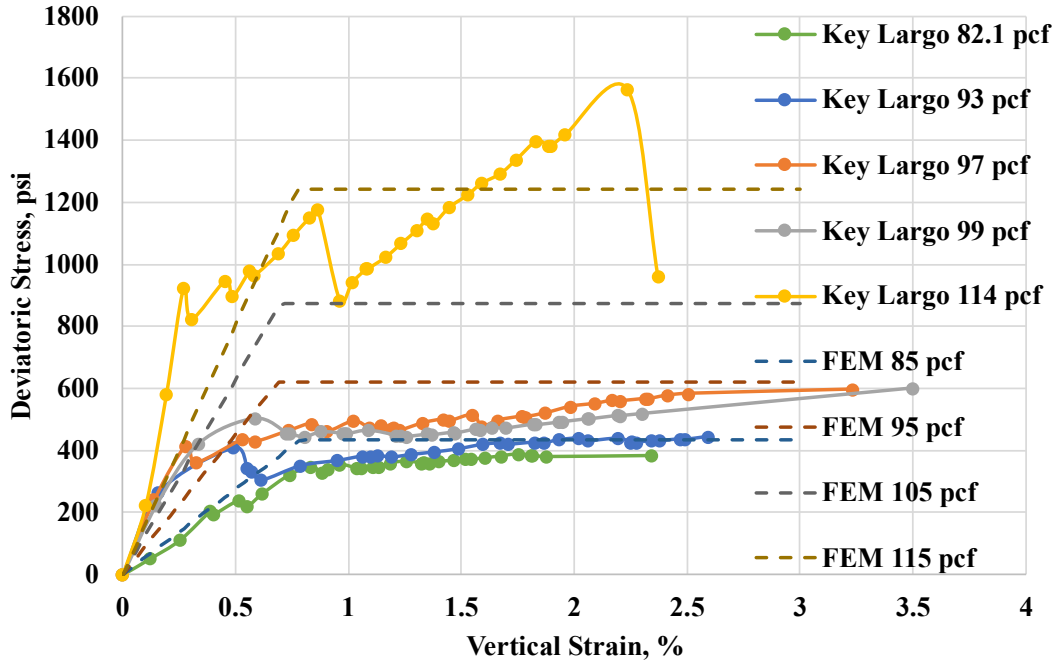


(a)



(b)

Figure 2-1 Measured and predicted stress-strain response for (a) Miami limestone, (b) Ocala limestone and (c) Key Largo (Phase I) limestone under 50-psi confining stress



(c)

Figure 2-1 Measured and predicted stress-strain response for (a) Miami limestone, (b) Ocala limestone and (c) Key Largo (Phase I) limestone under 50-psi confining stress

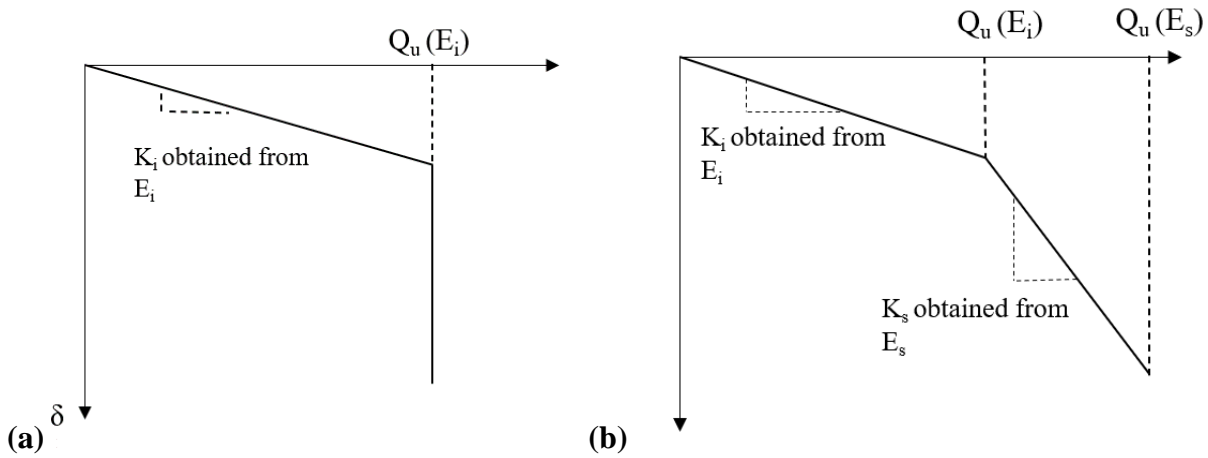


Figure 2-2 Load-settlement response for (a) single layer and (b) rock-over-sand case

2.1.2. Volumetric Response and Poisson's Ratio

Significantly impacting the bearing resistance and vertical settlement beneath the footing are the lateral stress changes (e.g., $\epsilon_v = \frac{1}{E} [\Delta\sigma_v - \mu(\Delta\sigma_H + \Delta\sigma_L)]$). For instance, knowing the horizontal to vertical stress ratio, K (Eq. 2-1), the stress path (p - q , Eq. 2-2) may be established

(Figure 2-5) and stress vs strain response may be found. Influencing the latter is the Poisson's ratio (Eq. 2-1) of the rock up to failure/yield.

$$K = \frac{\mu}{1-\mu} = \frac{\sigma_h}{\sigma_v} \quad (2-1)$$

$$\frac{q}{p} = \frac{1 - K}{1 + K} \quad (2-2)$$

Ductile stress-strain behavior is generally indicative of contractive volumetric response due to the porous nature of the Florida limestone (Phase I). For instance, shown in Figure 2-3 is the contractive measured volumetric strain versus the vertical strain at 50 psi confining stress, triaxial compression tests for multiple limestone formation. Using the volumetric and axial strain, the horizontal strain may be found along with the Poisson's ratio ($\mu = -\frac{\epsilon_H}{\epsilon_V}$). Shown in Figure 2-4 is measured the Poisson's ratio versus the vertical strain from 50 psi confining stress tests. A few tests show negative Poisson's ratio under the initial loading which indicates the specimen was undergoing crushing due to their porous nature. However, at yielding/failure (0.5% to 0.7% strain), the average Poisson's ratio of approximately 0.1 is obtained. Subsequent FEM analysis of footing on rock to bearing failure with a Poisson ratio of 0.1, supports a lateral stress at $3R/2$ (Lambe and Whitman average point, 1969) of approximately 50 psi (i.e., recommended triaxial confining pressure) when assessing Young's Moduli.

Also of interest is the volumetric response of the rock under isotropic loading ($K=1$, Figure 2-5) which occurs when applying the cell pressure prior to shearing (axial stress) when assessing the Mohr-Coulomb strength envelope of the rock. Shown in Figure 2-6 is the volumetric response of Miami, Key Largo, and Anastasia formations at application of 50 psi confining stress. Evident from Figure 2-6, Miami, Key Largo, and Anastasia has significant more

contractive behavior (crushing) for low dry unit weight (less than 110 pcf) compared to Ocala. This behavior is a major reason why Ocala does not exhibit a change Mohr-Coulomb strength with higher pressures as the Miami, Key Largo and Anastasia (e.g., 300 psi) formations undergo.

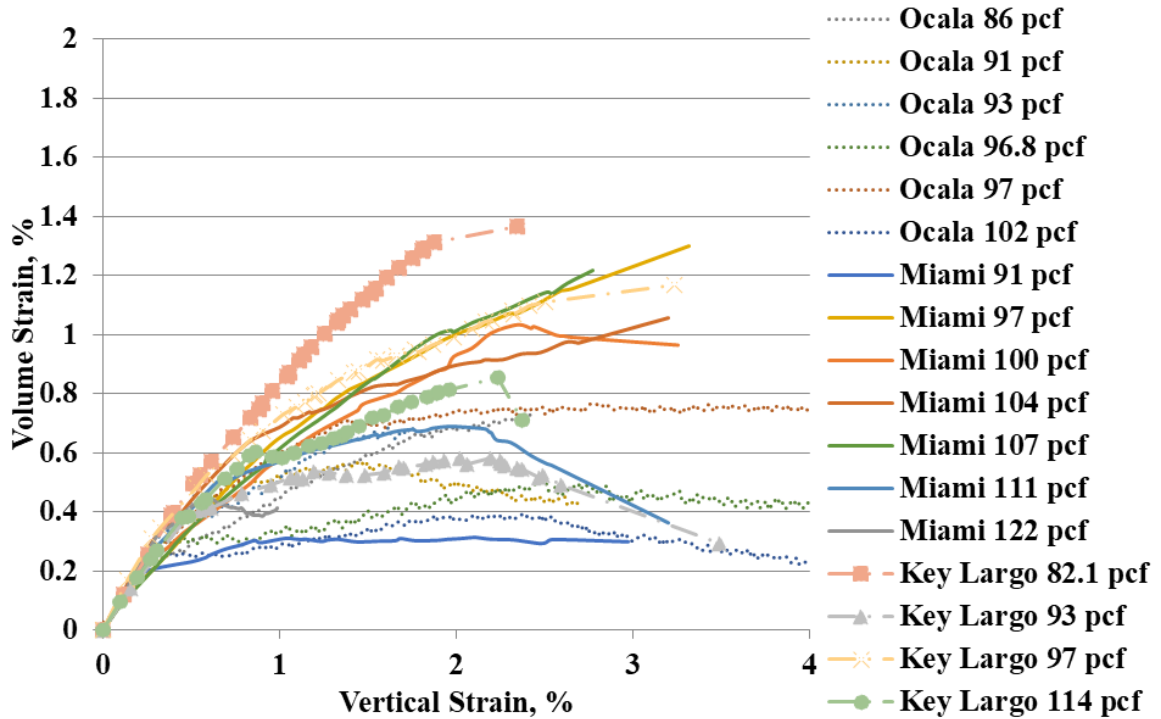


Figure 2-3 Volume strain versus vertical strain for Ocala, Miami, Key Largo limestone under 50-psi confining stress

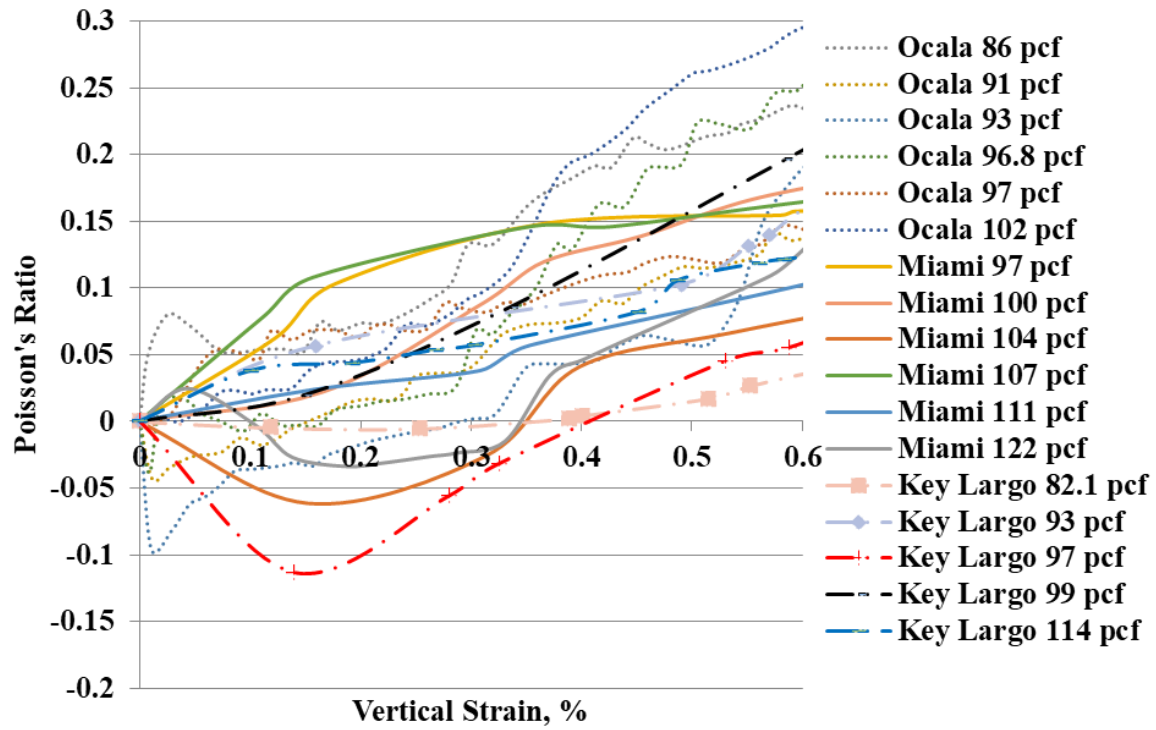


Figure 2-4 Poisson's ratio versus vertical strain for Ocala, Miami, Key Largo limestone under 50-psi confining stress

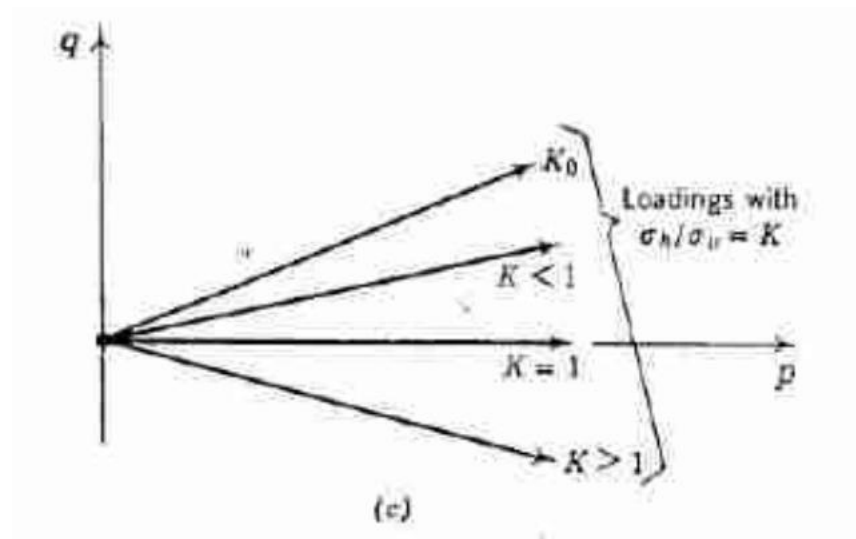


Figure 2-5 Examples of stress paths (Lambe and Whitman, 1969)

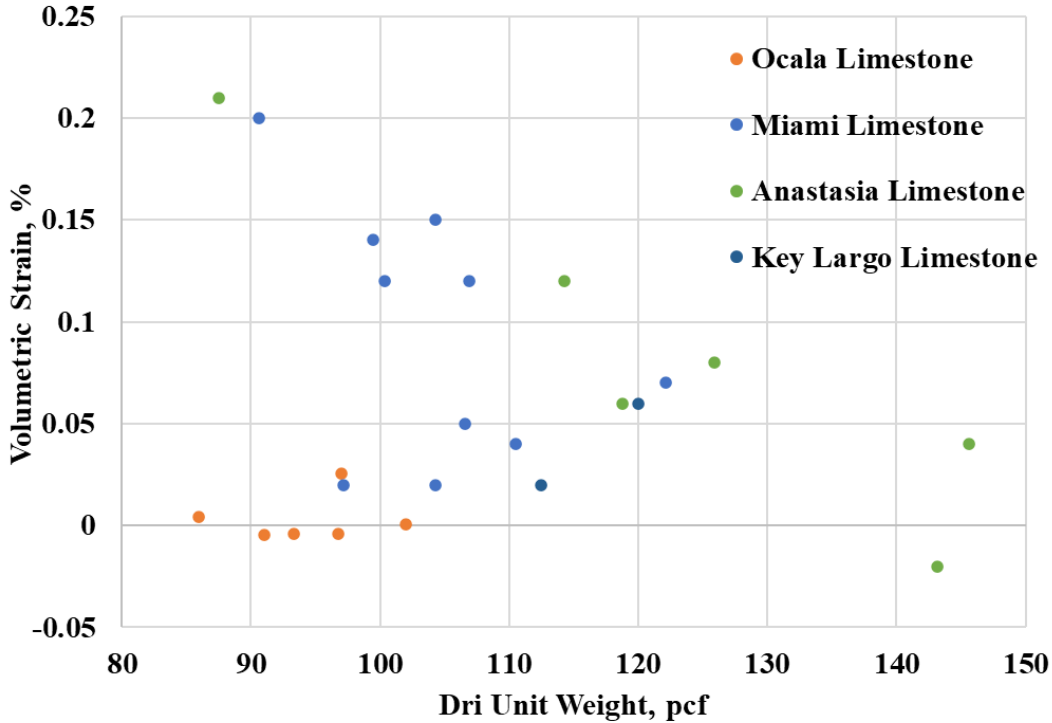


Figure 2-6 Volumetric strain versus dry unit weight for isotropic loading

2.2. Strength Envelope and Bearing Capacity Equations

2.2.1. Intact Rock Strength Envelope and Bearing Capacity Equations

The strength envelopes of multiple rock formations for different dry unit weight were developed from core samples tested under multiple stress states (split tension, unconfined compression, and triaxial compression at 50 psi, 130 psi, and 600 psi) in Phase I. As part of the load tests at each site, intact rock core samples were recovered and tested at the SMO. For this research, it was observed that the rock strength envelope for Miami reported in Phase I were accurate based on their dry unit weight. In addition, the strength envelope for the Ocala formation was developed based on dry unit weight and is presented in Figure 2-7 for a comparison with the Miami formation. Evident, the Ocala formation does not exhibit the loss of strength at the higher confining pressures (e.g., 130 psi and 600 psi). As discussed earlier

(section 2.1.2) this is attributed to particle microcracking (crushing) under isotropic loading ($K=1$), of Miami, Key Largo, etc. vs. Ocala formations.

The bi-linear strength envelope of Florida limestone in Lambe's p-q space is formulated in Equations 2-3. The bi-linear Mohr-Coulomb strength parameters are given in both τ - σ (c , ϕ , and ω and σ_p , Eq. 2-4) and p-q space (Eq. 2-5) with strength parameters: a , α , β and P_p . Note, the change in slope of the strength envelope occurs at σ_p in τ - σ plot and P_p in the p-q plot. The P_p location is a conservative representation of the onset of ductile flow (crushing and cementation breakage), which is corresponding to the confining stress at 50 psi (Eq. 2-6).

Given the strength envelope, researchers in Phase I used the linear elastic perfectly plastic model with bi-linear Mohr-Coulomb strength to model different geometries of footing (strip to square footing) and boundary conditions (rock over sand) and developed the Florida limestone bearing capacity equations (Eqs. 2-7 to 2-18). The equations can account for any footing width (n , a function of footing width, B), shape (ξ), embedment depth (N_q) and rock over sand (N_R) scenario. Note, Q_u is the minimum of Q_{u1} and Q_{u2} , which reflects the stress state occurring on the initial slope (ϕ), or the reduced slope (ω), which is a function of the dry unit weight, formation, and the adjusted-recovery. For the rock over sand case, as the rock thickness (T) or the modulus ratio (E_{soil}/E_{rock}) increase, smaller rock over sand reduction factor and higher bearing capacity of upper rock layer will be obtained.

Presented in Table 2-2 is the digital strength parameters by formation and dry unit weights and corresponding bearing pressure for a representative 15 ft by 15 ft footing (no embedment, single rock layer) by using the Equations 2-7 ~ 2-18. Please note that the values shown in Table 2-2 were derived from intact rock specimens instead of rock mass parameters. To account for

rock mass behavior and its influence on the bearing pressures, the adjusted-recovery must be introduced. For instance, for $REC_{adjusted} = 80\%$, the 105 pcf Miami limestone's bearing resistance would reduce from 61 tsf (Table 2-2) to 25.1 tsf. Discussion of reduction is presented in the next section.

$$F = \begin{cases} q - (\tan\alpha)p - a & \text{if } p \leq p_p \\ q - (\tan\alpha - \tan\beta)p_p - (\tan\beta)p - a & \text{if } p > p_p \end{cases} \quad (2-3)$$

$$c = 0.5\sqrt{q_u q_{dt}}; \sin\phi = \frac{q_u - q_{dt}}{q_u + q_{dt}} \quad (2-4)$$

$$\sin\phi = \tan\alpha; a = c \cos\phi; \sin\omega = \tan\beta \quad (2-5)$$

$$p_p \text{ (psi)} = \frac{50+a}{1-\tan\alpha} = \frac{50+c \cos\phi}{1-\sin\phi} \quad (2-6)$$

$$Q_u = \min(Q_{u1}, Q_{u2}) \times \xi / N_R \quad (2-7)$$

$$Q_{u1} = n \times c \times N_c + q \times N_q \quad (2-8)$$

$$Q_{u2} = n \times [c \times N'_c + p_p \times N_\gamma] + q \times N_q \quad (2-9)$$

$$n = \left(\frac{4}{B \text{ in meter}} \right)^{-0.055} \quad \text{or} \quad n = \left(\frac{4}{0.3B \text{ in ft}} \right)^{-0.055} \quad (2-10)$$

$$\xi = \text{shape factor} = 1 + 0.245 \left(\frac{B}{L} \right)^{0.66} \quad (2-11)$$

$$N_R = \text{Rock thickness reduction factor} \quad (2-12)$$

$$N_R = 0.86 * R^{-0.25} \text{ if } R < 0.3$$

$$N_R = 1.2 - 0.1 \times R \text{ if } R \geq 0.3$$

$$R = T^2 E_{soil} / E_{rock}, \text{ limit } R \text{ to } 2.0 \quad (2-13)$$

$$T = \text{Rock thickness in meter (if } T \text{ is in ft, then } R = 0.093 T^2$$

$$E_{soil} / E_{rock})$$

$$E_{soil} / E_{rock} = \text{Modulus ratio of soil and rock layers}$$

$$N_c = \frac{1.8 \cos\phi}{0.8 - \sin\phi} \quad (2-14)$$

$$N'_c = \frac{1.8 \cos\phi}{0.8 - \sin\omega} \quad (2-15)$$

$$N_\gamma = \frac{1.8 [\sin\phi - \sin\omega]}{0.8 - \sin\omega} \quad (2-16)$$

$$q = \gamma' \times D \quad (2-17)$$

$$N_q = \left(1.5 \times \frac{p_p}{\sigma_a} - 10 \right) \times (3 \times \sin\phi - 1) \quad (2-18)$$

$$\sigma_a = \text{Sea level standard atmospheric pressure}$$

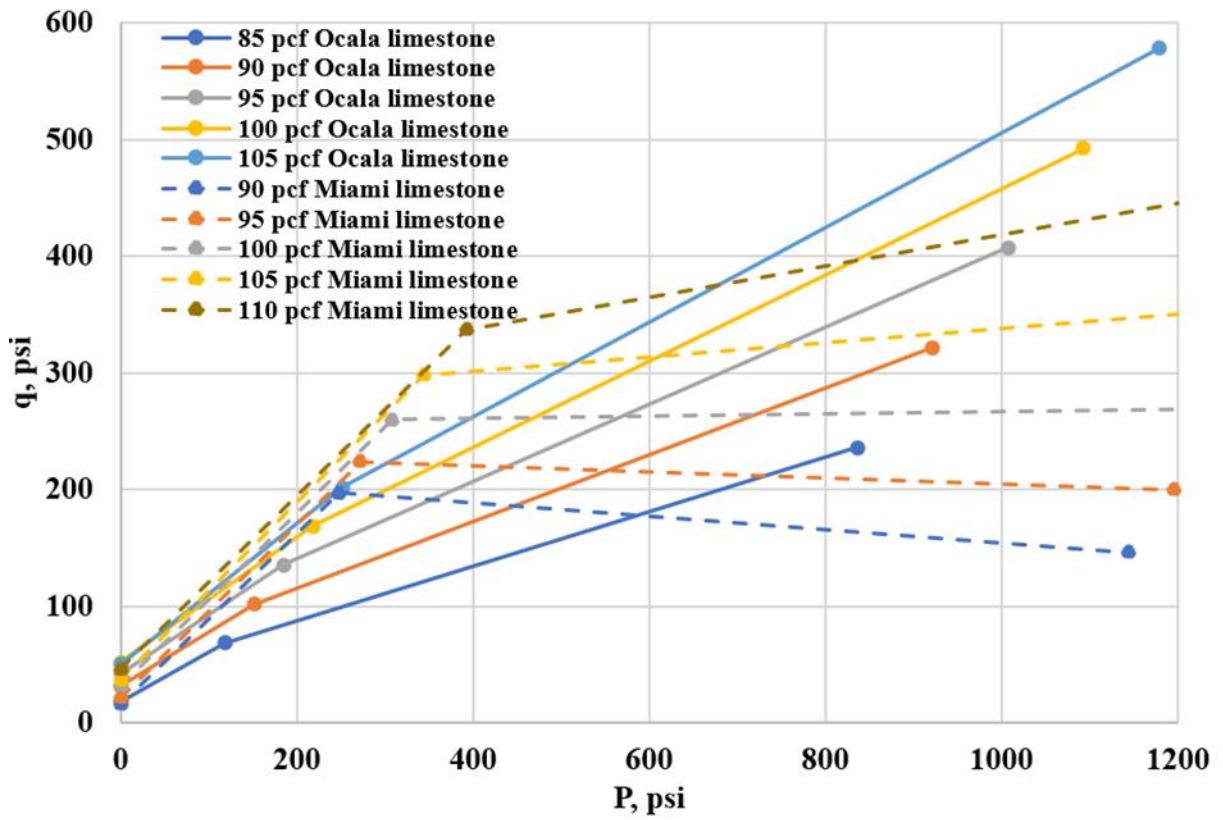


Figure 2-7 Intact rock strength envelopes of Miami limestone and Ocala limestone

Table 2-2 Strength parameters and bearing pressure of a 15 ft by 15 ft footing for different formation and dry unit weight

Formation	γ_{dt} , pcf	c, psi	ϕ , °	σ_p , psi	ω , °	a, psi	α , °	P_p , psi	β , °	Q_u , tsf
Miami Limestone	90	23.4	46.9	446	-3.2	16	36.1	248	-3.2	37.3
	95	32.2	48.0	494	-1.5	21.5	36.6	272	-1.5	45.4
	100	47.6	47.8	566	0.5	32	36.5	308	0.5	52.8
	105	56.9	49.5	638	3.5	37	37.2	344	3.5	61.0
	105 (80%)	37.3	37.5	582.8	2.8	29.6	31.3	344	2.8	25.1
	110	68.7	47.9	734	7.7	46	36.6	392	7.6	69.4
	115	81.8	49.6	846	11.6	53	37.3	448	11.3	82.5
	120	107.4	50.0	966	16.5	69	37.5	508	15.8	98.8
	125	133.5	50.4	1126	22.1	85	37.6	588	20.6	121.5
Anastasia Limestone	90	43.8	38.8	428.9	-6.7	34.1	32.1	239.4	-6.7	31.9
	95	53.5	40.0	479.7	-6.7	41.0	32.8	264.9	-6.7	42.5
	100	61.8	40.5	551.0	-6.4	47	33.0	300.5	-6.4	49.1
	105	83.5	42.6	622	-6.7	61.4	34.1	336	-6.7	58.1
	110	97.7	42.8	722	-6.7	71.7	34.2	386	-6.7	67.1
	115	113.5	43.8	846	-6.7	81.9	34.7	448	-6.6	78.7
	120	144.9	45.2	978	-6.7	102	35.4	514	-6.6	93.4
	125	176.2	45.7	1140	-4.3	123	35.6	595	-4.3	110.2
	130	208.9	46.8	1344	1.6	143	36.1	697	1.6	132.8
	135	255.0	47.0	1600	10.8	174	36.2	825	10.6	165.0
	140	300.4	48.0	1904	23.6	201	36.6	977	21.8	217.6
Hawthorn Limestone	85	9.4	43.2	381.2	1.4	6.8	34.4	215.6	1.4	9.6
	90	14.6	45.4	412	2.6	10.3	35.5	231	2.6	19.1
	95	19.8	46.2	453.21	4.2	13.7	35.8	251.6	4.2	28.6
	100	25.5	47.8	514.9	6.3	17.1	36.5	282.4	6.2	45.9
	105	31.3	49.0	576.6	9.1	20.5	37.1	313.3	9.0	52.5
	110	42.7	50.1	638	12.3	27.4	37.5	344	12.1	60.3
	115	57.4	49.0	741.1	16.4	37.7	37.0	395.5	15.7	70.4
	120	74.9	50.2	833.6	20.7	47.94	37.5	441.8	19.4	84.1
	125	89.7	52.3	946	25.7	54.8	38.4	498	23.4	103.3
	130	114.9	51.2	1111.2	31.0	72	37.9	580.6	27.3	128.5
135	149.9	51.9	1265.5	37.2	92.46	38.2	657.8	31.2	176.8	

Table 2-2 Continued

Key Largo Limestone	65	17.8	39.7	347.0	-21.6	13.69	32.6	198.5	-20.2	13.8
	75	27.8	42.3	428	-15.8	20.5	34.0	239	-15.2	26.4
	80	37.7	43.3	489.2	-12.9	27.4	34.4	269.6	-12.6	39.0
	85	47.0	43.2	550.2	-9.2	34.2	34.4	300.1	-9.0	48.2
	90	58.7	45.6	622	-5.9	41.1	35.5	336	-5.9	56.8
	95	73.8	45.9	712.8	-2.4	51.4	35.7	381.4	-2.4	65.8
	100	92.6	48.3	814	1.0	61.64	36.7	432	1.0	78.1
	105	116.2	47.3	946.5	4.5	78.77	36.3	498.3	4.5	91.4
	110	137.2	47.6	1109.2	8.1	92.5	36.4	579.6	8.0	108.1
	115	185.0	48.2	1281.8	11.4	123.3	36.7	665.9	11.1	131.6
	120	213.2	50.0	1505.4	14.7	137.0	37.5	777.7	14.3	159.2
Shallow Ft. Thompson Limestone	90	15.8	40.6	316	-23.1	12	33.0	183	-21.5	13.0
	95	22.7	41.4	346	-15.4	17	33.5	198	-14.9	19.9
	100	29.3	40.9	388	-6.9	22.2	33.2	219	-6.9	24.8
	105	34.9	42.9	431.4	0.0	25.6	34.2	240.7	0.0	34.8
	110	40.4	44.0	485.1	8.1	29.0	34.8	267.6	8.0	43.7
	115	48.9	45.7	541.5	15.8	34.1	35.6	295.7	15.2	50.8
Ocala Limestone	120	67.7	45.1	618.3	23.4	47.8	35.3	334.1	21.6	61.2
	85	9.0	30.8	187.0	13.5	7.8	27.1	118.5	13.1	4.4
	90	17.1	35.4	253.6	16.6	13.9	30.1	151.8	15.9	10.2
	95	28.1	37.5	320.1	19.3	22.3	31.4	185.0	18.3	19.0
	100	43.0	38.0	386.6	21.8	33.9	31.6	218.3	20.4	29.9
	105	62.7	37.0	453.1	24.0	50.0	31.1	251.5	22.1	41.0

2.2.2. Rock Mass Strength Envelope

Using individual laboratory strength tests on specimens, a bi-linear strength envelope and bi-linear stress-strain response may be developed. However, the behavior of intact rock specimens may not represent the behavior of rock mass beneath the footing due to the presence of voids (i.e., Adjusted-recovery) and spatial variability (e.g., dry unit weight) over the width of the footing. Furthermore, the reduction for rock mass properties from intact rock not only affects the strength, but also its stiffness (moduli), i.e., both the bearing pressure and settlement response of footing will be reduced for the rock mass vs the specimen properties.

There were two recommended methods in Phase I to obtain the reduced rock mass strength envelope: weight-adjusted and recovery-adjusted strength envelope. The weight-adjusted strength envelope used the dry unit weight of untested rock in the recovered core runs to determine a weighted average unit weight (Equation 2-19, where d was for dry, t for total, w for weighted average). The second approach, recovery-adjusted, reduced the strength envelope by the factor of $REC_{adjusted}$ (Equation 2-20). In the implementation of Phase II, researchers ignored the untestable rubble portion and identified the $REC_{adjusted}$ as testable cores (q_t , q_u and triaxial tests), and used this $REC_{adjusted}$ to obtain the bi-linear rock mass strength envelope as shown in Figure 2-8. The latter approach was recommended by Hassan and O'Neil et al., (1997) and Carter and Kulhawy (1988) to characterize the E_m/E_i ratio using RQD (4 in length vs q_t testable) ratio:

$$\gamma_{dtw} = \Sigma(\gamma_{dti} L_i) / \Sigma L_{ie} \quad (2-19)$$

$$q_m = q \times REC_{adjusted} \quad (2-20)$$

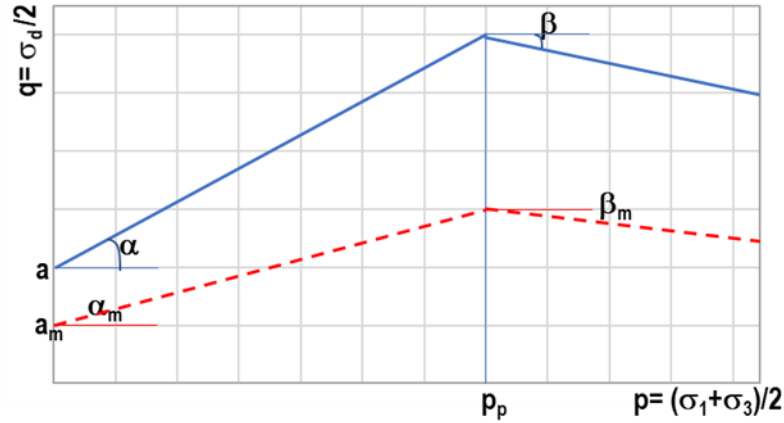


Figure 2-8 Bilinear strength envelope for rock mass from intact rock (Phase I)

2.2.3. Comparison of Phase I Bearing Capacity vs. Carter-Kulhaway Method

Carter and Kulhaway (1988) utilized the Hoek-Brown criterion (Hoek and Brown, 1980, 1988, and 2018) for rock with brittle failure characteristics and developed the only semi-empirical bearing capacity method for rocks (Equation 2-21). This approach is referenced in the current AASHTO LRFD Bridge Design Specification (AASHTO 2017). Instead of the $REC_{adjusted}$, GSI (Geological Strength Index) is used in the Hoek-Brown criterion, which is a function of rock joint spacing and rock joint quality. Since, Florida limestones has no joints, but is porous with varying voids (i.e., $REC_{adjusted}$), with a ductile stress-strain response, contractive volumetric behavior, as well bilinear strength envelope, the Carter and Kulhaway (1988) bearing capacity equation (2-21) was not considered suitable for Florida limestone (Phase I). However, under suitable strength conditions, a representative GSI may be selected vs. $REC_{adjusted}$, of Carter and Kulhaway to yield similar results to the Florida bearing equation (Table 2-3).

$$p_u = \left[\sqrt{s} + \sqrt{m\sqrt{s} + s} \right] q_u \quad (2-21)$$

Where, p_u = bearing pressure

$s = \text{rock mass discontinuity factor} = e^{(GSI-100)/(9-3D)}$

$m = m_i e^{(GSI-100)/(28-14D)}$, $m_i = 10$ for Florida carbonate rocks

D = disturbance factor caused by the rock removal methodology. For shallow foundation excavation, D=0.

$q_u = \text{unconfined compression strength}$

Table 2-3 Hoek Brown with GSI values versus REC_{adjusted} and Florida bearing capacity equations

Analysis #	GSI	REC_{adjusted}
#a	81	100%
#b	71	85%
#c	62	70%
#d	53	55%
#e	41	40%
#f	29	25%

Chapter 3

Load-settlement Response of a Shallow Foundation on Florida Limestone

3.1. Load-settlement Response of Shallow Foundation on Rock

The design of a shallow foundation for a bridge abutment must consider both service and ultimate strength conditions. Ultimate strength involves bearing capacity as discussed in section 2.2.1-2.2.3; service conditions involve the estimate of settlements (up to 1” to 2” – Canadian Foundation Engineering Manual, FHWA, etc.). As identified in section 2.1.1, the stress – strain behavior of Florida limestone is bilinear up to yield/failure and constant at higher strains. Therefore, in case of a homogeneous rock mass, the load-settlement of a footing may be characterized as linear elastic up to bearing failure/yielding whereupon it undergoes general shear failure, i.e., excessive deformations with a small load increment, Figure 2-2a. A footing (width B) which resides on a finite thick (H) rock layer (e.g., $B \leq H$) over sand will undergo punching shear failure of the overlying rock, but will still carry additional load as a function of the stiffness of the underlying soil, Figure 2-2b. The latter may be characterized as linear elastic up to punching shear failure and linear afterward with a rock modulus that changes as function of strain level (secant modulus). For typical service limits (1 in to in of settlement), the modulus of rock and sand may be characterized with two linear secant moduli for each layer, Figure 2-2b.

There are several closed form solutions for homogeneous linear elastic single- and two-layer problems. For instance, employing a secant Young’s Modulus and Poisson’s ratio, Equation 3-1, provides the settlement for a homogenous layer under a circular loaded area (Lambe and Whitman 1969). Or in the case of a strongly layered soil (i.e., $CV > 1.5$) within the influence zone (Fenton and Griffiths, 2005), the harmonic modulus may be used in Equation 3-1 to predict the settlement. As discussed in section 2.1.1, the initial modulus, E_i at 50 psi confining stress as a

function of dry unit weight of rock, Figure 3-1, and Poisson's ratio 0.1 (section 2.1.2) would be used for settlement up to bearing capacity. Similarly for a homogenous rock layer over sand (i.e., 2 layers), Burmister (1958) developed several useful charts to predict the settlement based on the modulus ratio of two layers and the thickness of upper strong layer by elastic theory. Ueshita and Meyerhof (1967) performed a series of small-scale load tests on two-layer clays and developed settlement prediction charts by using the equivalent modulus method.

Unfortunately, the soil and rock in Florida are heterogeneous, i.e., inhomogeneous in terms of properties (e.g., unit weight, strength, stiffness, etc.). In addition, due to the high porosity of Florida limestone, both poor rock coring, and low core recoveries may result. Given the high CV of Florida limestone, fewer points (poor recoveries), and outliers (i.e., high CV), representative densities and moduli of the rock beneath the footing may be difficult. However, it is strongly recommended that at least 25 testable samples (10 q_u , 10 q_t and 5 triaxial tests) within the influence zone be obtained for parameter assessment (strength and moduli). To assist with rock coring issues (cost, time, coring process), the newer site investigation techniques (seismic shear testing, measuring while drilling, electrical resistivity, etc.) are recommended. All can distinguish variability on a smaller scale than 1 ft and can assist engineers in identify the dry unit weight (strength and modulus), and layering issues (e.g., 1' to 2' thick). For example, the seismic shear is able to characterize a very large volume (3D, 150 ft by 150 ft) on a 1-ft scale (horizontally) compared to traditional drilling or coring (1D vertical, 2.5 to 4 in diameter). Similarly, measuring while drilling (MWD) can correlate the rock strength to the specific energy in the drilling process at 1-cm resolution (0.4 in) in the vertical direction (excellent in identifying layering).

In general, the correlation length ($\mu_E = \sigma_E - \gamma_E$, Equation 3-2) and coefficient of variation (CV, Equation 3-3) are used to characterize the variability of rock and soil. The correlation length (also called scale of fluctuation) is the distance over which the properties are significantly correlated. CV is a measure of normalized dispersion of a given probability distribution or normalized standard deviation. High variability of soil and rock causes the shallow foundation to have higher mean settlement as well as more differential settlement (Figure 3-2); as the ratio of correlation length to the footing width (W_f) increases, differential settlement increases, causing issues with bridge structures. For instance, continuous spans are not exceptionally tolerant to differential settlement. Hence, it is necessary to evaluate the variability of rock and determine the expected differential settlement for the planned footing designs on a site.

$$\rho = \Delta q_s \frac{B \times S_f}{E} 1.12(1 - \mu^2) \quad (3-1)$$

Where, Δq_s = bearing pressure

B = footing width

E = elastic modulus

μ = Poisson's ratio

S_f = shape factor

$$\gamma(h) = \frac{1}{2|N(h)|} \sum_{N(h)} (z_i - z_j)^2 \quad (3-2)$$

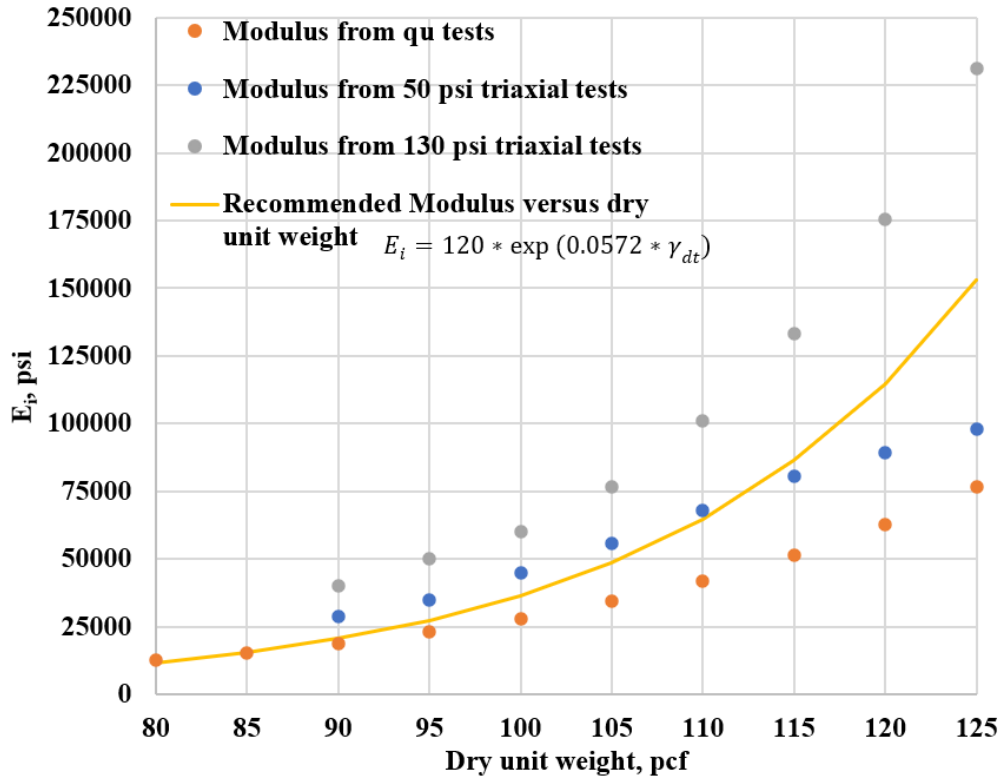
Where, h = lag distance

$N(h)$ = number of pairs for a lag distance

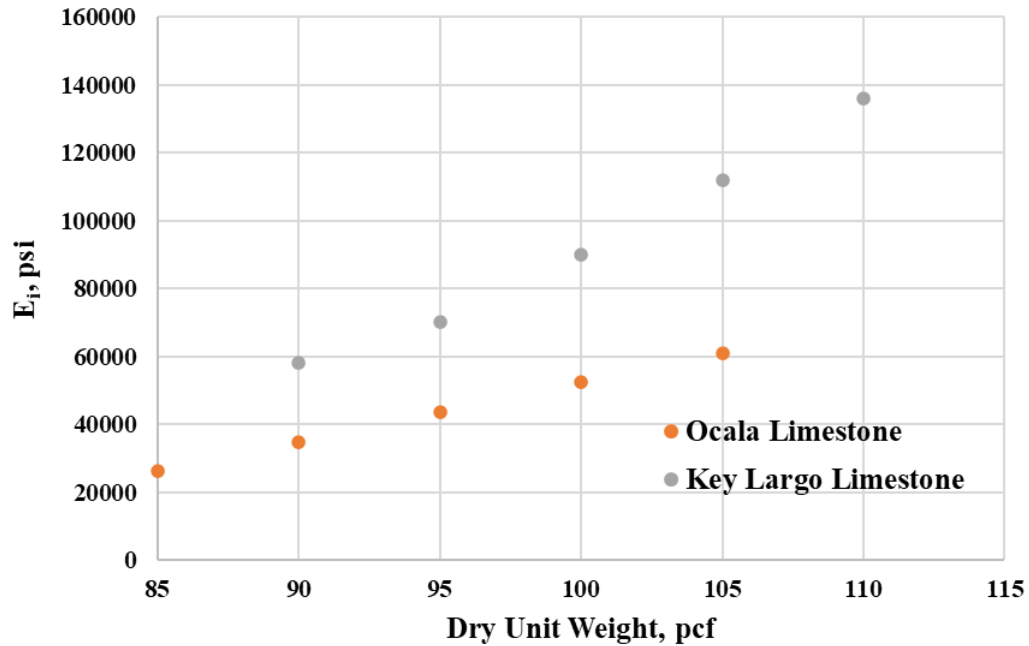
$$CV = \frac{\sigma}{\mu} \quad (3-3)$$

Where, σ = standard deviation

μ = mean



(a)



(b)

Figure 3-1 Initial modulus versus dry unit weight: (a) Miami limestone and (b) Ocala and Key Largo limestone (limited data)

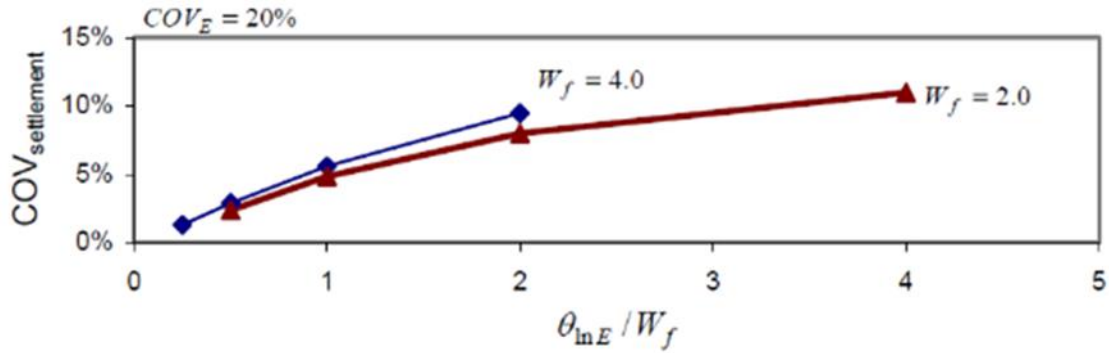


Figure 3-2 Coefficient of variation (COV or CV) of settlement with varying $\theta_{\ln E} / W_f$ (correlation length/footing width) for single soil layer profile (Fenton & Griffiths, 2002)

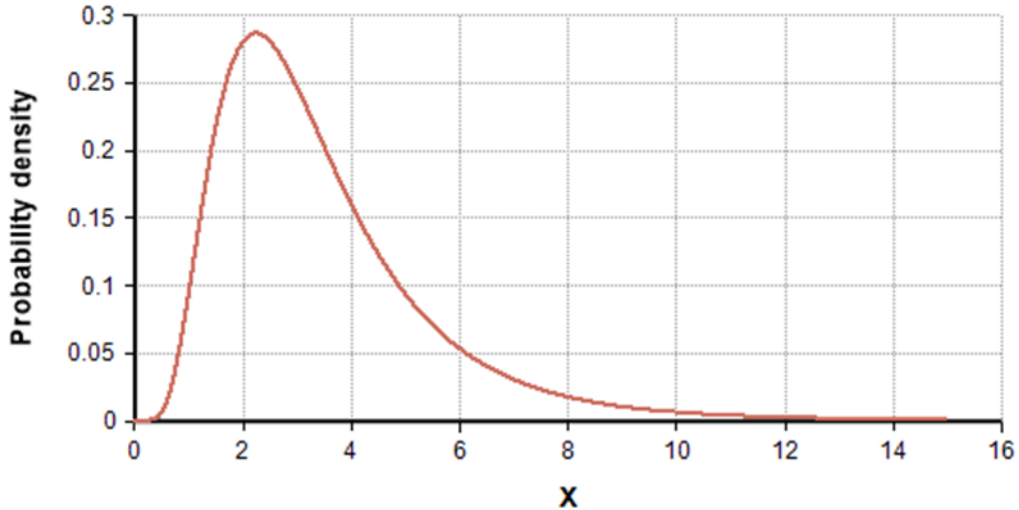


Figure 3-3 Log-normal distribution of mass modulus

3.2. Load-settlement Response of a Footing on a Heterogeneous Single Rock Layer

For single layer case, Fenton and Griffiths (2002) developed equations to estimate both the mean and differential settlement of a spread footing founded on variable correlated moduli (heterogeneous) material (Figure 3-4) through a series of finite element simulations of random correlated soil or rock profiles. Their development assumes a log-normal distribution for the

moduli (Figure 3-3) with an associated mean, standard deviation, and a correlation length ($\mu_E = \sigma_E - \gamma_E$). The mean settlement of the footing is still given by Equation 3-1; however, the homogeneous modulus is replaced with the geomean modulus of the initial modulus (E_i) which is function of dry unit weight and formation, Figure 3-1. The assessment of the dry unit weight of shallow rock layer is critical since the dry unit weight is correlated with bearing capacity (strength) and settlement (geomean initial modulus). Note, seismic testing will be shown (chapter 4) to do a good job in quantifying the unit weight (or density) of mass or volume beneath a footing.

For the differential settlement calculation, the moduli which are assumed to be log-normal, are converted into normally distributed through the standard deviation (Equation 3-4), and the natural log of the heterogeneous settlement (Eq. 3-5) is found and then the normal differential settlement (Eq. 3-6) is found. Subsequently, the natural log of heterogeneous settlement and differential is transformed back to the expected field settlement in Equation 3-7 and 3-8. Fenton and Griffiths approach for mean and differential settlement for single rock layer (Figure 2-2a), only requires summary statistics (mean and standard deviation) and correlation length of moduli for the settlement calculations. Please note, for a single footing, Fenton and Griffiths (Fenton and Griffiths, 2002 and 2005) consider the CV of a site's moduli from 0.1 to 4 (Florida is 1 to 3) and the ratio of footing width to correlation length from 0.02 to 160 (Florida is 3 to 15).

$$\sigma_{\ln E}^2 = \ln(1 + \sigma_E^2 / \mu_E^2) \quad (3-4)$$

$$\mu_{\ln \delta} = \ln(\delta_{det}) + \frac{1}{2} \sigma_{\ln E}^2 \quad (3-5)$$

$$\sigma_{\ln \delta} = \sqrt{\gamma(B, H)} \sigma_{\ln E} \quad (3-6)$$

where,

$$\gamma(d_1, d_2) = \frac{1}{2} [\gamma(d_1)\gamma(d_2|d_1) + \gamma(d_2)\gamma(d_1|d_2)]$$

$$\gamma(d_i) = \left[1 + \left(\frac{d_i}{\gamma(h)} \right)^2 \right]^{-\frac{2}{3}}$$

$$\gamma(d_i|d_j) = \left[1 + \left(\frac{d_i}{R_j} \right)^2 \right]^{-\frac{2}{3}}$$

$$R_j = \theta_{\ln E} \left[\frac{\pi}{2} + \left(1 - \frac{\pi}{2} \right) \exp \left\{ - \left(\frac{d_j}{\frac{\pi}{2} \gamma(h)} \right)^2 \right\} \right]$$

$$\mu_\delta = \exp \left\{ \mu_{\ln \delta} + \frac{1}{2} \sigma_{\ln \delta}^2 \right\} \quad (3-7)$$

$$\sigma_\delta = \mu_\delta \sqrt{e^{\sigma_{\ln \delta}^2} - 1} \quad (3-8)$$

where,

σ_E = standard deviation of elastic modulus

μ_E = mean elastic modulus

$\sigma_{\ln E}$ = standard deviation of log-elastic modulus

δ_{\det} = footing settlement when $E = \mu_E$ everywhere

$\mu_{\ln \delta}$ = mean of log-settlement

B = footing width

H = overall depth of soil layer

$\sigma_{\ln \delta}$ = standard deviation of log-settlement

μ_δ = mean footing settlement

σ_δ = standard deviation of footing settlement

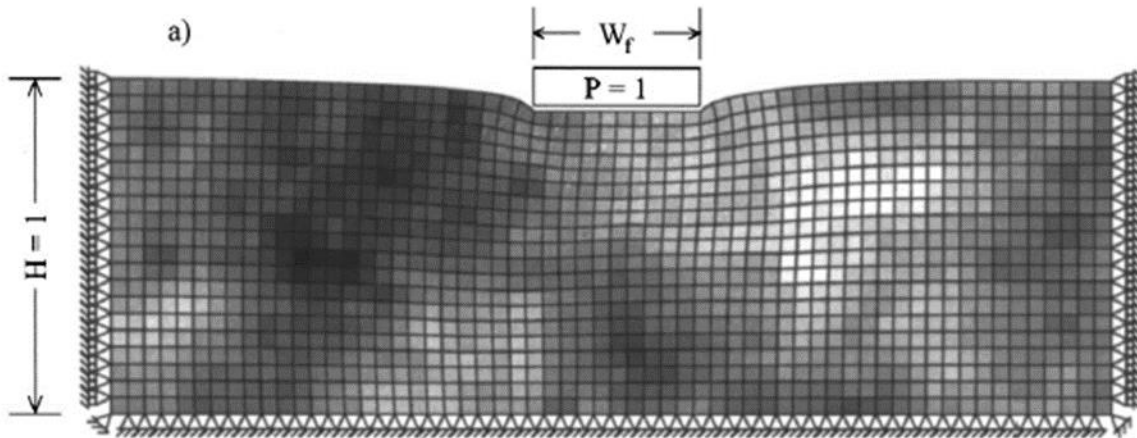


Figure 3-4 Random field representation of a single footing

3.3. Load-settlement Response of a Footing on two-layer heterogeneous System

The load-settlement response of shallow foundation residing on a strong layer overlying a weak layer is characterized in Figure 2-2b. The strong rock layer initially carries a higher percentage of the load and is characterized with and a linear load-settlement using the median initial mass modulus (E_i) up to shear failure which is accompanied by a change in modulus (secant) based on strain level (deformation and thickness of rock layer); the magnitude of settlement is a function of the modulus of each layer (E_1 and E_2), geometry of the footing and thickness of the rock layer. For the modulus of the weak layer (sand), Bowles Method (Bowles, 1996, Equation 3-9) has been shown to give reasonable results (chapters 6 & 7). Also, once shear/punching failure of rock occurs, the Bowles' modulus is reduced (secant) to 50% to account for increased shear within the 2nd layer in the following finite element analyses.

Burmister (1958) was the first to present the settlement for a two-layer system associated with a strong layer overlying a semi-infinite elastic weak layer (i.e., roadway). The properties of each layer are assumed homogeneous, isotropic, and linearly elastic. The method was developed

based on elastic theory and satisfies the continuity condition at the interface between two layers. For a rigid footing, Equation 3-10 is used, and δ is the footing settlement, p is the applied stress and a is half of the footing width ($B/2$), E_2 is the weak layer modulus and F is the deflection factor obtained by the moduli ratio, E_1/E_2 (strong/weak) and the ratio of rock thickness to half of the footing width) from Figure 3-5.

Similar to Burmister, Ueshita and Meyerhof, (1967, equation 3-11) presented a two-layer elastic solution for mean settlement but an equivalent modulus is required. Instead of Fenton and Griffiths' (2005) geometric mean, a number of different moduli have been recommended (Figure 3-6), i.e., harmonic, median, geomean, etc. Generally, the harmonic mean is more conservative than the geomean modulus or arithmetic modulus and it will be shown (Chapter 6 & 7) to be more reasonable for the rock-over-sand case (Fenton and Griffiths 2002 and 2005). Also shown in Figure 3-6 is the maximum relative error between the different estimates of moduli (Pantelidis, 2019). Note the least error occurs with Gorbunov-Possadov and Malikova (1973) who use the weighted harmonic mean modulus based on the stress at the middle of each layer and thickness of each layer (Eq. 3-12). For the two-layer problem, the stress for the strong layer is the half of the applied contact stress plus the interface stress and for the weak layer it is simply taken as half of the interface stress which can be obtained from Figure 3-7 (interface stress is a function of the modulus ratio and rock thickness). For the modulus of the top rock layer, it is recommended to use the median value due to the rock's low Poisson's ratio as well as to be conservative (median is less than geomean in a log-normal distribution). In addition, before rock failure it is the secant at the failure stress (E_i) and after rock failure, it is based on the strain level, (E_s) Figure 2-1. It is recommended that the secant modulus at 2% strain predicts the settlement at 10% higher contact stress (bearing) in the field.

$$E_s = 250 (N + 15), E_s \text{ in kPa} \quad (3-9)$$

$$\delta = \frac{1.18pa}{E_2} F \quad (3-10)$$

$$\delta = \frac{1.5pa}{E_h} \quad (3-11)$$

$$E_h = \frac{\sum h_i \sigma_i}{\sum \frac{h_i \sigma_i}{E_i}} \quad (3-12)$$

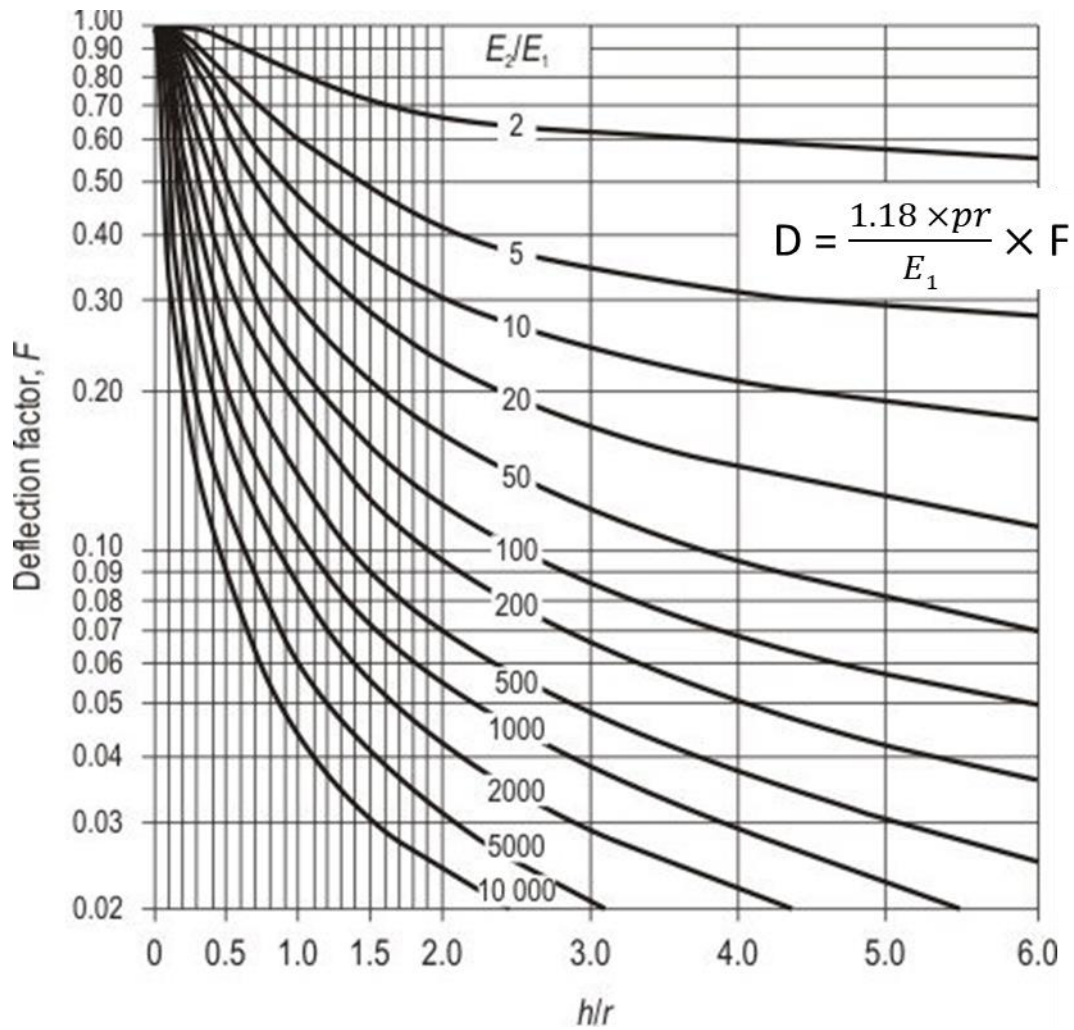


Figure 3-5 Burmister solution (Burmister, 1958) deflection factor versus the modulus ratio and rock thickness for rigid footing

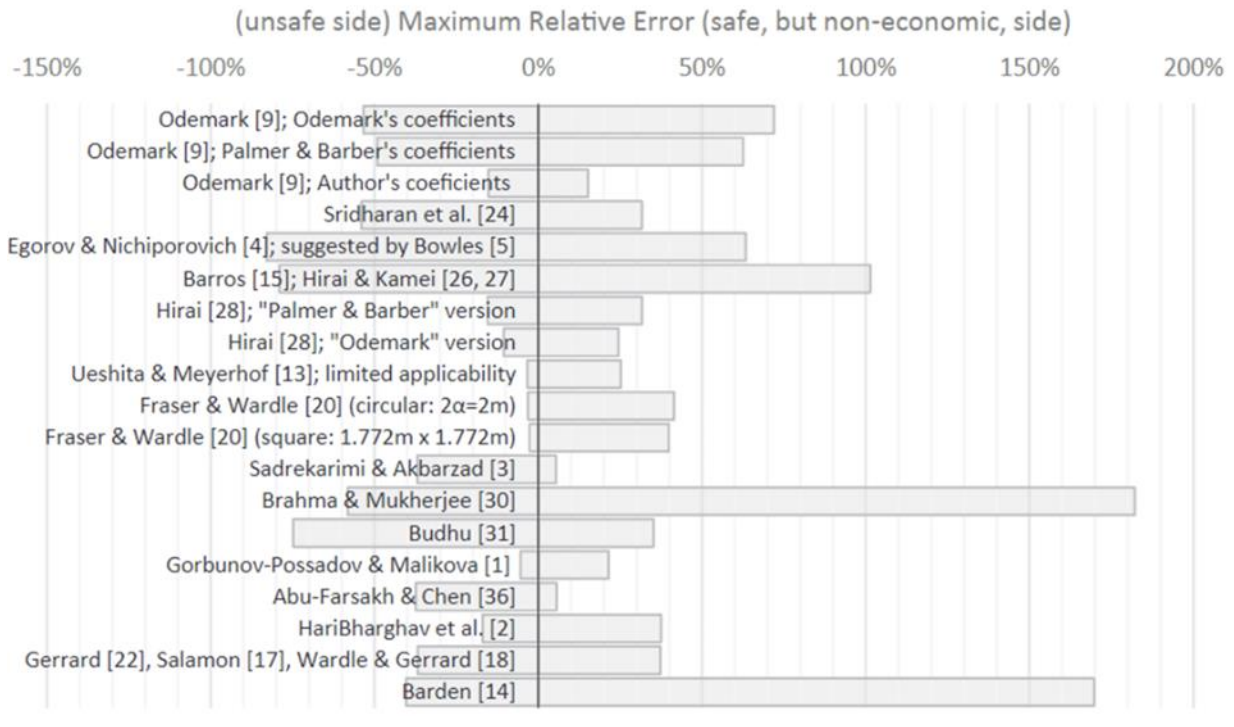


Figure 3-6 Maximum relative error between equivalent modulus methods (Pantelidis, 2019)

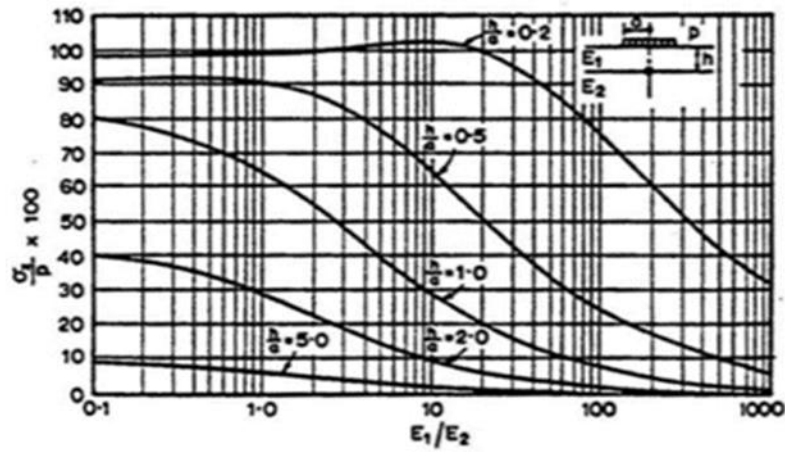


Figure 3-7 Vertical interface stress (Fox, 1948)

Chapter 4 Seismic Testing

4.1. Introduction

The goal of the seismic survey was to determine compressional (V_p), and shear (V_s) velocities, as well as density (ρ) of the underlying soil and rock at three load test sites in Florida. The distributions of these parameters were used to select the locations of test foundations, layering as well as the mean mass density for assessing rock strength (function of dry unit weight). In addition, the shear (G) and Young (E) moduli calculated from V_p , V_s and ρ may be used for estimating the foundation settlement. Accounting for 3D spatial variation of soil/rock properties, may be used to more accurately predict differential settlement of a footing.

For these purposes, 2D and 3D seismic data were acquired at the test sites. The 2D seismic data for horizontal shear waves (SH-waves) and Love-waves is obtained through horizontally striking a shear-beam using a sledgehammer and recording ground motions using a linear array of horizontal geophones. This data is then used in a 2D full waveform inversion analysis (2D SH-FWI) to determine V_s and ρ at the test sites. The V_s - ρ relationship is obtained through a regression analysis. This is useful in the subsequent analysis for the 3D full waveform inversion of the seismic data.

The 3D seismic data is obtained through dropping a weight on a steel plate and measuring ground motions using a 2D array of vertical geophones placed on the ground surface. The data obtained from this type of seismic testing are vertical P-wave and S-wave (PSV). The PSV data is good for imaging 3D V_s and V_p profiles. As the PSV data is not sensitive to density (ρ), the V_s - ρ relationship obtained from the 2D SH-FWI is used together with the 3D V_s for determination of 3D density. The 3D FWI results can also be used to calculate the Poisson's ratio

(ν) from the V_s and V_p . Finally, Young (E) and shear (G) moduli can then be obtained for the entire 3D subsurface. The field testing and FWI analyses of the 2D and 3D data are detailed in the following sections.

4.2. Cemex Site

Seismic testing was performed at the Cemex site shown in Figure 4-1. The center of the testing configuration was chosen based on the center line for the subsequent load test at this test site. The goal was to center the testing configuration on the foundation load test. Several lines of geophones and sources were used to gather data for the 2D and 3D FWI analyses. The details of the analyses at this test site including the specifics for testing configuration, analyses and results are elaborated in the following sections.



Figure 4-1 Testing setup at the Cemex site in Miami

4.2.1. 2D Full Waveform Inversion of SH-wave Data

The acquisition geometry is shown in Figure 4-2, which includes 13 shots and 24 receivers on the ground surface. The shots located at 1.5 m (5 ft) spacing, and the receivers located at 0.75 m (2.5 ft) spacing. Seismic wavefields were generated by horizontally striking a sledgehammer on a shear-beam, which was coupled to the soil by metal cleats. For each source location, two datasets (striking both ends of the beam) were acquired and stacked to eliminate noise and undesired off-line P-wave reflections. The wavefields were recorded by 24 4.5-Hz horizontal geophones for a total recording time of 1.0 second with a sampling rate of 0.5 millisecond.

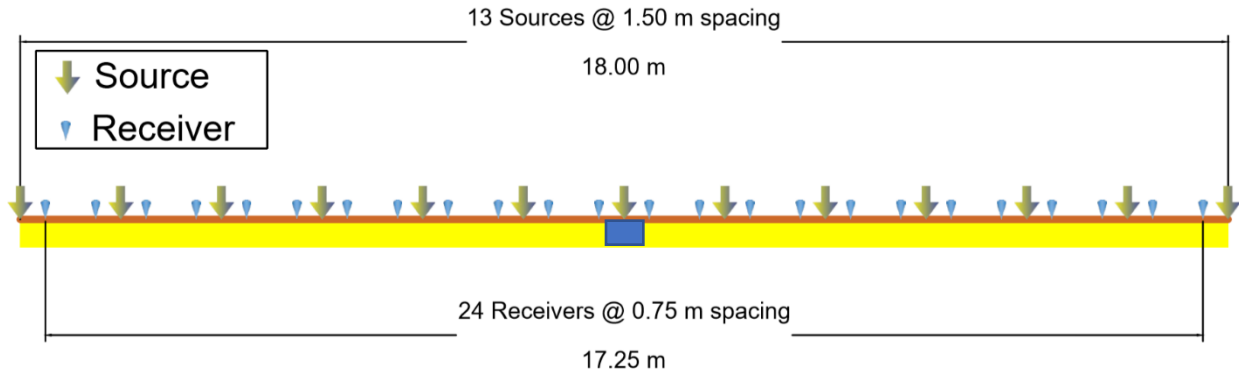


Figure 4-2 Acquisition geometry used for 2D SH-source at the Cemex site. The blue box is the planned foundation location (middle of test array)

The medium for modelling is $9 \text{ m} \times 18 \text{ m}$ ($30 \text{ ft} \times 60 \text{ ft}$), which was discretized into a 24×49 grid of 0.375 m (1.25 ft) spacing in the vertical and horizontal directions, respectively. The depth as a half of the test length was used to have good signals passing through the analyzed domain.

For data analysis, the initial model of V_s was built via spectral analysis of surface waves. The field data from the first shot were analyzed by the cylindrical beamforming technique (Figure 4-3a). The dominant energy of the wavefield is from Love-waves, which propagate with velocities approximately from 250 to 750 m/s (820 to $2,460 \text{ ft/s}$) for data at 20 to 70 Hz . As V_s is similar to the Love-wave velocity, the initial model of V_s (Figure 4-3b) was taken as 250 m/s (820 ft/s) on the ground surface and linearly increased to 750 m/s ($2,460 \text{ ft/s}$) at the model bottom. The initial model of density was assumed from $1,600$ to $2,000 \text{ kg/m}^3$ (100 to 125 pcf) as the characteristic value range for general rocks.

The recorded data was filtered through the frequency bandwidth of 15 to 50 Hz and utilized for one inversion run. The inversion started with the 1D initial model in Figure 4-3b. The termination criterion was established as when analysis reached a predefined maximum number

(50) of iterations, or the least-squares error decreased less than 1% (or increased) for ten iterations. The inversion run stopped at 19 iterations, which took only 6 minutes on a desktop computer (Dell Precision 5820 Tower, Intel Xeon CPU W-2145, 8 cores with 3.70 GHz each, 64 GB RAM).

The inversion analysis ran for 19 iterations and the waveform match improved during the process as the optimization algorithm approached the global minimum of the objective function. Figure 4-4 compares the waveforms of observed and estimated data. An excellent waveform match is observed at the end of the inversion, showing the good choice of the initial model. No cycle skipping or matching of the wrong peaks is observed.

The final inverted result is shown in Figure 4-3c, the inverted density (Figure 4-3c, top) is consistent with V_s (Figure 4-3c, bottom). There is a softer layer with $V_s \sim 200$ m/s (656 ft/s) and density $\sim 1,500$ kg/m³ (94 pcf). The soft layer is underlain by a stiffer layer. The stiffer layer starts at about 1.5 m (5 ft) depth to the bottom, with $V_s \sim 500$ -750 m/s (1640-2460 ft/s) and density $\sim 1,800$ -2,200 kg/m³ (112-137 pcf).

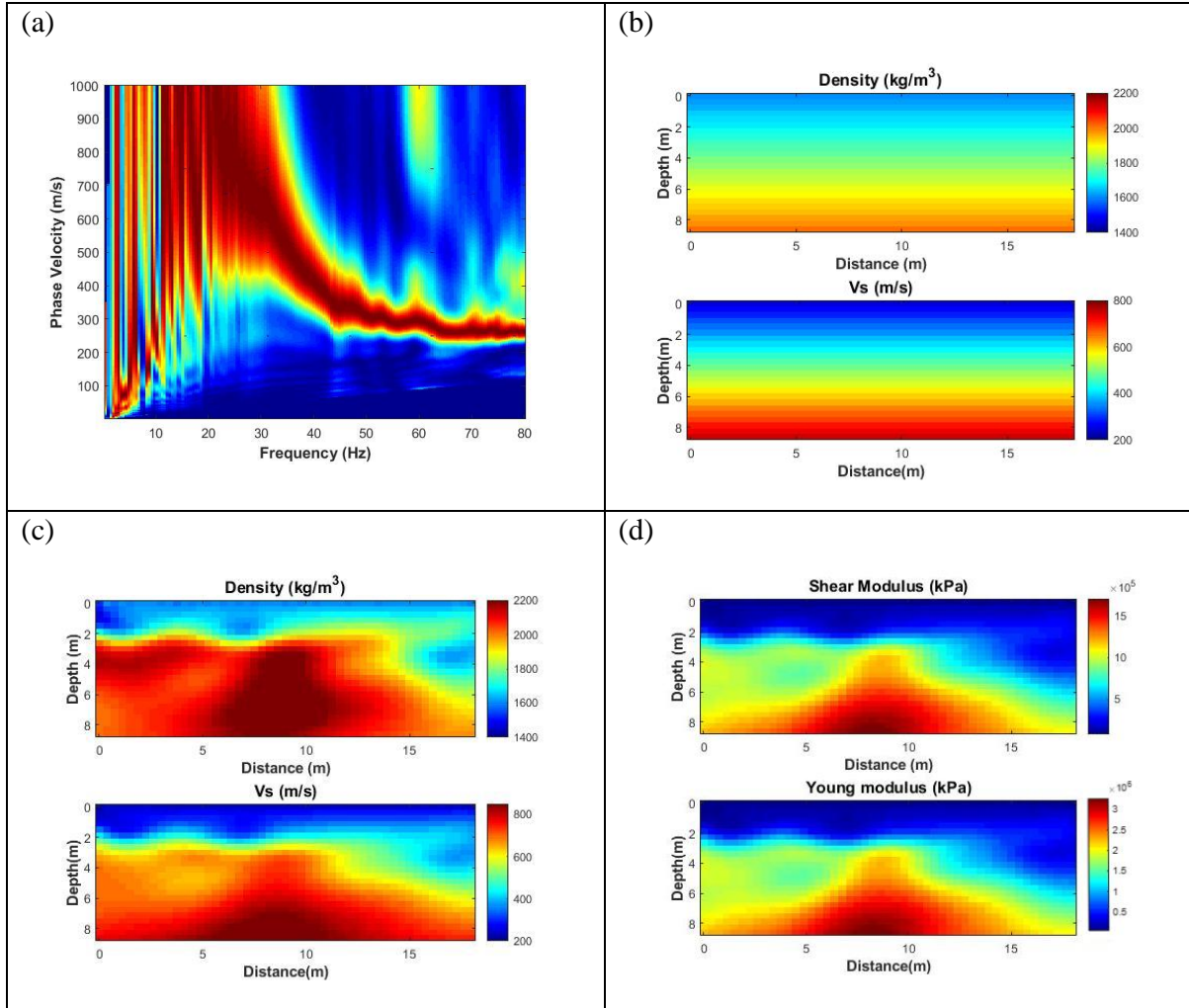


Figure 4-3 (a) spectral image of measured data from the first shot, (b) initial model based on the spectral analysis, (c) final inverted result of V_s and density, and (d) shear and Young's modulus calculated based on inverted result

Based on the inverted V_s and density, shear modulus (Figure 4-3d, top) and Young modulus (Figure 4-3d, bottom) are then calculated as:

$$G = \rho V_s^2 \quad (4-1)$$

$$E = 2G(1 + \mu) \quad (4-2)$$

where G represents the shear modulus, ρ is the density, V_s is the S-wave velocity, E represents Young's modulus, μ indicates the Poisson's ratio. The Poisson's ratio is assumed to be 0.1.

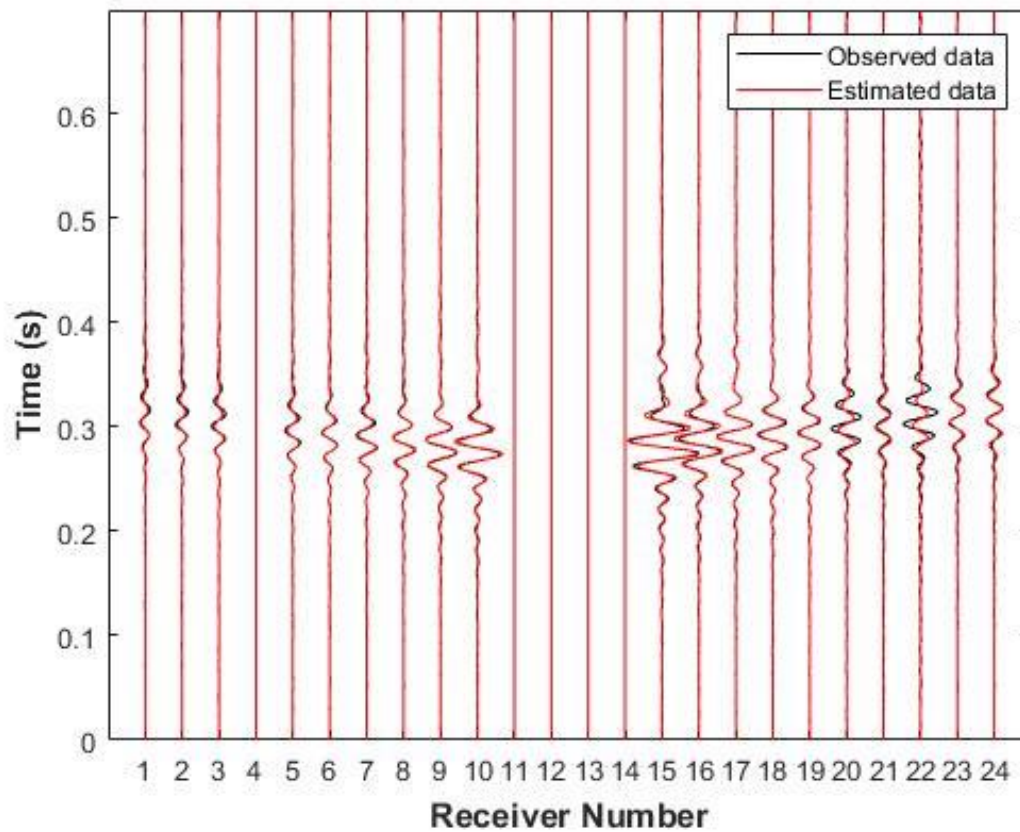


Figure 4-4 Waveform comparison of a sample shot for observed and estimated data at the end of inversion

The regression analysis was used for estimating the relationship between density and V_s as shown in Figure 4-5. The y-axis represents the density, and x-axis represents the V_s , R^2 is the coefficient of determination. For linear equation, the equation estimating the density value based on V_s value is $\rho = 1.0139 V_s + 1353.8 \leq 2,200$, with the R-square value of 0.9036. This relationship is used to determine 3D density in the next section.

Equation between Vs and Density (Linear)

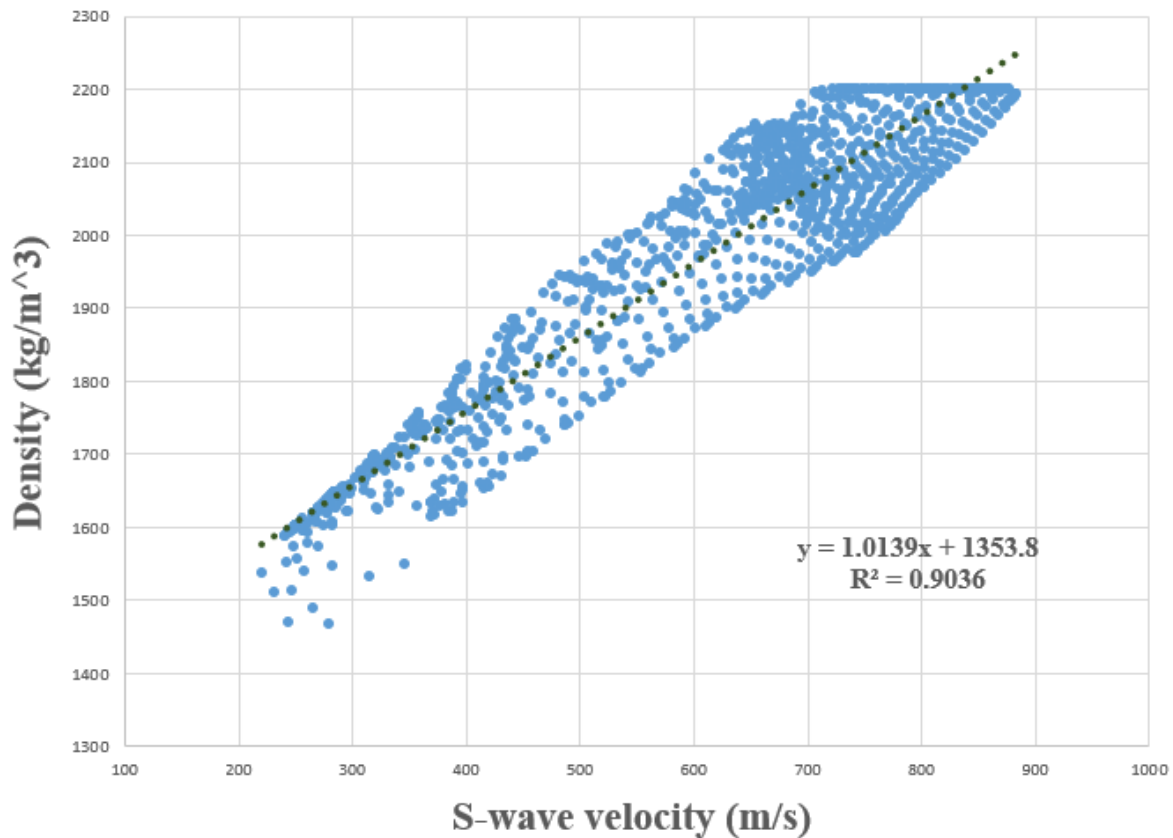


Figure 4-5 Equation to estimate the relationship between density and S-wave velocity

4.2.2. 3D Full Waveform Inversion of PSV-wave Data

To get a better understanding of the underlying soil features and material properties, a 3D full waveform inversion analysis was performed. The data was obtained using a 2D array of geophones and shots located on the ground surface. In total 48 geophones with a spacing of 1.5 (5 ft) were placed in 4 lines with 12 geophones each line. A total of 65 shots were applied on the ground surface each at 1.5 m (5 ft) spacing in 5 lines with 13 shots each line. The detail of the acquisition geometry is shown in Figure 4-6.

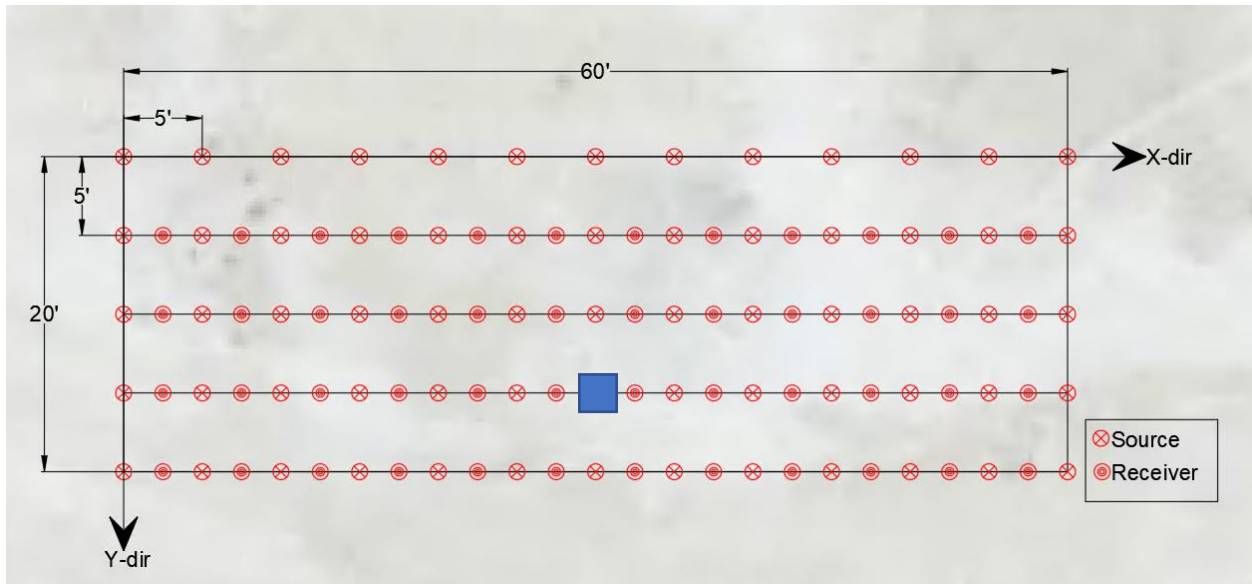


Figure 4-6 Detail of the acquisition geometry used to gather data for the 3D FWI analysis, The blue box is the foundation location.

The source was applied at each shot location through the strike of a 40-kg drop-weight using a propelled energy generator (PEG) shown in Figure 4-7. Each strike generated a wavefield that was recorded by all the 48 surface 4.5-Hz vertical geophones simultaneously. Each recording was performed for a total duration of 1 second using a sampling rate of 0.5 ms. This generated a total of 2,520 channels of data with 2,000 data points in each channel. The sampling rate allows sampling data up to 1,000 Hz (Niquist frequency). We only need frequencies less than 60 Hz to be able to characterize the medium at meter scales.

To facilitate source and receiver placement on the numerical mesh, a grid spacing of 0.375 m (1.25 ft) was chosen. Similar to the 2D analysis, a linearly increasing initial V_s of 250 to 750 m/s (820 to 2,460 ft/s) was determined and used to initiate the inversion analysis (Figure 4-8a). V_p was chosen to be twice that of V_s for this analysis. The inversion was performed in two frequency stages of 20-40 Hz and 40-60 Hz in time domain. This frequency range was chosen based on multimodal energy localization in the surface wave data (Figure 4-3a). This staged

frequency method is known to reduce local minima in the parameter space; hence helping to constrain the inversion problem to approach the global minimum.



Figure 4-7 Propelled energy generator (PEG) source

The two runs took a total time of 33 hours on a desktop computer with 32 CPUs each clocked at 4.2 GHz, and 320 GB of RAM. The waveform match improved considerably during the inversion analysis (Figure 4-9), as the optimization algorithm approached an appropriate minimum in the objective function. Overall, no cycle skipping or matching of the wrong peaks is seen, showing the good choice of the initial model and successful optimization.

During the inversion process, the entire 3D model was updated for each grid point on the numerical mesh. Shown in Figure 4-8b is the final inverted results for V_s and V_p . It can be seen that a shallow layer of low velocity zone with $V_s \sim 200$ m/s (656 ft/s) is overlying a zone of high velocity from 1.5 m (5 ft) depth to the bottom. This is representative of a shallow sandy layer on

top of limestone bedrock, which is consistent with previous results obtained through invasive SPT testing at the site location.

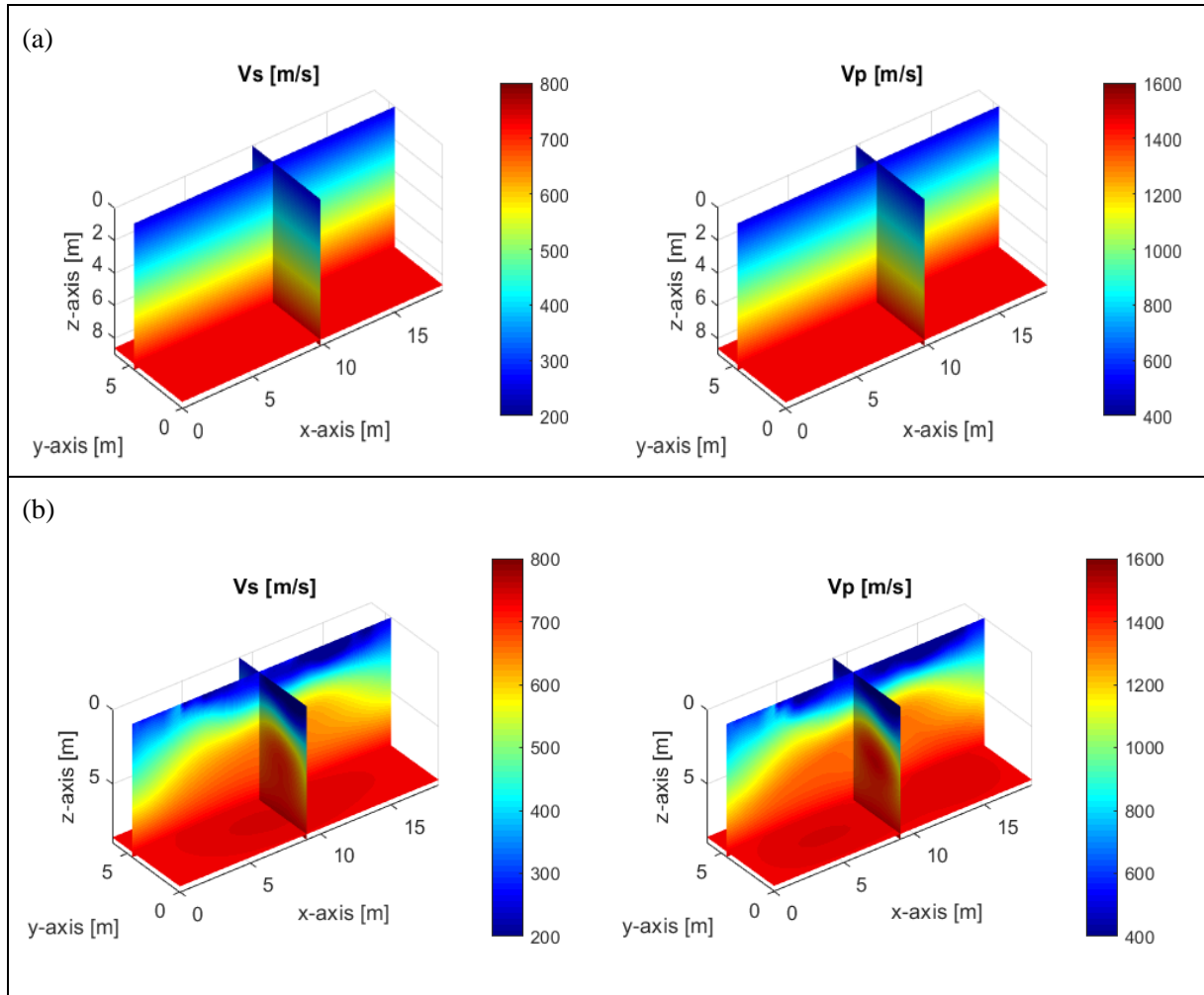


Figure 4-8 Distribution of V_s and V_p (m/s) for (a) the initial model and (b) final inverted result

Shown in Figure 4-10 is the 3D rendering of the final inverted result for both V_s and V_p . Variations of the high velocity zone is a prominent feature in these renderings. There is indication that the high velocity zone is shallower towards the 5th shot line and deeper closer to the 1st shot line in both V_s and V_p . Shown in Figure 4-11 are the mass density (ρ), shear modulus

(G), and Young's modulus (E) from left to right and top to bottom, respectively. These parameters were calculated from the inverted V_s and V_p using the linear relation of Figure 4-5 and the following equation along with equations (4-1) and (4-2):

$$\nu = \frac{1(V_p - V_s)^2 - 2}{2(V_p - V_s)^2 - 1} \quad (4-3)$$

where all the parameters were previously defined. Based on these results (Figure 4-11), mass density (ρ) variation is from 1,700 to 2,100 kg/m³ (106 to 131 pcf) consistent with that of sand and limestone, respectively. There is a small patch of soil volume close to the surface with a mass density of 1,400 kg/m³ (87 pcf), which is most likely due to the accumulation of drilling mud and water that was present at the site during the time of testing. Finally, shear modulus (G) and Young's modulus (E) variations are similar to that of V_s .

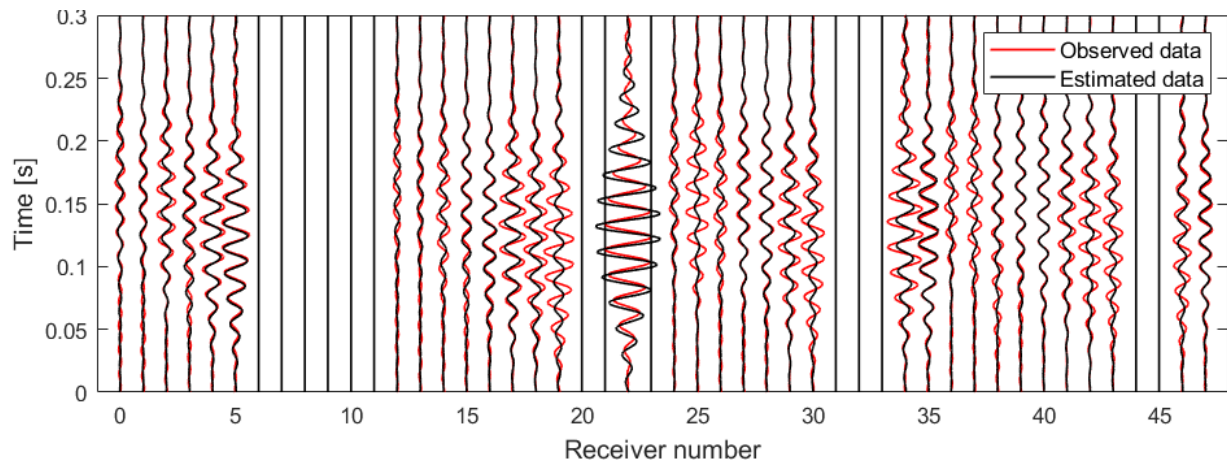


Figure 4-9 Waveform comparison for a sample shot for observed and estimated data at the end of inversion

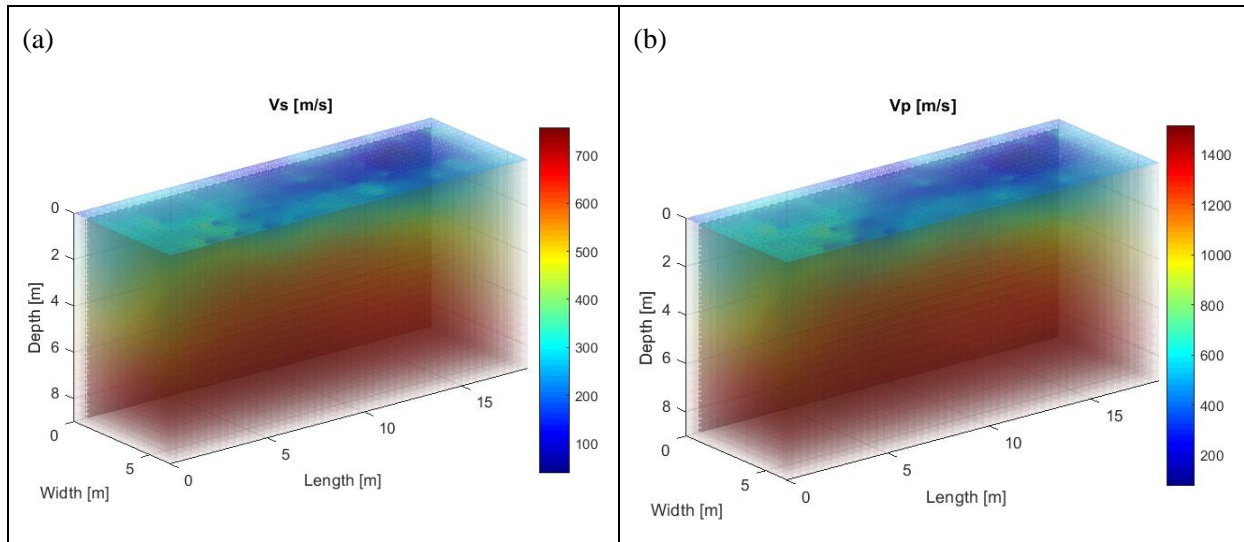


Figure 4-10 3D rendering of the final inverted result for (a) V_s and (b) V_p with transparent features

Summaries of findings

Field seismic testing was performed at the Miami Cemex site for noninvasive characterization of soil/rock properties using 2D and 3D full waveform seismic analyses. SH- and Love-wave seismic data were gathered using a linear array of 24 4.5 Hz horizontal geophones placed 0.75 m (2.5 ft) apart with 13 sources applied at every 1.5 m (5 ft). Sources were applied by horizontally striking a shear beam using a sledgehammer. The seismic waveform was recorded for all the 24 geophones simultaneously for each strike. The acquired data was used in a 2D full waveform inversion analysis to determine V_s and ρ independently for the underlying material. This was then utilized to obtain a linear relationship between density and V_s using regression analysis. Young and shear's moduli were also obtained indirectly using inverted results for V_s , density, and assumed Poisson's ratio.

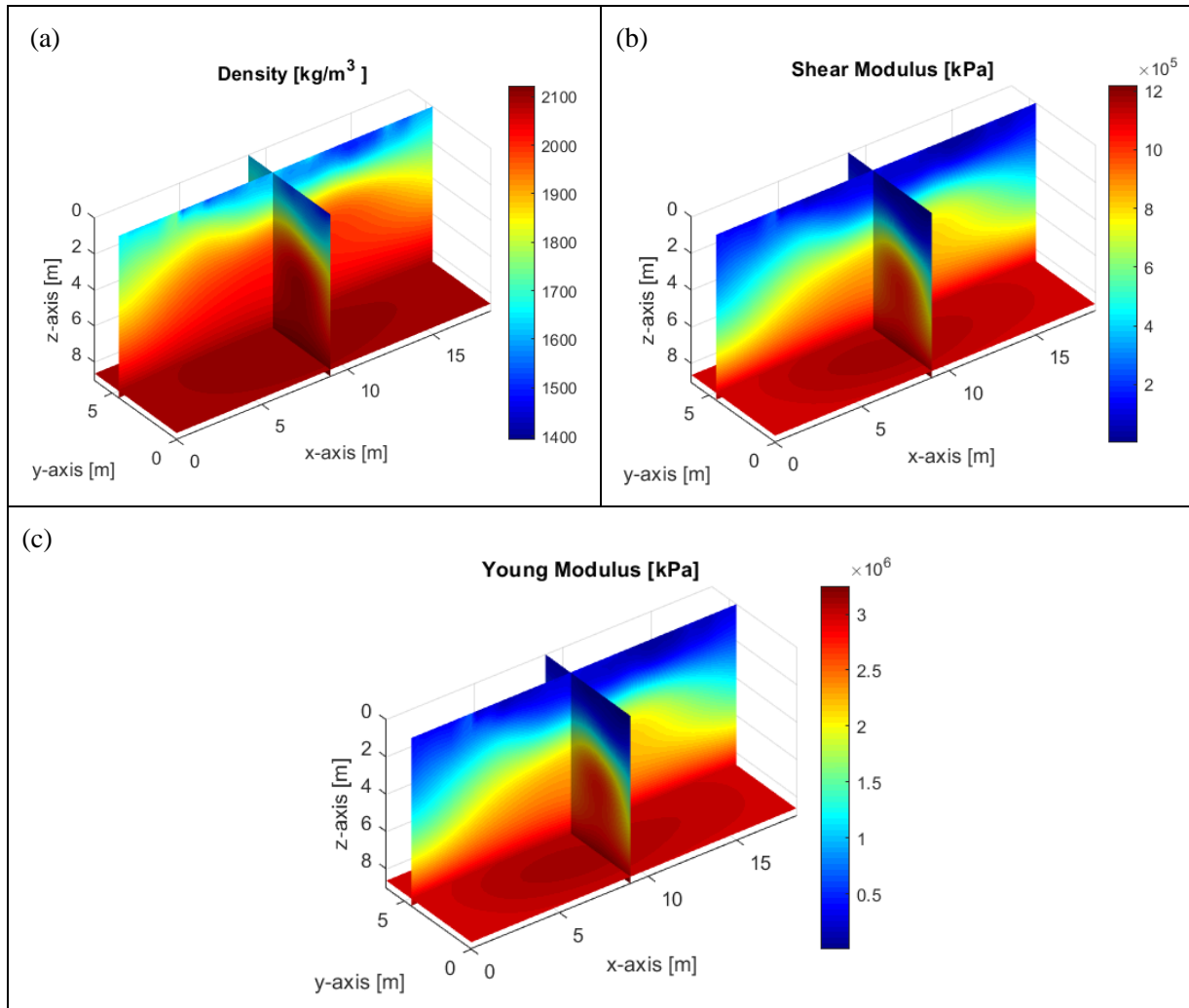


Figure 4-11 Distribution of (a) density, (b) shear modulus, and (c) the Young’s modulus for the analyzed medium

3D full waveform inversion analysis was then performed using data gathered at the site. Seismic data was acquired using a 2D array of sources and receivers placed on the ground surface. In total, 48 receivers were placed 1.5 m (5 ft) apart in a 4×12 grid with 65 shots applied in a 5×13 grid with a spacing of 1.5 m (5 ft). The shots were applied one by one and the entire seismic wavefield was recorded by all the 48 channels simultaneously. The acquired data was then analyzed to invert for subsurface V_s and V_p velocity variations independently. This

was then used to obtain Poisson ratio (ν) variations. Mass density (ρ) was obtained from the inverted V_s results using the $\rho - V_s$ relationship previously obtained from the 2D analysis. Finally, Young and shear moduli were obtained from V_s , ν , and ρ .

There is a good agreement between the results of the 2D and 3D analyses for V_s . Variations of elastic and shear moduli from both analyses suggests existence of softer material for the first 2 m (6.6 ft), underlain by stiffer material at deeper depths. There was an indication of a shallower high velocity zone towards the end of the source line and deeper zone close to the first source line. The seismic result was used to place the footing, with the soil properties at the footing shown in Table 4-1.

Table 4-1 Cemex site: soil and rock properties at the footing location

Depth (m)	Density (kg/m ³)	S-wave velocity (m/s)	Shear modulus (kPa)	Young's modulus (kPa)
0.000	1,600.0	248.9	99,117.2	218,057.7
0.375	1,644.6	276.5	125,757.1	276,665.6
0.750	1,688.3	302.7	154,699.2	340,338.1
1.125	1,738.2	330.5	189,842.7	417,653.8
1.500	1,788.5	368.9	243,423.8	535,532.3
1.875	1,859.6	428.9	342,095.1	752,609.2
2.250	1,941.3	510.0	504,858.9	1,110,689.5
2.625	2,023.7	596.5	720,097.1	1,584,213.6
3.000	2,078.8	668.3	928,503.3	2,042,707.2
3.375	2,099.3	712.3	1,065,173.3	2,343,381.3
3.750	2,101.1	730.2	1,120,181.2	2,464,398.6
4.125	2,100.1	735.4	1,135,825.0	2,498,815.1
4.500	2,106.0	739.6	1,151,897.0	2,534,173.4
4.875	2,122.1	748.0	1,187,330.4	2,612,126.9
5.250	2,143.3	761.4	1,242,694.8	2,733,928.6
5.625	2,164.4	778.3	1,311,004.3	2,884,209.6
6.000	2,182.0	796.4	1,383,846.5	3,044,462.2
6.375	2,193.7	814.0	1,453,634.7	3,197,996.3
6.750	2,198.7	830.1	1,515,070.2	3,333,154.5
7.125	2,197.2	844.0	1,565,049.3	3,443,108.6
7.500	2,189.3	855.4	1,601,833.5	3,524,033.7
7.875	2,175.1	864.4	1,625,063.2	3,575,139.1
8.250	2,156.3	871.4	1,637,358.9	3,602,189.7
8.625	2,134.0	877.7	1,643,781.0	3,616,318.2

4.3. SR-84 Site

Seismic testing was performed at the second test site shown in Figure 4-12. The site is located on Florida State Road 84 near South-West 148th Avenue, Davie, Florida. According to borings conducted at this site, the subsurface profile consists of shallow sand underlain by limestone. Similar to the first site, the testing configuration was setup in a way to be centered on the foundation load line. Both 2D SH and 3D full-waveform seismic data were gathered at this test site. Details regarding the testing setup, analysis, and results are elaborated in the following sections.



Figure 4-12 Testing setup at SR-84 site in Miami

4.3.1. 2D Full Waveform Inversion of SH-wave Data

The acquisition geometry includes 13 sources (shots) and 24 receivers on the ground surface as shown in Figure 4-13. The shots were located at a spacing interval of 1.2 m (4 ft), and the receivers were located at a spacing interval of 0.6 m (2 ft). Seismic wavefields were generated by horizontally striking a sledgehammer on a shear-beam (Figure 4-14). The shear-beam was pressed by a vehicle-mounted hydraulic jack, which forced the beam to be coupled well with the soil. For each shot, two datasets were acquired by striking both ends of the beam and stacked to remove noise and reduce offline P-wave reflections from the medium. The generated wavefields were recorded by 24 4.5-Hz horizontal geophones for a total recording time of 1 second with a sampling rate of 0.5 millisecond.

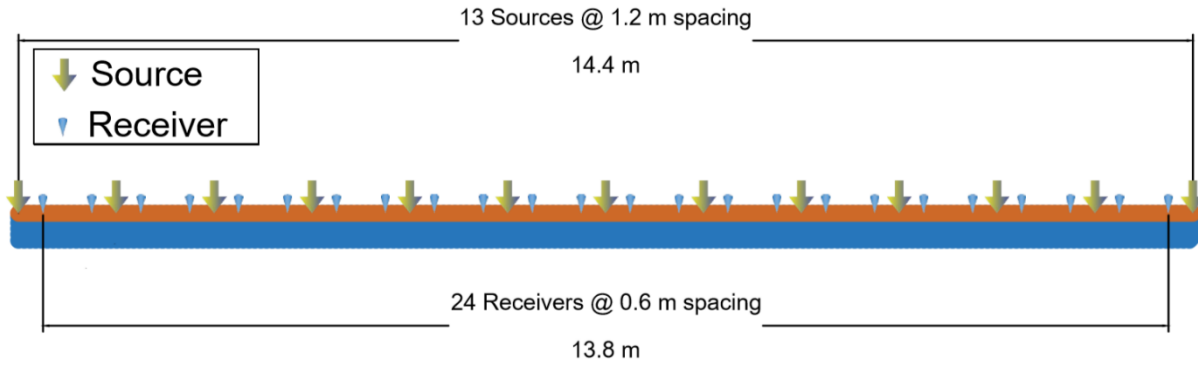


Figure 4-13 Acquisition geometry used for SR-84 site



Figure 4-14 The shear-beam pressed by the hydraulic jack

A numerical mesh of the size 8×15 m (26×50 ft) (depth \times length) was used for the inversion analysis. The entire medium was discretized into a 27×51 grid of 0.3 m (1 ft) spacing in the z- and x-directions, respectively. This grid spacing was chosen for convenient placement

of source and receiver positions on the numerical mesh. The depth of the analyzed domain was selected as about a half of the testing length for good signal coverage.

Based on the spectral analysis of surface waves (Figure 4-15), a linearly increasing velocity of 450 to 700 m/s (1476 to 2296 ft/s) was determined and used during the analysis. For the analysis, the recorded data was filtered through the frequency bandwidth of 60-100 Hz and utilized for one inversion run. The termination criterion of inversion was determined as when the analysis reached a predefined maximum number (50) of iterations, or the least-squares error decreased less than 1% (or increased) for ten iterations. For this inversion run, it stopped at 45 iterations, which took a total of about 20 minutes on a desktop (Dell Precision 5820 Tower, Intel Xeon CPU W-2145, 8 cores with 3.70 GHz each, 64GB RAM).

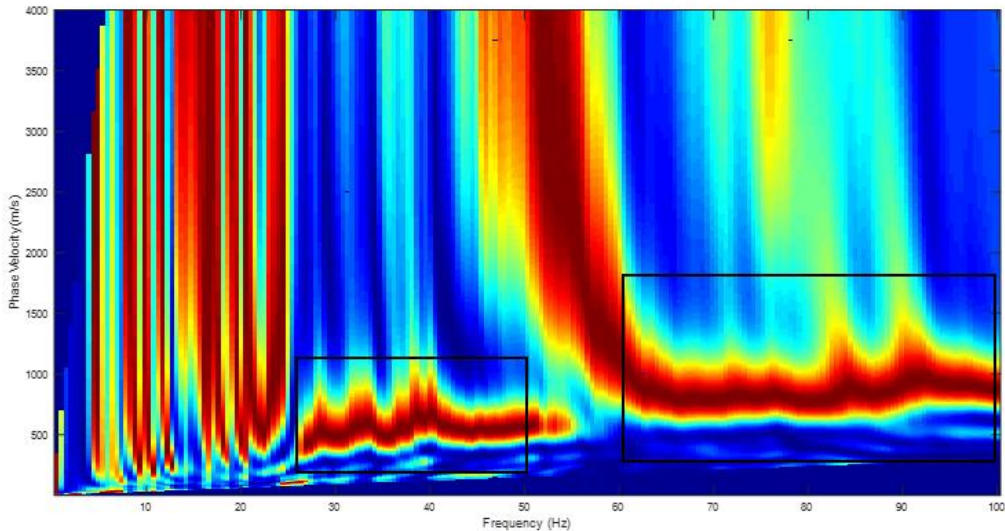


Figure 4-15 Spectral image of measured data from the first shot and first line of receivers

The entire medium was updated cell by cell during the inversion process, and the waveform match improved. Shown in Figure 4-16 is the waveform match at the end of the inversion run. It is seen that a very good match for most of the channels is obtained. Some

channels close to the source were removed to reduce the effect of source-receiver coupling on the inversion process. The good match of the first arrivals shows that the choice of the initial velocity was sufficient. There is some indications of phase and amplitude mismatch for some of the channels. This is likely due to the noise that was not accounted for in the forward simulation.

The final inverted result is shown in Figure 4-17a, the inverted density (Figure 4-17a, top) is consistent with V_s (Figure 4-17a, bottom). At 0-1.5 m depth (0-5 ft), there is a softer layer with $V_s \sim 450$ m/s (1475 ft/s) and density $\sim 1,700$ kg/m³ (106 pcf). It is underlain by a stiffer layer. The stiffer layer starts at 1.5 m (5 ft) to the depth of 4.5-5.5 m (14-18 ft), with $V_s \sim 800$ -1100 m/s (2,624-3,608 ft/s) and density $\sim 1,750$ -1,850 kg/m³ (109-115 pcf). There is another softer layer beneath the stiff layer. This softer layer starts at the depth of about 5 m (16 ft) to the bottom. Shown in Figure 4-17b top and bottom are the shear and Young's moduli, whose variations closely resemble that of V_s and show the existence of three distinct layers.

The relationship between density and V_s is shown in Figure 4-18. The density value can be computed from V_s value as $\rho = 0.6828 V_s + 1256.3 \leq 2,000$. Again, this relationship is used to determine 3D density in the next section.

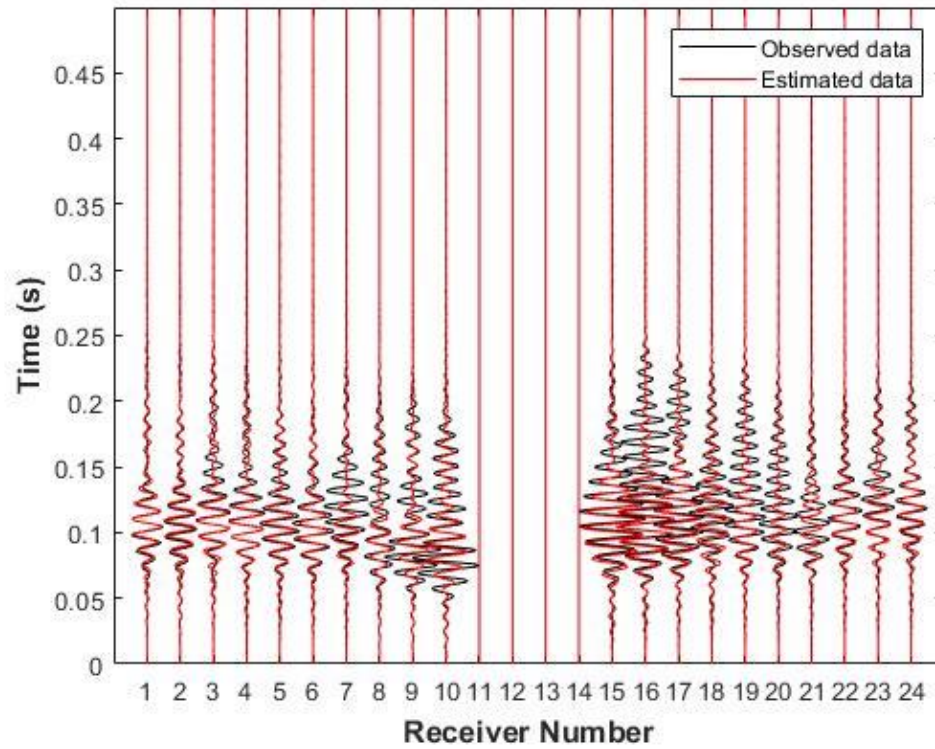


Figure 4-16 Waveform comparison of observed data and estimated data from the final inverted model

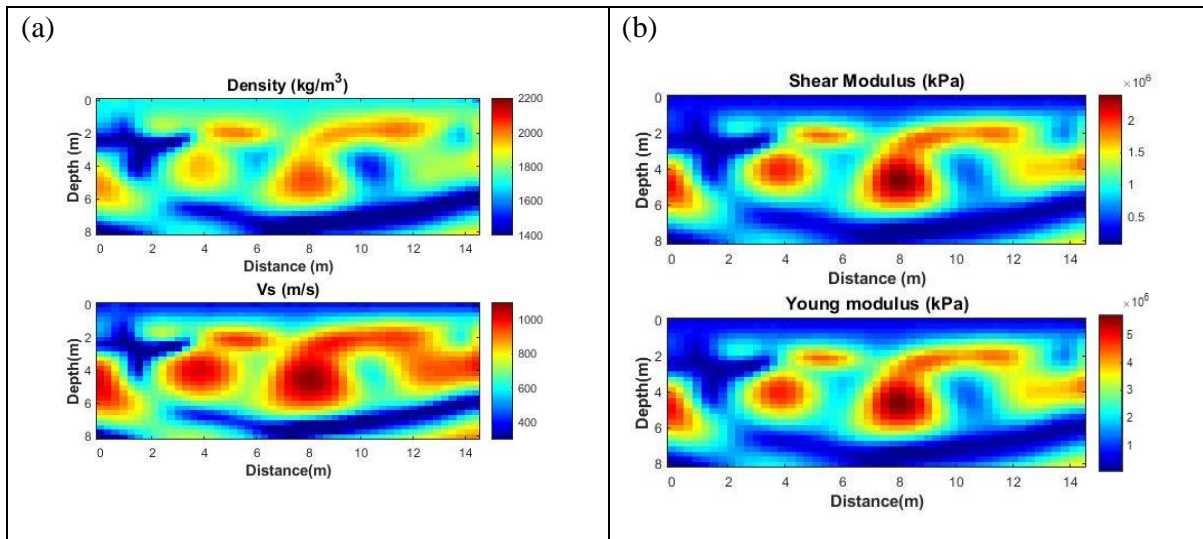


Figure 4-17 SR-84 site: (a) Density and V_s profiles and (b) shear and Young's moduli

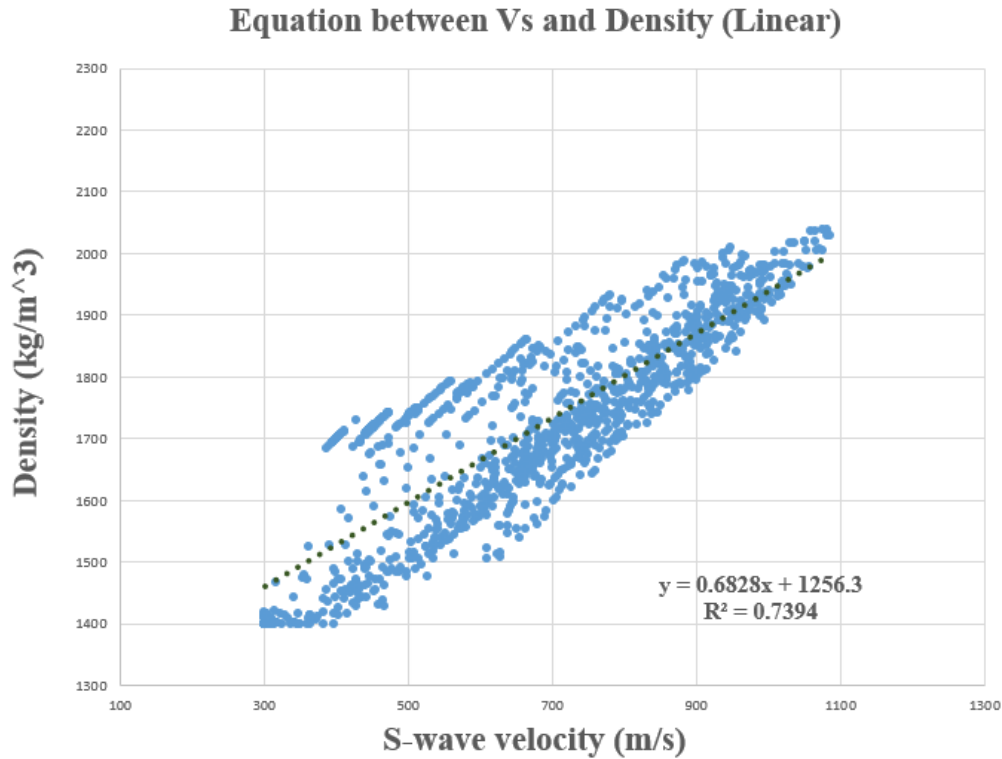


Figure 4-18 SR-84 site: Equation to estimate the relationship between S-wave velocity and density

4.3.2. 3D Full Waveform Inversion of PSV-wave Data

Similar to the previous testing site, a 3D FWI analysis was performed. The data was obtained using a 2D array of geophones and shots located on the ground surface. In total, 48 geophones with a spacing of 1.5×3 m (5×10 ft) were placed in 4 lines with 12 geophones each line. A total of 60 shots were applied on the ground surface in a 1.5×3 m (5×10 ft) configuration in 5 lines with 12 shots each line. The acquisition geometry is shown in Figure 4-19.

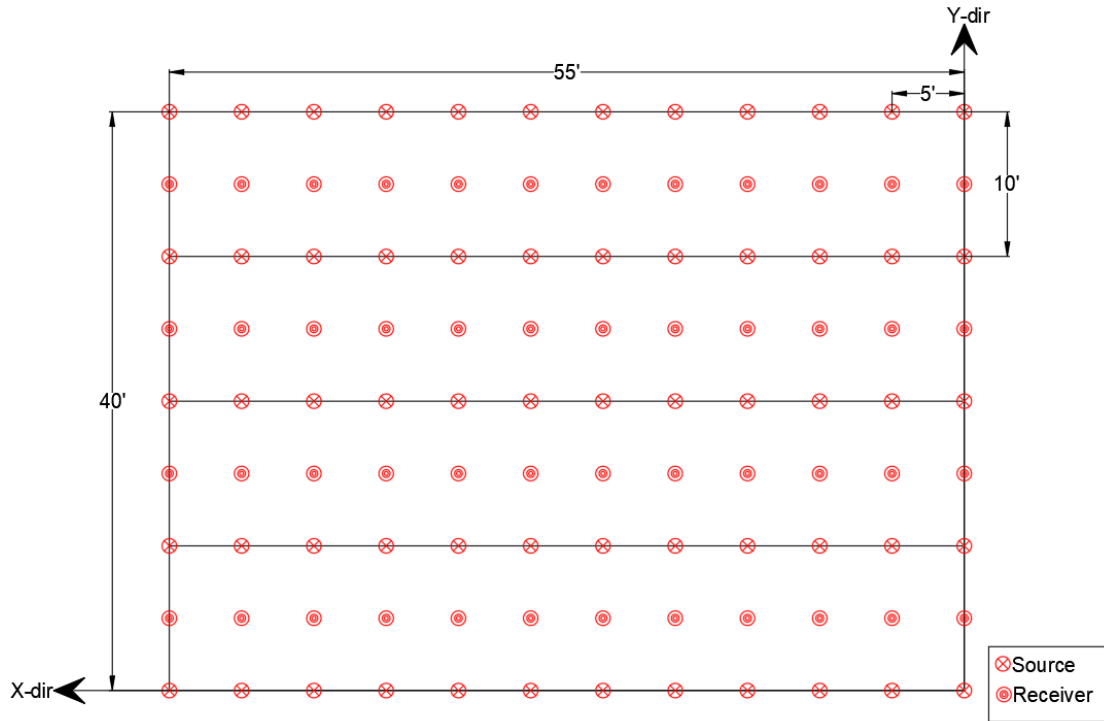


Figure 4-19 The acquisition geometry used to gather data for the 3D FWI analysis

The source was applied at each shot location through the strike of a 40 kg (88 lb) drop-weight using the propelled energy generator (PEG) shown in Figure 4-7. Each strike generated a wavefield that was recorded by all the 48 surface 4.5-Hz vertical geophones simultaneously. Each recording was performed for a total duration of 1 second using a sampling rate of 0.5 ms. This allows for frequencies as much as 1000 Hz ($1/2 \times \text{sampling rate}$) to be sampled without aliasing.

To facilitate source and receiver placement on the numerical mesh, a grid spacing of 0.375 m (1.25 ft) was chosen for the first and second frequency stages. Based on spectral analysis of surface waves (Figure 4-15), a linearly increasing initial V_s of 450 to 700 m/s (1,476 to 2,296 ft/s) was determined and used to initiate the inversion analysis (Figure 4-20a). V_p was chosen to be twice that of V_s for this analysis. The inversion was performed in one frequency

stage of 10-50 Hz in time domain. This frequency range was chosen based on multimodal energy localization in the surface wave data (Figure 4-15).

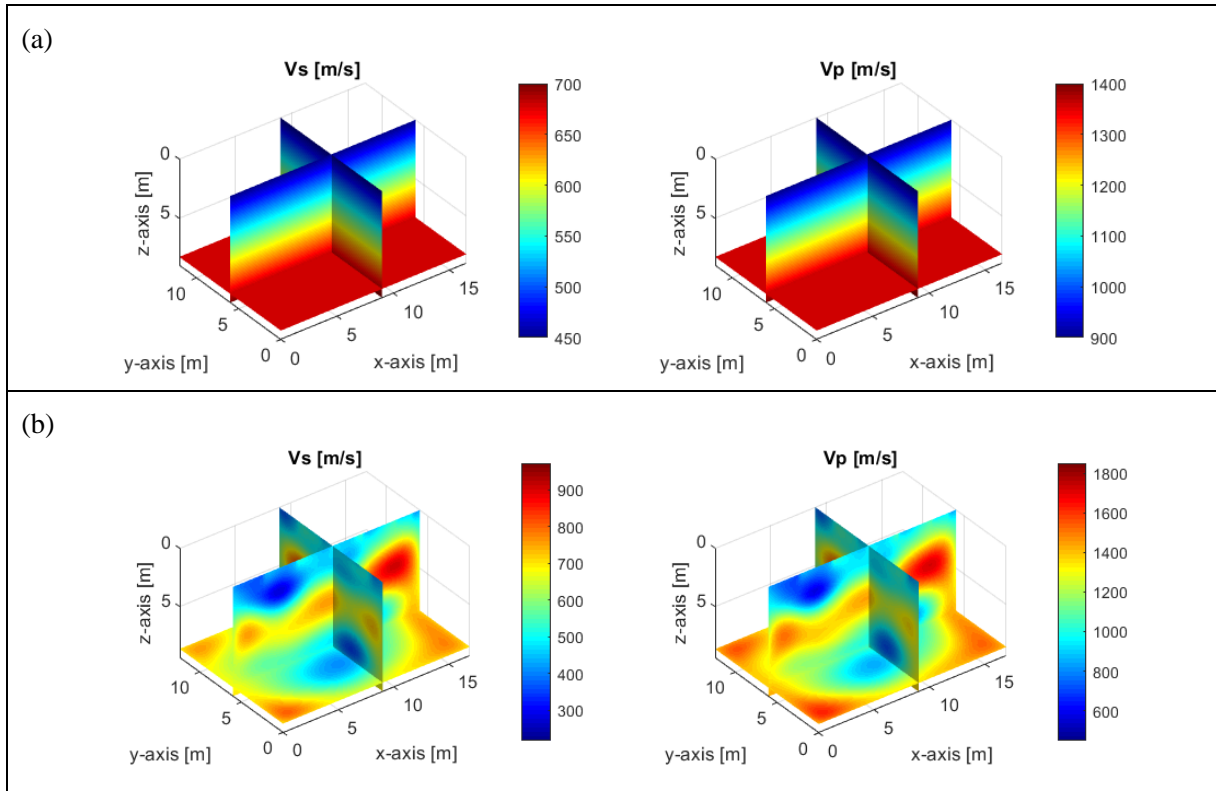


Figure 4-20 SR-84 site: V_s and V_p (m/s) for (a) the initial model (b) the final inverted result

Shown in Figure 4-20b is the final inverted results for V_s and V_p at the end of the inversion run. There is indication of three distinct layers in the final inverted image. The shallow layer ends at about 1.5 (5 ft) from the surface, which is underlain by a high velocity zone of rock. The third layer shows another low velocity zone with similar characteristics to that of the first layer. This third layer starts at about 5 m (16 ft) from the ground surface and continues all the way down to the bottom of half-space. There is indication of a deeper first layer to the left of the inverted image. Shown in Figure 4-21 is the 3D rendering of the final inverted result for both V_s

and V_p for the final inverted result. There is clear indication of an intermediate high velocity zone separating lower and upper layers of low velocity.

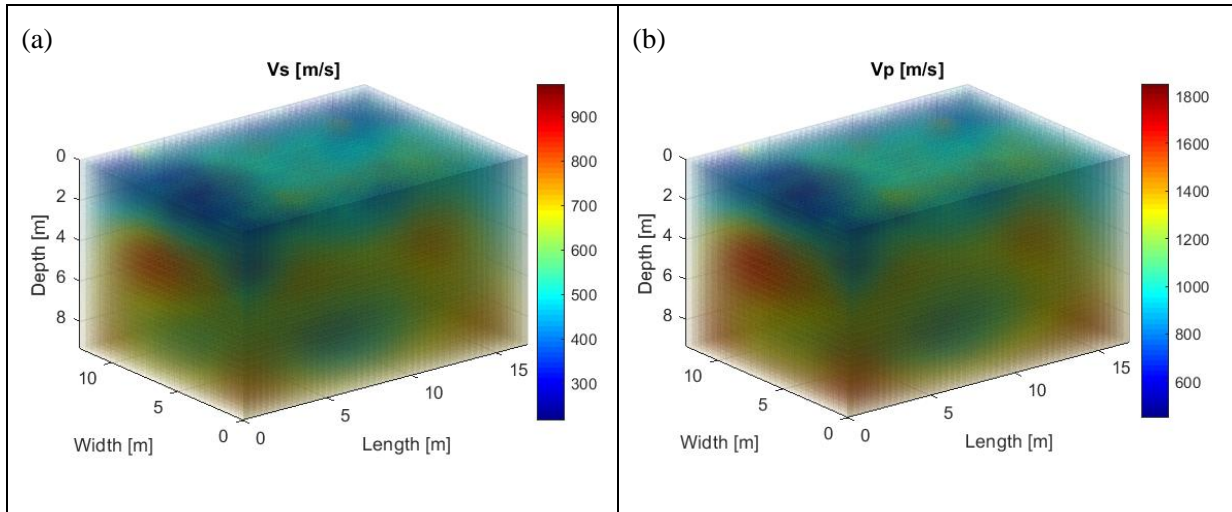


Figure 4-21 SR-84 site: 3D rendering of the final inverted result for (a) V_s and (b) V_p with transparent features

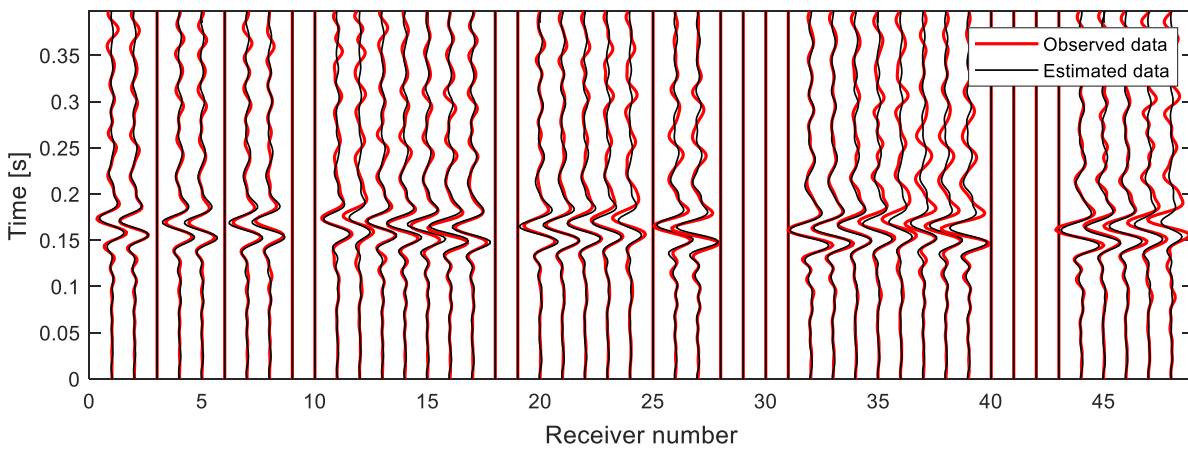


Figure 4-22 SR-84 site: waveform comparison for a sample shot for the observed and estimated data at the end of inversion

Shown in Figure 4-22 is the waveform comparison of a sample shot corresponding to the true and estimated wavefields. There is a good match of the first arrival signal that shows the initial model was sufficient. No cycle skipping or matching of wrong peaks is seen, which shows the optimization was able to well approach an appropriate minimum of the objective function.

Finally, Figure 4-23 shows the mass density (ρ), shear modulus (G), and Young's modulus (E). These parameters were calculated from the inverted V_s and V_p using the linear relation of Figure 4-18. Again, the results suggest the existence of a high-velocity zone of rock separating two layers of sand. The density of rock varies from about 1,700 kg/m³ (106 pcf) to 1,900 kg/m³ (118 pcf), showing good agreement with the median values of at boring B-3 (110 pcf) and B-2 (114 pcf).

The existence of the three layers is more prominent in Figure 4-23b & c, where shear and Young's moduli are shown, respectively. The results obtained from the analysis including the existence of three separate layers, with a layer of high-velocity zone (limestone) in the middle and two layers of low-velocity zone (sand) in the top and bottom, are consistent with the invasive testing previously performed at the test site.

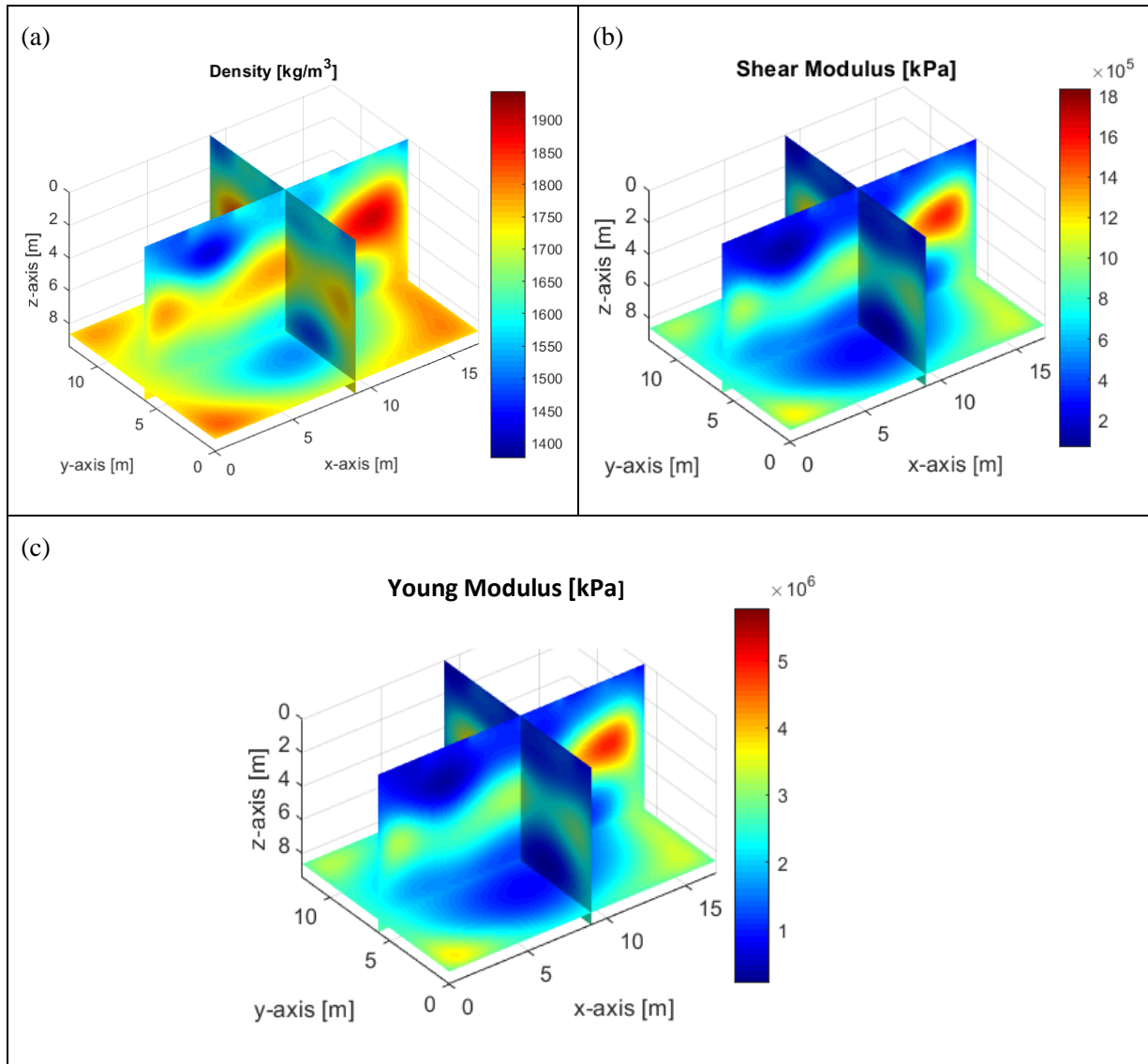


Figure 4-23 SR-84 site: (a) density, (b) shear modulus, and (c) Young's modulus

Summaries of findings

2D and 3D seismic surveys were performed at SR-84 site in Ft. Lauderdale. The 2D SH-wave data were obtained through horizontally striking a shear-beam using a sledgehammer and recording ground motions by a linear array of horizontal geophones. The 3D PSV data were obtained through dropping a weight and recording ground motions using a 2D array of vertical geophones. The 2D FWI analysis of SH-waves produces 2D profiles of V_s and density, and the

3D FWI analysis of PSV waves produces 3D profiles of V_s and V_p . Both analyses revealed the existence of three distinct layers, with a layer of high-velocity zone (limestone) in the middle and two layers of low-velocity zone (sand) in the top and bottom. These seismic results are consistent with the invasive testing previously performed at the test site. 3D images of density, Young's and shear moduli are also computed from the inverted results. The seismic result was used to place the footing, and the soil/rock properties at the footing are shown in Table 4-2.

Table 4-2 SR-84 site: soil/rock properties at the test footing

Depth (m)	Density (kg/m ³)	S-wave velocity (m/s)	Shear modulus (kPa)	Young's modulus (kPa)
0.000	1700.0	400.0	272000.0	598400.0
0.300	1730.0	460.8	367330.9	808128.0
0.600	1762.6	526.0	487755.5	1073062.2
0.900	1805.0	604.5	659572.2	1451058.8
1.200	1865.4	705.5	928572.9	2042860.3
1.500	1939.4	825.0	1319967.0	2903927.4
1.800	1995.3	929.9	1725229.9	3795505.8
2.100	1987.6	972.1	1878106.5	4131834.4
2.400	1889.1	921.7	1604923.0	3530830.6
2.700	1717.8	795.0	1085660.3	2388452.7
3.000	1553.9	665.5	688107.7	1513836.9
3.300	1522.0	641.4	626178.1	1377591.9
3.600	1608.0	719.4	832117.0	1830657.5
3.900	1710.1	810.7	1123968.0	2472729.7
4.200	1797.0	882.8	1400322.8	3080710.1
4.500	1864.7	930.8	1615409.8	3553901.6
4.800	1912.4	956.5	1749545.9	3849001.0
5.100	1940.1	963.2	1800004.0	3960008.8
5.400	1948.2	953.7	1771990.5	3898379.1
5.700	1935.5	927.7	1665923.0	3665030.5
6.000	1896.9	879.8	1468446.3	3230581.8
6.300	1821.6	795.6	1153134.3	2536895.5
6.600	1688.1	644.8	701751.4	1543853.1
6.900	1445.9	366.1	193775.3	426305.6
7.200	1400.0	300.0	126000.0	277200.0
7.500	1400.0	300.0	126000.0	277200.0
7.800	1448.9	400.9	232901.1	512382.5
8.100	1573.0	589.4	546443.0	1202174.6

4.4. Bell Site

The seismic testing was performed at the third site (Figure 4-24). The site is located at the 301-399 SW 50th Ave in Bell, Florida. As an effort to image the shallow soil/rock at high resolution (ft pixels), only SH-wave testing was conducted at this test site. Six lines of SH-wave data were collected at high frequencies (10-60 Hz) for the targeted resolution. Details regarding the testing setup, analysis, and results of SH-wave testing are elaborated in the following.



Figure 4-24 Testing setup at Bell site

For selection of the test foundation location, six test lines were conducted as shown in Figure 4-25. Lines 1, 3, and 5 are along east-west direction, and lines 2, 4, and 6 are along north-south direction. The acquisition geometry of each test line (Figure 4-26) includes 25 shots and 24 receivers on the ground surface. Both shots and receiver were uniformly placed at a spacing interval of 1.5 m (5 ft). Seismic wavefields were generated by horizontally striking a sledgehammer on a steel shear-beam (Figure 4-27). A vehicle wheel was on top of the shear-

beam to couple it with soil. For each shot, wavefield was generated by striking one end of the beam and recorded by 24 4.5-Hz horizontal geophones for a recording time of 1 second with a sampling rate of 0.5 millisecond.

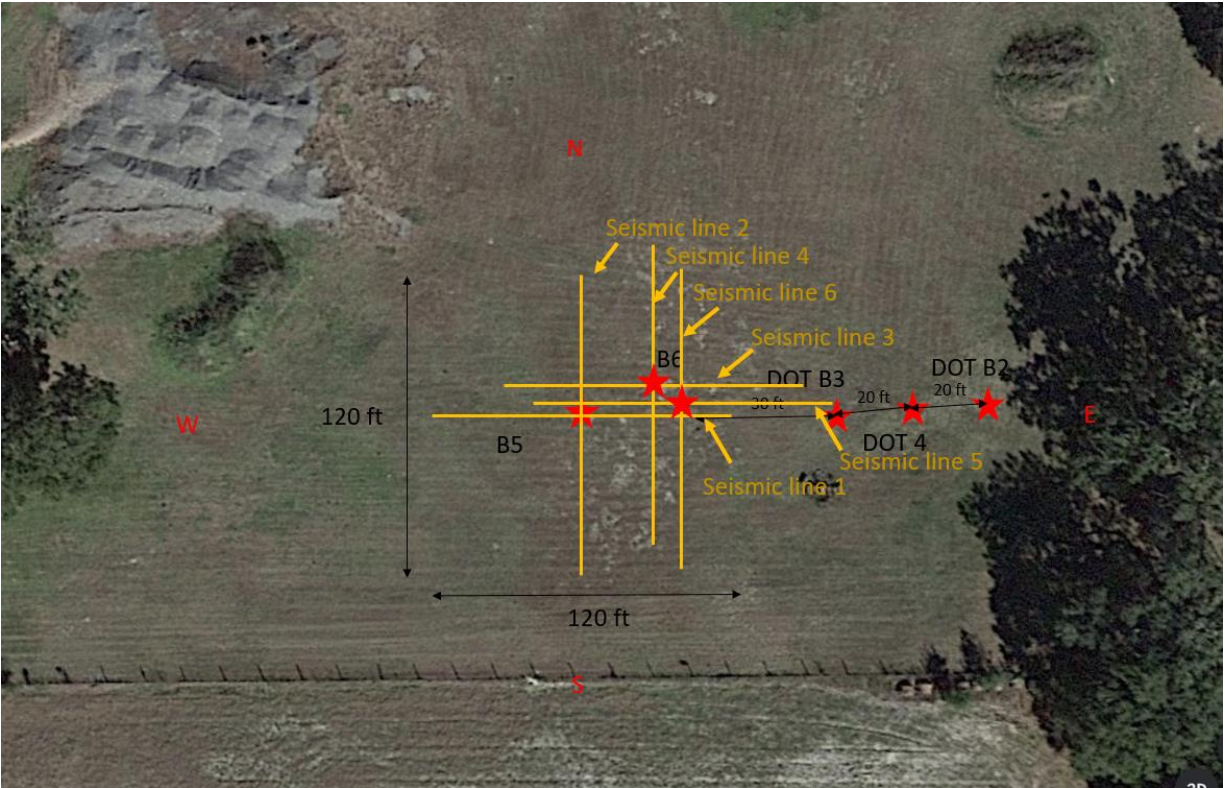


Figure 4-25 SH-wave testing setup at Bell site

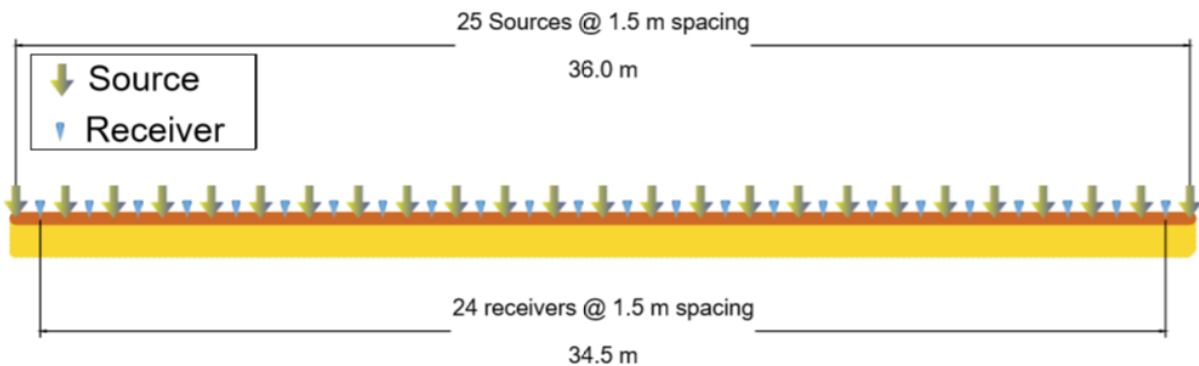


Figure 4-26 Acquisition geometry

A numerical mesh of the size 36×18 m (120×60 ft) (length \times depth) was used for inversion analysis. The entire medium was discretized into a 48×96 grid of 0.375 m (1.25 ft) spacing in the z- and x-directions, respectively. This grid spacing was chosen for convenient placement of source and receiver positions on the numerical nodes. The depth of the analyzed domain was selected as a half of the testing length for good signal coverage.



Figure 4-27 The shear-beam pressed by the vehicle wheel

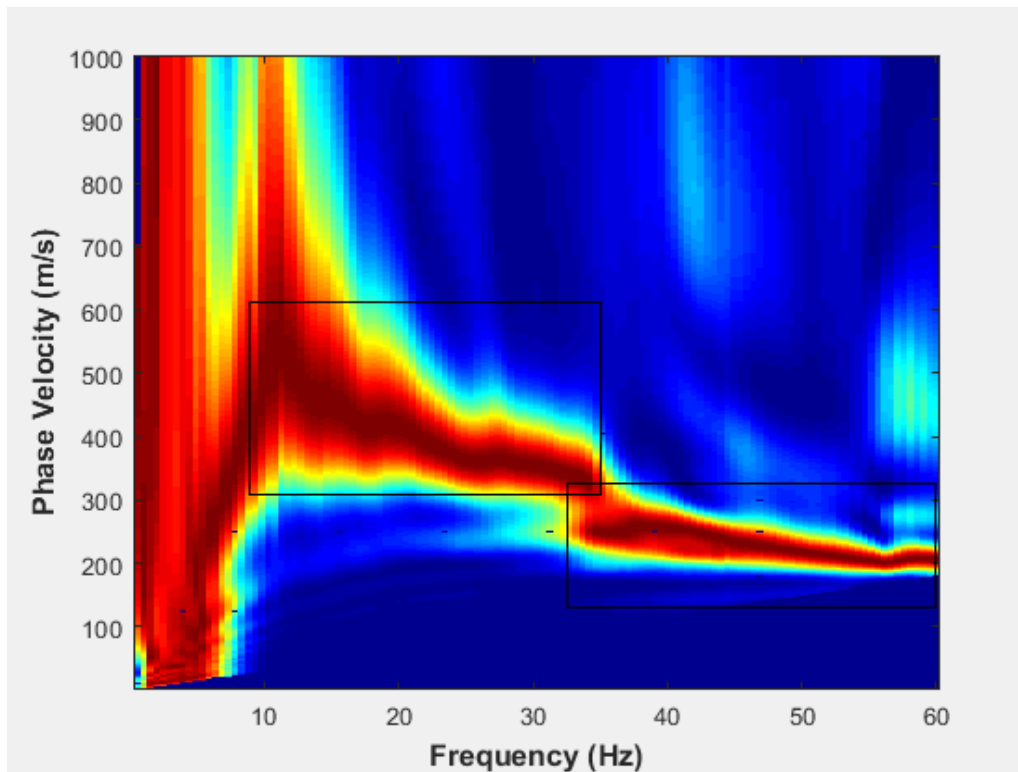


Figure 4-28 Spectral image of measured data from the first shot and first line of receivers

Based on the spectral analysis of surface waves (Figure 4-28), a linearly increasing velocity of 200 to 500 m/s (656 to 1640 ft/s) was determined and used during the analysis. For the analysis, the recorded data was filtered through the frequency bandwidth of 10-60 Hz and utilized for one inversion run for each test line. The termination criterion of inversion was determined as when the analysis reached a predefined maximum number (20) of iterations, or the least-squares error decreased less than 1% (or increased) for ten iterations. The computation time for each test line was about 25 minutes on a desktop (Dell Precision 5820 Tower, Intel Xeon CPU W-2145, 8 cores with 3.70 GHz each, 64GB RAM).

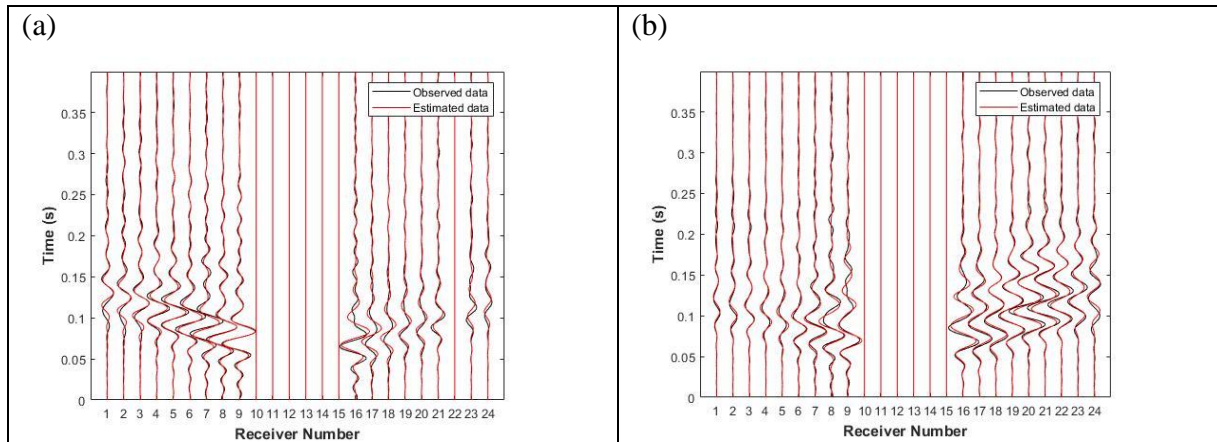


Figure 4-29 Waveform comparison of observed and estimated data from the final inverted model: (a) line 1 and (b) line 2

The entire medium was updated cell by cell during the inversion process, and the waveform match improved. Shown in Figure 4-29 is a waveform comparison at the end of the inversion run for line 1 and line 2. It is noted that channels close to the source were removed to reduce the effect of source-receiver coupling on the inversion process. Apparently, the estimated and observed data agree for most of the channels. The waveform match shows that the choice of the initial velocity was sufficient. All other test lines have a similar waveform match.

The final inverted results for all six test lines are shown in Figure 4-30. The three parallel lines (lines 1, 3, and 5 in Figure 4-30a, c, e) show similar profiles with the inverted density (top) consistent to the V_s (bottom). They consist of four layers: (1) a soft soil layer from the surface to about 1.0 m depth (3 ft) with density of about $1,400 \text{ kg/m}^3$ (87 pcf), (2) a stiff rock layer at 1.0–2.5 m (3–8 ft) depth with density of about $1,700 \text{ kg/m}^3$ (106 pcf), (3) another soft soil layer 2.5–5 m (8–16 ft) with density of about $1,400 \text{ kg/m}^3$ (87 pcf), and (4) a limestone layer from about 5 m (16 ft) to the bottom of the model, with a density of about $1,600$ (100 pcf). Note, the multiple 2D seismic lines were used to place the footings, identify layering, voids, as well as mass density of

the bearing rock layer. The latter is critical for assessing rock strength (function of dry unit weight) used in determining bearing capacity.

The three other parallel lines (lines 2, 4, 6 in Figure 4-30b, d, f) also show similar profiles. They consist of four layers: 1) a soft soil layer from the surface to about 1.0 m depth (3 ft) with density of about 1,400 kg/m³ (87 pcf), 2) a stiff rock layer at 1.0-3.0 m (3 to 10 ft) depth with density of about 1,700 kg/m³ (106 pcf), 3) another soft soil layer 3-6 m (10 to 20 ft) with density of about 1,400 kg/m³ (87 pcf), and 4) a limestone layer from about 6 m (20 ft) to the bottom of the model, with the density of about 1,600 kg/m³ (100 pcf).

Shown in Figure 4-31 are the calculated shear modulus (top) and Young's modulus (bottom). Each result is obtained based on the inverted V_s and density using equations (4-1) and (4-2). For example, the shear and Young moduli of line 1 are shown in Figure 4-31a, which are calculated from the inverted V_s and density from Figure 4-30a. The variations in the shear and Young's moduli for all six lines, closely resemble that of V_s and show the existence of four distinct layers.

The regression analysis is used for estimating the relationship between density and V_s as shown in Figure 4-32. The data of all six seismic lines are used for the analysis, and the density is determined from V_s as $\rho = 0.6849 \cdot V_s + 1262.5 \leq 1,800$. Again, the density and V_s are well correlated.

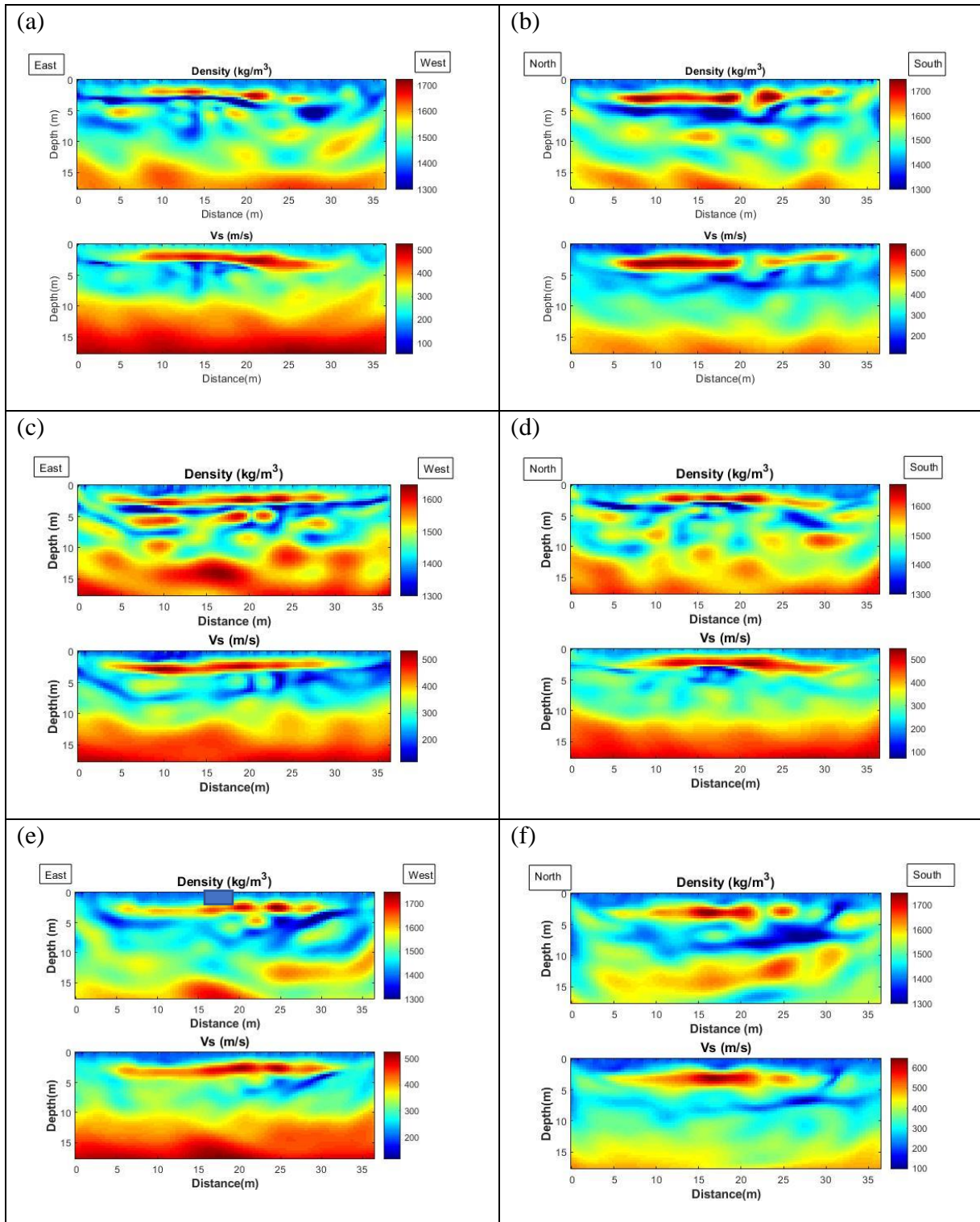


Figure 4-30 Density and V_s profile for (a) line 1, (b) line 2, (c) line 3, (d) line 4, (e) line 5, and (f) line 6. The blue box in (e) denotes the test foundation location.

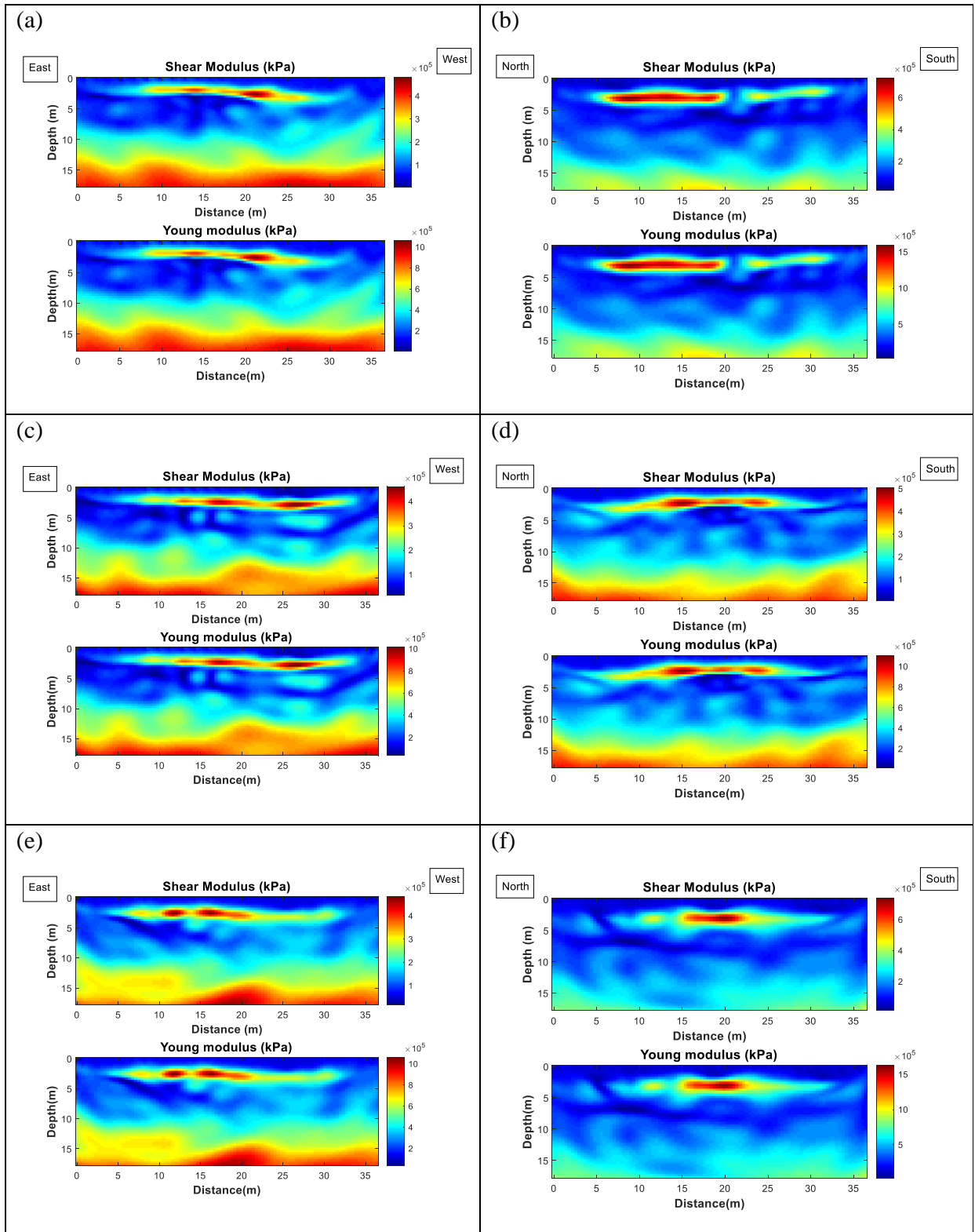


Figure 4-31 Shear and Young moduli calculated from inverted results for (a) line 1, (b) line 2, (c) line 3, (d) line 4, (e) line 5, and (f) line 6

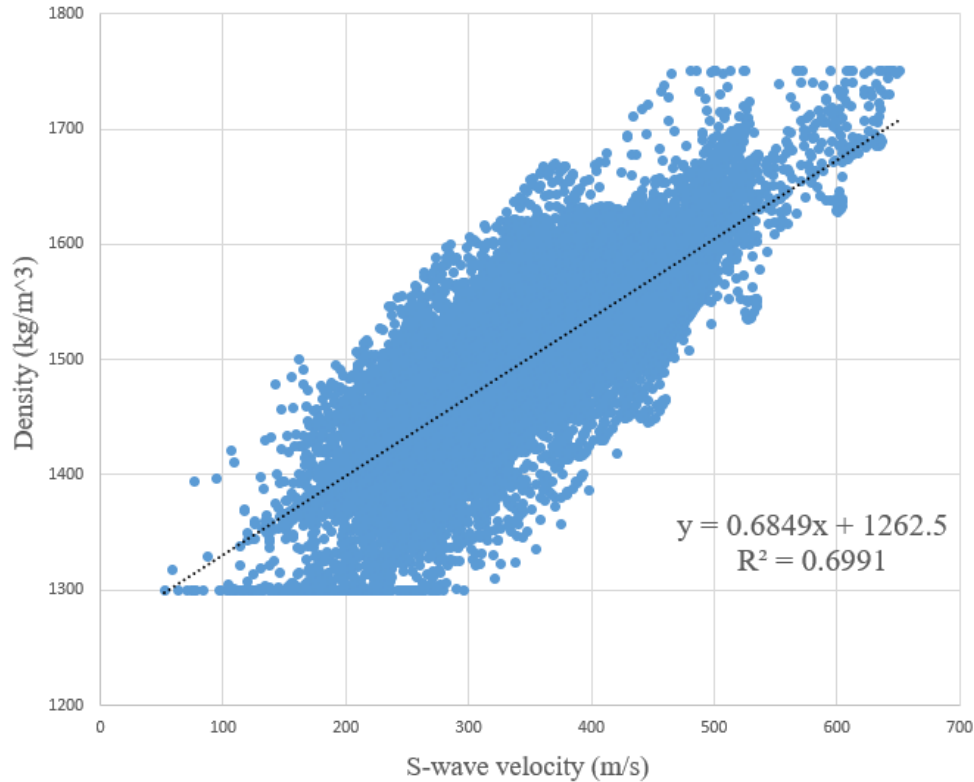


Figure 4-32 Bell site: relationship between S-wave velocity and density for data from all six seismic lines

Summaries of findings

Six lines of 2D SH-wave testing were conducted at this test site. With the collected data at high frequencies (10-60 Hz), the soil/rock profiles were able to image at high-resolution (1.25 ft pixel). Results from all six lines are similar, showing four distinct layers (shallow sand, stiff rock, soft sand, and limestone). The characterized V_s and density are consistent with the invasive tests. The seismic results were used to place the footing, with the soil properties at the footing center is shown in Table 4-3.

Table 4-3 Soil properties at the footing location

Depth (m)	Density (kg/m ³)	S-wave velocity (m/s)	Shear modulus (kPa)	Young's modulus (kPa)
0.000	1405.8	203.1	57983.6	127563.8
0.375	1417.6	215.2	65675.5	144486.2
0.750	1436.6	233.6	78411.5	172505.3
1.125	1463.8	263.5	101641.6	223611.6
1.500	1501.8	311.5	145739.6	320627.1
1.875	1553.1	375.6	219113.5	482049.6
2.250	1607.0	438.8	309467.2	680827.9
2.625	1638.1	479.2	376182.4	827601.3
3.000	1625.2	482.4	378126.5	831878.4
3.375	1573.9	451.3	320554.9	705220.8
3.750	1515.3	405.5	249217.3	548278.1
4.125	1479.8	367.9	200248.3	440546.3
4.500	1473.1	345.5	175805.0	386771.1
4.875	1485.6	335.2	166895.5	367170.1
5.250	1502.8	330.5	164152.1	361134.7
5.625	1513.1	326.2	161014.4	354231.8
6.000	1511.3	319.6	154373.2	339621.0
6.375	1497.4	309.9	143807.7	316376.9
6.750	1474.8	297.9	130872.0	287918.4
7.125	1449.9	286.0	118617.7	260958.9
7.500	1430.2	278.0	110509.2	243120.1
7.875	1421.2	276.5	108647.1	239023.6
8.250	1423.7	281.4	112704.4	247949.8
8.625	1433.9	290.2	120791.1	265740.4
9.000	1447.1	300.9	131036.6	288280.5
9.375	1460.0	312.1	142238.4	312924.5
9.750	1470.5	323.2	153652.2	338034.9
10.125	1477.8	333.9	164739.0	362425.8
10.500	1481.5	343.7	174989.0	384975.7
10.875	1481.8	352.4	184018.8	404841.3
11.250	1479.2	360.0	191686.7	421710.8
11.625	1474.8	366.6	198253.8	436158.4
12.000	1470.2	372.9	204415.6	449714.4
12.375	1467.2	379.4	211197.2	464633.8
12.750	1468.0	387.0	219814.2	483591.2
13.125	1474.0	396.1	231279.4	508814.7
13.500	1486.1	407.1	246241.4	541731.1
13.875	1504.1	419.6	264777.5	582510.4
14.250	1526.8	433.1	286402.3	630085.2
14.625	1552.5	447.0	310238.7	682525.2
15.000	1579.6	460.7	335261.4	737575.1
15.375	1606.1	473.6	360310.3	792682.6
15.750	1630.8	485.5	384428.4	845742.5
16.125	1652.5	496.1	406750.0	894850.0
16.500	1670.4	505.4	426615.9	938554.9
16.875	1684.1	513.2	443591.9	975902.3
17.250	1693.3	519.7	457396.3	1006271.9
17.625	1698.0	525.0	467948.7	1029487.1

4.5. Conclusion

The seismic task was to determine wave velocity and density profiles of the underlying soil and rock at three sites (Cemex, SR-84, and Bell). The distributions of these parameters were used for selection of test foundation locations. For this purpose, 2D seismic tests of SH- and Love-waves were first conducted at the three sites. The 2D seismic data was obtained through horizontally striking a shear-beam using a sledgehammer and recording ground motions using a linear array of horizontal geophones. The recorded data was then analyzed by a 2D SH-FWI algorithm for determination of soil/rock properties. Specifically, the 2D full waveform inversion analysis determined V_s and ρ independently for the underlying material. This was then utilized to obtain a linear relationship between density and V_s using regression analysis. Young's and shear moduli were also obtained indirectly using inverted results for V_s , density, and assumed Poisson ratio.

Results from the 3 sites show that both S-wave velocity (V_s) and density can be characterized by the SH-FWI. The characterized V_s and density are typically consistent with the invasive tests at these sites. Moreover, for each load test, the seismic densities were used to estimate the mean mass density beneath each footing which is critical to obtain the rock strength (function of dry unit weight) when computing bearing capacity. Also, unlike the electrical resistivity which exhibit similar resistivities for sand and weak limestone (Harro, D., & Kiflu, H, 2018), the seismic densities were used to identify rock vs sand layering (SR 84 and Bell) as well as voids and chimneys (Bell). Finally, knowing both V_s and density of the underlying soil and rock, estimates of shear modulus ($G=\rho V_s^2$) and Young's modulus (assumed Poisson's ratio 0.1)

can be determined for subsequent foundation settlement analyses (e.g., settlement or bearing capacity).

In addition, 3D seismic tests of vertical P and S-waves (PSV) were also conducted at two sites: Cemex and SR-84. The 3D seismic data was obtained through dropping a weight on a steel plate and measuring ground motions using a 2D array of vertical geophones placed on the ground surface. The data was then analyzed by the 3D FWI algorithm to extract V_s and V_p profiles. 3D results typically agree with the 2D results and invasive tests. By combining 2D SH-FWI and 3D PSV-FWI results, shear (G) and Young's (E) moduli can then be obtained for the entire 3D subsurface. The 3D moduli (G and E) and density are particularly useful for determination of foundation settlement and bearing capacity. Accounting for 3D spatial variation of soil/rock properties is expected to improve the foundation design.

Chapter 5

Load Test at Cemex

5.1. Site Investigation

The Cemex Site is located at the Cemex Miami Cement Plant (25°46'59.0"N 80°26'25.6"W - Figure 5-1) with 20,000 ft² set aside (outdoors) for the planned FDOT load test. The latter was required for the operation of the drilling rig, 50 ton crane and 18 wheel flatbed truck, etc. Based on the data provided by FDOT District 4/6 and site visits, the researchers concluded that the Miami limestone started at a depth of 5 ft and extended beyond a depth of 55 ft (nearby mine pit – lake). Two SPT tests and two rock core borings were conducted to characterize the rock strength and variability of Miami limestone at the site; the distance between each boring was 40 ft, which is equal to the length of each Acosta type “A” Girders, as shown in Figure 5-2. Important in sizing the footing and the length of the micropiles/anchors was assessing the reduced rock strength envelope (Recovery-adjusted and Weight-adjusted, section 2.2.2).

District 4/6 provided both SPT borings and rock coring (Appendix) through their district consultant contract (Terracon). The borings and cores showed the competent rock appears starting at 5 ft depth and spanned 60 ft (Miami limestone) with both loss of circulation and variable sand content. The water table at time of coring was at depth of 3.5 ft; however, the water table was found to fluctuate between ground surface and 1 ft below due to the seasonal precipitation during the construction of micropiles and load test, as shown in Figure 5-19. All the rock cores were tested at the State Material Office in Gainesville. A total of 5 triaxial tests, 8 unconfined compression tests, and 36 split tension tests were used to construct the strength envelope at the site as function of bulk dry unit weight. Figure 5-3 depicts the frequency

distribution of bulk dry unit weights at Cemex Site with a mean value of 119.3 pcf and a median value of 119.6 pcf, and a standard deviation of 18.2 pcf; most (80%) of the rock cores have bulk dry unit weights between 85 and 135 pcf. The direct tensile strength values (q_{dt}) were computed as 70% of split tensile strength values (q_t) as the recommendations of Perras and Diederichs (Perras and Diederichs, 2014) for sedimentary rocks. Figure 5-4 plots the direct tension strength values (q_{dt}) versus depth and Figure 5-5 shows the unconfined compression strength values (q_u) versus depth; the maximum q_u value is 1463.3 psi at the Cemex Site. By using q_{dt} and q_u test results as well as the five triaxial test results, five mass strength envelopes of Miami limestone were developed, Figure 5-6. Although the REC values are near 100% (reported by Terracon), there were large amounts of rubble zones in the recovered core boxes (Appendix), with many of the particles less than 1 in. Phase I recommended two options: (1) obtain the dry density of rubble and reduce the strength envelope based on the weighted average bulk dry unit weight; or (2) count the rubble portion as unrecovered material and reduce the strength envelope based on the new $REC_{adjusted}$ value. The second option is easier to perform, and researchers recalculated the $REC_{adjusted}$ value for Cemex Site as 72%, Table B-1. The recovery-adjusted strength envelope at Cemex Site showed excellent agreement with Phase I results (Figure 5-6) for the Miami limestone at 97.3 pcf, 105.5 pcf, and 116.9 pcf.

To further understand the variability and the correlation structure of Miami limestone, a variogram analysis of Miami limestone q_u values (68 data points from Phase I) is constructed by using Equation 3-2. Based on Figure 5-7, a correlation length of 3 ft was determined. The Coefficient of Variation (CV) of Miami limestone strength values at the Cemex Site was also obtained (1.05) by using Equation 3-3, indicating the high variability of Miami limestone.



Figure 5-1 Dimension of planned Cemex site

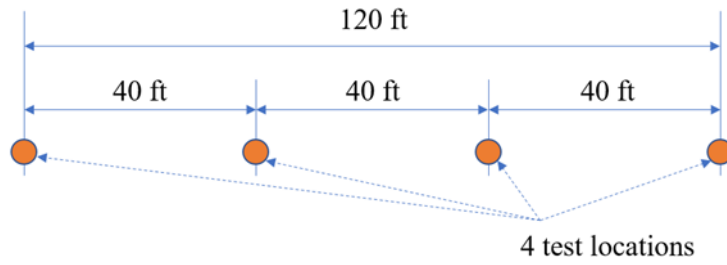


Figure 5-2 Locations of SPT and rock coring tests

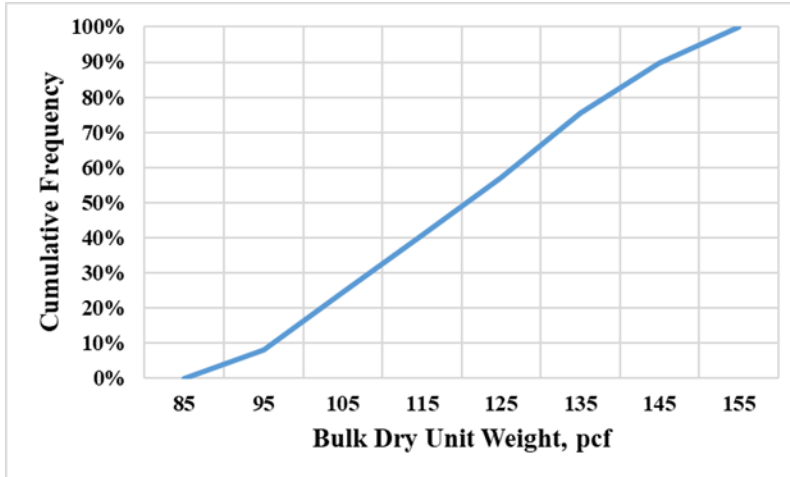


Figure 5-3 Frequency distribution of bulk dry unit weight at Cemex site

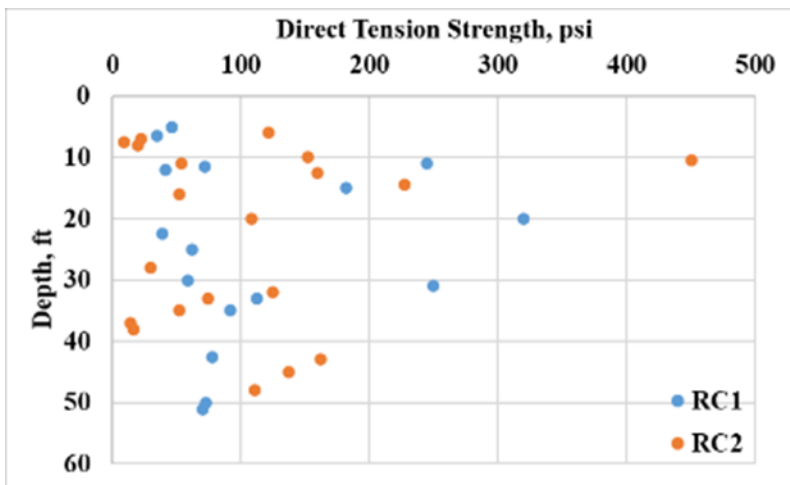


Figure 5-4 Direct tension strength values versus depth at Cemex site

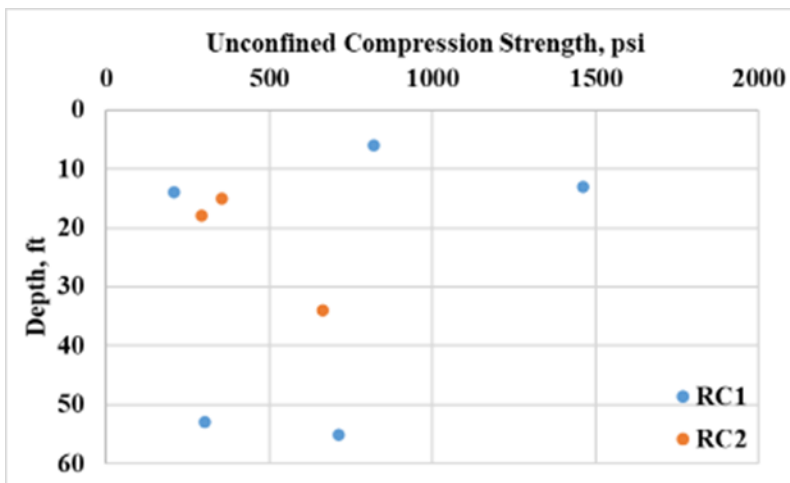


Figure 5-5 Unconfined compression strength values versus depth at Cemex site

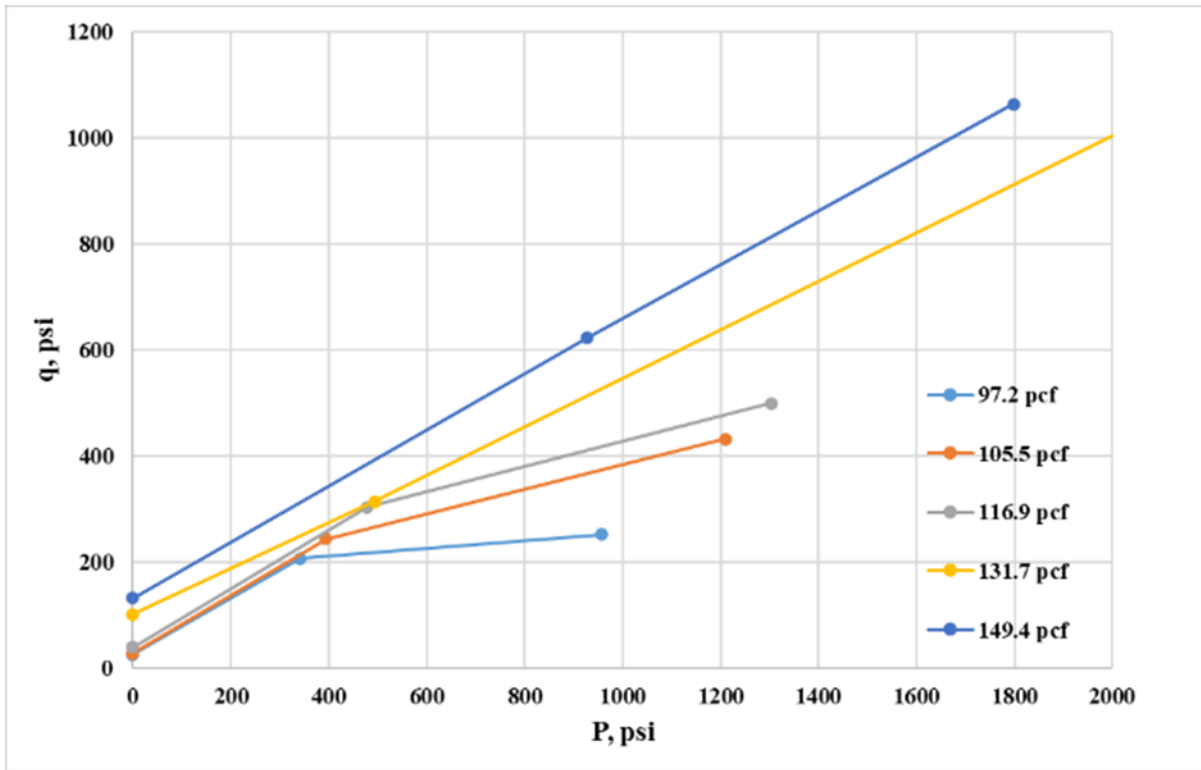


Figure 5-6 Mass strength envelope of Miami limestone at Cemex site

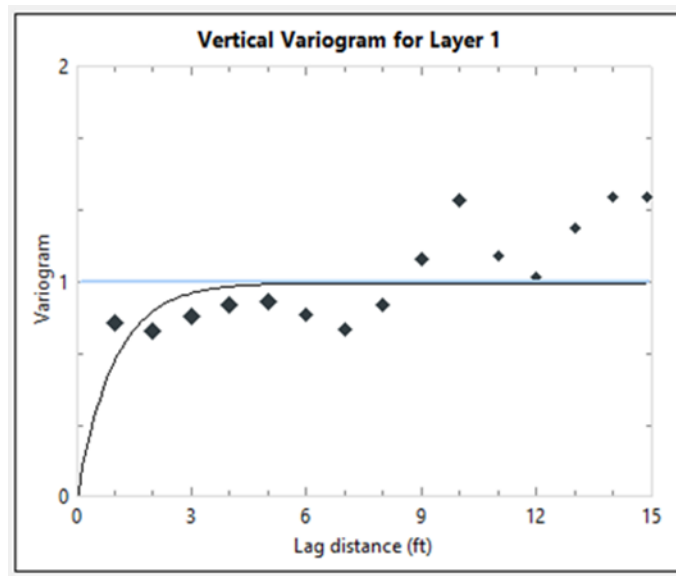


Figure 5-7 Variogram for Miami limestone

5.2. Construction of Load Test

5.2.1. Micropiles Installation

As proposed in the scope of services, eight micropiles composed of Grade 80 36-ft-, 20-ft-, and 10-ft-long threaded rods and grouted 25-ft from the bottom were installed at the Cemex Site, Figure A-1 (Appendix). The micropile installation service was provided by H2R Corp and involved drilling 8 borings down to 55 ft, placing 2.25” threaded rods to the bottom and subsequently grouting the hole up with the rod at the center (centralizer). The entire 8 anchor installation took over five weeks. Using the recommendation of the Florida Department of Transportation (FDOT, 2020), a tri-cone drill bit was used for the borehole drilling, Figure 5-8. The outer diameter of the tri-cone drill bit was 6 in, and it fit inside the casing but was smaller than the outside diameter of the casing. The 6 in diameter casing, Figure 5-9, had a cutting shoe and it was progressed by turning the casing using NW rods and the rig’s turntable.

The length of the grouted sections of each micropile was determined by Equation 5-1 based on the rock core strength tests. Using unconfined compression and direct tension, a unit side shear friction of 104 psi was found. For 8 micropiles at the Cemex Site with the bottom 25 ft grouted, a safety factor of 2.6 was found for a planned 900 tons load test (i.e., 2,351 tons available).

$$f_s = REC \times \frac{1}{2} \sqrt{q_u \times q_{dt}} \quad (5-1)$$



Figure 5-8 Tricone drill bit



Figure 5-9 6 in casing used for drilling



Figure 5-10 S5Z WIL-X hydraulic expansive cement

Due to the use of cement and water for the grout, S5Z WIL-X hydraulic expansive cement was used for grouting the micropiles, which conforms to ASTM C845 Type K, Figure 5-10. The ASTM C494 Type D retarder admixture (Eucon Stasis, 4oz/100lbs) and the ASTM C494 Type F superplasticizer admixture (Eucon 37, 10 oz/100 lb) were also used in the mix to slow down the setting time, increase the workability and obtain higher early and ultimate grout strengths. It should be noted that is the temperature in summer at Doral, Miami varied from 78°F up to 92°F, with chilled water recommended at the higher temperatures. The water/cement ratio was 0.44 as recommended by Williams Form, the grout provider. The cement specimens were collected in-situ with 4 in by 8 in molds as specified in section 455-43 of the FDOT Specifications. After placement, the specimens were brought to Weil Hall Structures Materials Laboratory for unconfined compression tests. The summary of break type, setting time, and the compressive strength values are shown in Table 5-1; all specimens had 21-day compressive strength values larger than 3 times the maximum side shear (1463.3 psi - hole size/diameter of GR 80 threaded rods = 2.67) at the wall of the threaded rod. Figure 5-11 are typical fracture patterns of cylindrical concrete specimens (ASTM C39/C39M-20) identifying the break types – note, if the specimens experienced a type “III” failure without reasonably well-formed cones on both ends, the actual compressive strength values may be larger than the test results. Figure 5-12 are some pictures of type “III” failure specimens.

Table 5-1 Summary of compression tests for cement grout

Sample ID	Break Type	Set Time, Days	Compressive Strength, psi
1st	III	21	4497.3
2nd	III	14	2911.2
3rd	II	14	6731.4
4th	I	15	6166.4
5th	I	14	4483.1
6th	I	7	6219.2
7th	III	8	3687.8
8th	II	7	5590.5

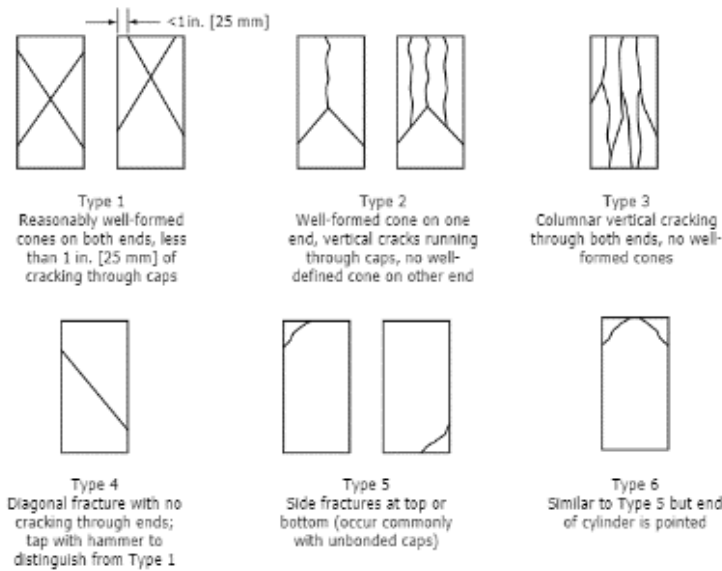


Figure 5-11 Schematic of typical fracture patterns (ASTM C39/C39M-20)

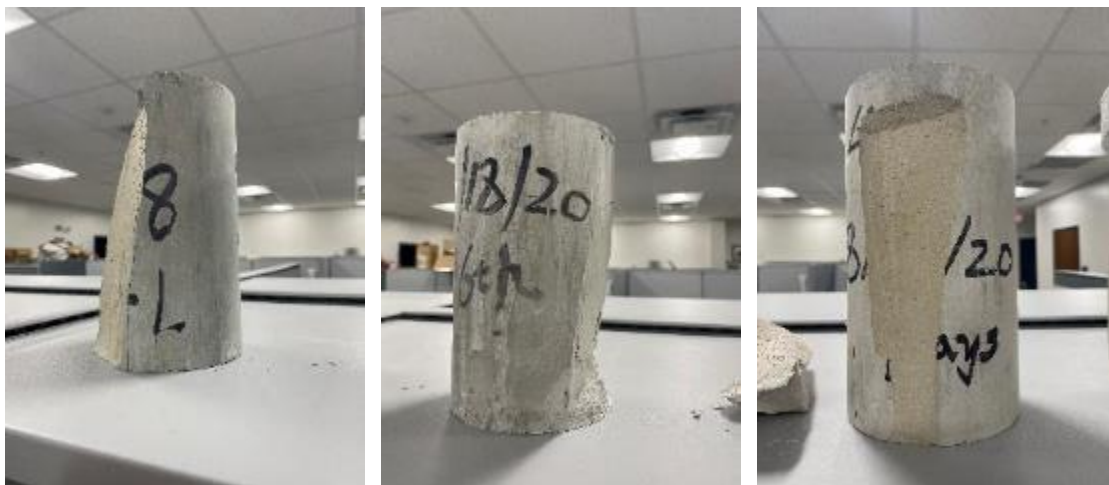


Figure 5-12 Broken specimens, type "III"

The borehole drilling, placement of threaded rods, and grouting process are shown in Figure 5-13 through Figure 5-15. One thing observed during the drilling process was that the use of clear water for circulation resulted in the removal of extra material, i.e., the hole was bigger (approx. 8 in) resulting in twice the grout take, as well as longer drilling times. Researchers subsequently changed the use of plain water to polymer mud to stabilize the hole with a constant diameter of just over 6 in, Figure 5-16. The completed installation of 8 anchors is shown in Figure 5-17.



Figure 5-13 Drilling process with threaded rods nearby



Figure 5-14 Placement of 36-ft- and 20-ft-long threaded rods with centralizers



Figure 5-15 Grouting process (the grout mixed with ASTM C494 Type D retarder admixture and the ASTM C494 Type F superplasticizer admixture)

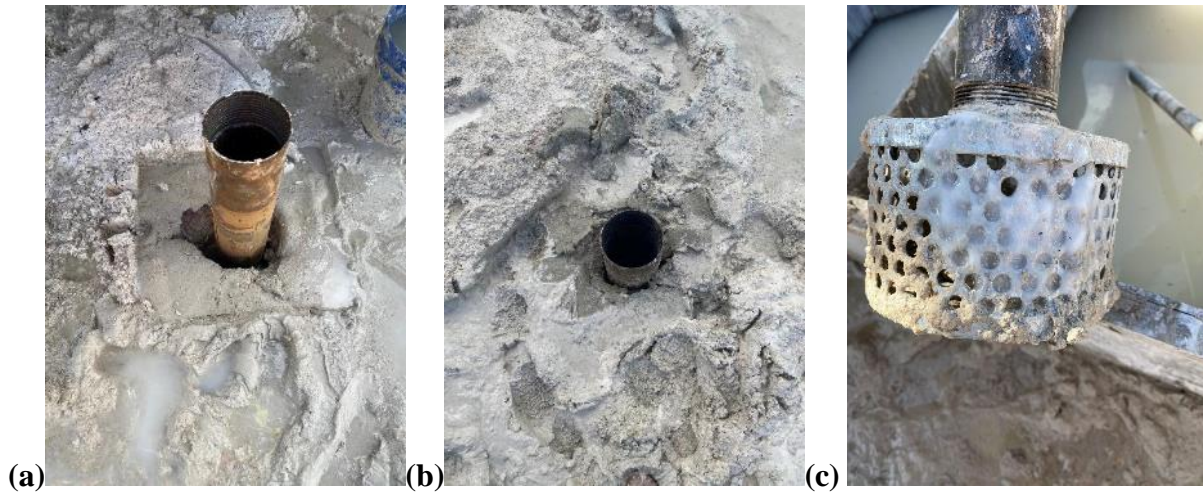


Figure 5-16 (a) Drill with clear water-lose holes; (b) drill with polymer mud-tight holes; (c) polymer mud



Figure 5-17 Eight micropiles after installation

5.2.2. Construction of the Load Test Frame

The load test system consisted of eight micropiles (36-ft-, 20-ft-, and 10-ft-long GR 80 threaded rods with 25-ft grouted length as well as GR 50 C channels and bearing plates), two Acosta type “A” girders, loading devices (calibrated 2,000-kips hydraulic jack and load cell), support systems (wide flange beams and steel square channels), and measuring instrumentations (a total station and an aluminum measuring frame). As identified earlier, the competent Miami limestone started at a depth of 5 ft, so a track hoe (Figure 5-18, a) was rented to excavate a 16-ft wide by 13-ft long, by 5-ft deep excavation to place the footing (Figure 5-18b). As the excavation reached 5-ft depth, much larger rock pieces were recovered (Figure 5-18c) and the excavator had a difficult time in penetrating and removing some of the rock. For instance, as

shown in Figure 5-18c and Figure 5-20, rock unit weight varied from 85 to 135 pcf in RC-2 (location of footing test).

Because the water table was near the ground surface, the researchers used a 2-in diameter semi-trash water pump (158 gallons per minute), Figure 5-19, to dewater the excavation. However, even after 2 hours of pumping, the water level only dropped 2 ft. Upward flows were observed at several locations at the bottom of the excavation by the researchers. Nevertheless, whenever working in the excavation, the dewatering pump was needed so the bottom of excavation could be reached by hand. Some close-up pictures of native rock pieces from the bottom of the excavation are shown in Figure 5-20. Evidently, there is very high variability as well as the wide range of porosities in the vicinity of the load test.

To prepare the bottom of the excavation for loading, it was first cleaned with a pick and shovel to make it flat (water surface was used for measurements). Note, some rock pieces fell from the sides of the excavation to the bottom and could be removed with a shovel. However, to flatten and smooth the bottom of the excavation, a pick was required. Subsequently 3 ft³ of fast-setting concrete was tremied to the bottom of the excavation with a 6-in PVC pipe to fill any voids at the rock surface and troweled smooth. Prior to placement of the steel plates (i.e., load test) and overlying steel spreader plates, the distance from the bottom of the excavation to the top of the ground surface had to be measured very accurately to identify the required Acosta girder stand heights. It was found that three additional concrete blocks were required in order fit load spreader, jack, load cell, etc. between the footing and bottom of the girders.



(a)



(b)



(c)

Figure 5-18 Excavation of tested Pit: (a) bucket teeth of the excavator; (b) pit; (c) excavated rocks (deeper rocks are closer to the screen)



Figure 5-19 Water pump



Figure 5-20 Pictures of rock pieces from tested pit during excavation: high variability with low (middle) and high (left) porosity of Miami limestone

For placement of the foundation, an 8,000-lbs forklift, a 40-ft man lift, and a 50-ton crane were rented. In addition, two 3,667-lbs D-rings, Figure 5-21, were welded on the corners of both load spreader, and steel plates prior to being installed for the forklift to place in the excavation beneath the water. After placing the 42 in square steel plate at the bottom of the excavation, researchers again measured the elevation of the plate surface using a total station and a measuring rod. To meet the vertical layout of (Figure A-1), 12 concrete blocks (4 locations)

were used at each end of the girders to raise the elevation of the support system (two wide flange beams, square channel, etc.). Then the support systems were assembled on the top of the bricks and leveled, Figure 5-23. Next, eight 10 ft long threaded rods were lifted by crane and connected with the threaded rods from the anchors. Subsequently, the first girder (9.25 tons) was lifted and placed on the top of the support system. The second girder was set next to the first one with an inside flange to flange spacing of $15\frac{3}{8}$ in. Two 2 in×27-ft 3333-lb heavy-duty straps were placed around the two girders and tied down to improve the stability of the whole system during the placement of the C channels on top of the girders and subsequent tightening. A 40 ft boom lift was used during the installation of the C channels - at least two men (safety requirement at Cemex Site) were required inside the boom lift to install the two grade 50 C15×40 channels (170 lbs) along with two 2.5-in-thick steel plates (100 lbs) through the center hole for each anchor system. Care had to be taken to ensure that the C channels were an equal distance from the girder ends (Figure A-2). After placement of the girders, and attachment of the anchor system, the pyramid load spreader was installed and positioned by 4 steel channels and 4 threaded rods with lock washers and nuts, Figure 5-24, beneath the 2 girders. Next, two steel plates (36 in and 28 in) were placed by forklift on the top of 42-in steel plate under the water level, followed by the load spreader on the top of the plates. Then the 2,000-kips calibrated hydraulic jack (oil hoses were connected while the jack suspended in the air by forklift) was placed. Finally, the calibrated load cell was installed on top of the jack, Figure 5-25, and positioned by hand.

To measure vertical displacement of the four corners of the foundation, a 3-ft tall aluminum frame (Figure 5-26, a), specially constructed to allow individual leg movement, was placed on top of the corners of the 42 in steel plate. Next, four sections of tape measure (12 in long) were attached to each corner of the measuring frame (L aluminum channels) and a total

station was used to measure vertical displacement at each corner. The total station was placed over 30 ft from the load test and each corner of 42-in steel plate movement are noted as BL, FL, FR, and BR, Figure 5-26. Note, the first symbol represents back or front and refers to leg position relative to the total station (e.g., front closer to the total station, and the lake). The 2nd letter, L and R, refers to left or right relative to the total station. The completed assembly of the load frame, footing and instrumentation at the Cemex Site is shown in Figure 5-27.



Figure 5-21 D-rings welded on the plates and the new load spreader



Figure 5-22 Twelve bricks under support systems at each end of girders



Figure 5-23 Bubble level on the two wide flange beams



Figure 5-24 Pyramid load spreader



Figure 5-25 Hydraulic jack and load cell setup



(a)



(b)

Figure 5-26 (a) locations of tape measures and measuring frame; (b) total station



Figure 5-27 Completed construction of load test at Cemex site

5.3. Bearing Capacity

The load test, i.e., both loading and unloading occurred in 9 increments with the load being maintained for 20 minutes (creep) for each increment. Researchers recorded the load versus displacement response with the total station and the load cell at the end of each increment. The loading and unloading versus settlement curves and bearing capacity predictions are shown in Figure 5-28 (permanent deformation occurred according to the unloading curve). A maximum load of 325 tons was reached and maintained for 20 minutes, when the inclination of the jack became pronounced, Figure 5-29, and it decided to unload the foundation, Figure 5-28. The footing experienced a local out of plane (of the girders) shear failure with a differential settlement of 2.01 in between the front and rear of the footing with a mean settlement of the footing of 2.74 in.

For estimation of bearing capacity of the footing, a representative set of strength parameters is required based on the dry unit weight profile and layering. Figure 5-30 presents the recorded dry unit weights from boring B-2 at the center of the footing. Unfortunately, only 50% to 67% of the 5 ft core run was available for testing. Due to variability and outlier issues, it was decided to incorporate the seismic shear results, Figure 5-30; as discussed earlier (chapter 3) at least 20 points (i.e. population) within the influence zone should be used to infer strength parameters when assessing bearing capacity (due to size of bearing rupture surface). Evident, the seismic test data (from Figure 4-3c), agrees on average well with the layering of the rock core data. In the case of no seismic data, it is recommended to obtain dry density of rock pieces not tested for strength. For instance, at the end of core run 1, almost 2 ft of non-tested rocks exist; similarly, the middle core run of B-2 had large vugs and the samples could not be tested, Figure B-4. It is recommended to measure the dry unit weight (strength and moduli correlated with) of these non-tested samples in order to have at least 20 samples within the influence zone.

Evident from Figure 5-30, there exists approximately a 5-ft-thick medium strength rock (95 pcf) underlain by a much stronger (120 pcf) layer beneath. Generally, a shallow footing has a bearing failure zone $1.5B$ to $2B$ below the bottom of footing. However, in case of a much stronger below, the rupture surface may penetrate from B to $1.5B$ (Button, 1953) depending on location of strong layer. Since, the strong layer is at $1.5B$, (depth 10.25 ft, Figure 5-30), this depth will be used. Using the dry unit weights within 5 to 10.25 ft, a geomean of 93 pcf was obtained, Table 5-2. Using the closest mass strength envelope available (97.2 pcf -Figure 5-6), and the derived mass strength parameters (ϕ , c , P_p , and ω , Table 5-3), the bearing capacity (BC) was evaluated through Equations 2-7 to 2-18 in Table 5-4 and plotted in Figure 5-28. Please note that the bearing capacities from 105.5 pcf and 116.9 pcf mass strength envelopes are also plotted

in Figure 5-28 for comparison. Evident, the bearing capacity falls between 105.5 pcf (295.1 tons) and 97.2 pcf (245 tons) based on the orange and grey lines (FL and FR).

Also considered in the analysis was inclination of load on bearing capacity. Given the 2.01 in differential settlement between BR and FL, Figure 5-28, and the distance between two diagonal corners of the footing – 59.4 in, the footing approximately inclined 2° due to the loading. The measured bearing capacity from the load cell is 325 tons, so the vertical force is 324.8 tons and horizontal force is 11.3 tons. Using Meyerhof (1953) inclination factors, Equation 5-2 and 5-3, the inclination factors were found to be minimal (e.g., i_q is 0.96) and were subsequently ignored.

$$i_q = \left(1 - \frac{\alpha}{90^\circ}\right)^2 \quad (5-2)$$

$$i_r = \left(1 - \frac{\alpha}{\phi}\right)^2 \quad (5-3)$$

where α is the angle of the inclined load to the vertical

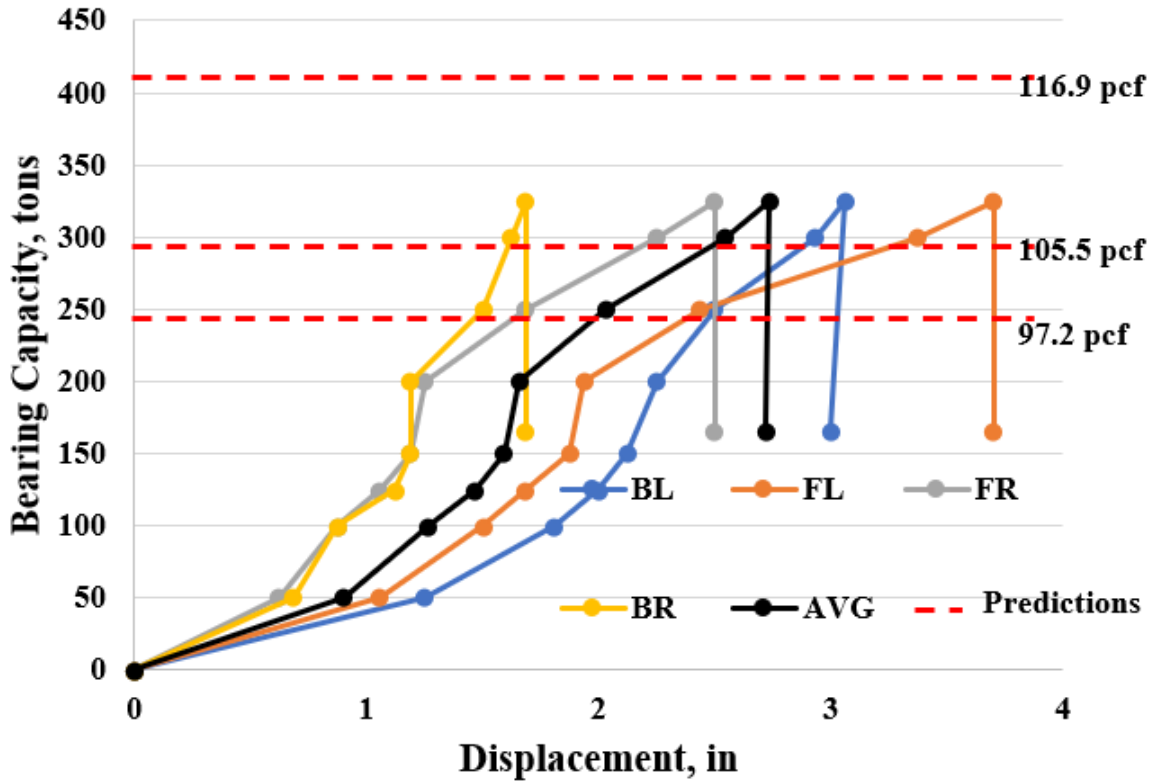


Figure 5-28 Measured bearing capacity versus displacement curve and predicted bearing capacity



Figure 5-29 Inclination of the loading jack and load cell

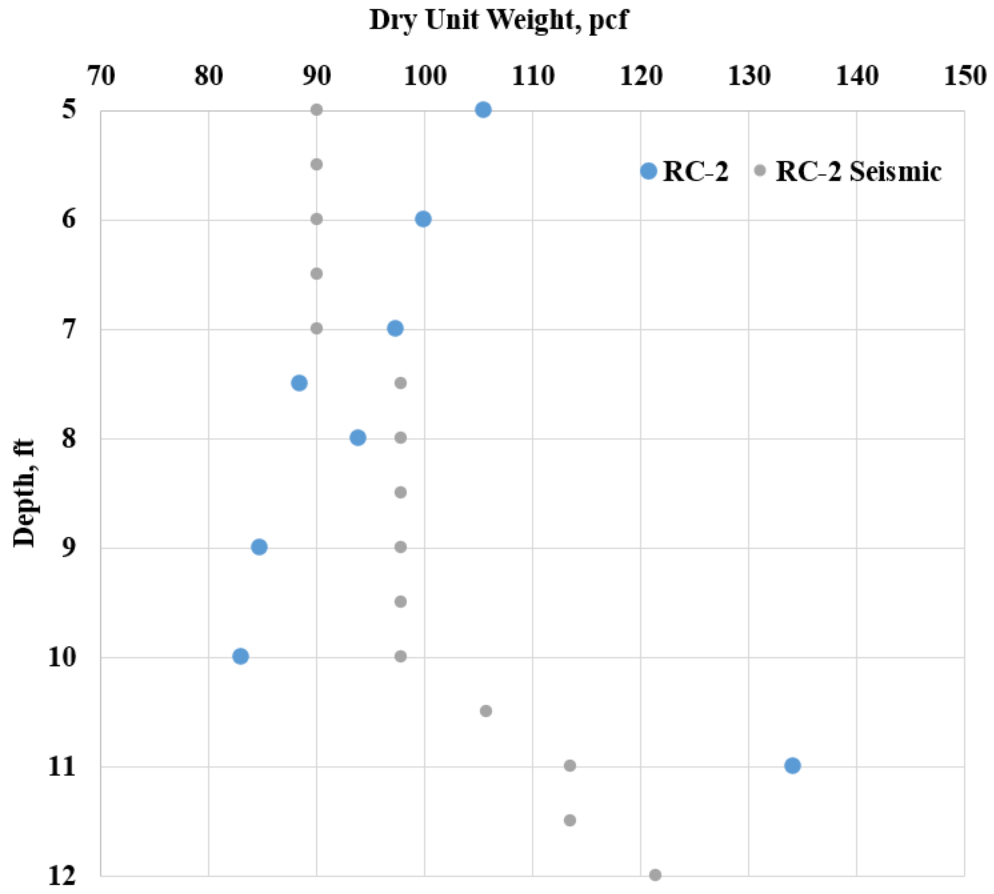


Figure 5-30 Depth versus dry unit weight at RC-2

Table 5-2 Statistical summary at boring location (RC-2)

Depth, ft	γ_{dt} , pcf	Modulus E_i , psi
5	105.5	50,115.8
6	99.9	36,389.5
7	97.3	31,352.6
7.5	88.4	18,869.8
8	93.9	25,782.5
9	84.7	15,248.0
10	83	13,836.9
11	134.2	258,183.1
Summary Statistics		
Count	7	8
Mean	93.2	56,222.3
Geomean	92.9	33,309.0
Harmonic Mean	92.6	25,572.5
Median	93.9	28,567.5
Standard Deviation	7.7	77,164.2
CV	0.08	1.37

Table 5-3 Mass strength properties for Cemex site bearing capacity prediction

	τ - σ space			p-q space			
	c, psi	ϕ , °	ω , °	a, psi	α , °	P_p , psi	β , °
Mass properties	31.9	32.4	4.35	26.9	28.2	341.8	4.3
Note	$\frac{a}{\cos\phi} = \frac{26.9}{\cos(32.4)} = 31.9$	$\text{asin}(\tan\alpha) = \text{asin}(0.5362) = 32.4^\circ$	$\text{asin}(\tan\beta) = \text{asin}(0.0752) = 4.35^\circ$	From Figure 5-6			

Table 5-4 Bearing capacity calculations for Cemex load test

Footing Geometry	B, ft	3.5
	L, ft	3.5
	D _f , ft	5
Mass Properties	c, psi	31.9 (Table 5-3)
	φ, °	32.4 (Table 5-3)
	P _p , psi	341.8 (Table 5-3)
	ω, °	4.35 (Table 5-3)
Florida Bearing Capacity Equations	N _c	$\frac{1.8 \cos \phi}{0.8 - \sin \phi} = \frac{1.8 \cos (32.4)}{0.8 - \sin (32.4)} = 5.75$ (Equation 2-14)
	N' _c	$\frac{1.8 \cos \phi}{0.8 - \sin \omega} = \frac{1.8 \cos (32.4)}{0.8 - \sin (4.35)} = 2.10$ (Equation 2-15)
	N _γ	$\frac{1.8 [\sin \phi - \sin \omega]}{0.8 - \sin \omega} = \frac{1.8 [\sin (32.4) - \sin (4.35)]}{0.8 - \sin (4.35)} = 1.14$ (Equation 2-16)
	q, psi	5 (D _f) × 100/144 = 3.47 (Equation 2-17, overburden stress)
	N _q	$(1.5 \times \frac{P_p}{\sigma_a} - 10) \times (3 \times \sin \phi - 1) = (1.5 \times \frac{341.8}{14.7} - 10) \times (3 \times \sin (32.4) - 1) = 15.1$ (Equation 2-18)
	n	$(\frac{4}{0.3B \text{ in ft}})^{-0.055} = (\frac{4}{0.3 \times 3.5})^{-0.055} = 0.93$ (Equation 2-10)
	ξ	$1 + 0.245 (\frac{B}{L})^{0.66} = 1 + 0.245 (\frac{3.5}{3.5})^{0.66} = 1.245$ (Equation 2-11)
	N _R	1 (Equation 2-12)
	Q _{u1} , psi	$n \times c \times N_c + q \times N_q = 0.93 \times 31.9 \times 5.75 + 3.47 \times 15.1 = 223.1$ (Equation 2-8)
	Q _{u2} , psi	$n \times [c \times N'_c + p_p \times N_\gamma] + q \times N_q = 0.93 \times [31.9 \times 2.1 + 341.8 \times 1.14] + 3.47 \times 15.1 = 477.7$ (Equation 2-9)
Q _u	$\min (Q_{u1}, Q_{u2}) \times \xi / N_R = \min (223.1, 477.7) \times 1.245 / 1 = 277.8 \text{ psi} = 20 \text{ tsf}$ (Equation 2-7)	

5.4. Load-settlement Response

Besides mean settlement, differential settlement (Figure 5-32) is a major issue for serviceability limit state of a footing. Required in estimating the load-settlement response is the mass modulus (E_m), which is from the ratio of E_m/E_i (Figure 5-31, trend line). The E_i depends upon confining pressure (Figure 5-34), axial stress vs. strain response as well as the rock's dry density (Figure 5-33). The footing resided on the top of the RC-2 boring which is a major

indicator of the expected settlement (i.e., localized phenomenon vs. bearing capacity). The boring identified a strong limestone layer underlain by a weaker limestone layer followed by the high strength limestone layer (130 pcf, Figure 5-30). Due to natural heterogeneous of the Miami limestone (correlation length: 3 ft, CV = 1.06), the single Miami limestone layer is strongly layered. For the bearing capacity, as the load progresses, the stress bulb (Figure 5-35) grows and each layer carries the load. However, under initial loading, the 2nd layer's low unit weight (85 pcf) underwent the highest vertical deformation/strain as result of low stiffness (Young's modulus) as well as negligible confining stress from low Poisson's ratio (Figure 2-4). In addition, due to the rock's high CV (>1), the left and right sides of the footing exhibited appreciable settlement difference due to dry density variations. Moreover, in the early portion of vertical loading (Figure 5-28), as the vertical strains increase, the Poisson's ratio increases (Figure 2-4) and horizontal stresses and associate moduli increases. Directly beneath the footing, the stress path runs into the strength envelope, yielding occurs (Figure 5-35– grey area) and stress change in this area is limited to strength envelope. Further vertical loading shifts the stress change deeper (Figure 5-35 b- size of the yielded zone goes deeper and wider) and will be carried by the stronger/stiffer deeper layers (Figure 5-30) of the rock mass. During the last few steps of loading, the stress bulb continually expands and the shear stress of the rock mass under the footing is mobilized to push the rock mass outward. The extent of the yielded zone and motion field are shown in Figure 5-35 c, the deeper rocks start to yield and the entire rock mass in the plastic zone (zone II) is pushed outward from the center of the footing.

To validate the nonlinear behavior of the load vs. settlement response of the footing, a FEM analysis was performed with the secant modulus $E_{sec} = \sigma_d/\epsilon$ evaluated as a function of confining pressure as well as axial strain. Since, the footing was placed on highly variable rock (80 -130

pcf dry unit weight, strength, $CV > 1$), its' affect was also considered. Layer 2 which exhibited large unit weight changes would be modeled as 2 separate side by side zones.

Finally, to assist with defining the mean settlement as well as the differential settlement, the probabilistic method of shallow foundation settlement developed by the Fenton and Griffith (2002, equation 3-4 to 3-8) was applied. A discussion of both follows.

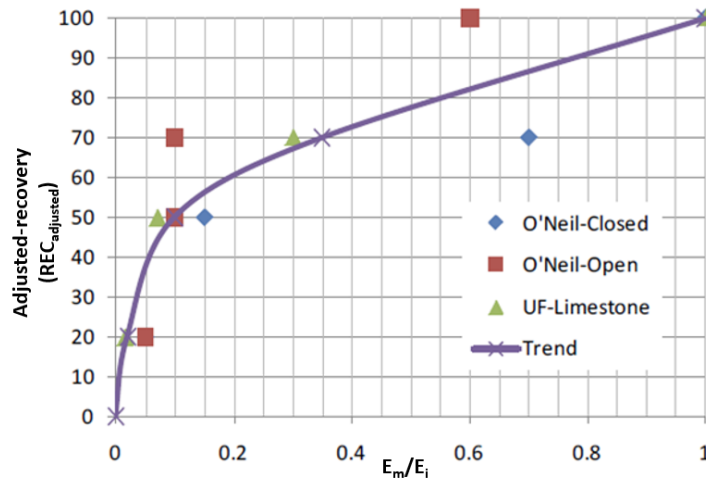


Figure 5-31 Adjusted-recovery ($REC_{adjusted}$) versus E_m/E_i

5.4.1. Finite Element Modeling

As shown in Figure 5-36, a 3D finite element model with 90 ft by 90 ft by 65 ft domain was discretized into 30000 15-noded triangular finite elements. The left and right, front and back sides of the domain are fixed in the normal direction, and the bottom of the domain is fixed in all three directions. Three layers at the top were used to characterize embedment (5-ft thickness), followed by weak limestone (5-ft thickness) and then the dense limestone (55-ft thickness) based on Figure 5-30. The material model for all three layers is linear-elastic-perfectly-plastic with Mohr-Coulomb strength parameters based on the recovery-adjusted strength envelopes (i.e., mass strength envelope, Table 5-3) of the Miami limestone, as shown in Table 5-5. The weak limestone layer 2 was separated into left (90 pcf) and right (97 pcf) zones to characterize the dry

density variations and high CV of the layer. Also, for layer 2, the Poisson's ratio was set to 0.01 (note PLAXIS 3D 2016 doesn't allow negative Poisson's ratio) for the initial loading stages and subsequently changed to 0.1 as the axial strains and confining pressure increased based on Figure 2-4. Due to the low lateral stress and Poisson's ratio, initially, the unconfined compression strength tests were used to estimate the Young's modulus. Compared to the 50-psi confining stress, Figure 2-1, the yielding strain from q_u tests were larger (average 1%) and a lower initial modulus (E_i) was obtained, as shown in Table 5-6. By using 1% strain and the q_u vs. dry unit weight correlation from Phase I (q_u (psi) = $3.24 F_u e^{2C/3} \times e^{0.04 \gamma dt B}$), the initial modulus (E_i) with 0.4 reduction factor (E_m/E_i ratio, Figure 5-31) for each dry unit weight gives: 7,544.7 psi for 90 pcf; 9,982 psi for 97 pcf; 11,255 psi for 100 pcf, and 37,369 psi for 130 pcf. The elastic modulus ranges are selected based on the dry density (Figure 5-33) of Miami limestone and confining pressure (Figure 5-34). The modulus and Poisson's ratio used in each load step with the stress state at the 3R/2 depth is summarized in Table 5-7.

The FEM results for all the loading steps for the left and right side of the footing are shown in Figure 5-37 along with the measured field response. Evident from the load vs. deflection response, the FEM's estimates (left and right) response agreed with the measured FR and FL field response, which are also displayed in Figure 5-37.

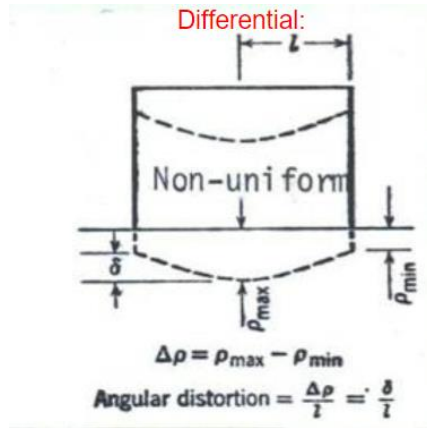


Figure 5-32 Differential settlement

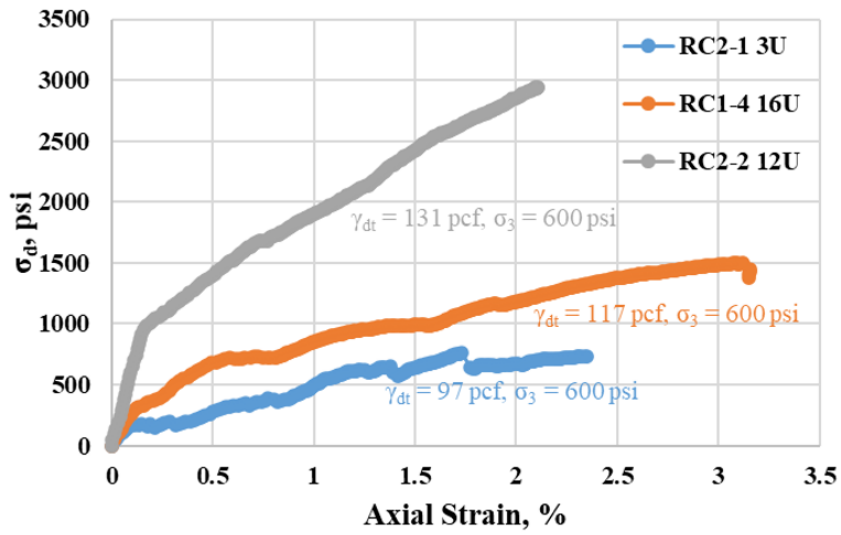


Figure 5-33 Different elastic modulus of Miami limestone with different bulk dry unit weights

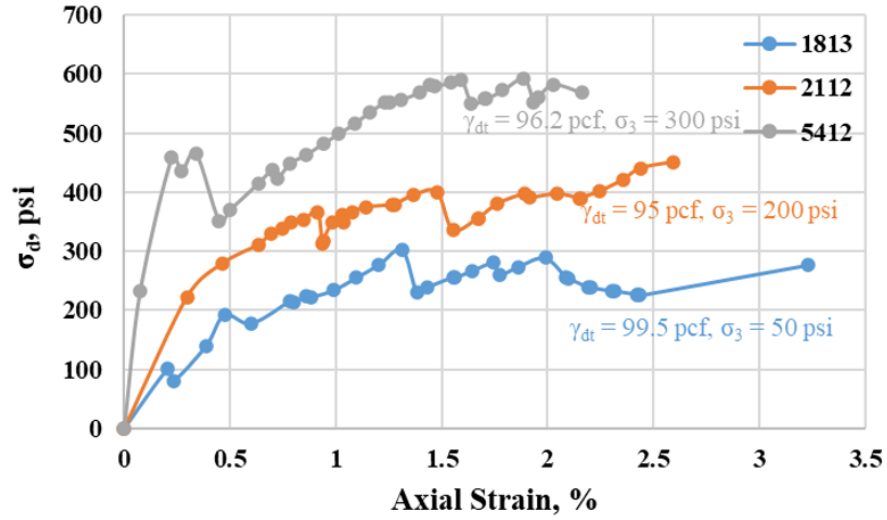


Figure 5-34 Different elastic modulus of Miami limestone under the different confining pressure

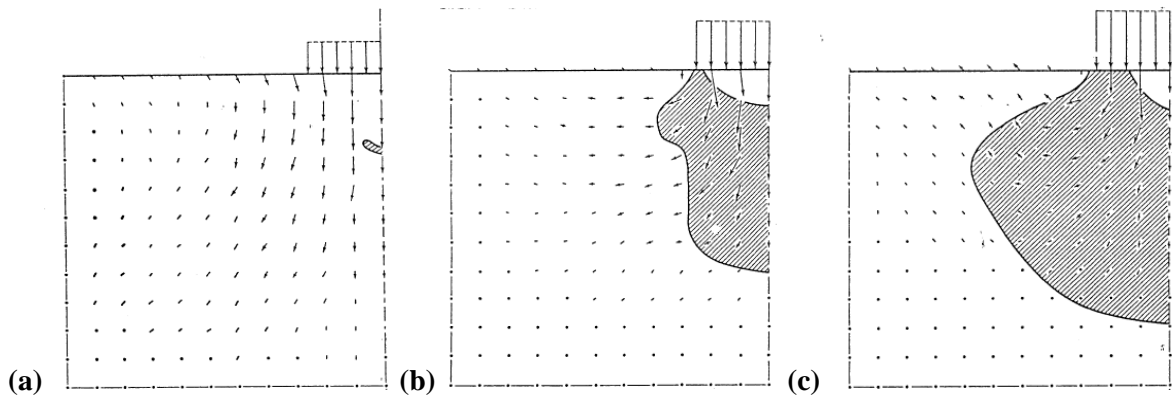


Figure 5-35 Yielded zone and motion field under different load: (a) 4.52 tsf; (b) 7.0 tsf; (c) 8.5 tsf (Lambe and Whitman, 1969)

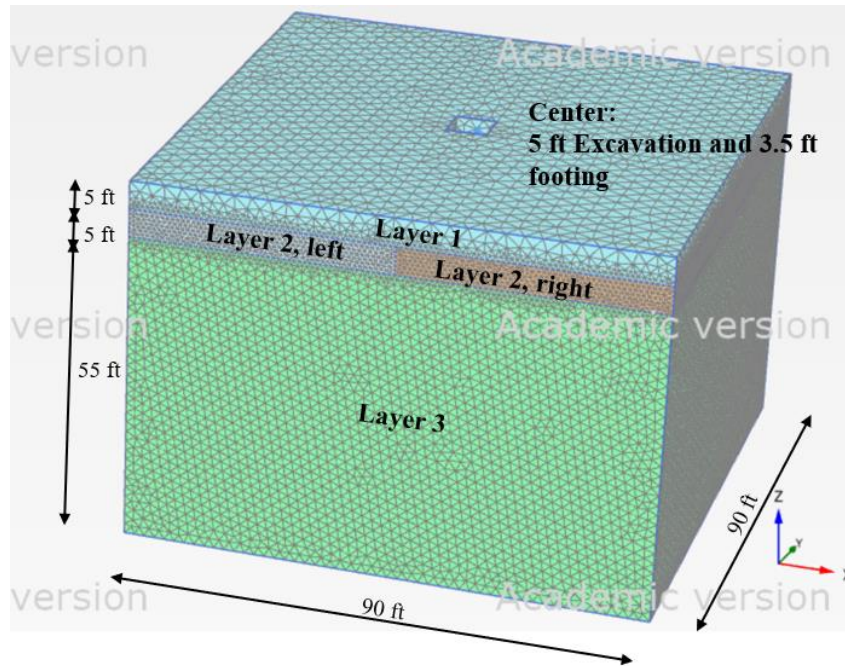


Figure 5-36 Finite element model

Table 5-5 Strength and stiffness parameters of different layers

Layer	γ_{dt} , pcf	Material Model	c, psi	ϕ , °	μ	Young's Modulus, psi
1	97	Mohr-Coulomb	32	32.4	0.05	10,514
2, Left	90	Mohr-Coulomb	13.5	31.7	0.01	1,000 ~ 21,636
2, Right	97	Mohr-Coulomb	32	32.4	0.05	1,500 ~ 31,542
3	130	Mohr-Coulomb	103.5	32.5	0.2	50,000

Table 5-6 Elastic modulus of unconfined compression strength test from Cemex and SR-84 site

dry unit weight, pcf	q _u , psi	strain, %
90.07	429.75	1.02
97.51	292.77	0.62
105.13	251.68	0.95
105.78	353.43	0.65
106.45	304.55	0.6
106.74	821.46	0.89
107.80	259.99	0.59
113.78	266.70	0.65
114.18	196.03	0.69
116.73	300.83	0.47
119.62	712.39	0.75
124.24	663.57	0.88
125.83	433.25	1.04
127.72	208.45	0.54
136.30	1206.26	1.06
137.56	1463.26	2.37
144.75	1545.48	1.81
150.77	3018.12	2.17

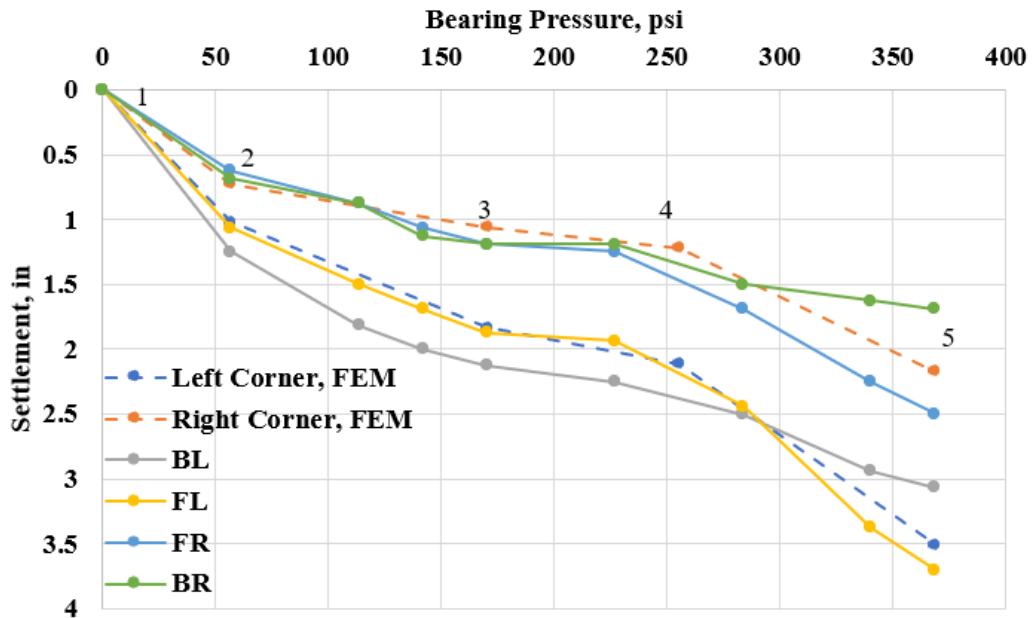


Figure 5-37 Finite element vs. measured results

Table 5-7 Stress state, Young's modulus, and Poisson's ratio of different layers in each loading stage

Loading Step	Load, tons	Layer 2							
		Left: 90 pcf				Right: 97 pcf			
		σ_1' , psi	σ_3' , psi	Elastic Modulus, psi	Poisson's Ratio	σ_1' , psi	σ_3' , psi	Elastic Modulus, psi	Poisson's Ratio
1	0	2.90	2.47	1000	0.01	2.56	2.17	1500	0.05
2	50	19.71	-0.31	1000	0.01	24.74	-0.40	1500	0.05
3	150	71.89	7.26	6500	0.01	105.87	-1.53	9000	0.05
4	225	117.16	21.34	21636	0.1	190.24	22.31	31542	0.1
5	325	195.78	45.79	6500	0.1	263.81	44.55	9000	0.1

5.4.2. Fenton and Griffith Method

Estimation of mean settlement and differential settlement of highly variable ($CV_E = 1.37$, Table 5-2) soil/rock is of great concern for shallow foundations. Generally, the use of FEM for foundation design is not viable due to the cost and time for the analysis. In practice, engineers usually compare the boring profiles and determine the layering within the footing influence zone and use the harmonic mean modulus of each layer to obtain the deterministic settlement (mean settlement), Equation 3-1.

According to the dry unit weight in boring RC-2 (footing location), the rock was divided into 4 layers, Table 5-8, with variable thicknesses; the initial modulus (E_i) of each layer was obtained from Figure 3-1 and the vertical stress (σ_i) at center of each layer obtained from Boussinesq's solution. Note, the representative depth is 12 ft (7 ft below footing) or $2B$ (typically used in settlement estimation). The stress-dependent weighted harmonic mean was computed as shown in Table 5-8. The mass modulus (E_m) was computed from the E_m/E_i ratio (0.4 from 72% $REC_{adjusted}$) from Figure 5-31, i.e., $E_m = E_h \times 0.4 = 27442 \times 0.4 = 10977$ psi. Then the deterministic

settlement was obtained as 1.18 in as shown below and presented in Figure 5-38. Again, this approach does not account for variability within a layer.

$$\rho = \Delta q_s \frac{B \times S_f}{E} 1.12(1 - \mu^2) = 277.8 \frac{42 \times 1}{10977} 1.12(1 - 0.1^2) = 1.18 \text{ in}$$

Table 5-8 Stress-dependent weighted harmonic mean calculation

h_i , ft	γ_{dt} , pcf	E_i , psi (Figure 3-1)	σ_i , psi
2	100.9	38524.9	236.1
1	91.2	22057	152.8
2	83.8	14525.3	83.3
2	134.2	258183.1	27.8
$E_h = \frac{\sum h_i \sigma_i}{\sum \frac{h_i \sigma_i}{E_i}} = \frac{2 \times 236.1 + 1 \times 152.8 + 2 \times 83.3 + 2 \times 27.8}{2 \times 236.1 / 38524.9 + 1 \times 152.8 / 22057 + 2 \times 83.3 / 14525.3 + 2 \times 27.8 / 258183.1} = 27,442 \text{ psi}$			

Fenton and Griffiths (2002) developed equations to estimate both the mean and differential settlement under a single spread footing founded on variable modulus material through a series of finite element simulations using a correlated variable modulus (Equation 3-4 to 3-8) for soil or rock. They generally recommended the geomean modulus within the influence zone for the single layer case; a geomean modulus of 33,309 psi (E_i) was obtained based on Table 5-2. Again, the mass modulus (E_m) was taken as $0.4 \times E_i = 13,323.6$ psi. Then using a Poisson's ratio of 0.1 (lower dry unit weights), the deterministic settlement (Equation 3-1) was computed followed by the differential and mean heterogeneous field settlement (Eqs. 3-4 to 3-8, shown in Table 5-9) and plotted in Figure 5-38 as a function of load along with the measured response.

A comparison of the measured load (pressure) versus settlement response of the footing vs Fenton and Griffiths predicted approach is shown in Figure 5-38. Evident, Fenton and Griffiths underpredicts the initial mean and differential settlements (higher modulus vs. initial modulus)

but agrees quite well at the higher contact stresses. Also shown in Figure 5-38 is layered approach (harmonic stress dependent modulus). Evident, the layered stress dependent harmonic mean is less (1.18 in) vs. the Fenton and Griffiths approach (1.88 in) due to the variability within the layer; however, it is within 1 standard deviation as identified by Fenton and Griffiths site variability.

Table 5-9 Load-settlement prediction calculation: $\sqrt{\gamma(B, T)}$ calculation

Parameter	Value or Calculation
$\gamma(h)$, ft	3 (Correlation Length)
B, ft	3.5 (Footing width)
T, ft	7 (2B)
$\gamma(B)$ ($\gamma(d_1)$ in Equation 3-6)	$\left[1 + \left(\frac{B}{\gamma(h)}\right)^{\frac{3}{2}}\right]^{-\frac{2}{3}} = \left[1 + \left(\frac{3.5}{3}\right)^{\frac{3}{2}}\right]^{-\frac{2}{3}} = 0.58$ (Equation 3-6)
$\gamma(T)$ ($\gamma(d_2)$ in Equation 3-6)	$\left[1 + \left(\frac{T}{\gamma(h)}\right)^{\frac{3}{2}}\right]^{-\frac{2}{3}} = \left[1 + \left(\frac{7}{3}\right)^{\frac{3}{2}}\right]^{-\frac{2}{3}} = 0.36$ (Equation 3-6)
R_B (R_1 in Equation 3-6)	$\gamma(h) \left[\frac{\pi}{2} + \left(1 - \frac{\pi}{2}\right) \exp \left\{ -\left(\frac{B}{\frac{\pi}{2}\gamma(h)}\right)^2 \right\} \right] = 3 \left[\frac{\pi}{2} + \left(1 - \frac{\pi}{2}\right) \exp \left\{ -\left(\frac{3.5}{\frac{\pi}{2}}\right)^2 \right\} \right] = 3.73$ (Equation 3-6)
R_T (R_2 in Equation 3-6)	$\gamma(h) \left[\frac{\pi}{2} + \left(1 - \frac{\pi}{2}\right) \exp \left\{ -\left(\frac{T}{\frac{\pi}{2}\gamma(h)}\right)^2 \right\} \right] = 3 \left[\frac{\pi}{2} + \left(1 - \frac{\pi}{2}\right) \exp \left\{ -\left(\frac{7}{\frac{\pi}{2}}\right)^2 \right\} \right] = 4.5$ (Equation 3-6)
$\gamma(B T)$ ($\gamma(d_1 d_2)$ in Equation 3-6)	$\left[1 + \left(\frac{B}{R_T}\right)^{\frac{3}{2}}\right]^{-\frac{2}{3}} = \left[1 + \left(\frac{3.5}{4.5}\right)^{\frac{3}{2}}\right]^{-\frac{2}{3}} = 0.71$ (Equation 3-6)
$\gamma(T B)$ ($\gamma(d_2 d_1)$ in Equation 3-6)	$\left[1 + \left(\frac{T}{R_B}\right)^{\frac{3}{2}}\right]^{-\frac{2}{3}} = \left[1 + \left(\frac{7}{3.73}\right)^{\frac{3}{2}}\right]^{-\frac{2}{3}} = 0.42$ (Equation 3-6)
$\gamma(B, T)$ ($\gamma(d_1, d_2)$ in Equation 3-6)	$\frac{1}{2} [\gamma(B)\gamma(T B) + \gamma(T)\gamma(B T)] = \frac{1}{2} [0.58 \times 0.42 + 0.36 \times 0.71] = 0.25$ (Equation 3-6)
$\sqrt{\gamma(B, T)}$ ($\sqrt{\gamma(d_1, d_2)}$ in Equation 3-6)	$\sqrt{\gamma(B, T)} = \sqrt{0.25} = 0.5$ (Equation 3-6)

Table 5-9 (Continued) Load-settlement prediction calculation

Mass Properties	μ_E	Mass effect (Figure 5-31) $\times E_h$ (Table 5-2) = $0.4 \times 33309 = 13323.6$ psi
	σ_E	CV (Table 5-2) $\times \mu_E = 1.37 \times 13323.6 = 18253.6$ psi
	ν	0.1 (Poisson's ratio)
	$\gamma(h)$, ft	3 (Correlation length)
Geometry	B, ft	3.5 (Footing width)
	T, ft	7 (2B)
Fenton and Griffiths' method	δ_{det} , in	$\Delta q_s \frac{B}{\mu_E} 1.12(1 - \nu^2) = \frac{277.81 \times 3.5 \times 12 \times 1.12 \times (1 - 0.01)}{13323.6} = 0.97$ (Equation 3-1)
	σ_{lnE}	$\sqrt{\ln(1 + \sigma_E^2(above) / \mu_E^2(above))} = \sqrt{\ln(1 + 18253.6^2 / 13323.6^2)} = 1.03$ (Equation 3-4)
	$\sqrt{\gamma(B, T)}$ (Table 5-9a)	0.5 (Table 5-9a)
	$\sigma_{ln\delta}$	$\sqrt{\gamma(B, T)} \sigma_{lnE}(above) = 0.5 \times 1.03 = 0.52$ (Equation 3-6)
	$\mu_{ln\delta}$	$\ln(\delta_{det}(above)) + \frac{1}{2} \sigma_{lnE}^2(above) = \ln(0.97) + \frac{1}{2} 1.03^2 = 0.5$ (Equation 3-5)
	μ_δ , in	$exp\left\{\mu_{ln\delta}(above) + \frac{1}{2} \sigma_{ln\delta}^2(above)\right\} = exp\left(0.5 + \frac{1}{2} 0.52^2\right) = 1.88$ (Equation 3-7)
σ_δ , in	$\mu_\delta(above) \sqrt{e^{\sigma_{ln\delta}^2(above)} - 1} = 1.88 \sqrt{e^{0.52^2} - 1} = 1.04$ (Equation 3-8)	
Settlement shape Factor (L/B= 1)		1

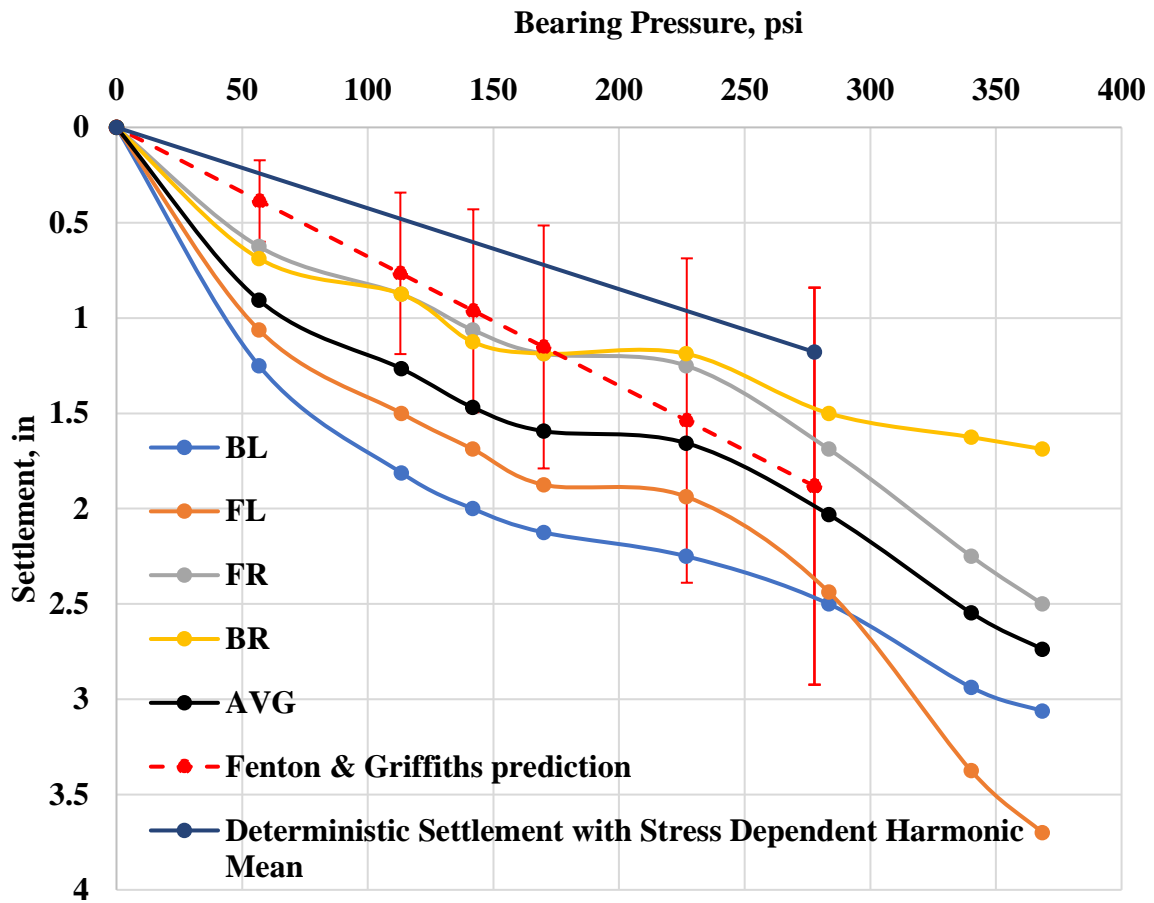


Figure 5-38 Measured and predicted Bearing stress versus Displacement Curve

Chapter 6

Load Test at SR-84

6.1. Site Investigation

The site is located on Florida State Road 84 near Southwest 148th Avenue, Davie, Florida. The site had approximately 5,000 ft² of space with 40 ft offset for vehicles adjacent to the load test, Figure 6-1 with 4 borings (provided by District 4/6). Besides space, the site was selected after reviewing bridge piers plans for I-75, I-595 and Sawgrass Expy (provided by District 4/6), along with site visits (auger to locate the top of rock), as well borings at the intersection of SR-84 and SW 148th. Of interest was thickness of both Miami and Fort Thompson limestone formations for both footing and drilled shaft sizing. One SPT and three rock core borings (PSI) were provided by the district at a spacing of approximately 40 ft, Figure 6-2, equal to the length of girders.

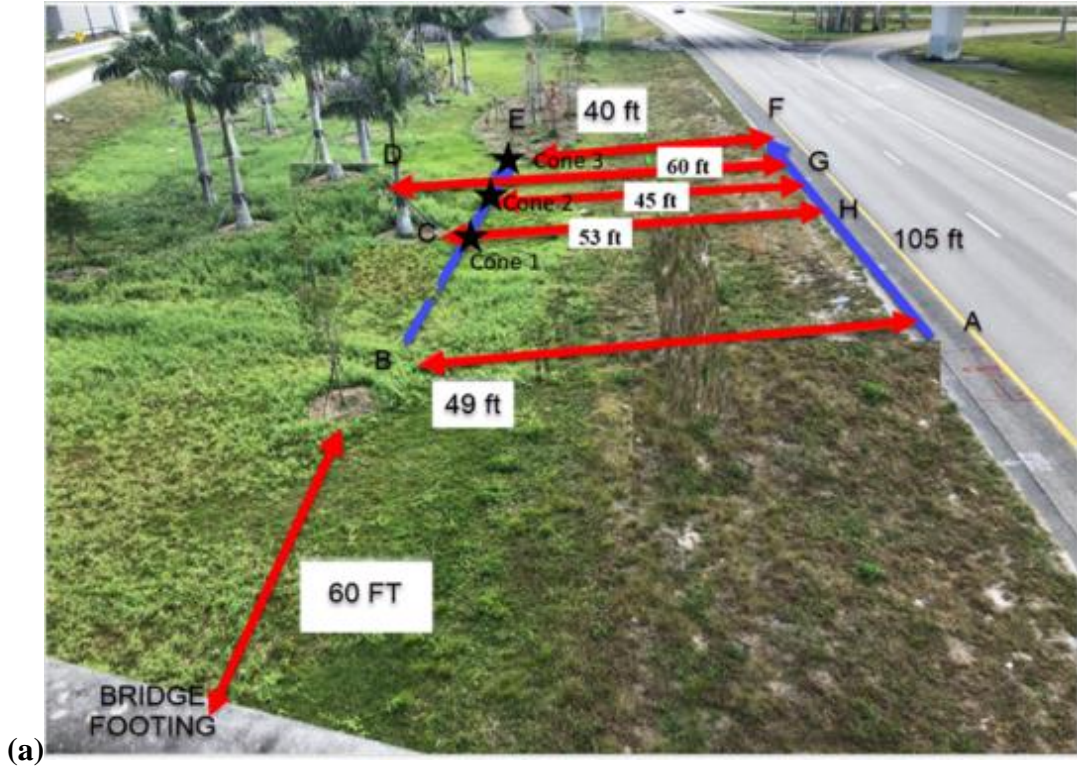


Figure 6-1 SR-84 site picture and test layout

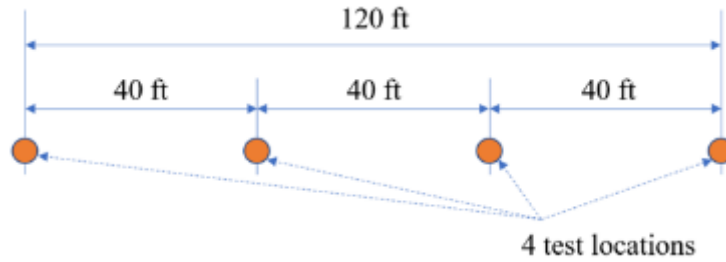


Figure 6-2 Locations of rock coring and SPT tests

Based on the Rock Coring and SPT, the subsurface stratigraphy, Figure 6-3, was developed before construction. The Miami limestone layer starts at a depth of 3 ft and extends 13 ft downward to a 20 ft thick sand layer overlying the Fort Thompson limestone layer which extends down to a depth of at least 65 ft (depth of boring). The water table at the time of borings was at the depth of 3 ft (top of rock) below the ground surface. The dry unit weights of rock cores at B-1, B-2 and B-3 are summarized in Table 6-1. The B-1 location was ruled out as the footing location since no competent Fort Thompson rock was found below the sand layer to provide reactions for the load test.

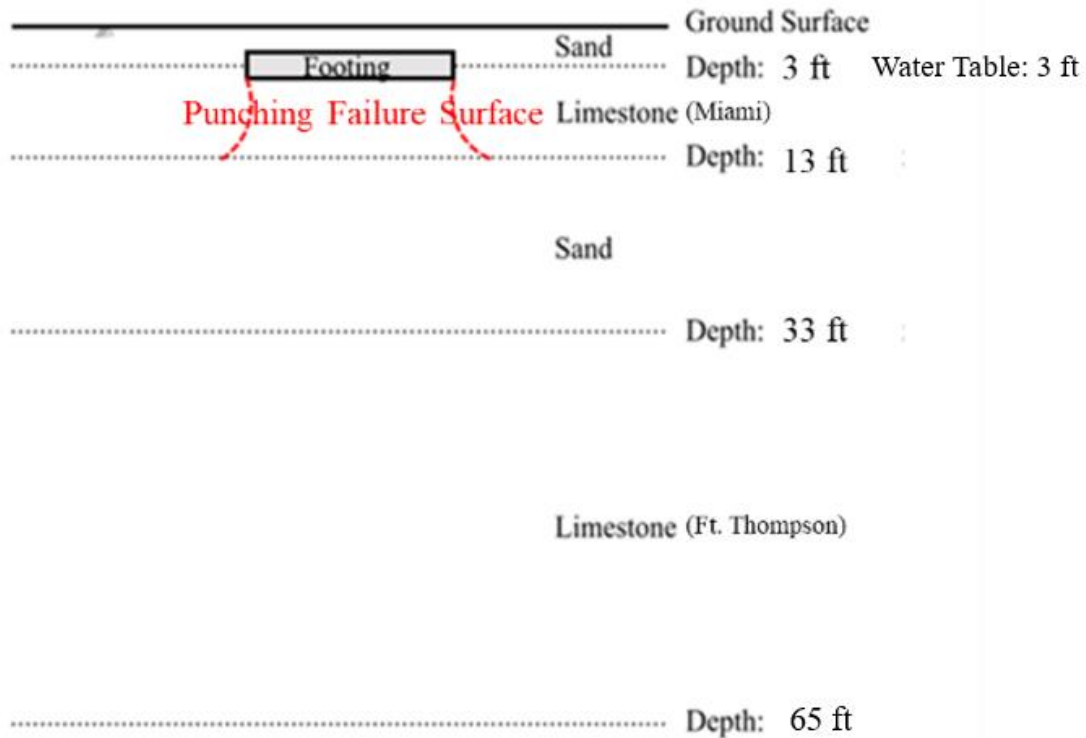


Figure 6-3 Subsurface layering system at SR-84 Site

The dry unit weights of the top 10 ft of rock (3 to 13 ft) decreased from the B-1 to B-3. Given the size of footing (5 ft by 6 ft) and high variability of Miami limestone (around 15 pcf standard deviation), it was decided to use the median value instead of mean or geomean value to characterize the Miami limestone layer. Furthermore, the median value was validated through the 3D seismic shear test results, Figure 6-4 (seismic testing); note the x-axis represents the line of borings and B-3 is at approximately $x = 6$ m and B-2 is located at $x = 15$ m. From the seismic scan, the dry unit weight of rocks increases from 109.2 pcf ($1,750 \text{ kg/m}^3$) to 115.5 pcf (1850 kg/m^3), showing great agreement with the median values of B-3 (110 pcf) and B-2 (114 pcf). Photographs of the rock cores prior to strength testing are presented in the Appendix. In addition, the adjusted-recovery was used to adjust the strength envelope as identified in the Phase I report;

the rubble portion of the core run (cannot retain the cylindrical shape) was also subtracted (performed on the CEMEX site) for adjusted-recoveries of 78% for the Miami limestone and 70%

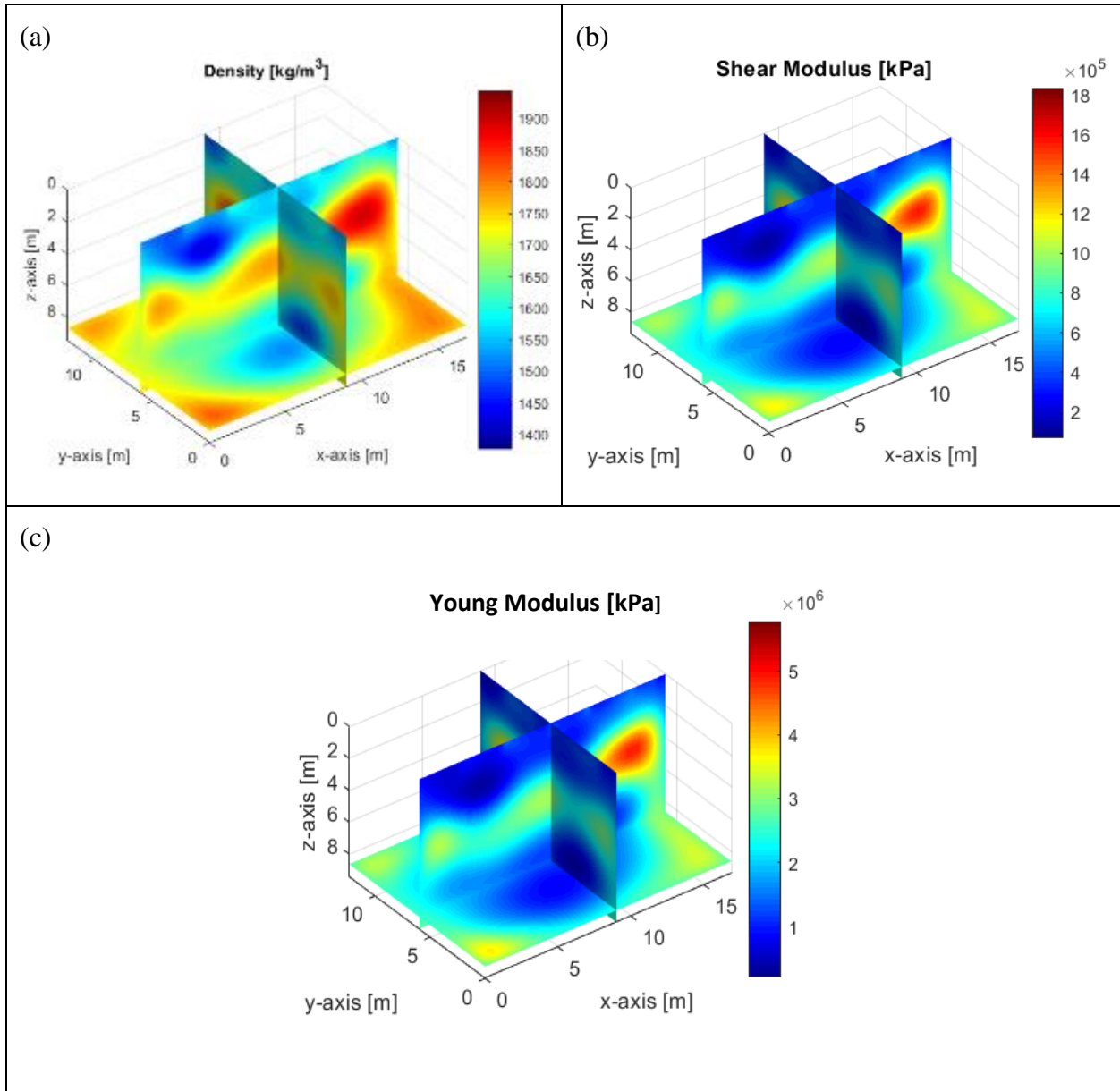


Figure 6-4 Distribution of (a) density, (b) shear modulus, and (c) the Young's Modulus for the SR-84 site (reproduced of Figure 4-23)

Table 6-1 Summary of bulk dry unit weight of Miami limestone, 3 ft to 13 ft depth

Boring Number	B-1	B-2	B-3
Count	13	10	10
Median, pcf	127	114	110
Mean, pcf	126	122	118
Geomean, pcf	125	121	117
Std, pcf	15	15	16
Adjusted-recovery (neglecting rubble portion), %	78	75	82
Competent Fort Thompson limestone to provide reaction (33 to 55 ft depth)	No	Yes	Yes

for the Fort Thompson limestone formation. All the rock cores were sent to the SMO and tested through unconfined compressive tests (q_u), split tension tests (q_t), and triaxial compression tests. The unconfined compressive strength (q_u) and the direct tension strength ($q_{dt} = 0.7 \times q_t$, Perras et al., 2014) versus depth are presented in Figure 6-5 and 6-6. Note, the break in Figure 6-5 and Figure 6-6 indicates the location of the sand layer. It is evident that the rock cores in the B-1, B-2 and B-3 are quite variable.

In order to size the footing, two Recovery-adjusted strength envelopes were constructed for Miami limestone ($REC_{adjusted} = 78\%$, 109 pcf and 145 pcf, Figure 6-7) and two Recovery-adjusted strength envelopes were evaluated for Fort Thompson limestone ($REC_{adjusted} = 70\%$, 129 pcf and 137 pcf, Figure 6-8). Considering the median of top 10 ft of rock (3 to 13 ft) for B-2 and B-3 are 114 pcf, 110 pcf, respectively, the researchers identified the closest estimated existing strength envelopes as 110 pcf and 115 pcf from Phase I (Table 2-2), and are compared in Figure

6-9 (with 109 pcf and 145 pcf Strength Envelope, SR 84). The 110 pcf strength envelope was used in the subsequent analysis for the upper 10 ft of Miami limestone at SR 84 since it is near the load test (B-3). Again, note the lower or negative Poisson's ratio for the lower dry unit weights which result in reduced lateral stresses, and lower estimated bearing capacities, Figure 2-4.

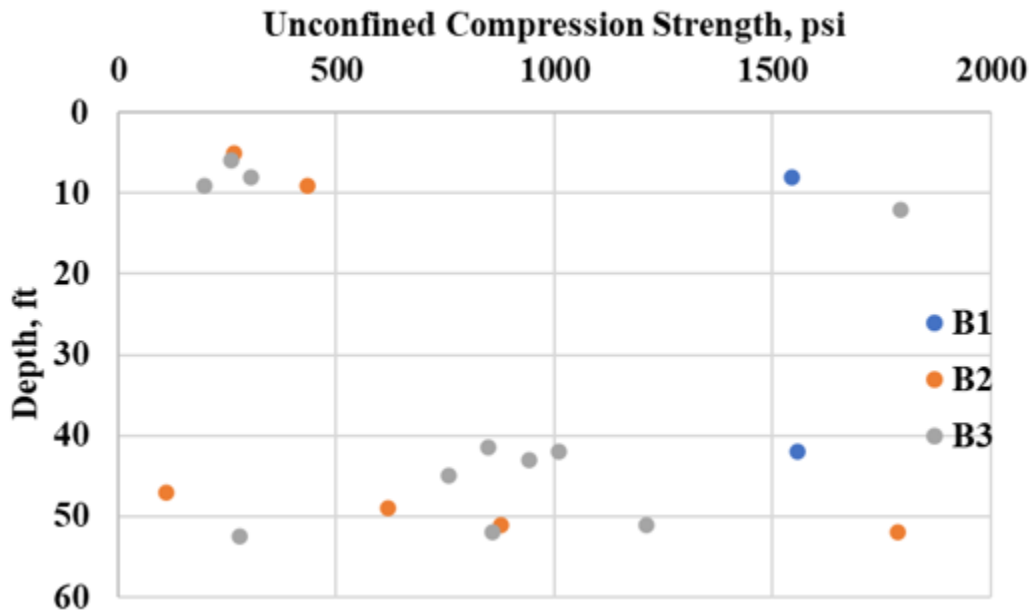


Figure 6-5 Unconfined compression strength versus depth at SR-84 site

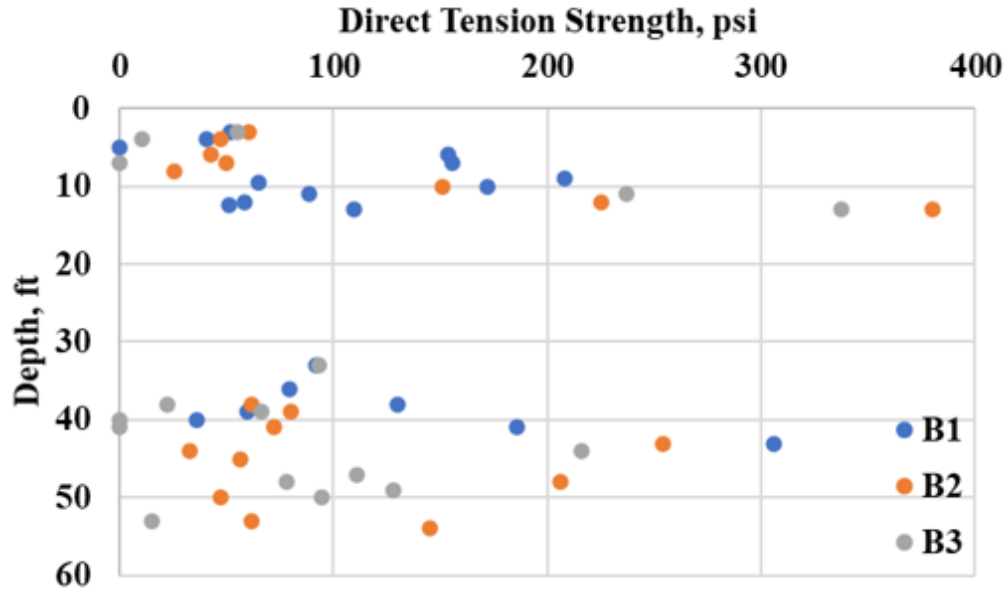


Figure 6-6 Direct tension strength versus depth at SR-84 site

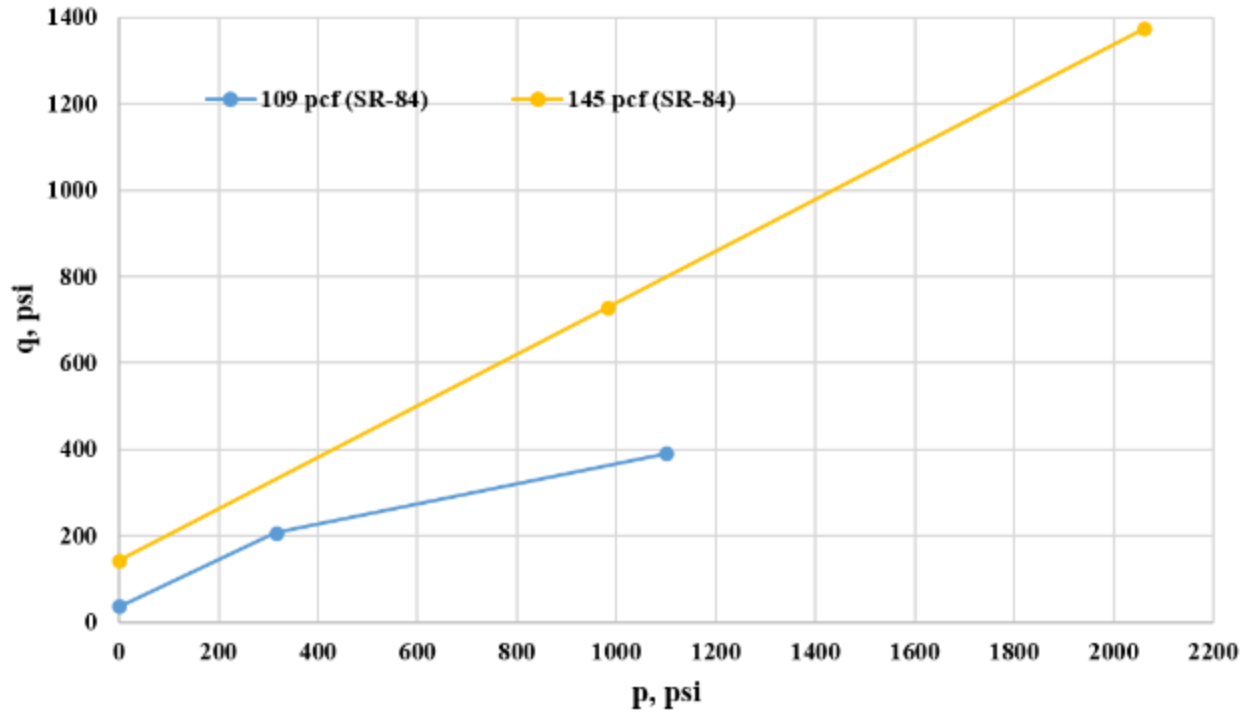


Figure 6-7 Mass strength envelopes of 109 pcf and 145 pcf, Miami limestone, SR-84 (REC_{adjusted} = 78%)

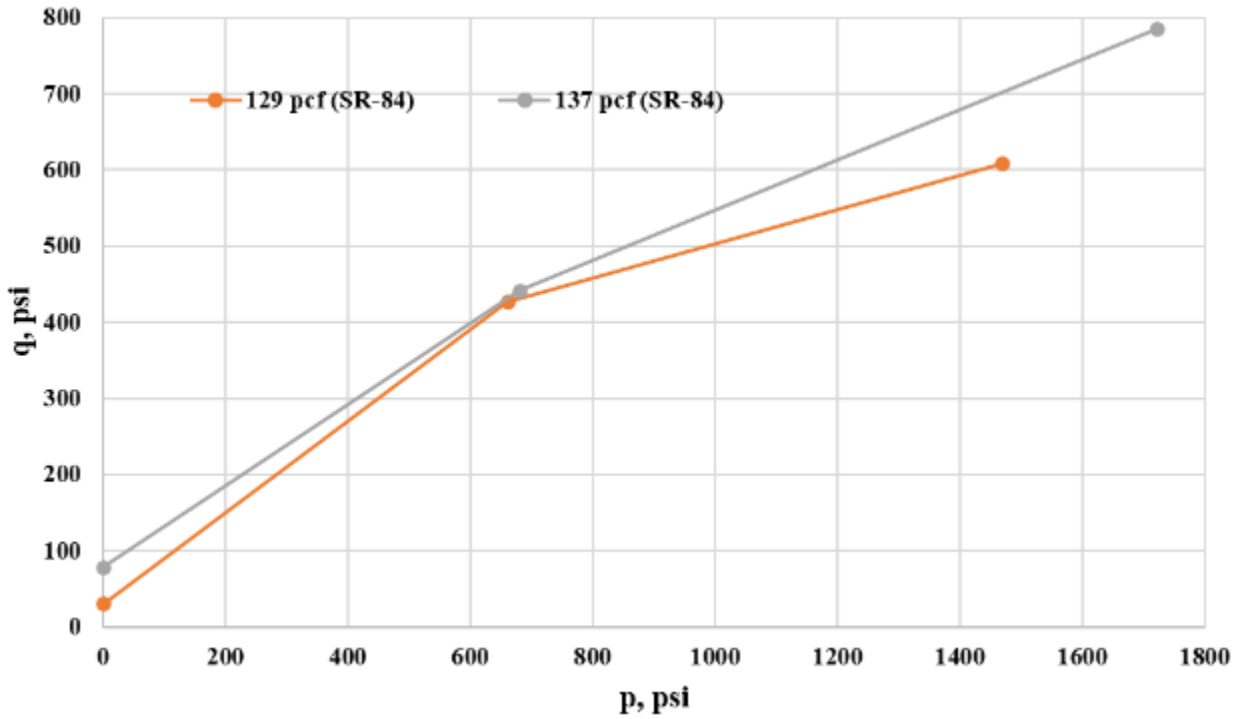


Figure 6-8 Mass strength envelope of 129 pcf and 137 pcf, Fort Thompson limestone, SR-84 (REC_{adjusted} = 78%)

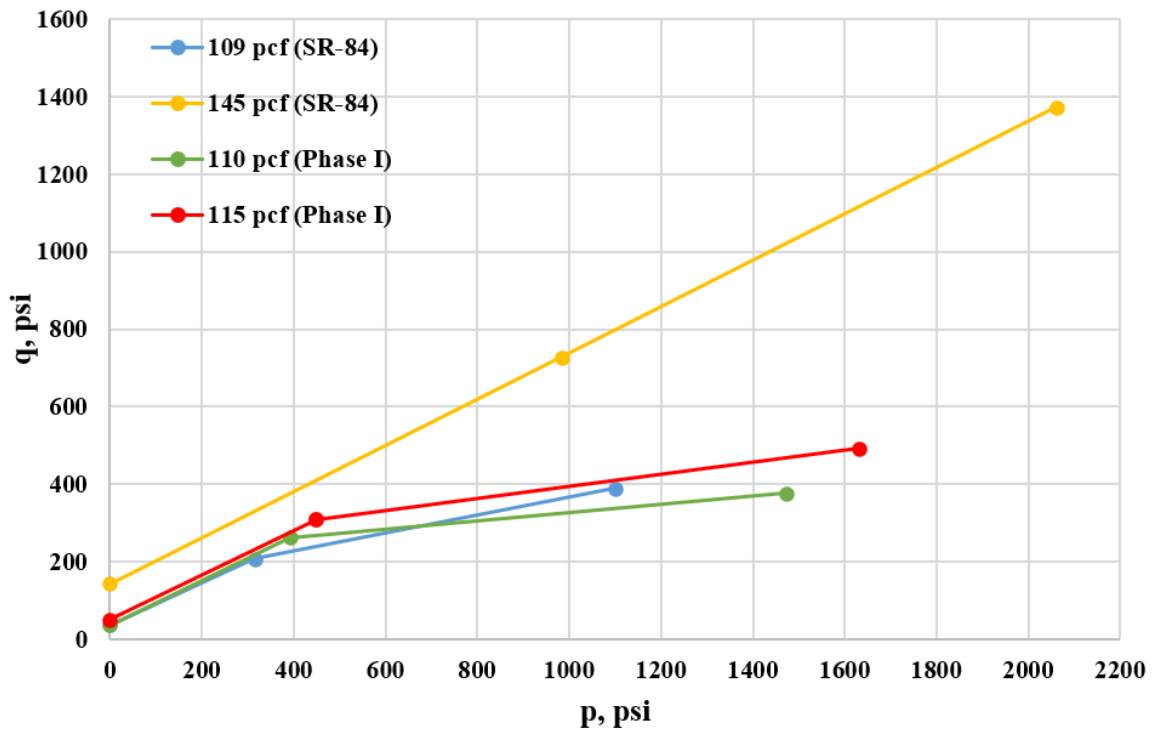


Figure 6-9 Comparison of mass strength envelope at 109 pcf, 110 pcf, 115 pcf, and 145 pcf, for Miami limestone (REC_{adjusted} = 78%)

The spatial variability of Miami limestone has a significant impact on the load versus deformation behavior, as well as differential settlement (due to the distance within which points are significantly correlated). Specifically, the higher ratio between the correlation length (scale of fluctuation) and footing width (e.g., smaller footing), the higher coefficient of variation of the expected settlement, i.e., differential settlement, Figure 6-10. It is recommended to use a larger footing compared to the correlation length in order to reduce the differential settlement (For example, the smaller 42 in square footing had 2 in of differential settlement at 650 kips with a 3 ft correlation length at the Cemex Site). Also, Figure 6-10 use a maximum CV of 0.2 for the strong upper layer, which it is not the case of Florida limestone (1~3).

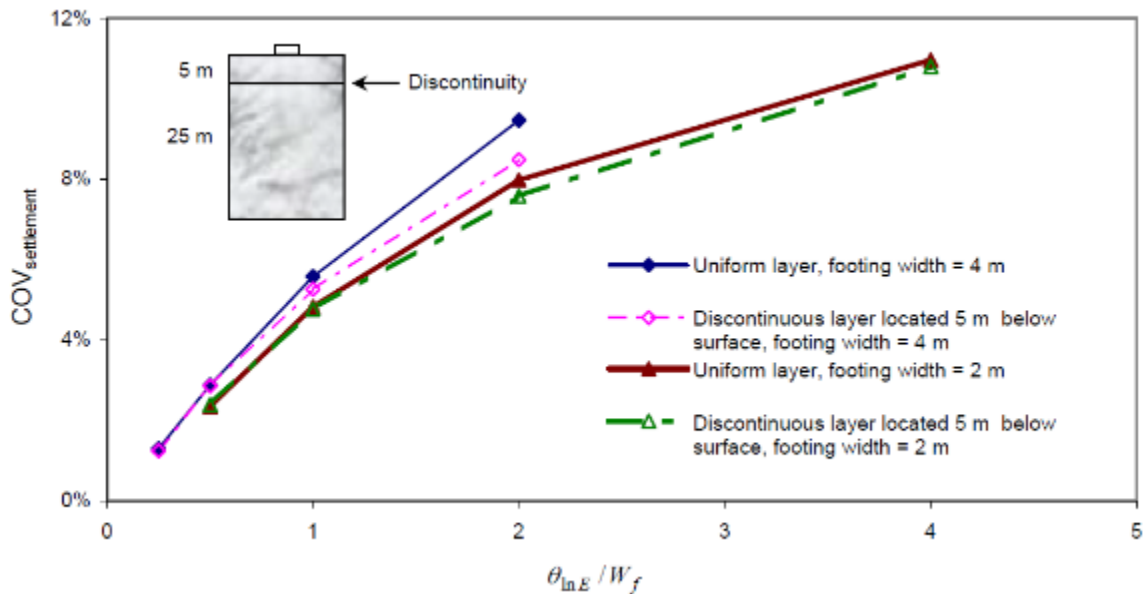


Figure 6-10 Coefficient of variation of settlement with varying θ_{lnE}/W_f for a two soil layers profile. θ_{lnE} : scale of fluctuation; W_f : footing width. (Kuo, et al., 2004)

6.2. Construction of Load Test

6.2.1. Construction of the Drilled Shaft

Eight threaded anchors/micro-piles were designed to provide the reaction force in the plate load testing in the scope of services to limit cost and footing influences. However, the Cemex load test, identified that the installation of anchors could not be achieved in a week (required 6 weeks) and the contractor requested a *renegotiation* of their contract for SR-84. Consequently, site 2 (SR-84) obtained new quotes on multiple foundation types (micropiles and drilled shafts). Based on 3 quotes, the researchers and FDOT decided to use two 36 in \times 55 ft drilled shafts spaced 36 ft center to center to transfer the 900 tons of load test into the Fort Thompson formation.

Based on the boring logs, the Fort Thompson limestone was located 33ft beneath the ground surface and extended to depths greater than 65 ft (depth of boring). According to Equation 5-1, using the unconfined compression and direct tensile strengths (Figure 6-5 & 6-6) Fort Thompson formation at the site had a unit side shear friction of 98 psi with 70% $REC_{adjusted}$. Using two 36" drilled shafts installed 3 ft below the ground surface (required for remediation) to a depth of 58 ft (shafts 55 ft long), a safety factor of 3.7 was estimated for the planned 900 tons load test (i.e., 3,323 tons available).

The designed drilled shafts are shown in Figure 6-11; shear reinforcement includes No. 4 rebar rings spaced 12 in on center with 24 in lap; for axial and flexure, 8 No. 10 longitudinal rebars (exceeds 1%) with 3 in clearance both on the top and bottom as well as on the sides of the shaft. To transfer the 900 tons (450 tons each) to the drilled shafts, 4 - 2.25 in \times 36 ft William threaded rods (Figure 6-12) were purchased for anchors and attached to the rebar cage with 3

steel templates (Figure 6-12 a & b). The drilled shaft contractor fabricated and secured the threaded rods to the templates with steel nuts. The 4 threaded rods extended 12" above the top of each shaft for couplers to be attached for 15 ft of threaded rod extending above the 40 ft Acosta Girders. The 15' threaded rods were attached to the girders with C channels, plates and nuts as shown in Figure 6-30.

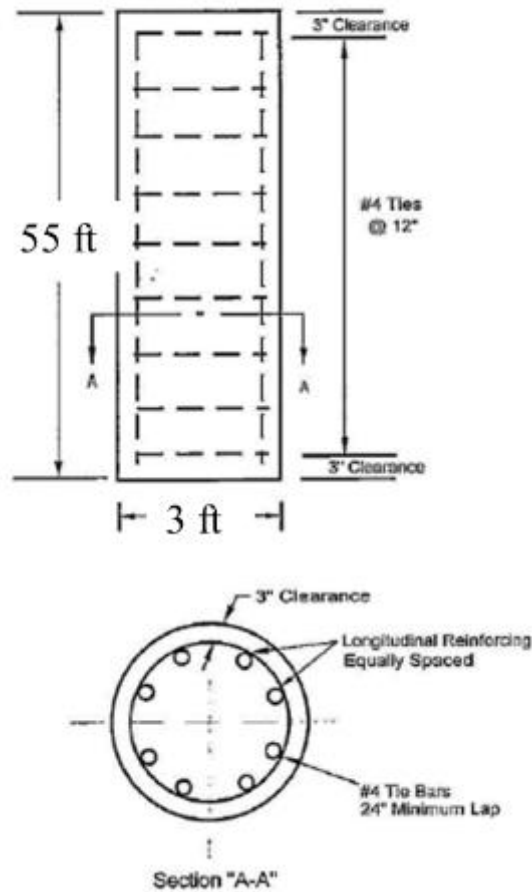


Figure 6-11 Design of the drilled shaft at SR-84 site

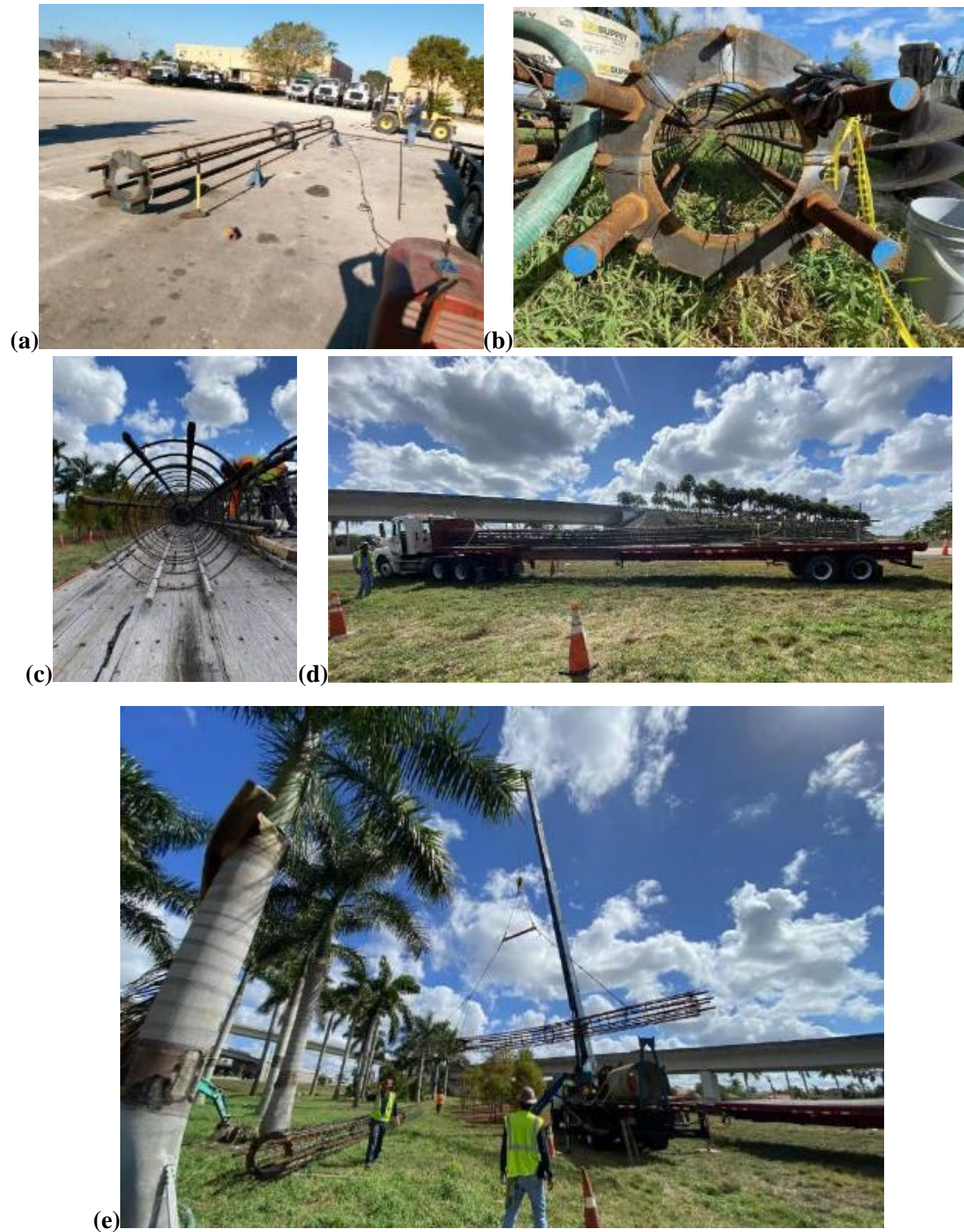


Figure 6-12 Picture of steel rebar cages: (a) templates position: top, middle, bottom; (b) William threaded rods with templates secured by the nuts; (c) 8 of No. 10 rebars; (d) rebar cages at the site; (e) unloading the rebar cages at the site

The installation of the drilled shafts at the SR-84 site by the contractor required two weeks, instead of the planned one week. The major issue encountered at the site was that the depth to rock was not accurate (6" instead of 3 ft, Figure 6-13) and the use of polymer slurry was not sufficient to stabilize the holes during construction. However, because the shafts had to be located 3 ft below the ground surface (site remediation) and girder support, foundation size, etc., were already selected, it was decided to continue to excavate to this depth with 42" casing and place a Sonotube to form the top few feet of the shaft. In addition, during the construction of the first shaft, the west shaft (near B-2), a polymer drilling fluid (Figure 6-14) was employed when the sand layer was encountered. Unfortunately, at a depth of approximately 45 ft, the borehole started to collapse. That is after drilling down to a depth of 60 ft; the bottom of the borehole would rise back to 45 ft in about 5 minutes. After doing this a few times, the researchers and drilled shaft contractor decided to fill the hole back in and to re-drill the hole the following week using bentonite slurry.



Figure 6-13 Miami limestone layer: (a) excavated down to 15 in; (b) excavated down to 3 ft.



Figure 6-14 First attempt to install the west shaft

For the installation of the east shaft, a 42 in rock auger bit was used to drill down 8 ft, then a 42 in temporary casing was installed, Figure 6-15. Subsequently, the drill bit was changed to the 36 in rock auger bit and premixed mineral slurry, Figure 6-16 was introduced to the hole at approximately 18 ft. Past experience has shown that bentonite forms a filter cake against the walls of the borehole and assists with limiting collapse of the hole, but could also limit the mobilize side shear. Consequently, it was decided to drill through the sand layer with bentonite the first day, and to drill the underlying rock and concrete the hole the following day. The latter would limit the cake formation in the Fort Thompson limestone layer (i.e., load transfer layer), as well as limit the sloughing of the walls in the 20 ft sand layer. As planned, the driller

continuously drilled down to 59 ft the next day and changed to a bailing bucket to stabilize the borehole and clean the bottom of the hole, Figure 6-17. The pH, viscosity and density of the bentonite slurry were measured at every 10 ft drilling increment and the sand content was tested after the borehole stabilized, Table 6-2; note, each parameter meets the requirement of FDOT Specification: 455-15.8.1. Subsequently, the steel rebar cage with spacers was placed by crane in the east borehole at the desired depth (i.e., top of concrete is 3 ft from the ground surface and the 36 ft threaded rods are stuck out 1 ft above the top of concrete), Figure 6-18. Note, the steel rebar cage had to be placed precisely because the center of the east drilled shaft needed to align with the center of the west shaft, and the directions of the threaded rods also need to be aligned for the placement of girders, Figure 6-19. During rebar placement, the mounted boom concrete pump truck was positioned at the site and a delivery pipe and end hose were placed in the shaft hole. Next, 3 concrete trucks were used, and 20 cubic yards of concrete were pumped into the east borehole (at least 14.65 cubic yards needed for a 3 ft × 56 ft deep borehole), Figure 6-20. Researchers collected 4 in × 8 in specimens of the concrete sample (ASTM C39/C39M-20) for each truck as well as measured the slump of placed concrete. Table 6-3 presents the compressive strength of the concrete and Table 6-4 shows the measured values of slump test. The 36 in cardboard Sonotube was installed, and 42 in temporary casing was removed (Figure 6-21) and concrete pumped until 3 ft from the ground surface measured by a total station and tape. The picture of the east drilled shaft two days after construction is shown in Figure 6-22. Based on the construction of the east shaft, no drilling concerns were noted (i.e., heaving, caving, slurry loss, etc.), and the planned subsurface layering (10 ft of rock beneath footing) was obtained.

Table 6-2 Measured range of properties of bentonite slurry for East shaft

Properties	Measured	Range Specified in FDOT Specification: 455-15.8.1 (65°F)
Density, pcf	66 ~ 67	64 ~ 73
Viscosity, seconds	34 ~ 36	30 ~ 40
pH	9	8 ~ 11
Sand Content	2%	≤4%

Table 6-3 Measured compressive strength of concrete specimens for East shaft

Days	Compressive Strength, psi
14	9,108
21	8,973
28	9,926

Table 6-4 Measured properties of concrete for East shaft

Properties	Measured	Range specified in 346
Slump, in	9 ~ 10	7 ~ 10



(a)



(b)



(c)



(d)

Figure 6-15 Drilling for the East shaft: (a), (b), and (c): 42-in rock auger bit; (d): 42-in temporary casing



Figure 6-16 Change to the 36-in rock auger bit

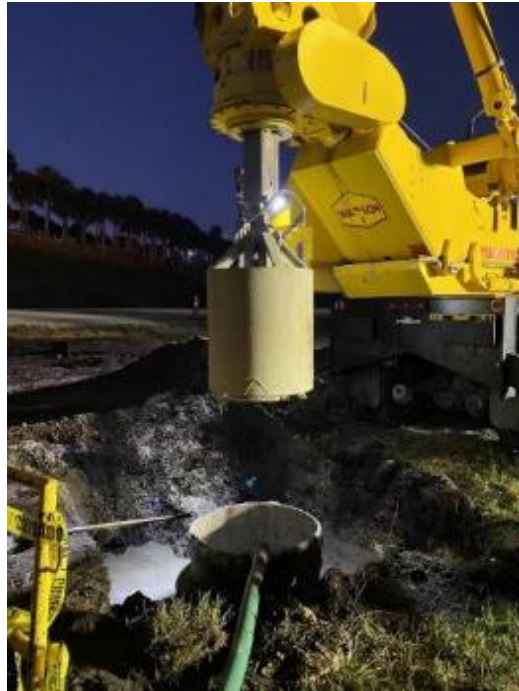


Figure 6-17 Bailing bucket



(a)



(b)

Figure 6-18 (a) Placement of the rebar cage (b) spacer installation



Figure 6-19 Measure the depth of the top of the threaded rods (2 ft from the ground surface) and align the drilled shafts

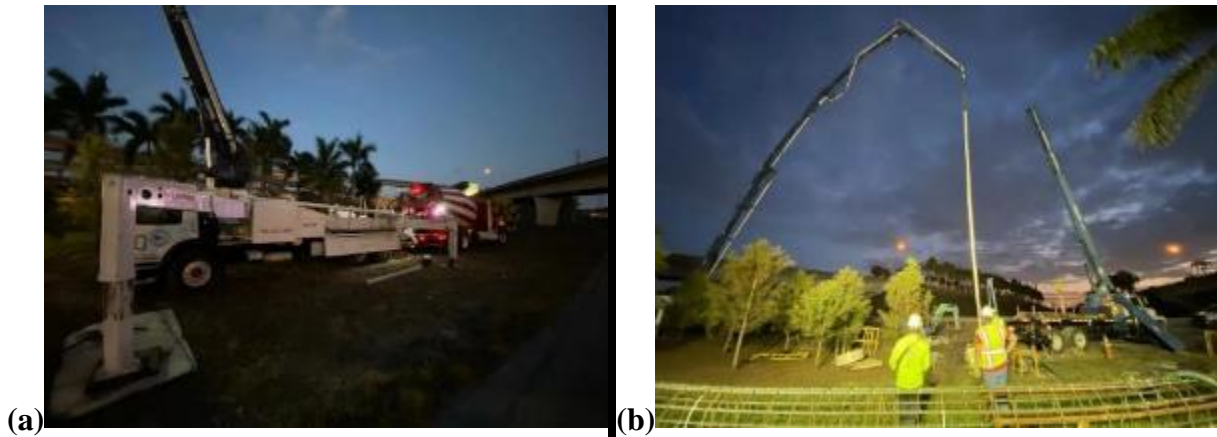


Figure 6-20 (a) mounted boom concrete pump truck and concrete truck; (b) delivery pipe and end hose



Figure 6-21 Temporary casing pull out and concrete overflow



Figure 6-22 Picture of the east drilled shaft after two days of installation

The drilling team subsequently redrilled the west shaft with bentonite slurry instead of synthetic polymer, following the procedure developed for the east shaft. However, some collapses still occurred around the 60 ft depth (i.e., the borehole went back to 59 or 58 ft in 10 minutes after 60 ft was reached), the driller spent 3 hours of drilling and cleaning the west

borehole. After the sand content at the bottom of the hole dropped to 1%, the drilling team placed the steel rebar cage employing side spacers and adjust the direction of the threaded rods to align the center of the rebar cage to the center of the east shaft, Figure 6-23. Figure 6-24 shows the concrete pumping with a total of 21 cubic yards of fresh concrete being placed (Note, 16.0 cubic yards needed for a 3 ft × 61 ft deep borehole, 30% volume increase). Table 6-5 summarizes the measured properties of the bentonite slurry during the drilling process and Table 6-6 summarizes the measured compressive strength of concrete specimens for the West shaft. The measured slump values are the same as the East shaft, shown in Table 6-4.

Table 6-5 Measured properties of the bentonite slurry for the West shaft

Properties	Measured	Range Specified in FDOT Specification: 455-15.8.1 (65°F)
Density, pcf	66 ~ 67	64 ~ 73
Viscosity, Seconds	32 ~ 40	30 ~ 40
pH	9	8 ~ 11
Sand Content	1%	≤4%

Table 6-6 Measured compressive strength of concrete specimens for West shaft

Days	Compressive Strength, psi
14	7,822
21	9,061
28	9,625

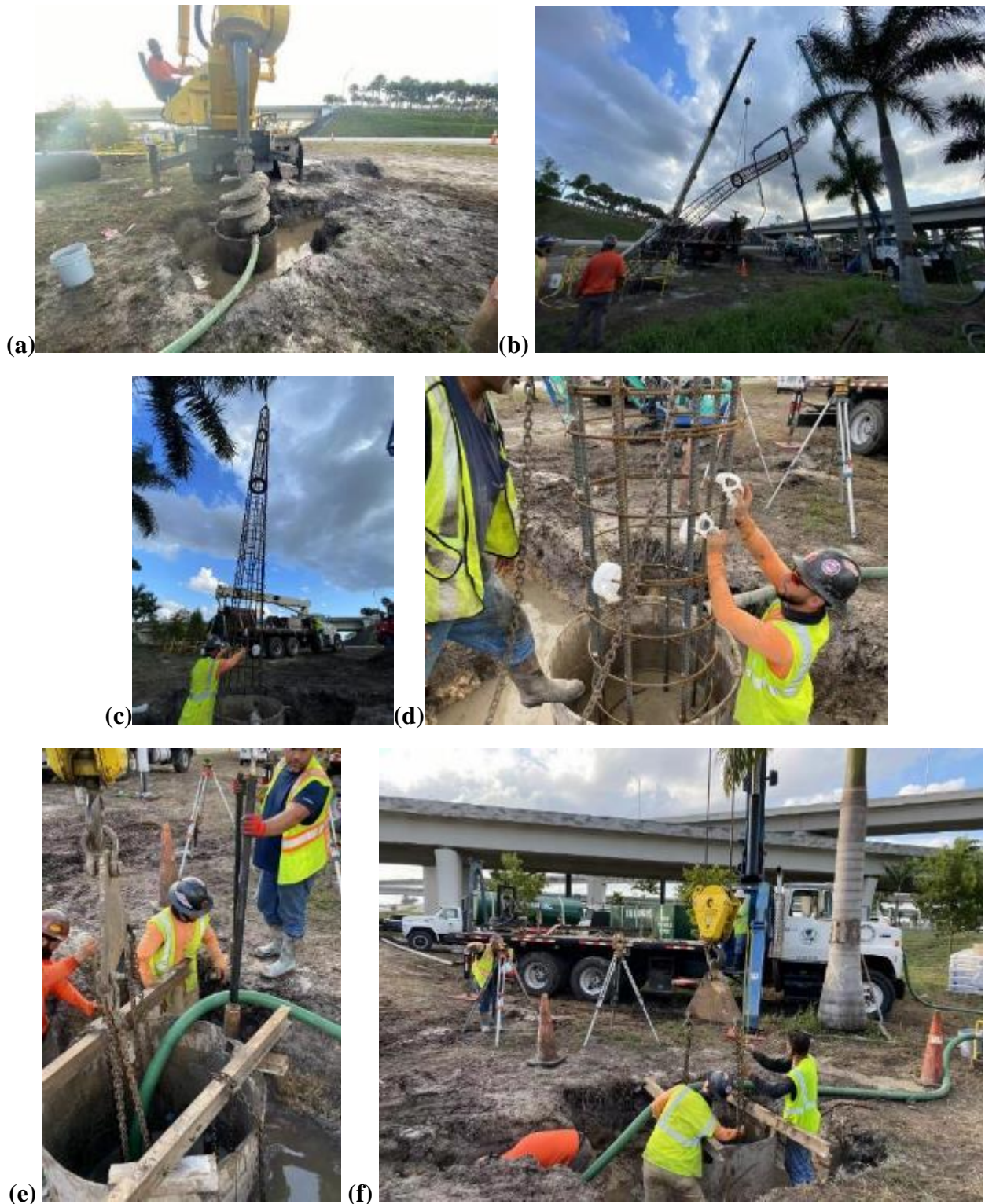


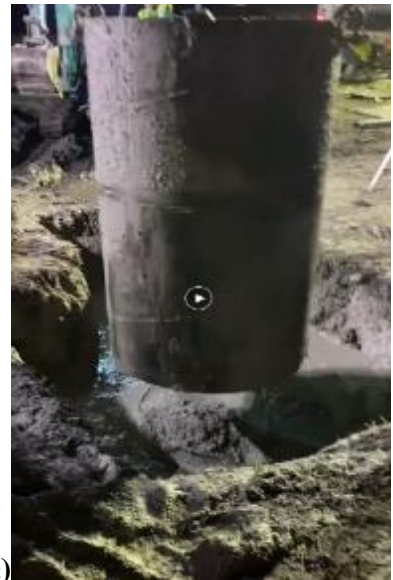
Figure 6-23 (a) drilling for the West shaft; (b-c) placement of the steel rebar cage; (d) spacers installation; (e) extension bar for alignment; (f) alignment and elevation measurement



(a)



(b)



(c)

Figure 6-24 (a-b) concrete pumping; (c) overflow

6.2.2. Construction of the Load Test Frame

The load test system consisted of two drilled shafts (3 ft × 55 ft), Support System (SMO Stands, Figure 6-25), Reaction System (15 ft William Threaded Rods, GR 50 C channels and bearing plates), two Acosta type “A” Girders, load spreader, hydraulic jack, load cell, measuring system and 8 steel plates representing the footing. For the construction of the load test, an 8000

lbs telescopic forklift, a 40 ft man lift, and a 60 tons crane were rented. Note, the 5 ft x 6 ft, 4 ft x 6 ft and 2 – 4 ft x 4 ft plates were also rented (called road plates) to be used to simulate the shallow foundation. Although the competent Miami limestone started at depth of 6 in, the footing size was designed based on the boring log: rock started at 3 ft, and extended to a depth of 13 ft. To replicate the design, the Miami limestone layer had to be excavated to the depth of 3 ft which resulted in a 10 ft thick layer. Consequently, a track hoe was rented and used to dig a 3 ft deep × 7 ft wide × 10 ft long excavation for the footing placement. Researchers then mixed and placed a 1 in thick fast-setting concrete seal layer in the bottom of the excavation to level and fill any voids etc., in rock surface, Figure 6-26. Note, the water came up into excavation approximately 3-4 in and was pumped out prior to placement of concrete, footings, etc.

Prior to the setup of the load test system, researchers measured the elevation difference between the top of shafts and the top of fast-setting concrete by total station and measuring rods. It was identified that both shafts had to be raised 4 in, which was accomplished with bricks and wood spacers placed on the top of each shaft, Figure 6-27. After leveling, the stands were lifted by the crane and placed on the top of bricks and leveled again, Figure 6-28. Then the elevation difference between the bottom of stands and bottom of steel plates (footing) were checked to meet the vertical layout of Figure A-2. Next, the 15 ft long threaded rods were lifted by crane and connected to the 4 threaded rods in each shaft. Subsequently, the 40 ft long Acosta Girders were lifted by the crane and set on the top of stands and wrapped with two 3,333 lb heavy-duty ratchet straps to prevent toppling. With the crane holding the girders along with straps, the researchers installed two sets of C channels and bearing plates with nuts at each end of girders, Figure 6-30. After the girders were securely attached to underlying drilled shafts, the pyramid load spreader was installed beneath the girders and positioned with 4 steel channels and 4

threaded rods by the forklift. Next, work focused on the placement of components beneath the girders. The 8 A36 steel plates were placed on the top of fast-setting concrete to represent the footing in a bottom-up sequence: 60 in \times 72 in, 48 in \times 72 in, 48 in \times 48 in, 48 in \times 48 in, 42 in \times 42 in, 36 in \times 36 in, 28 in \times 28 in and 28 in \times 28 in, as shown in Figure 6-31. Note, after placing the second 48 in \times 48 in steel plates, researchers measured the distance between the bottom of girders and top of steel plates to ensure 69 in (with less than half in of tolerance available). The hydraulic jack was first placed at the center of the completed footing and the load cell was installed on the top of hydraulic jack. Finally, the measuring system composed of a total station, 4- 5 ft long PVC pipes inserting into four 5 in by 5 in base plates, measuring sight attached to the jack base. The 4 base plates were placed at the corners of 5 ft by 6 ft steel plates and measuring tapes were attached to the top of PVC pipes, Figure 6-32. Researchers also measured the stroke movement of the jack as well as the distance between bottom of the girders and the top of 48 in \times 48 in steel plate after test to validate the tape measurements from the hydraulic jack as well as 4 corners. The completed construction of the load test at SR-84 site is shown in Figure 6-33.



Figure 6-25 Stands to support the girders



Figure 6-26 Fast setting concrete placement



Figure 6-27 Bricks and wood spacers on top of shafts beneath test stands



Figure 6-28 (a) stands on the top of bricks; (b-d) stands are leveled in both directions



(a)



(b)

Figure 6-29 Placement of girders: (a-b) girders lifted by the crane



(c)



(d)

Figure 6-29 Placement of girders: (a-b) girders lifted by the crane; (c) using forks to against the girders; (d) ratchet straps around the girders



Figure 6-30 Installation of two sets of C channels and plates



(a)



(b)

Figure 6-31 Eight steel plates representing the footing. (a): lower 4 steel plates, top to down: 4 ft by 4 ft, 4 ft by 4 ft, 4 ft by 6 ft and 5 ft by 6 ft; (b): upper 4 steel plates, top to bottom: 28 in by 28 in, 28 in by 28 in, 36 in by 36 in and 42 in by 42 in



(a)



(b)

Figure 6-32 Measuring system. (a): from a ground surface view; (b): bricks used to make the scaffolding base plate fully contact with the footing (5 ft by 6 ft steel plate)



(a)



(b)

Figure 6-33 Completed construction of the load test at SR-84

6.3. Bearing Capacity

The shallow foundation load test at SR 84 was completed in 3 ½ hours utilizing 50 ton load increment/decrements with the last 4 loading steps at 25 ton increments. Each load was maintained for 10 minutes with deformation measurements occurring after application of each load and prior to placement of the next load step (i.e., creep). A peak load of 1,740 kips with vertical movement of 2.41 in was observed and a permanent settlement at center of 1.75 in was measured when the load was removed. Figure 6-34 shows the load versus the loading time, and Figure 6-35 presents the load-settlement response at the center of the footing. The cumulative settlement response measured during the test with the total station was also validated by measuring the distance between the bottom of girders and the top of 48 in × 48 in steel plates after the test. Figure 6-36 (a) and (b) compares the top 28 in × 28 in steel plates before and after the test; (c) has a clear view of the 48 in × 48 in steel plates after the test and is marked with the settlements at each location based on the distance between the bottom of girders and top of plate before and after test (1 in differential settlement was observed on the 48 in × 48 in plate).

It is believed that the footing underwent a punching shear failure of the rock into the underlying sand layer at approximately 680 tons (or 23 tsf, Figure 6-35 - the intersection of 2 linear trend lines). This is supported by Kenny et al., (1997), a small-scale load testing of footing on a sand layer overlying soft clay (Figure 6-37). It can be observed that a much stiffer (low settlement vs. load) and higher strength is observed at high H/B; however, at low H/B, a flatter or much softer stiffness of clay controls both settlement and bearing capacity of the system. Similarly, for SR-84, a much higher modulus of the rock (10x) controls the initial load vs. deformation; however, after shear failure, the lower modulus of sand controls the load vs. deformation.

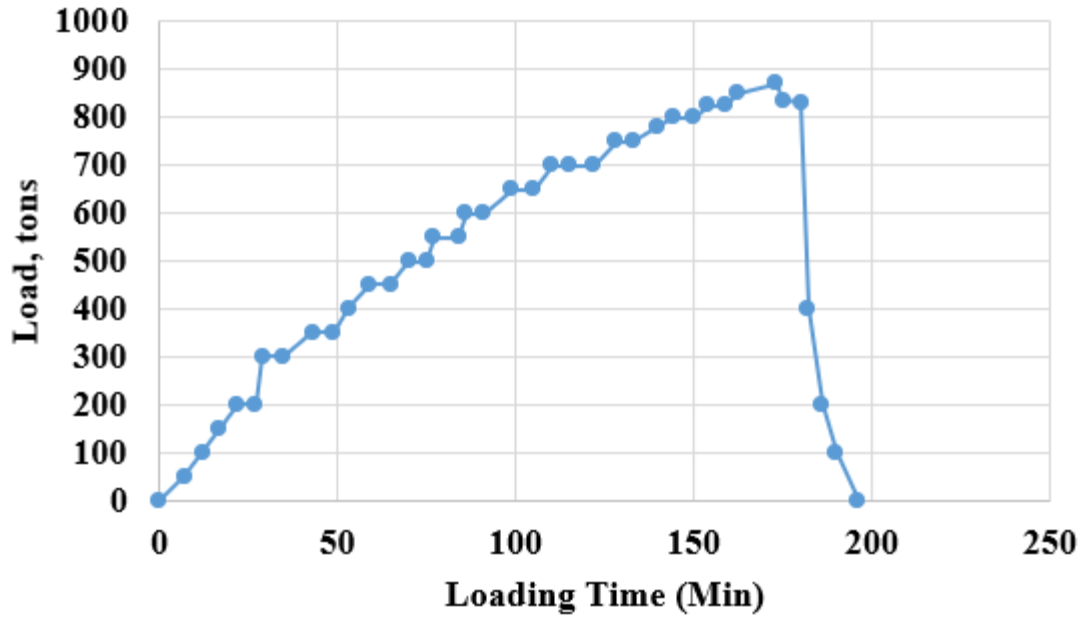


Figure 6-34 Load versus loading time curve

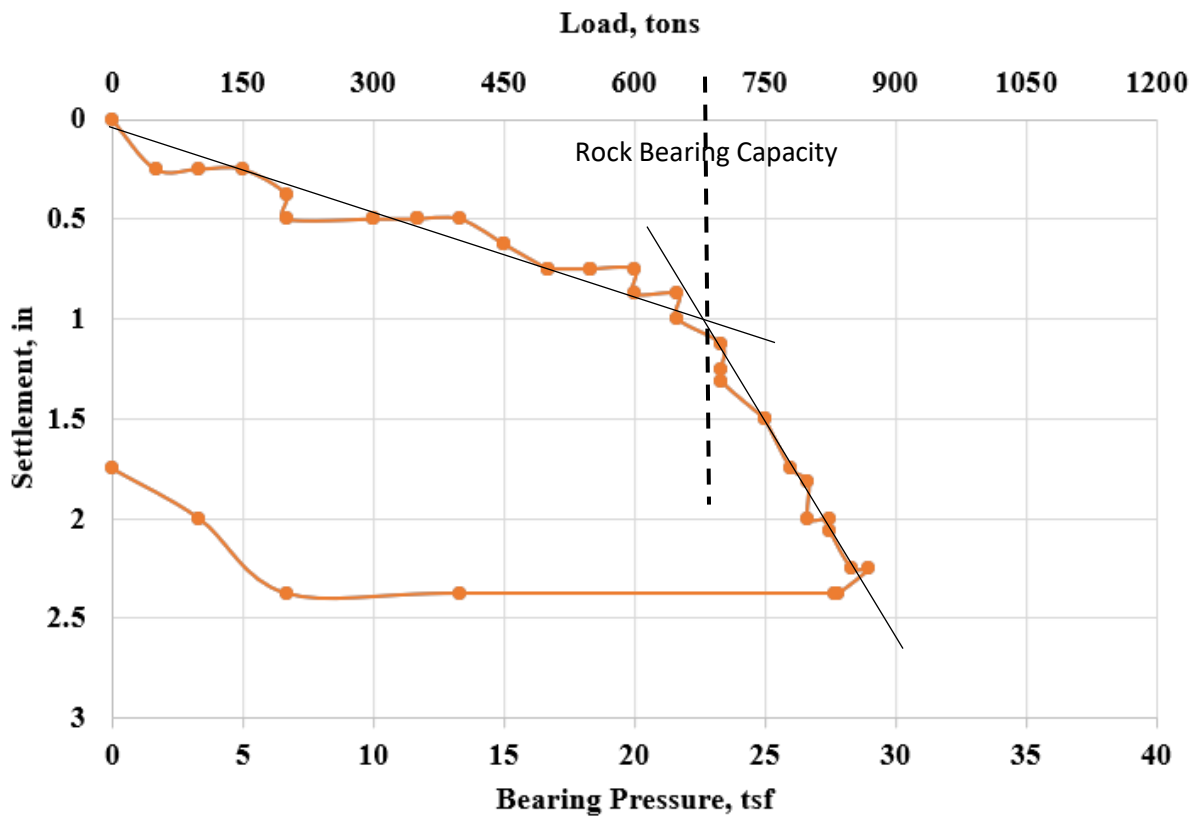


Figure 6-35 Load versus settlement curve



(a)

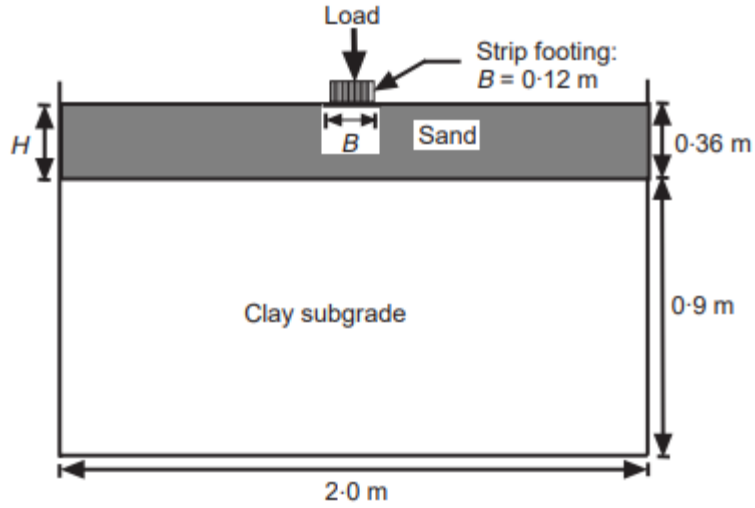


(b)

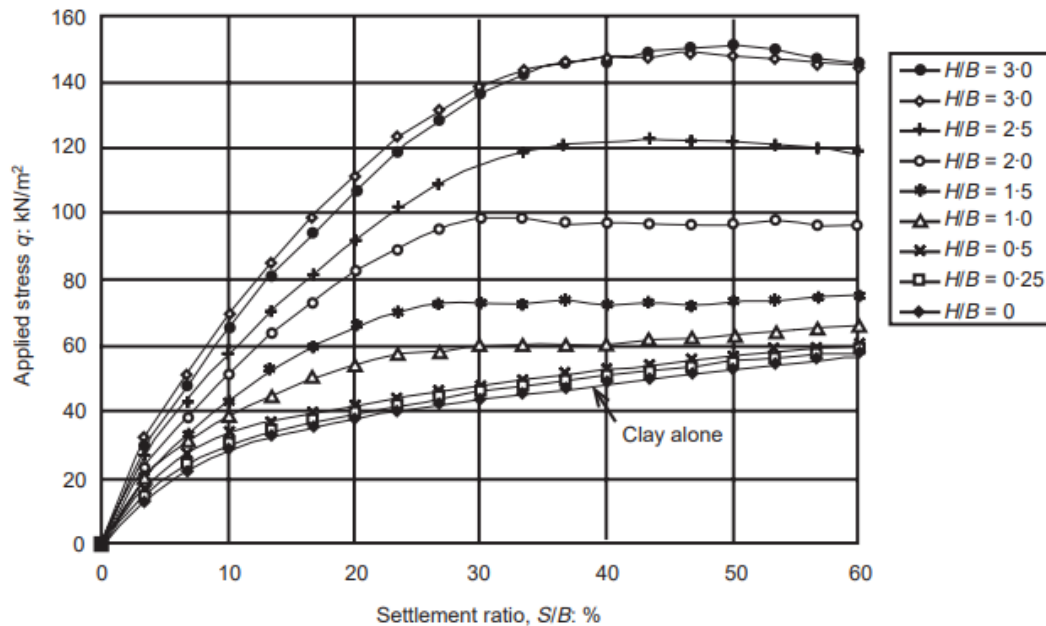
Figure 6-36 (a) picture of 28 in by 28 in steel plate before test; (b) picture of 28 in by 28 in steel plate after test; (c) picture of 48 in by 48 in steel plate after test with settlements at each location



Figure 6-36 (a) picture of 28 in by 28 in steel plate before test; (b) picture of 28 in by 28 in steel plate after test; (c) picture of 48 in by 48 in steel plate after test with settlements at each location



(a)



(b)

Figure 6-37 (a) experimental setup for footing residing on a sand layer overlying soft clay; (b) stress-settlement relationships for sand over clay. (Kenny et al., 1997)

Following Chapter 5, the bearing capacity was predicted by the bearing capacity equations developed in Phase I. Important in the prediction are both the geometry, layering, strength and properties of rock and sand. According to Table 6-1, the median bulk dry unit weight of the top Miami limestone layer is 114 pcf for B-2 and 110 pcf for B-3. Given the size of the footing and its location, it was decided to use 110 pcf strength envelope based on nearest boring, B-3, as well

as seismic shear results (110 pcf - Figure 6-4) to estimate the bearing pressure. Note, a 20 ft sand layer is beneath the 10 ft Miami limestone layer, Figure 6-3. The dry unit weight and modulus profile for boring B-3 is shown in Table 6-7, and the corresponding summary statistics as well as the sand modulus based on the SPT N value (Bowles' method, Equation 3-9) are shown in Table 6-8. Based on the mass p-q strength envelope (Figure 6-9) for 110 pcf (right side of Table 6-9), the Mohr Coulomb strength properties (ϕ , c, P_p , and ω ,) for 110 pcf rock may be determined (see Eqs in Table 6-9).

Knowing the strength parameters of the rock (Table 6-9) and modulus of the sand (Table 6-8), the bearing capacity of a 5 ft by 6 ft footing may be estimated, as shown in Table 6-10. First, the bearing capacity factors N_c , N_c' , N_q , N_R and N_γ (see Table 6-10) are determined based on the rock mass angles of friction (ϕ , ω), along with overburden bearing stress, q. Next, the reduction of rock bearing due to the sand layer is found N_R , which requires R, or an estimate of ratio of sand modulus to rock mass modulus (E_{sand}/E_{rock} , Table 6-8) and distance below footing to rock (T) (see Table 6-10). The median modulus (35,261.8 psi, Table 6-8) is used here due to the low Poisson's ratio of Florida limestone. Using R, the value of N_R (bearing capacity reduction) is found, 1.17, along with the footing shape factor ξ (1.22). Finally, the footing bearing capacity, Q_u (340.8 psi = 24.54 tsf) was found, Table 6-10. Note, the bearing capacity of a strong over weak layer ($E_{rock}/E_{soil} \sim 32$) will be associated with a punching shear type failure of the upper rock layer.

Table 6-7 Dry unit weight and modulus profile (B-3)

Depth, ft	γ_{dt} , pcf	E_i , psi (Figure 3-1 trendline)
3	109.9	64,526.7
4	109.7	63,698.1
5	105.3	49,513.1
6	107.8	57,158.5
7	97.7	32,064.1
8	106.4	52,911.9
9	114.2	82,335.1
10	127.5	176,151.0
11	150.8	667,624.3
13	140.3	367,148.5

Table 6-8 Summary statistics for B-3 and sand layer

	γ_{dt} , pcf	E_i , psi	E_m , psi (Mass effect – 0.55, Figure 5-31)
Count	10	10	10
Mean	117	161,313.1	$0.55 \times E_i = 88,722.2$
Geomean	115.9	96,518.0	$0.55 \times E_i = 53,084.9$
Harmonic Mean ($E_h = \frac{n}{\sum \frac{1}{E_i}}$)	115	70,912.3	$0.55 \times E_i = 39,001.8$
Median	109.8	64,112.4	$0.55 \times E_i = 35,261.8$
Standard Deviation	16.16	193,875.4	$0.55 \times E_i = 106,631.5$
CV	0.138	1.2	1.2
SPT N average value = 16, $E_{sand} = 250(N+15) = 250 \times (16+15) = 7,750$ kPa = 1,100 psi (Equation 3-9)			

Table 6-9 Mass strength properties for SR-84 site bearing capacity prediction

	τ - σ space			p-q space			
	c, psi	ϕ , °	ω , °	a, psi	α , °	P_p , psi	β , °
Mass properties	44	35.4	6	35.88	30.1	392	6.0
Note	$\frac{a}{\cos \phi} = \frac{35.88}{\cos(35.4)} = 44$	$\text{asin}(\tan \alpha) = \text{asin}(0.58) = 35.4^\circ$	$\text{asin}(\tan \beta) = \text{asin}(0.1) = 6^\circ$	From Figure 6-9			

Table 6-10 Bearing capacity calculation at SR-84 site

Footing Geometry	B, ft	5
	L, ft	6
	D _f , ft	3
	T, ft	10
Mass Properties	c, psi	44.08
	φ, °	35.4
	P _p , psi	392
	ω, °	6.01
	E _{sand} /E _{mass}	E _{sand} /E _{mass} (Table 4) = 1100/35261.8 (median) = 0.031
Florida Bearing Capacity Equations	N _c	$\frac{1.8 \cos \phi}{0.8 - \sin \phi} = \frac{1.8 \cos (35.4)}{0.8 - \sin (35.4)} = 6.64$ (Equation 2-14)
	N' _c	$\frac{1.8 \cos \phi}{0.8 - \sin \omega} = \frac{1.8 \cos (35.4)}{0.8 - \sin (6.01)} = 2.11$ (Equation 2-15)
	N _γ	$\frac{1.8 [\sin \phi - \sin \omega]}{0.8 - \sin \omega} = \frac{1.8 [\sin (35.4) - \sin (6.01)]}{0.8 - \sin (6.01)} = 1.23$ (Equation 2-16)
	q, psi	3 (D _f) × 110/144 = 2.29 (Equation 2-17, overburden stress)
	N _q	$(1.5 \times \frac{P_p}{\sigma_a} - 10) \times (3 \times \sin \phi - 1) = (1.5 \times \frac{392}{14.7} - 10) \times (3 \times \sin (35.4) - 1) = 22.11$ (Equation 2-18)
	R	$0.093T^2 E_{soil} / E_{rock} = 0.093T^2 E_{sand} / E_{mass} = 0.093 \times 10^2 \times (0.031) = 0.29$ (Equation 2-13)
	N _R	$0.86 \times R^{-0.25} = 0.86 \times 0.29^{-0.25} = 1.17$ (Equation 2-12)
	n	$\left(\frac{4}{0.3B \text{ in ft}}\right)^{-0.055} = \left(\frac{4}{0.3 \times 5}\right)^{-0.055} = 0.95$ (Equation 2-10)
	ξ	$1 + 0.245 \left(\frac{B}{L}\right)^{0.66} = 1 + 0.245 \left(\frac{5}{6}\right)^{0.66} = 1.22$ (Equation 2-11)
	Qu1, psi	ncN _c + qN _q = 0.95 × 44.08 × 6.64 + 2.29 × 22.11 = 327.6 (Equation 2-8)
	Qu2, psi	n[cN' _c + p _p N _γ] + qN _q = 0.95 × [44.08 × 2.11 + 392 × 1.23] + 2.29 × 22.11 = 594.8 (Equation 2-9)
	Qu	min (Q _{u1} , Q _{u2}) × ξ/N _R = min(327.6, 594.8) × 1.22/1.17 = 340.8 psi = 24.54 tsf (Equation 2-7)

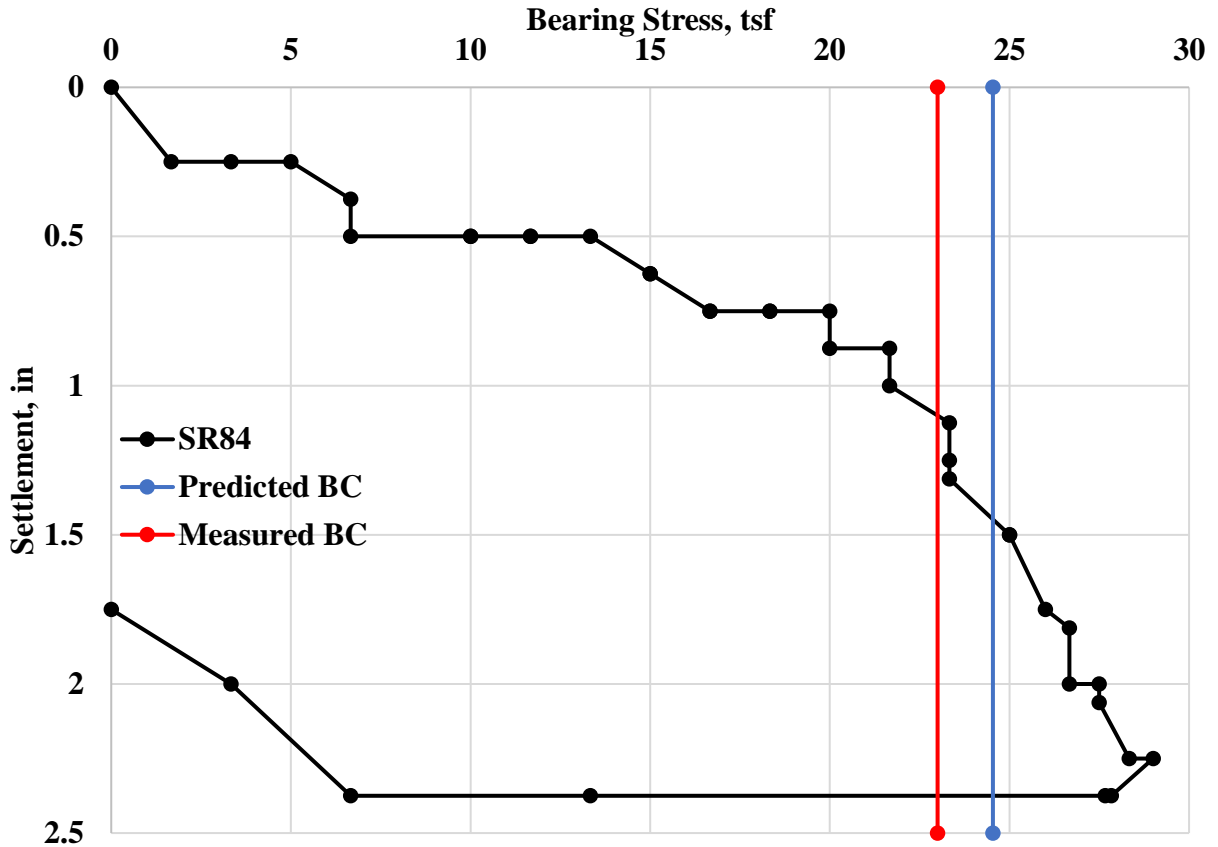


Figure 6-38 Bearing capacity predictions and load versus settlement curve

Of great interest is the comparison of bearing capacity estimates of existing and nearby footings to measured/predicted SR-84 response. A review of locations of FDOT bridge piers with spread footing in comparison to SR-84 load test is summarized in Figure 6-39. Specifically, Location #1 is the load test site and the 13 piers spread footings and piers 4 to pier 16 within the blue lines, are locations of shallow foundations on I-75 Express Lanes Segment E. Parsons Brinckerhoff Foundation Certification Packages for these footings report footing sizes, and estimated rock properties as well as calculations of each footing’s bearing capacity, using AASHTO LRFD Bridge Design (Empirical Hough Method). The footing geometries, limestone thickness and strength properties, along with the nominal bearing pressure for each footing bridge pier as well as SR-84 load test are summarized in Table 6-11.

A review of Table 6-11 shows that the I-75 bridge pier foundations are generally conservative vs. SR-84 results for a number of reasons. First (Table 6-11), they were all designed with the cohesion term being zero, second, the rock's angle of internal friction was 32° instead of 35.4° determined from triaxial testing at the SMO, and finally the B term in all of the piers' bearing capacity calculations was 3 to 4 times greater than SR-84 (e.g. 5 vs. 19.6 – Pier 12). It should be noted however that the Foundation Certification Packages made no allowance for moduli of rock to underlying sand. That is, the SR-84 predicted bearing capacity from Phase I has a 20% reduction (i.e., N_R) for the thickness of rock layer and moduli ratio of the rock to the underlying sand layer.



Figure 6-39 Boring and pier locations at the SR-84 site (I-75 express lanes segment E)

Table 6-11 Bearing pressure comparison of the nearest bridge pier spread footings

Locations	Design Method	Footing Geometry			Rock Thickness, ft	Rock Strength			Nominal Bearing Pressure, ksf
		B', ft	L', ft	D _f , ft		γ at D _f , pcf	c, psf	φ _f , °	
Load Test at SR-84	FL Bearing Capacity Equations	5	6	3	10	110	6336	35.4	48
Pier 4 Spread Footing	AASHTO LRFD Bridge Design	17.49	21.5	8	6	130	0	32	36.4
Pier 5 Spread Footing	AASHTO LRFD Bridge Design	16.7	23	8	9	130	0	32	37.8
Pier 6 Spread Footing	AASHTO LRFD Bridge Design	17.8	23.51	8	6	130	0	32	34.6
Piles used for Pier 7 and Pier 8									
Pier 9 Spread Footing	AASHTO LRFD Bridge Design	16.8	25.3	9	9	130	0	32	45.4
Pier 10 Spread Footing	AASHTO LRFD Bridge Design	15.6	25.8	8	12	130	0	32	57.5
Pier 11 Spread Footing	AASHTO LRFD Bridge Design	18.8	24.1	8	8	130	0	32	35.8
Pier 12 Spread Footing	AASHTO LRFD Bridge Design	19.6	20.4	10	10	130	0	32	50.3
Pier 13 Spread Footing	AASHTO LRFD Bridge Design	17.48	24.66	8	11	130	0	32	43.2
Pier 14 Spread Footing	AASHTO LRFD Bridge Design	19.6	22.8	8	9	130	0	32	40.7
Pier 15 Spread Footing	AASHTO LRFD Bridge Design	19.3	24.7	8	12	130	0	32	44.6
Pier 16 Spread Footing	AASHTO LRFD Bridge Design	17.4	23.3	8	11	130	0	32	45.2

6.4. Load-settlement Response

A Plaxis 3D analysis was carried out to validate the load and settlement response. The subsurface geometry of Figure 6-3 was used. The strength parameters of the bottom Fort Thompson layer are characterized based on the layer mean value: dry unit weight = 137 pcf mass strength envelope, Figure 6-8: $c = 122$ psi and $\phi = 32.2^\circ$. The top Miami limestone layer will be simulated by using the 110 pcf mass strength envelope: $c = 44$ psi and $\phi = 35.4^\circ$. The mass strength parameters of the sand layer are characterized based on the average SPT-N value (16) of B-4, Appendix. Based on Figure 6-40, a friction angle of 32° was obtained. Also, for the numerical simulations, a 1,100 psi Young's modulus of the sand layer was used from Bowel's Method, Equation 3-9, and SPT $N=16$.

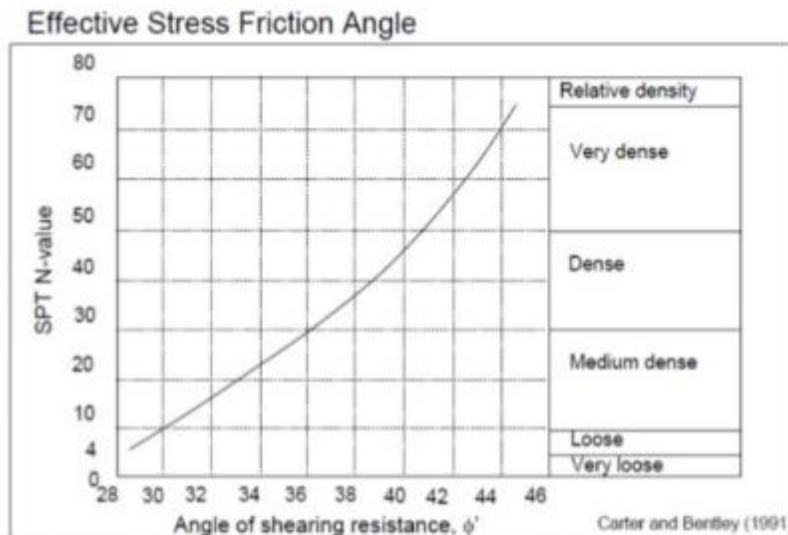


Figure 6-40 Effective friction angle and SPT N-value (Peck et al., 1974)

6.4.1 Finite Element Modeling

For SR-84, Figure 6-3, the stratigraphy is separated into three layers with 3 ft thick embedment in the Miami limestone with 10 ft thickness overlying the 20 ft thick sand layer and a 30 ft Fort Thompson limestone beneath. A 3D model with 150 ft \times 150 ft by 63 ft region is

discretized into 53,200 15-noded Triangular finite elements, Figure 6-41. The four sides of the model are fixed in the normal directions and the bottom boundary was fixed in all directions. The water table is located at the top of Miami limestone Layer or 3 ft from the ground surface. For material properties of Miami limestone and Fort Thompson limestone layer, the strength parameters were obtained from the corresponding strength envelope (110 pcf and 136.5 pcf) and the stiffness parameters were assessed through the triaxial tests with different confining stresses. As identified in Chapter 2, the elastic modulus of Florida limestone is based on its bulk dry unit weight, stress state and strain level. For the rock over sand case, the initial modulus (E_i) based on the median dry unit weight (110 pcf) is from Figure 3-1 and the mass modulus (E_m) based on 78% $REC_{adjusted}$ is from Figure 5-31. The material properties for each layer are summarized in Table 6-12. Furthermore, the dry unit weight ($1750 \text{ kg/m}^3 \approx 110 \text{ pcf}$) and the modulus used in the bearing capacity predictions and load-settlement response validations also agree with the seismic testing results (Chapter 4).

The simulation was performed with 2.5 tsf load increment with predicted and measured response shown in Figure 6-42. The stiffness parameters used in each loading step and stress state beneath the footing are presented in Table 6-13. The initial load vs settlement was controlled by the 10 ft limestone layer. Then the secant modulus of limestone dropped (E_s) and the rock mass underwent a punching shear failure from 22 to 24 tsf. That is, as load kept increasing, the sheared rock mass acted as a rigid body and pushed through the sand layer beneath it. So, between the 20 and 25 tsf in Figure 6-42, a significant slope change is identified because of different material responses (limestone versus dense sand). Figure 6-43 (a) and (b) present the shear failure planes in the FEM mesh as well as the shear stress bulb at failure (23 tsf), which extend into the sand layer and progress downward. Such punching failure planes

could be observed in other plate load tests on strong soil overlaying weak soil, for example: the work of Consoli et al., (2009), Figure 6-44. It should be noted from Figure 6-43 (c) and (d) that at peak load (31 tsf), i.e., after punching shear failure, approximately 70% of the total settlement occurs within the dense sand layer.

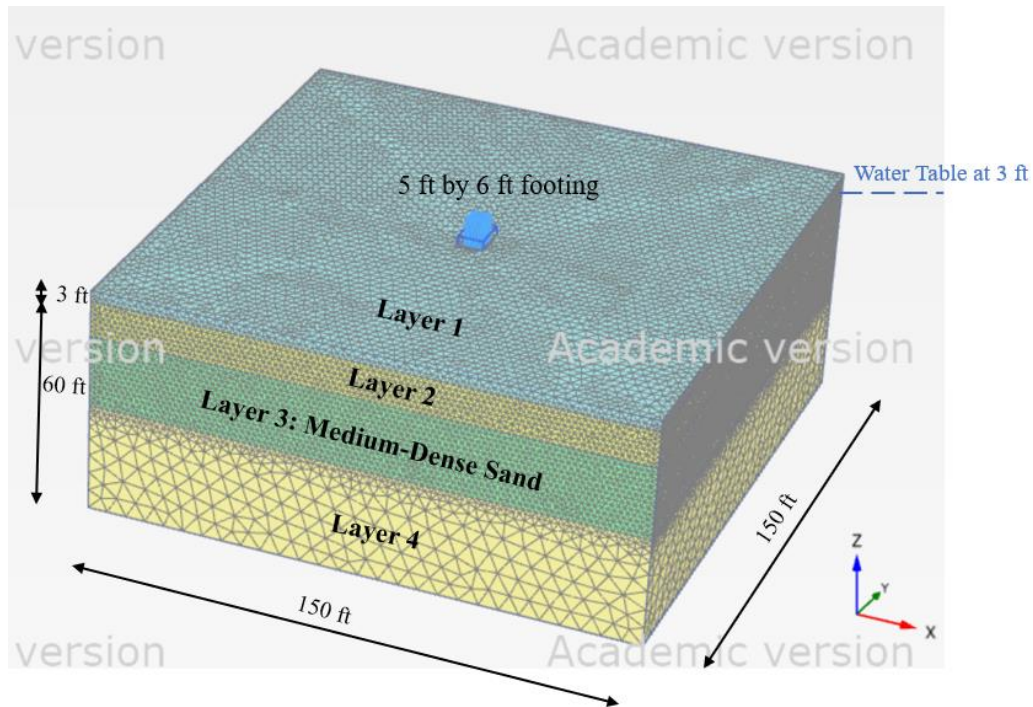


Figure 6-41 Geometry of finite element modeling

Table 6-12 Material properties of SR-84 finite element model

Layer	γ_{sat} , pcf	Material	Material Model	c, psi	ϕ , °	ψ , °	μ	Young's Modulus, psi
1	90	Miami Limestone	Mohr-Coulomb	25	31	0	0.10	30,000
2	110	Miami Limestone	Mohr-Coulomb	44	35.4	0	0.10	35,262 ~ 8,815
3	108	Medium-Dense Sand	Mohr-Coulomb	0	32	32	0.3	1,087 ~ 500
4	136.5	Fort Thompson Limestone	Mohr-Coulomb	93.3	32.2	0	0.3	60,000

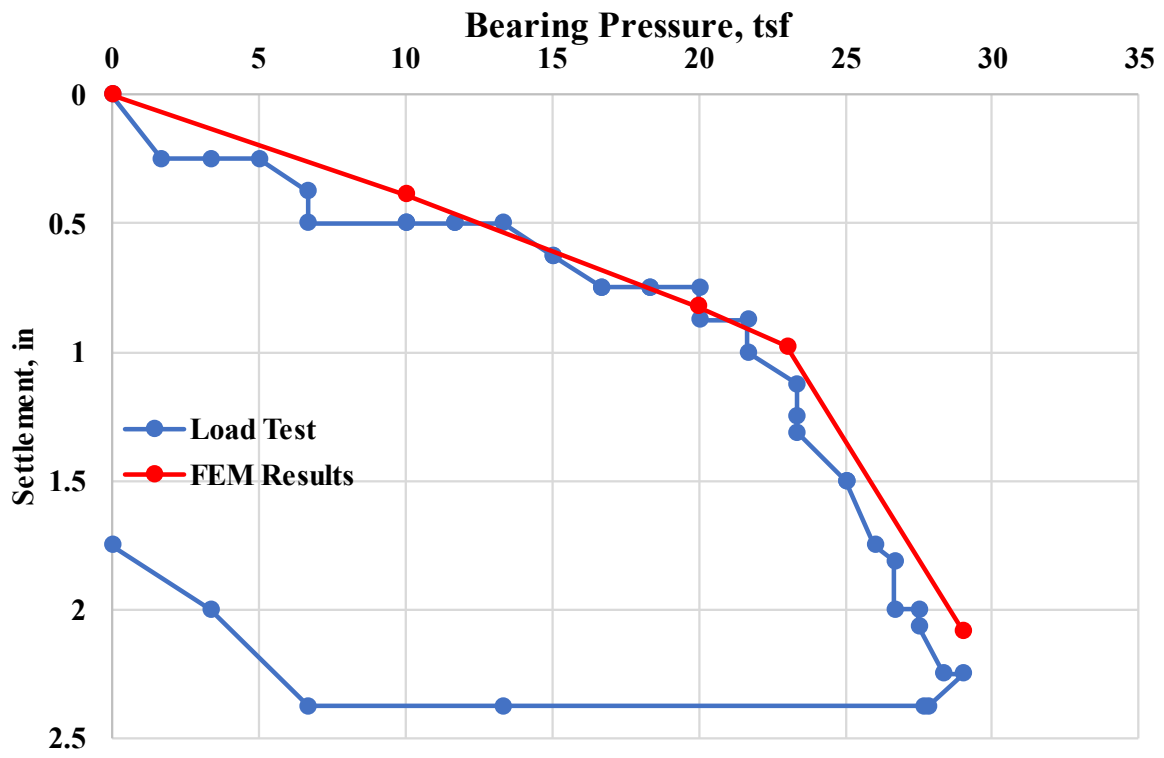


Figure 6-42 Numerical results of SR-84 finite element model

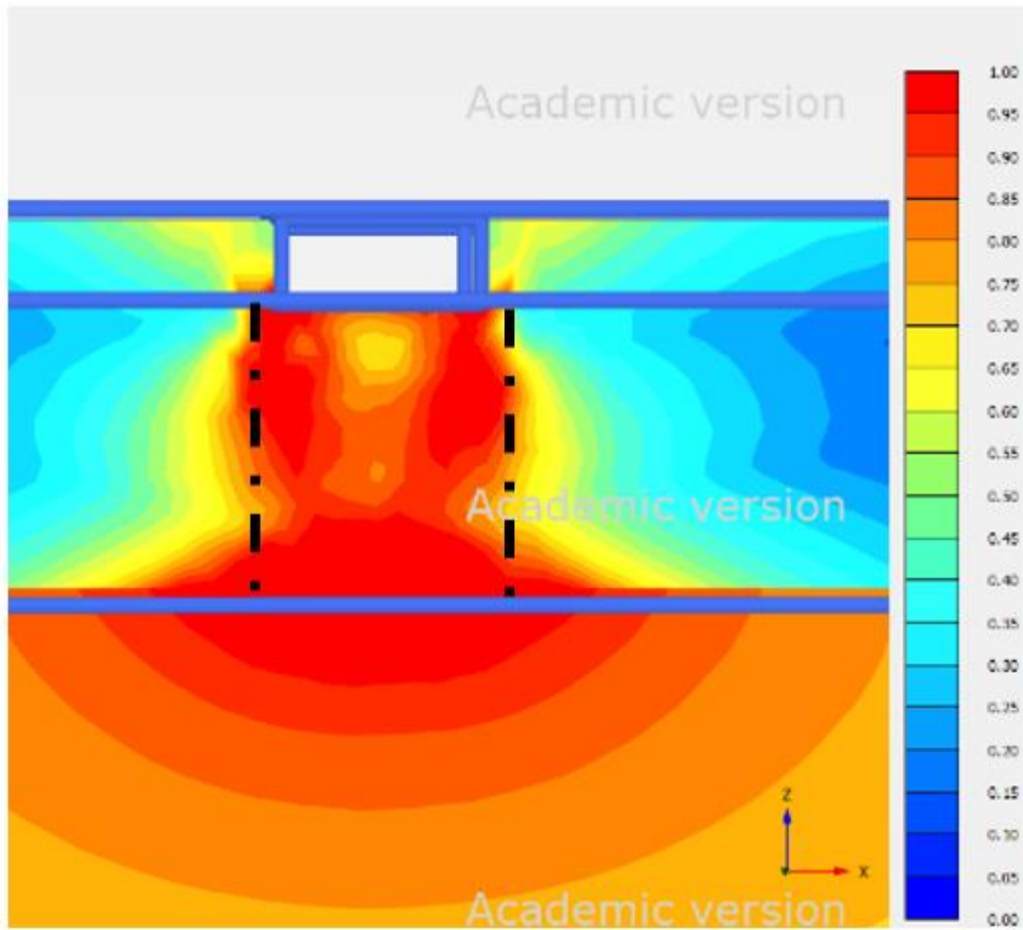
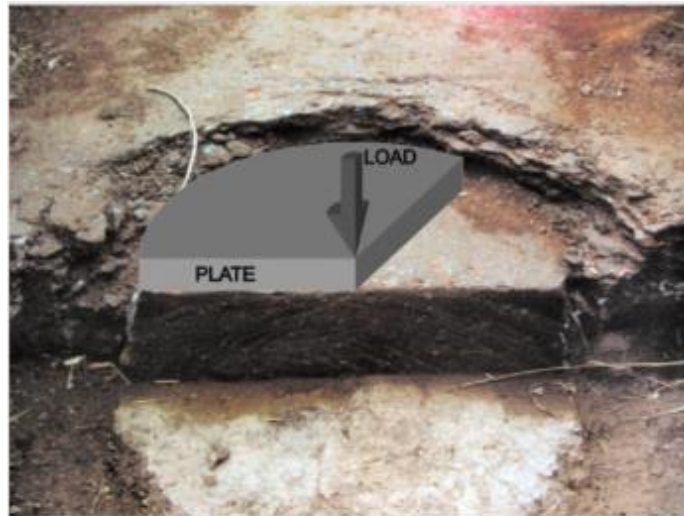


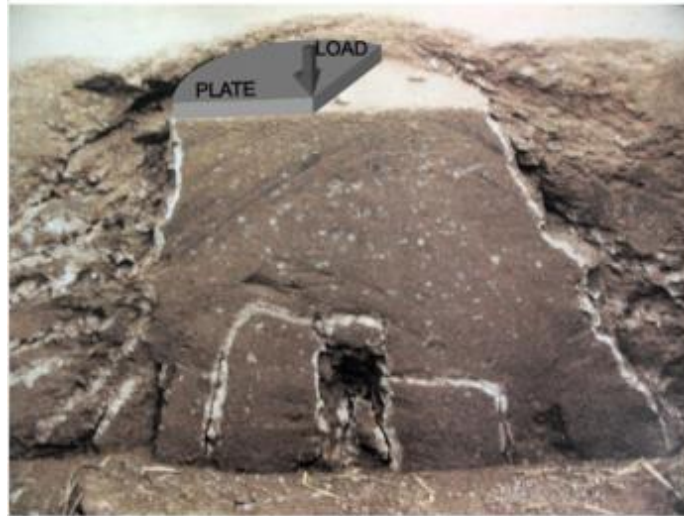
Figure 6-43 Shear failure plane in Miami limestone layer under 23-tsf load

Table 6-13 Stiffness and stress state in each loading step for Miami limestone layer

Loading Step	Bearing Pressure, tsf	Layer 2			
		110 pcf			
		σ_1' , psi	σ_3' , psi	Elastic Modulus, psi	Poisson's Ratio
1	0	3.7	1.5	35,262	0.1
2	10	2.7	1.6	35,262	0.1
3	19.95	40.5	-3.5	35,262	0.1
4	23	91.7	-7.0	35,262	0.1
5	29	112.2	-3.9	8,815	0.1



(a)



(b)

Figure 6-44 Photos of the failure mechanism observed in the plate load tests (a) $H/D = 0.25$; (b) $H/D = 1$. H = thickness of top strong layer: D = footing width (plate load tests on cemented soil layers overlaying weaker soil, (Consoli et al., 2009))

6.4.2. Burmister Method

Burmister (1958) developed one of the first methods to estimate the load-settlement response for a rock over sand scenario, which uses a closed form equation to predict the settlement for a two-layer system. Burmister considered a strong layer overlying a semi-infinite elastic weak layer. The soil of both layers is assumed to be homogeneous, isotropic, and linearly elastic. The method was developed using the theory of elasticity and satisfies continuity at the interface between both layers, Equation 3-10 and Figure 3-5.

Similar to the FEM analysis, the Burmister Method used the median modulus 35,261.8 psi as the mass initial modulus (E_m) of the overlying rock until the bearing capacity was reached and then the modulus of the rock layer is lowered to the 2% strain secant modulus ($E_{mass, secant}$, yielding/crushing of rock), Figure 2-1. The sand modulus is remains – 1,100 psi from Bowel’s method (constrained by overlying rock). Based on the thickness of each layer and modulus ratio, the deflection factor F is determined from Figure 3-5., then the mean settlement at bearing stress and post bearing stress (10% higher) are calculated through Equation 3-10, and shown in Table 6-14 along with calculations. The Burmister’s predicted load vs. settlement is shown in Figure 6-45 (a shape factor of 1.1 used based on $L/B = 1.2$) and indicates good agreement with the measured load-settlement response, both pre and post bearing failure.

Table 6-14 Burmister calculations for rock-over-sand case

	p, contact stress, tsf	Figure 3-5			Settlement, in
	0	$\frac{h}{r} \left(\frac{T}{\left(\frac{B}{2}\right)}, \right)$ Table 6-10)	$\frac{E_2}{E_1}$ (E_{mass}/E_{sand})	F	0
Burmister	24.54 (Bearing stress, Table 6-10)	$\frac{10}{\left(\frac{5}{2}\right)} = 4$	$\frac{35261.8}{1100} = 32.05$ (See Table 6-10)	0.11	$\frac{1.18pa}{E_2} F = \frac{1.18 \times 24.54 \times 12 \times 2.5 \times 0.11}{\left(\frac{1100}{13.89 \text{ psi/tsf}}\right)} = 1.21$ (Equation 3-10)
	27* (Post bearing stress)	$\frac{10}{\left(\frac{5}{2}\right)} = 4$	$\frac{E_{mass, secant}^{**}}{E_{sand}} = \frac{8815}{1100} = 8.01$	0.22	$\frac{1.18pa}{E_2} F = \frac{1.18 \times 27 \times 12 \times 2.5 \times 0.22}{\left(\frac{1100}{13.89 \text{ psi/tsf}}\right)} = 2.66$ (Equation 3-10)

* $p = Qu \times 1.1 = 24.54 \times 1.1 = 27$ tsf

** $E_{mass, secant} = E_{mass} \times \text{strain at yield} / \text{strain of interest} = 35261.8 \times 0.5\% (\text{yielding}) / 2\% = 8815$ psi.

6.4.3. Proposed FB-Multiplier Settlement of Two-layer System

Section 3.3 discussed the equivalent modulus method and introduced the two stage Winkler model by using the Equations 3-11 and 3-12 (Ueshita and Meyerhof), and Figure 3-7. By using the initial mass modulus before failure (35,261.8 psi), and the secant mass modulus after failure (8,815 psi), the bi-linear load-settlement is calculated in Table 6-15. Agreement pre and post bearing is quite good, Figure 6-45. Note, that the thickness of the sand layer (layer 2) is 15 ft and a shape factor 1.1 is used here due to L/B ratio (1.2).

Table 6-15 Winkler model calculations for rock-over-sand case

FB-M	Bearing Stress, tsf	Figure 3-7		σ_i , tsf	h_i , ft	E_h , psi	Settlement, in
	0	Use h/a same values as h/r and E_1/E_2 same values as E_2/E_1 in Table 6-10	$\frac{\sigma_{sand}}{p}$ (function of h/a and E_1/E_2)	For sand layer, take half of the σ_{sand}			$E_{sand} = 1100$ psi (Table 6-10) $E_{mass} = 35261.8$ psi (Table 6-10 Median) $E_{mass,secant} = 8815$ psi (Table 6-14)
24.54 (Bearing stress, Table 6-10)	0.025		Rock**: 12.59	Rock: 10 ft	$E_h = \frac{\sum h_i \sigma_i}{\sum \frac{h_i \sigma_i}{E_i}} = \frac{10 \times 12.58 + 15 \times 0.31}{10 \times \frac{11.39}{35261.8} + 15 \times \frac{0.31}{1100}} = 16883$ (Equation 3-12)	$\frac{1.5pa}{E_h} = \frac{1.5 \times 24.54 \times 12 \times 2.5}{16883} = 0.91$ (Equation 3-11)	
			Sand***: 0.31	Sand: 15 ft (5B depth)			
27* (Post bearing stress)	0.04	Rock: ($0.04 \times 27 + 27$)/2 = 15.39	Rock: 10 ft	$E_h = \frac{\sum h_i \sigma_i}{\sum \frac{h_i \sigma_i}{E_{secant}}} = \frac{10 \times 15.39 + 15 \times 0.532}{10 \times \frac{15.39}{8815} + 15 \times \frac{0.532}{1100}} = 6376.1$ (Equation 3-12)	$\frac{1.5pa}{E_h} = \frac{1.5 \times 27 \times 12 \times 2.5}{6376.1} = 2.65$ (Equation 3-11)		
		Sand: $0.04 \times 26.6/2 = 0.532$	Sand: 15 ft (5B depth)				

** $p = Q_u \times 1.1 = 24.54 \times 1.1 = 27$ tsf

$E_{mass,secant} = E_{mass} \times \text{strain at yield/strain of interest} = 35261.8 \times 0.5\% (\text{yielding}) / 2\% = 8815$ psi.

** σ_1 at the center of the rock layer = $(\sigma_{top} + \sigma_{bottom})/2 = (p + \sigma_{sand})/2 = (24.54 + 24.54 \times 0.025)/2 = 12.59$ tsf

*** σ_2 at the center of the sand layer = $(\sigma_{top} + \sigma_{bottom})/2 = (\sigma_{sand} + 0)/2 = (0.025 \times 24.54 + 0)/2 = 0.31$ tsf

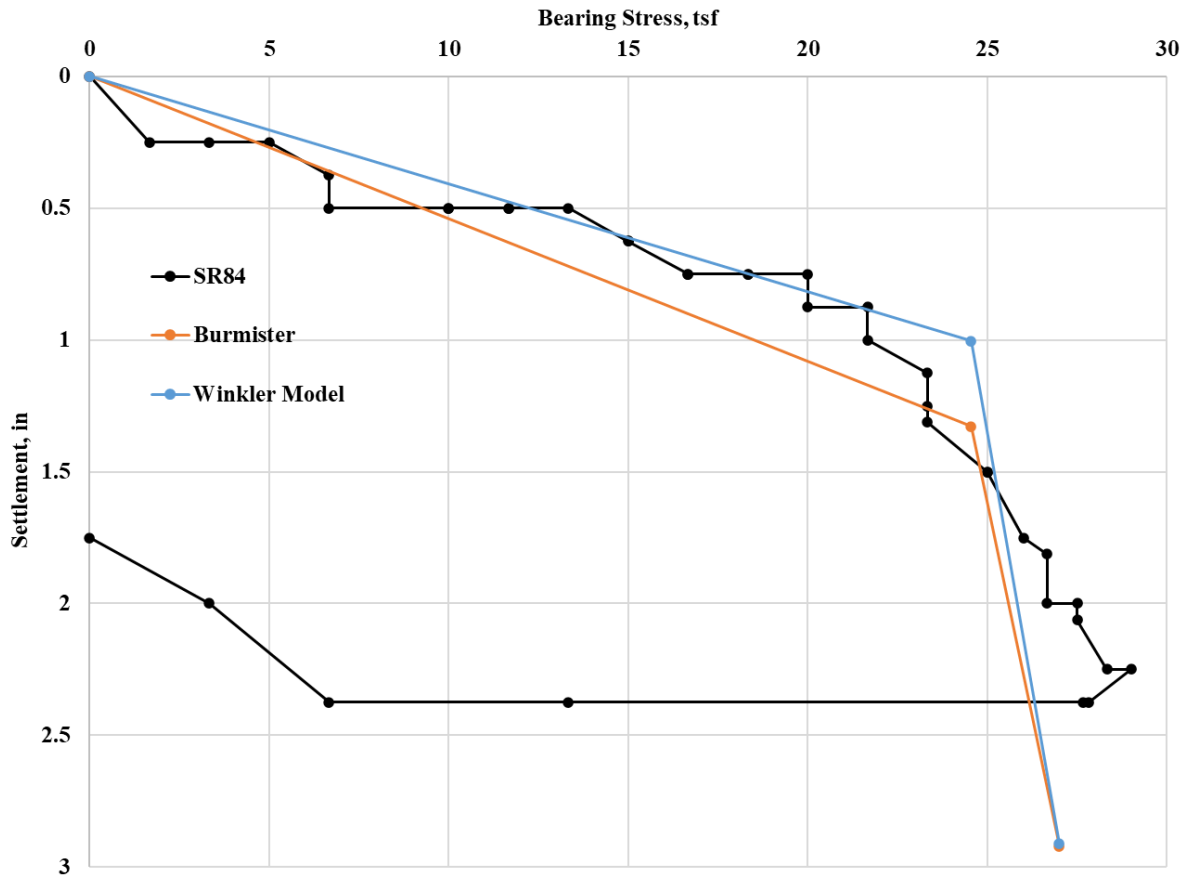


Figure 6-45 Measured vs. Winkler model vs. Burmister's solution: load-settlement response

Chapter 7

Load Test at Bell

7.1. Site Investigation

The site is located near the city of Bell in Gilchrist County, Florida. The site layout including boring locations are shown in Figure 7-1a. Various Destructive and Non-Destructive methods were conducted at the site because of high variability. Figure 7-1b shows the top of rock based on hand augers as well as the test lines for the seismic shear and electrical resistivity Non-Destructive methods. Borings B2 and B3 are SPT holes (Appendix); borings B4, B5 and B6 (no rock down to 10 ft) are MWD rock coring holes and borings B7 and B8 included only MWD and boring B10 had MWD (Appendix) in combination with rock coring. The line delineations, Figure 7-1b, represent the seismic shear and resistivity testing, with seismic (red) labeled as S1 to S6 and resistivity (yellow) R1 to R4. The surface of the rock (pinnacled) is summarized in Figure 7-1b based on 200 hand auger holes; the black dashed square marks the footing test location based on invasive and non-invasive testing at the site. A discussion of layering and properties of rock and soil within the dashed black box, Figure 7-1b follows.

Based on MWD strength profiles, the subsurface stratigraphy, Figure 7-2, beneath the footing was developed. The Ocala limestone layer starts at a depth of 5 ft and extends 5 ft downward to a 2 ft thick weathered limestone layer overlying weak Ocala limestone extending down to a depth of at least 50 ft (boring and seismic shear results). The water table at the time of borings was fluctuating around 12 ft beneath the ground surface.

Non-Destructive testing was used to characterize the stratigraphy and shear velocity of a much larger area of rock and soil (2D -23,800 sq ft²) beneath the footing compared to the traditional standard penetration tests along a line (1D with spoon or core barrel size - 2.5 in diameter). In addition, based on prior testing (load tests at Cemex and SR-84 sites), seismic shear testing was shown to provide reliable estimation of the dry unit weight of rock within the influence zone as discussed in CEMEX & SR-84. However, in the case of the resistivity tests, Figure C-1, (footing approximately at 80 ft between R1 and R2), Harro and Kiflu (2018), identified that the resistivity of sand, clay and weathered limestone (Figure C-1) are similar; suggesting that layering of sand, clay or weathered limestone cannot be differentiated as well as estimate their properties (e.g., dry unit weight). Consequently, prior to the load test, multiple seismic shear lines were conducted to find a relatively flat strong rock surface within 5 ft of the ground surface elevation of at least 5 ft thickness.

Shown in Figure 7-3 are the seismic shear testing lines 5 and line 6 (Figure 7-1b), with the footing location at approximately $x = 18$ m, and the reaction drilled shaft locations at $x = 12.5$ m and $x = 23.5$ m along the line 5. It is evident that the layering information agreed with the MWD profile (Figure C-2), rock over a weathered layer), with the average unit weight for the top rock layer (bottom of footing) from the seismic shear at 106.1 pcf (1,700 kg/m³). Note, that the horizontal and vertical blue zones representing the weak material or voids in line 5 were subsequently validated by layering and chimneys found in the drilled shaft installation (section 7.2.1). Specifically, 17 cubic yards of concrete was used for the East shaft and 14 cubic yards of concrete was cast in the West shaft, which exceeded the theoretical requirement of 12.3 cubic yards of concrete at each location. Moreover, a forty-foot chimney was found to open next to the East shaft during concreting.

Besides stratigraphy, strength and moduli of each layer are required to estimate bearing capacity and the load-settlement response of the foundation. Unconfined compression, split tension, and triaxial compression tests were performed on recovered cores from B4, B5 and B10. Similar to Miami limestone, the dry unit weight is used to correlate the strength envelope (Figure 7-6) and modulus (Figure 7-7). The unconfined compression strength versus depth and direct tension strength ($q_{dt} = 0.7 \times q_t$, Perras et al., 2014) versus depth are plotted in Figure 7-4 and Figure 7-5.

The intact strength envelopes of Ocala limestone based on q_u , q_t and triaxial (50 psi and 600 psi confining stress triaxial tests) are presented in Figure 7-6 vs. the Miami limestone (phase I). Evident, the Miami limestone has a higher initial friction angle but under higher initial confining stress, it undergoes crushing and a reduced 2nd strength slope. The latter was verified in Figure 2-6 by plotting the measured volumetric strain under isotropic loading (stress path along the p-axis ---- applying cell pressure prior to shearing) by dry unit weight. Note, the much higher volumetric strain of Miami limestone vs. Ocala, indicative of micro-cracking (compression positive and extension negative) of Miami vs. Ocala. Also, the Poisson's ratio of the Ocala limestone under shear was found from the triaxial tests vs the Miami limestone, Key Largo limestone (Phase I) and plotted in Figure 2-4. Again, the Poisson ratio starts very low, then slightly positive or negative under initial shear and builds to approximately 0.1 at 0.5% to 2% vertical strain at failure. As was discussed in Phase I, Poisson's ratio of 0.1 results in reduced lateral stresses at the average stress path location beneath the footing (Lambe and Whitman, 1969) which in turn affects the strength, bearing capacity and settlement (modulus) of the footing.

Due to the low Poisson's ratio, it is recommended that using the stress-strain relationship from 50 psi confining stress to obtain the moduli, Figure 7-7. The uncorrected E_i (initial modulus without $REC_{adjusted}$) for each dry unit weight is summarized in Table 7-1. Note, the initial modulus E_i of the rock and weak layer will be used to estimate bearing as well as load-settlement response up to rock failure. However, the E_s (secant modulus) based on the 2% strain level controls the load-settlement response after rock failure, and its estimate will be detailed in Section 7.4. Corresponding triaxial tests were predicted with FEM (Figure 7-7) and showed good agreement with the experimental results.

As recommended in Phase I, the strength envelope should be reduced based on the $REC_{adjusted}$ within the formation for the various dry unit weights. The $REC_{adjusted}$ for top rock layering was estimated as 83% (80.75% from B4 and 82.67% from B5) based on the soil filled voids found in the surface of the footing location during excavation of footing, Figure 7-13. Using the nearest strength envelope (105 pcf, $c = 48$ psi and $\phi = 30^\circ$ with $REC_{adjusted}$), a 5 ft x 5 ft footing will result in a bearing capacity of 16 tsf at failure (punching) of the rock and a safety factor of 2 for the load test (900 tons) that is reported in Section 7.3.

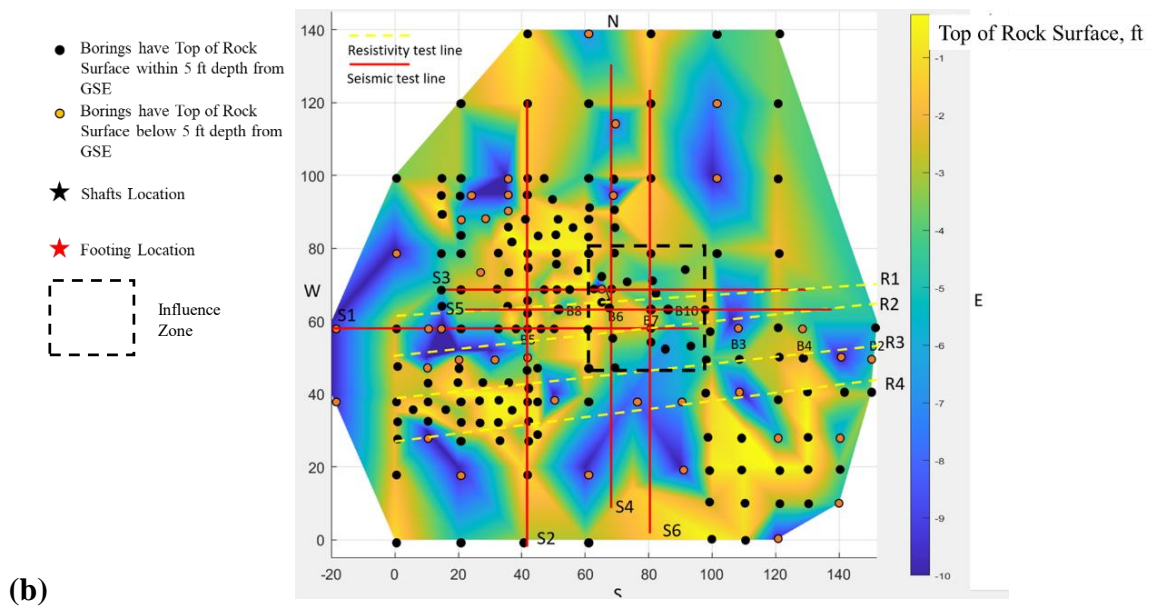


Figure 7-1. (a) Site investigation zone and boring location at Bell site and (b) top rock surface depth based on 200 hand auger holes at Bell site

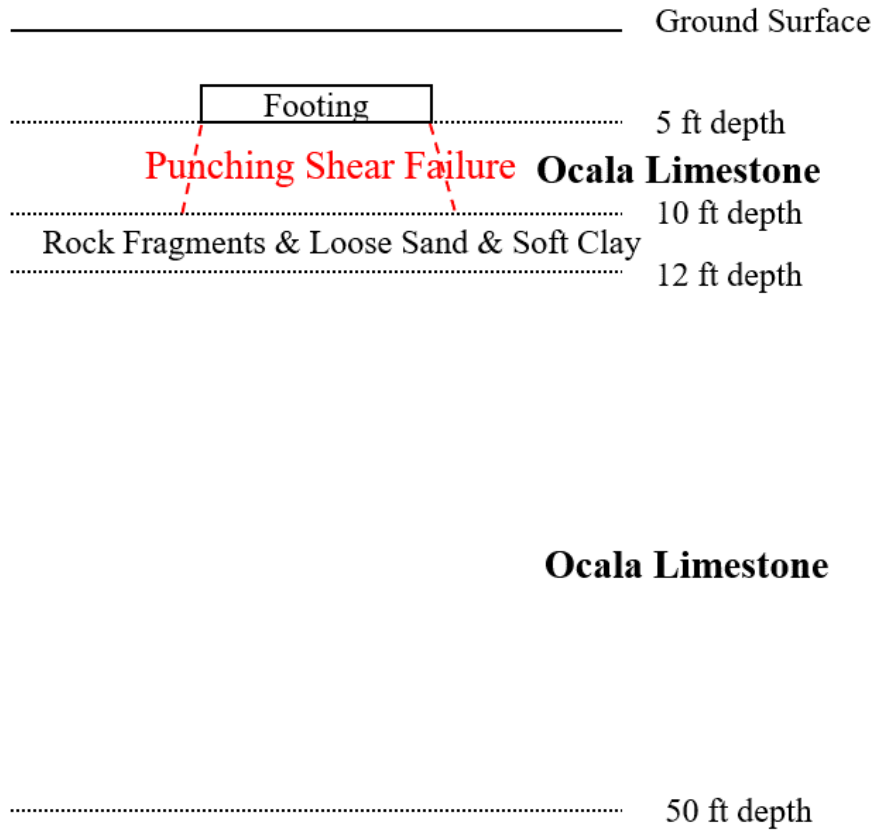
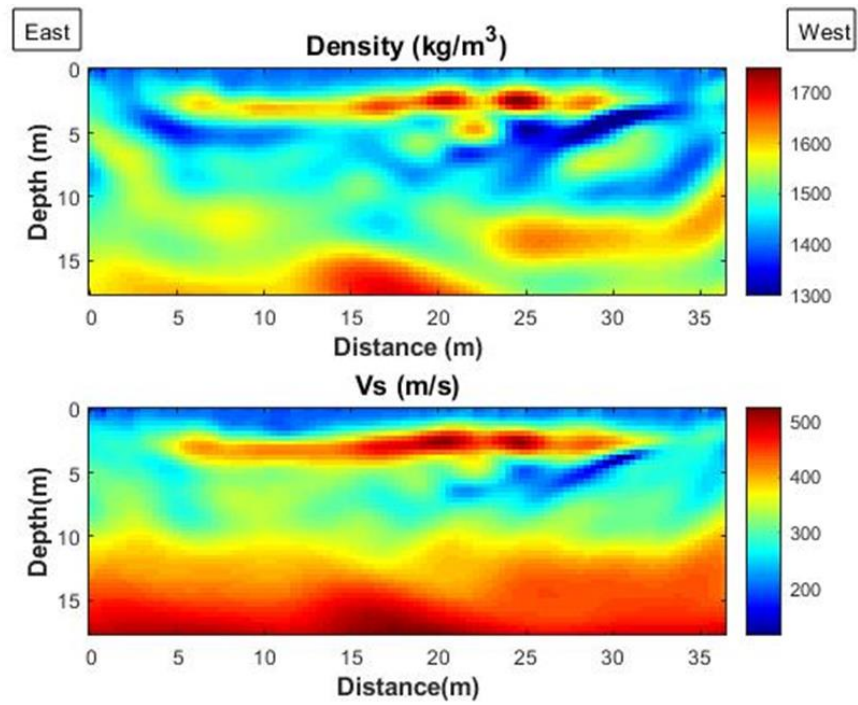
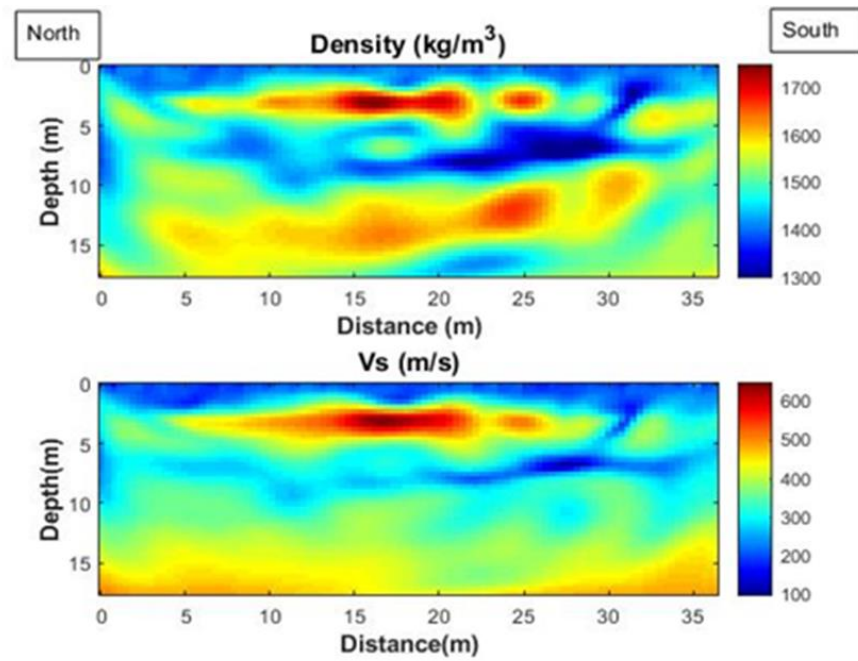


Figure 7-2. Subsurface layering at Bell site



(a)



(b)

Figure 7-3. Distribution of density and shear velocity for (a) seismic line 5 and (b) seismic line 6 (reproduced of Figure 4-31)

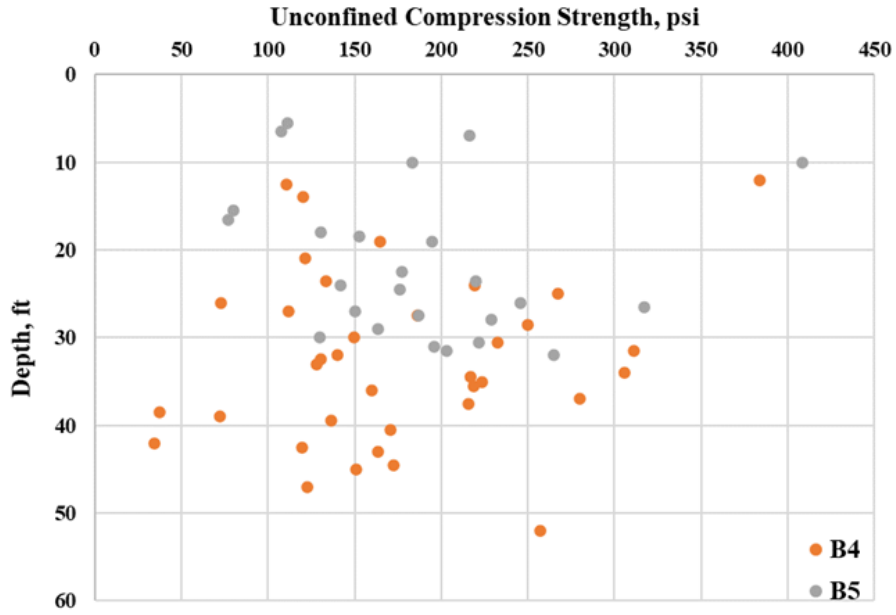


Figure 7-4. Unconfined compression strength versus depth at the Bell site

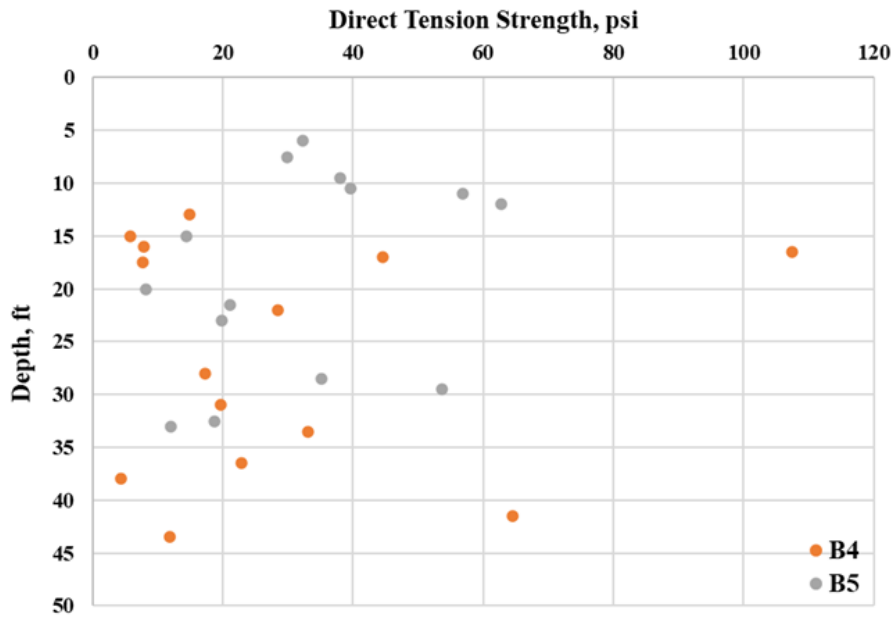


Figure 7-5. Direct tension strength versus depth at Bell site

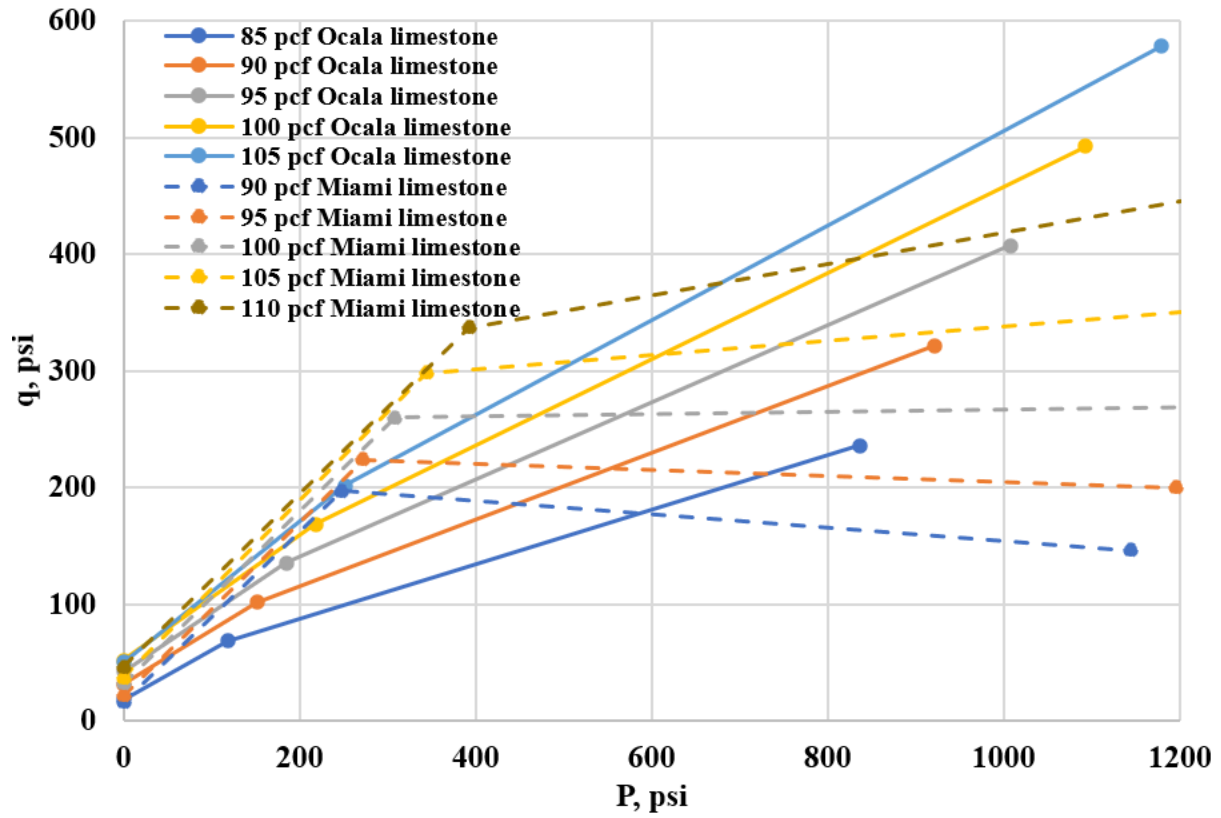


Figure 7-6. Comparison of intact strength envelopes between Miami limestone and Ocala limestone from 85 pcf to 105 pcf (reproduced of Figure 2-7)

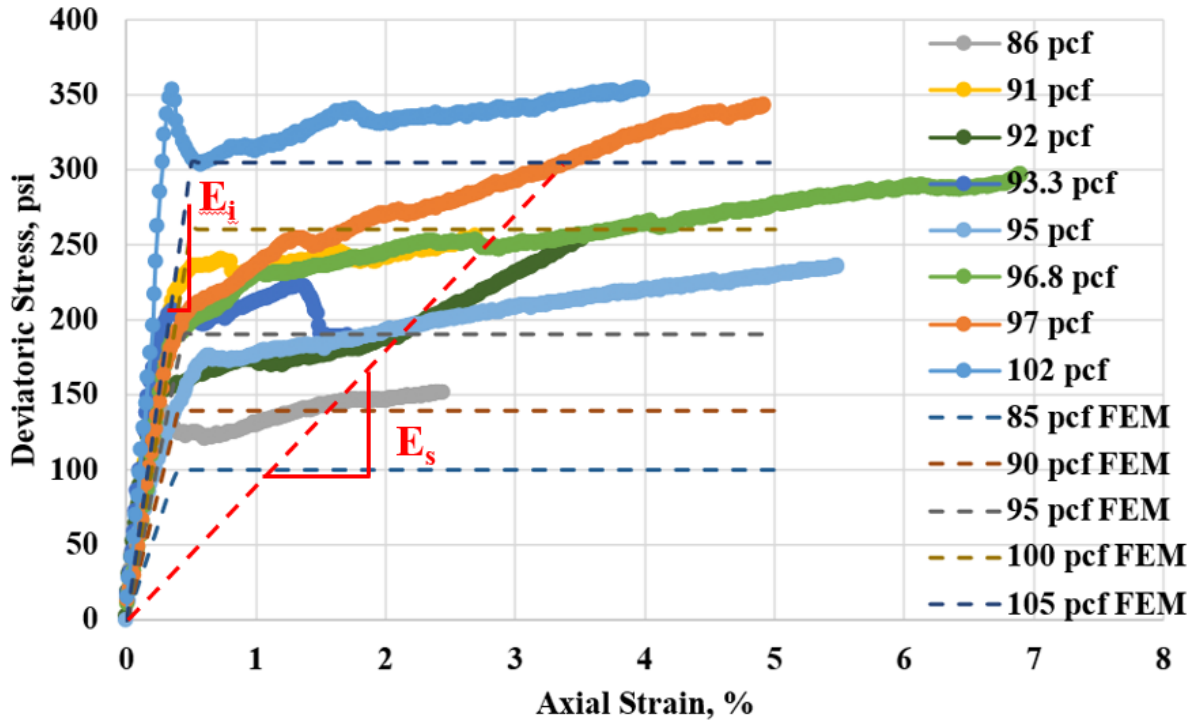


Figure 7-7. Measured vs. FEM stress-strain relationship for 50-psi confining stress triaxial tests (reproduced of Figure 2-1b)

Table 7-1. Initial modulus for Ocala limestone (without correction, reproduced of Figure 3-1)

γ_{dt} , pcf	E_i , psi
85	26,209.2
90	34,902.8
95	43,596.4
100	52,290.0
105	60,983.6

7.2. Construction of Load Test

7.2.1. Construction of the Drilled Shaft

Based on the recovered cores from B4 and B5, the median q_u strength was 172.5 psi and q_{dt} was 24.5 psi. Using Equation 5-1, and median rock strengths, a unit side shear friction of 26 psi was obtained with 80% $REC_{adjusted}$ (full depth). Using two 36" drilled shafts installed 3 ft below the ground surface to a depth of 50 ft (shafts 47 ft long), a safety factor of 1.84 was estimated for the required 900 tons load test (i.e., 1,658 tons available). Following a bid process, the contractor to install the drilled shafts of the load test was selected (same as SR 84).

The design of the drilled shafts are shown in Figure 7-8 (same with the drilled shafts at SR-84); shear reinforcement includes No. 4 rebar rings spaced 12 in on center with 24 in lap; for axial and flexure, 8 – No. 10 longitudinal bars (exceeds 1%) with 3 in clearance both at the top and bottom as well as on the sides of the shaft. To transfer the 900 tons (450 tons each) to the drilled shafts, 4 – 2.25 in \times 36 ft William threaded rods (Figure 7-9), arranged in 3 steel templates along the shaft, were anchored to each rebar cage (Figure 7-9 a & b). The contractor fabricated and secured the threaded rods to the templates. The 4 threaded rods extended 12" above the top of each shaft for couplers to be attached. Fifteen-foot threaded rods were later attached to the couplers to extend the anchorage above the 40 ft long Acosta girders used in the load test. The 15 ft threaded rods were anchored to the girders and steel support stands with C-channels, plates and nuts as shown in Figure A-3.

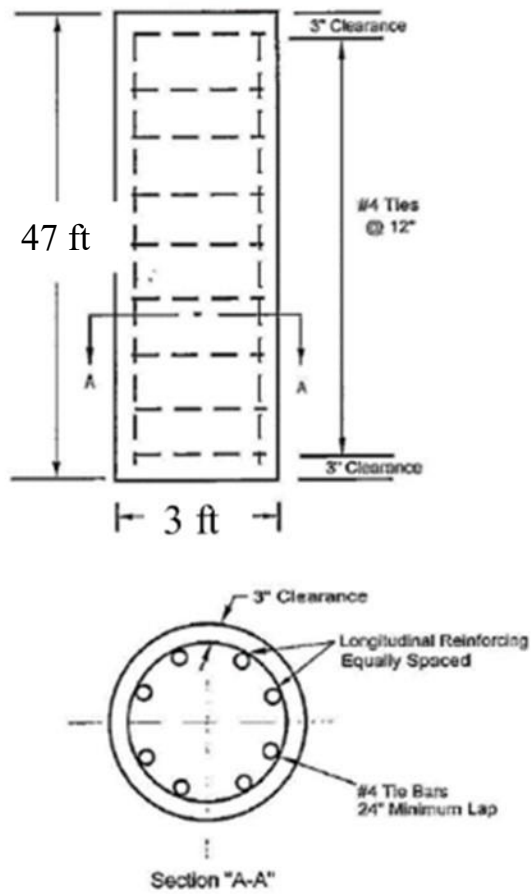


Figure 7-8. Design of the drilled shaft at Bell site

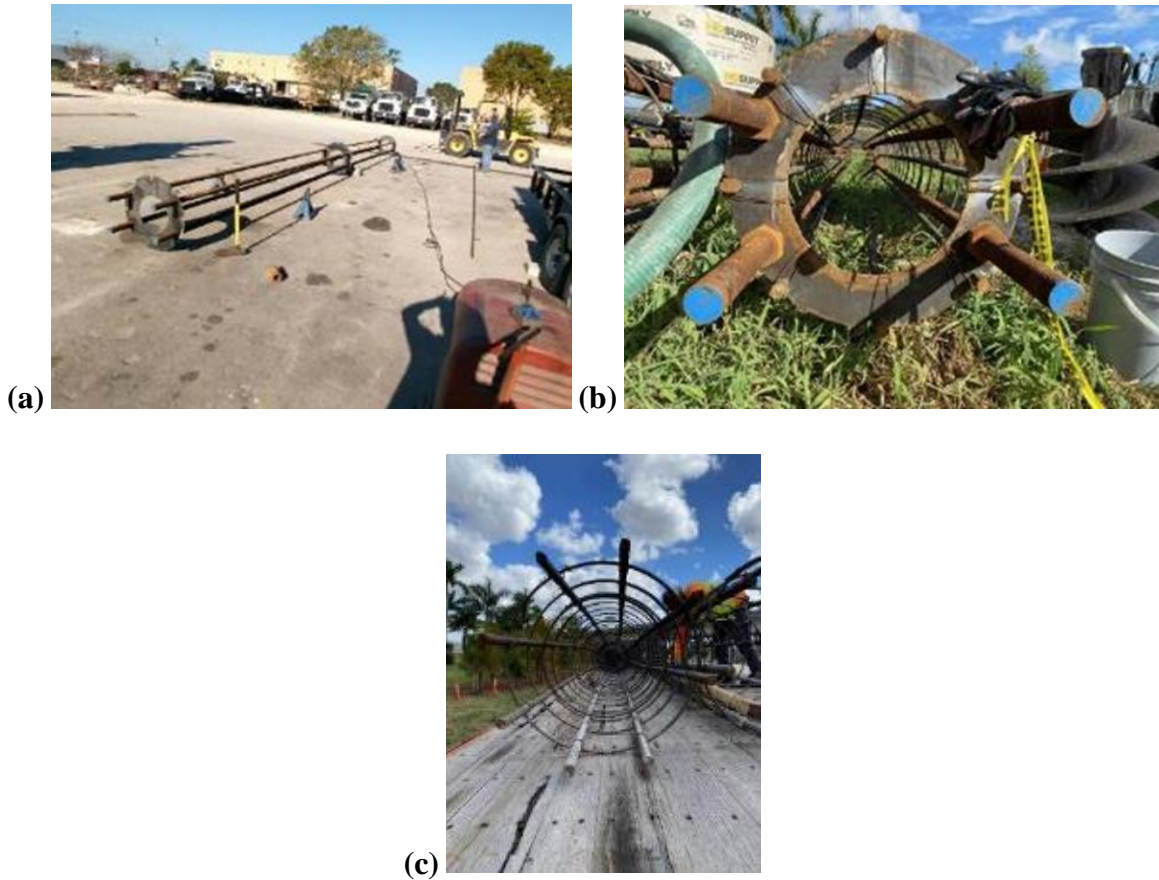


Figure 7-9. Picture of steel rebar cages: (a) templates position: top, middle, bottom and (b) William threaded rods with templates secured by the nuts and (c) 8 of No. 10 rebars

In construction of the west shaft, a 42 in rock auger bit was used to drill the first 8 ft, then a 42 in temporary casing was installed, Figure 7-10a. Subsequently, the drill bit was changed to the 36 in rock auger bit and bentonite slurry was pumped into the hole. No drilling issues were encountered until 52 ft when the slurry elevation dropped 6 ft. Soil was placed back into the hole and allowed to set (1hr). Then the rock bit was switched to a bailing bucket to clean the hole, Figure 7-10b. The pH, viscosity and density of the bentonite slurry were measured at every 10 ft drilling increment and the sand content was tested after the borehole stabilized, Table 7-2 (Note: each parameter met the requirements of FDOT Specification: 455-15.8.1). Subsequently, the steel rebar cage with spacers was placed by crane in the west shaft hole at the desired depth (i.e.,

top of concrete was 3 ft from the ground surface and the 36 ft threaded rods were 1 ft above the top of concrete), Figure 7-10c. The steel rebar cage had to be placed precisely because the center of the east drilled shaft needed to align with the center of the west shaft, and the directions of the threaded rods also needed to be aligned for the placement of girders. Next, a mounted boom concrete pump truck was setup and a tremie pipe and end hose were placed in the shaft hole, Figure 7-10e. Approximately 3 hours later, 2 concrete trucks arrived on site and 14 cubic yards of concrete were pumped into the west borehole (12.3 cubic theoretical yards for a 3 ft × 47 ft deep shaft). Researchers collected 4 in diameter × 8 in length concrete samples (ASTM C39/C39M-20) from each truck along with a slump measurement of each concrete truck. Table 7-3 presents the compressive strength of the concrete and Table 7-4 shows the measured values of slump test. Based on the construction of the west shaft, no drilling concerns were noted (i.e., heaving, caving, with exception of filling and redrilling last 3 ft), and the planned subsurface layering (5 ft of rock beneath footing) was obtained.



(a)



(b)



(c)



(d)

Figure 7-10. Construction of West shaft: (a) casing placement; (b) bailing bucket to clean the hole; (c) rebar cage installation; (d) installation of spacers for rebar cage and (e) concrete pumping



(e)

Figure 7-10. Construction of West shaft: (a) casing placement; (b) bailing bucket to clean the hole; (c) rebar cage installation; (d) installation of spacers for rebar cage and (e) concrete pumping

Table 7-2. Measured range of properties of bentonite slurry for West shaft

Properties	Measured	Range Specified in FDOT Specification: 455-15.8.1 (65°F)
Density, pcf	64 ~ 65	64 ~ 73
Viscosity, Seconds	32 ~ 40	30 ~ 40
pH	9	8 ~ 11
Sand Content	0.25%	≤4%

Table 7-3. Measured compressive strength of concrete specimens for West shaft

Days	Compressive Strength, psi
14	6328
21	6999
28	7285

Table 7-4. Measured properties of concrete for West shaft

Properties	Measured	Range specified in 346
Slump, in	9.25 ~ 9.5	7 ~ 10

Initial construction of the East Shaft progressed similarly to the West Shaft, with a temporary 42" x 8' surface casing placed at the top of the shaft and a 36" auger and bentonite slurry used below the casing. However, unlike the West Shaft, the side wall of the East Shaft collapsed, and a void opened up at an approximate 15 ft depth, Figure 7-11c. An onsite waste asphalt material was placed into the hole to a depth of 10 ft and the hole was redrilled. At a depth of 50 ft, a 45 ft deep chimney sinkhole opened up adjacent to the shaft, Figure 7-11a. The vertical chimney and the horizontal chimney at 15 ft can also be viewed at $x = 13$ m and $y = 5$ m in Figure 7-3a from the seismic shear results. Because the resolution of the seismic shear test is approximately 2.5 ft, the smaller diameter chimneys (approximate 1 ft) are averaged with the competent rock resulting in dry unit weights of approximately 90.5 pcf (1450 kg/m³) as a result of the averaging (2.5 ft vs. 1 ft chimneys). The shaft hole was filled 30' with asphalt waste material, Figure 7-11b. After 1 hour, the hole was redrilled to 50 ft and cleaned with a clean out bucket and no loss of circulation occurred, Figure 7-11c. The slurry properties were measured every 10 ft of drilling and are summarized in Table 7-5 (met the requirements of FDOT 455-15.8.1). Next, the steel rebar cage with threaded rebar was placed with 4" side spacers utilized to align the cage vertically. The cage was rotated until the center of the West shaft aligned with the east shaft and the threaded rods were perpendicular to the girders (Figure 7-12). A total of 17 cubic yards of concrete was pumped into the East shaft (Note, 12.3 cubic yards needed for a 3 ft x 47 ft deep borehole, or 38% volume increase). Table 7-6 summarizes the measured compressive strength (ASTM C39/C39M-20) of concrete specimens for the East shaft. The measured slump values are the same as the West shaft, shown in Table 7-7.



(a)



(b)

Figure 7-11. Sinkholes that opened during the East shaft construction: (a) 12 in chimney sinkhole opened at 45ft depth near the East shaft; (b) filling the East shaft with asphalt waste (rap) to plug the chimney sinkhole alongside the shaft and (c) another sinkhole at 15' depth in wall of the East shaft

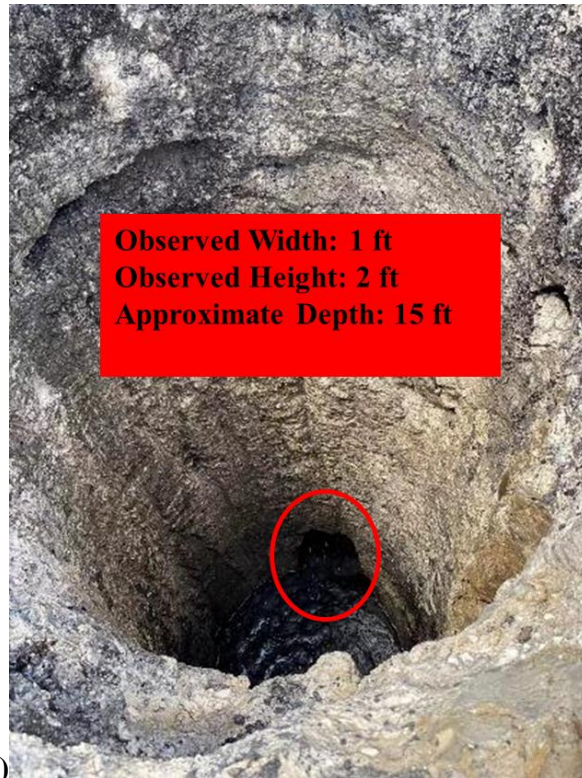


Figure 7-11. Sinkholes that opened during the East shaft construction: (a) 12” chimney sinkhole opened at 45ft depth near the East shaft; (b) filling the east shaft with asphalt waste (rap) to plug the chimney sinkhole alongside the shaft and (c) another sinkhole at 15’ depth in wall of the East shaft



Figure 7-12. Completed construction of the East shaft: (a) cage spacer installations and (b) leveling both shafts

Table 7-5. Measured range of properties of bentonite slurry for East shaft

Properties	Measured	Range Specified in FDOT Specification: 455-15.8.1 (65°F)
Density, pcf	64 ~ 66	64 ~ 73
Viscosity, Seconds	32 ~ 38	30 ~ 40
pH	9 ~ 10	8 ~ 11
Sand Content	0.5%	≤4%

Table 7-6. Measured compressive strength of concrete specimens for East shaft

Days	Compressive Strength, psi
14	4145
21	7034
28	6975

Table 7-7. Measured properties of concrete for East shaft

Properties	Measured	Range specified in 346
Slump, in	9.25 ~ 9.5	7 ~ 10

7.2.2. Construction of the Load Test Frame

The load test system consisted of two drilled shafts (3 ft × 47 ft), Support System (SMO Stands), Reaction System (15 ft William Threaded Rods, GR 50 C channels and bearing plates), two Acosta type “A” Girders, load spreader, hydraulic jack, load cell, measuring system and 24 in thickness steel representing the footing. For the construction of the load test, an 8,000 lbs telescopic forklift, a 40 ft man lift, and a 60 ton crane were rented. The Ocala limestone layer had to be excavated to the depth of 5 ft which resulted in a 5 ft thick layer (from 5 ft to 10 ft depth) to meet the planned load test, Figure A-3. FDOT maintenance provided a track hoe and an operator to dig a 5 ft deep × 7 ft wide × 10 ft long excavation for the footing placement, Figure 7-13. Following excavation, soil filled voids were found at multiple locations and upon accounting for their areas at the surface (20.8 ft²/25 ft²), a REC_{adjusted} of 83% was estimated,

which agreed with the average REC from boring B4 (80.75%) and B5 (82.67%). The top of rock surface depth varies up to 5 ft at a small amount horizontal distance (1 ft), which validates the contour of the top rock surface depth in Figure 7-1. Researchers then mixed and placed a 1 in thick fast-setting concrete seal layer on the rock surface to level and fill any small voids, etc., in rock surface, Figure 7-14. Note, the concrete seal layer is poured in a wood form, so no side friction effect occurred the interface between concrete and rock.

Prior to the construction of the load test system, researchers leveled the top of both shafts (wood shims) by total station and measuring rods. With the help of SMO drilling crew, the stands and the 15 ft long threaded rods were installed, Figure 7-15. One of the 5 ft × 5 ft road plate was then placed on the top of fast-setting concrete to provide a guide for installing the girder's load spreader. Next, the 40 ft long Acosta girders were lifted by the crane and set on the top of stands and wrapped with two 3,333 lb heavy-duty ratchet straps to prevent toppling. With the crane holding the girders along with straps, the SMO drilling crew installed two sets of C channels and bearing plates with nuts at each end of girders. After the girders were securely attached to underlying drilled shafts, the pyramid load spreader was installed beneath the girders and positioned center to center with the road plate with four steel channels and four threaded rods installed by the forklift. Next, two 5 ft × 5 ft road plates were placed on the top of the single bottom road plate and then three 12 in tall steel channels (4 ft x 4 ft in plan view) were placed on top of the road plates. Finally, three 3 in thick square steel plates were set on the top of steel channels with the length and width of the square plates reduced by 6 in with each addition, Figure 7-16b. In total, 24 in thick steel was used to represent the footing. Since the seal of the 1000 ton SMO hydraulic jack cracked and leaked during setup, a 500 ton hydraulic was borrowed from Applied Foundation Testing (AFT) for the load test. The new hydraulic jack had

a stroke (travel distance) of 13 in. The hydraulic jack and load cell were subsequently placed between the footing and load spreader by the forklift, Figure 7-15. Finally, the measuring system, composed of an auto level, four 5 ft long PVC pipes inserted into four 5 in by 5 in base plates and a measuring tape attached to the middle of jack, Figure 7-16 were placed. The four base plates were situated at the corners of the 5 ft by 5 ft steel plates and measuring tape was attached to the top of each PVC pipe. Researchers also measured the stroke movement of the jack as well as the distance between the bottom of the girders and the top of the 5 ft × 5 ft road plate after the test to validate the tape measurements from the hydraulic jack and the four corners. The completed construction of the load test setup at the Bell site is shown in Figure 7-15.



Figure 7-13. Footing location excavation (circles identify soil-filled voids)



Figure 7-14. One in concrete leveling pad for placement of the steel foundation elements



(a)



(b)

Figure 7-15. Construction of the load test: (a) excavation of 5 ft of overlying topsoil and placement of stands with threaded rods and (b) placement of steel plates, steel box sections, jack, and load cell



(a)



(b)

Figure 7-16. Measuring system: (a) auto-level to measure vertical deformations of the foundation and (b) four corner and center vertical scales to measure vertical deformations: 1, front left (FL); 2, front right (FR); 3, hydraulic jack, middle (courtesy of AFT); 4, rear left (RL); 6, rear right (RR)

7.3. Bearing Capacity

The shallow foundation load test was completed in 3 ½ hours using 20 tons load increments and 80 ton load decrements. Each load increment was maintained for 10 minutes with deformation measurements occurring after application of each load step and prior to placement of the next load step (i.e., creep). A peak load of 860 kips with vertical movement of 2 in was observed during loading and a permanent settlement at the center of the footing of 1.5 in was measured when the load was removed. Figure 7-17 presents the load-settlement response at the four corners (Figure 7-16b – locations 1, 2, 4 and 6) and at the center of the footing (Figure 7-16b – location 3). Evident, the SW corner – location 6 (Figure 7-16b) underwent the largest total settlement and the NE corner – location 1 (Figure 7-16b) underwent the least settlement. Drawing two tangents (black dashed lines) to the footing settlement at the center (location 3, Figure 7-17) with the first tangent to initial loading and the second tangent at the peak deformation, their intercept results in a bearing resistance of 14.8 tsf.

Phase I Florida Bearing Capacity equations are shown in Eqs. 2-7 through 2-18, which requires the strength parameters (c , ϕ , ω , p_p) and the modulus ratio between the competent rock layer and weathered limestone layer to account for the reduction in Bearing Capacity (General Shear vs. Punching Shear). The mass strength parameters (Table 7-9) are derived from the intact strength envelope (Table 7-8) constructed by triaxial tests with two confining stresses (50 psi and 600 psi), the 105 pcf Ocala limestone strength envelope used with a $REC_{adjusted} = 83\%$ and a cohesion intercept (c) of 48 psi, a friction angle (ϕ) of 30° , and a second slope angle (ω) of 19.7° . The rock over sand reduction factor is required for a modulus ratio between two layers, the E_i (obtained from 50 psi confining stress triaxial tests) for rock is shown in Table 7-1 ($E_m = 0.6 E_i$ with 83% $REC_{adjusted}$, Figure 5-31). The Bowles's Method (Bowles, 1996) to predict the modulus

of saturated sand shown in Eq. 3-9 is used to estimate the modulus of the weak layer (also used in load test at SR-84 Site), the SPT-N value at the nearest boring B3 (Figure C-3) is 39 which results in a modulus of 1,950 psi. The predicted 2 layer bearing capacity is 16.04 tsf, which compares favorably to the measured capacity of 14.8 tsf (detailed calculation in shown in Table 7-10).

Similar to the second load test (Figure 7-18), it is believed that the footing underwent a punching shear failure of the rock into the underlying weathered rock/sand layer at a load of approximately 370 tons (14.8 tsf), as indicated in Figure 7-17 by the intersection of the two linear trend lines. The modulus of rock at the initial loading is 18 times higher than the modulus of the weathered limestone layer, which controlled the stiffer initial load-settlement response; however, after punching shear failure occurs, the lower modulus of the weathered limestone zone controls the load-settlement response. In addition, for this load test, tension cracks at various locations opened in the ground surface approximately 60 ft from the center of the footing, shown in Figure 7-19.

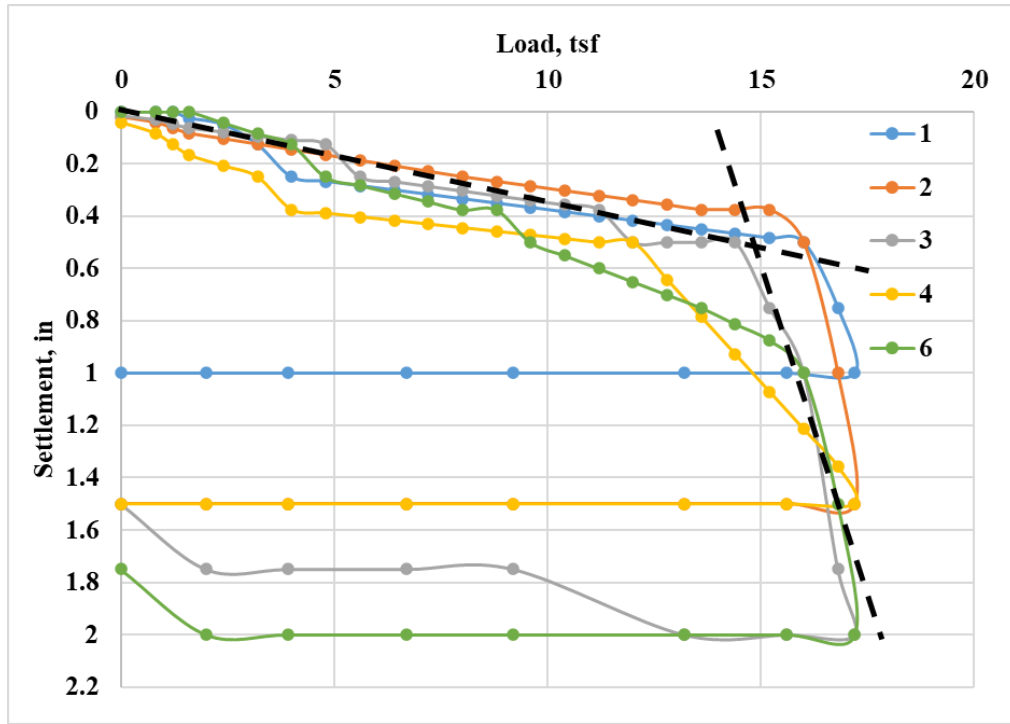


Figure 7-17. Measured load test results and bearing capacity at Bell site

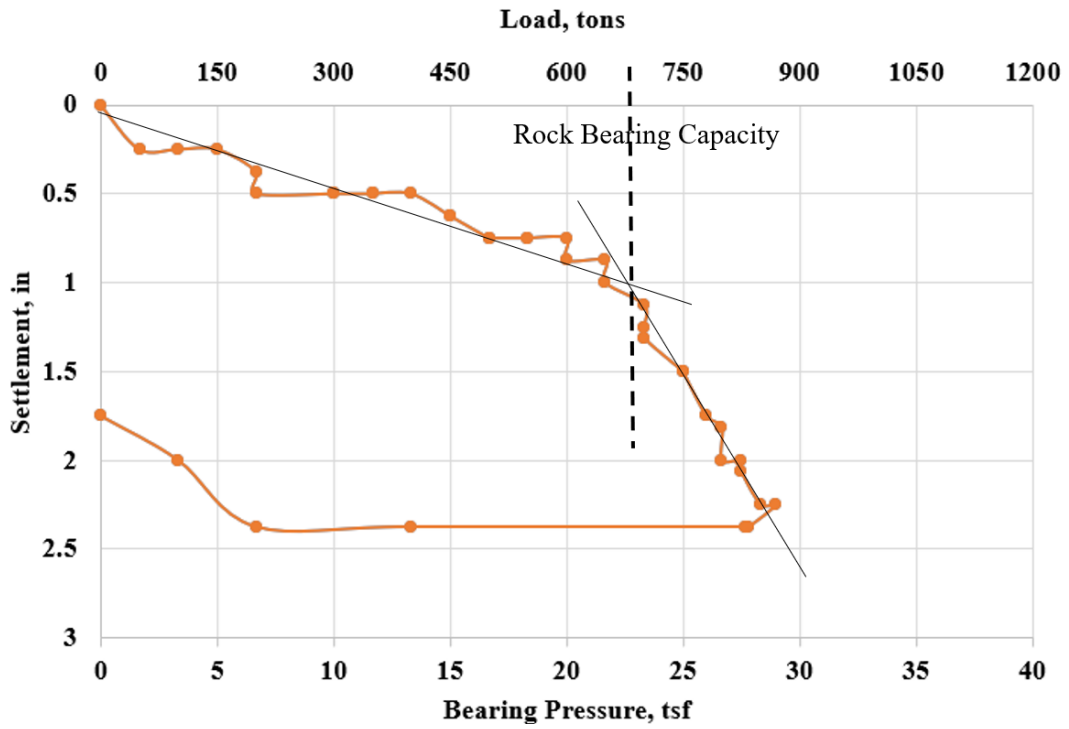


Figure 7-18. Measured results at SR-84 site, second load test

Table 7-8 Intact and mass strength envelope conversion

Point	p, psi	q, psi	Note
1A	0	50	From Figure 7-6
2B	251.5	201.5	
3C	1,178.5	578.5	
1a	0	50×0.83=41.5	REC _{adjusted} × q
2b	251.5	201.5×0.83=167.3	
3c	1,178.5	578.5×0.83=480.1	

Table 7-9 Intact strength versus mass strength properties

	τ-σ space			p-q space			
	c, psi	φ, °	ω, °	a, psi	α, °	P _p , psi	β, °
Intact properties	62.7	37	24	50	31	251.5, P(2B) from Table 7-8	22.1
Note	Intact properties from Table 2-2						
Mass properties	48	30	19.7	41.5	26.6	251.5, P(2b) from Table 7-8	18.7
Note	$\frac{a}{\cos\phi} = \frac{41.5}{\cos(30)} = 48$	$\text{asin}(\tan\alpha) = \text{asin}(0.5) = 30^\circ$	$\text{asin}(\tan\beta) = \text{asin}(0.3375) = 19.7^\circ$	From Table 7-8: $a = q(1a) = 41.5$, $\tan(\alpha) = \frac{q(2b)-q(1a)}{p(2b)} = \frac{167.3-41.5}{251.5} = 0.5$, $\alpha = \text{atan}(0.5) = 26.6^\circ$, $\tan(\beta) = \frac{q(3c)-q(2b)}{p(3c)-p(2b)} = \frac{480.1-167.3}{1178.5-251.5} = 0.3375$, $\beta = \text{atan}(0.3375) = 18.7^\circ$			

Table 7-10 Bearing capacity calculation at Bell site

Footing Geometry	B, ft	5
	L, ft	5
	D _f , ft	5
	T, ft	5
Mass Properties	c, psi	48
	φ, °	30
	P _p , psi	251.5
	ω, °	19.7
	E _{sand} /E _{mass}	E _{sand} /E _{mass} = 1950/36000 (median) = 0.054
Florida Bearing Capacity Equations	N _c	$\frac{1.8 \cos \phi}{0.8 - \sin \phi} = \frac{1.8 \cos (30)}{0.8 - \sin (30)} = 5.19$ (Equation 2-14)
	N' _c	$\frac{1.8 \cos \phi}{0.8 - \sin \omega} = \frac{1.8 \cos (30)}{0.8 - \sin (19.7)} = 3.37$ (Equation 2-15)
	N _γ	$\frac{1.8 [\sin \phi - \sin \omega]}{0.8 - \sin \omega} = \frac{1.8 [\sin (30) - \sin (19.7)]}{0.8 - \sin (19.7)} = 0.632$ (Equation 2-16)
	q, psi	3 (D _f) × 80/144 = 2.78 (Equation 2-17, overburden stress)
	N _q	$(1.5 \times \frac{p_p}{\sigma_a} - 10) \times (3 \times \sin \phi - 1) = (1.5 \times \frac{251.5}{14.7} - 10) \times (3 \times \sin (30) - 1) = 8.03$ (Equation 2-18)
	R	$0.093T^2 E_{soil} / E_{rock} = 0.093T^2 E_{sand} / E_{mass} = 0.093 \times 5^2 \times (0.054) = 0.13$ (Equation 2-13)
	N _R	$0.86 * R^{-0.25} = 0.86 \times 0.13^{-0.25} = 1.44$ (Equation 2-12)
	n	$\left(\frac{4}{0.3B \text{ in ft}}\right)^{-0.055} = \left(\frac{4}{0.3 \times 5}\right)^{-0.055} = 0.95$ (Equation 2-10)
	ξ	$1 + 0.245 \left(\frac{B}{L}\right)^{0.66} = 1 + 0.245 \left(\frac{5}{5}\right)^{0.66} = 1.245$ (Equation 2-11)
	Qu1, psi	$ncN_c + qN_q = 0.95 \times 48 \times 5.19 + 2.78 \times 8.03 = 258.4$ (Equation 2-8)
	Qu2, psi	$n[cN'_c + p_p N_\gamma] + q * N_q = 0.95 \times [48 \times 3.37 + 251.5 \times 0.632] + 2.78 \times 8.03 = 326.1$ (Equation 2-9)
	Qu	$\min (Q_{u1}, Q_{u2}) \times \xi / N_R = \min(258.4, 326.1) \times 1.245 / 1.44 = 222.8 \text{ psi} = 16.04 \text{ tsf}$ (Equation 2-7)



Figure 7-19 Tension cracks after load test

7.4. Load-settlement Response

7.4.1. Finite Element Modeling

Finite element modeling was performed using PLAXIS 3D to identify if an elastic-plastic stress-strain model of the rock could replicate the load-settlement response of the footing. The Finite Element model is shown in Figure 7-20. Again, the subsurface layering from MWD was used (Figure 7-2), and the dry unit weight of each layer was based on the seismic shear results (Figure 7-3). The strength parameters (c and ϕ in the Mohr-Coulomb Model) were obtained from the strength envelope based on dry unit weight, shown in Figure 7-6. The initial tangent

modulus (E_i), presented in Figure 7-7, is developed using Table 7-1 which is based on dry unit weights. However, the initial tangent moduli of the rock and sand layer were only used up to rock failure. As reported in Chapter 2 (triaxial results, Figure 2-1, the rock's stress-strain response is bilinear and a function of confining stress, stress/strain level, stress path, loading history, etc. Therefore, as the overlying layer of the rock yields/fails, and punching occurs, a new secant modulus of the rock must be employed, which is a function of strain. Considering a serviceability limit of 2" (commonly used in many states) and a 5 ft thick rock layer, a strain (2"/60") of 3.33% will develop. Using the latter strain and the stress-strain response, the secant moduli based on dry unit may be found as shown in Figure 7-7.

Table 7-11 summarizes the dry unit weight, strength, and stiffness parameters used in the FEM analysis of each layer. The first layer is 5 ft thick with an approximate dry unit weight of 80 pcf, which is based on the seismic shear results (Figure 7-3). However, 40 pcf is used in the simulation due to the dished shape excavation (Figure 7-13). The next layer (2nd, bottom of footing) is 5 ft thick and characterized with a 105 pcf strength envelope with $REC_{adjusted} = 83\%$. The third layer is the 2 ft thick weathered limestone layer. Beneath the weathered limestone zone, is a weak 5 ft thick 95 pcf (80% $REC_{adjusted}$) rock layer, followed by an 18 ft thick rock layer (85 pcf Ocala limestone with 80% $REC_{adjusted}$ is estimated from the Boring B5 and seismic shear test).

The FEM simulation results are shown in Figure 7-21, and compared to the measured response. Evident, the simulation replicated the field response up to the final load and displacement of 2". Shown in Figure 7-22 is the shear stress contour at the bearing capacity stress (14.8 tsf,) as well as the developed punching failure (black dash lines starting at the footing edge extending straight downward through the red zones), which indicates the block failure of

the overlying rock. The weathered limestone zone beneath the rock layer continues to carry more load but generates greater settlements (moduli – 22 times smaller).

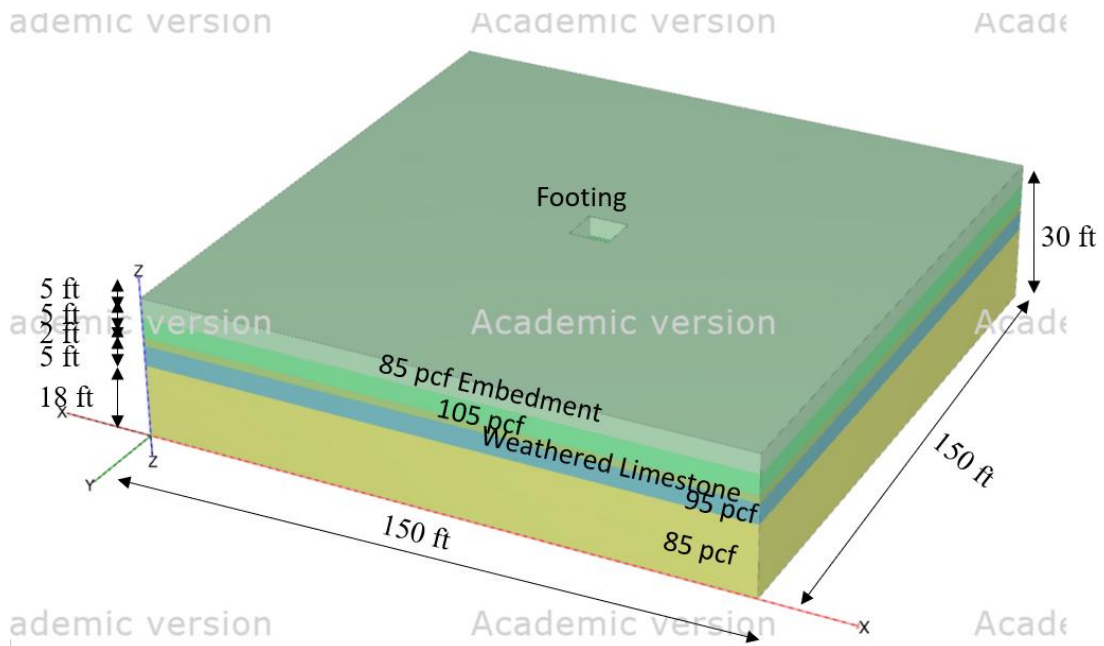


Figure 7-20. Finite element modeling for Bell load test

Table 7-11. Layering and parameters used in FEM

Layer	γ_{dt} , pcf	Thickness, ft	Material	Material Model	c, psi	ϕ , °	μ	Young's Modulus, psi
1	40	5	Ocala Limestone	Mohr-Coulomb	6.6	19.8	0.1	20,967
2	105	5	Ocala Limestone	Mohr-Coulomb	56.3	27.8	0.1	36,000 ~ 9,000
3	80	2	Weathered Limestone	Mohr-Coulomb	0	20	0.2	1,950 ~ 250
4	95	5	Ocala Limestone	Mohr-Coulomb	19.5	24	0.1	34,877
5	85	18	Ocala Limestone	Mohr-Coulomb	6.6	19.8	0.1	20,967

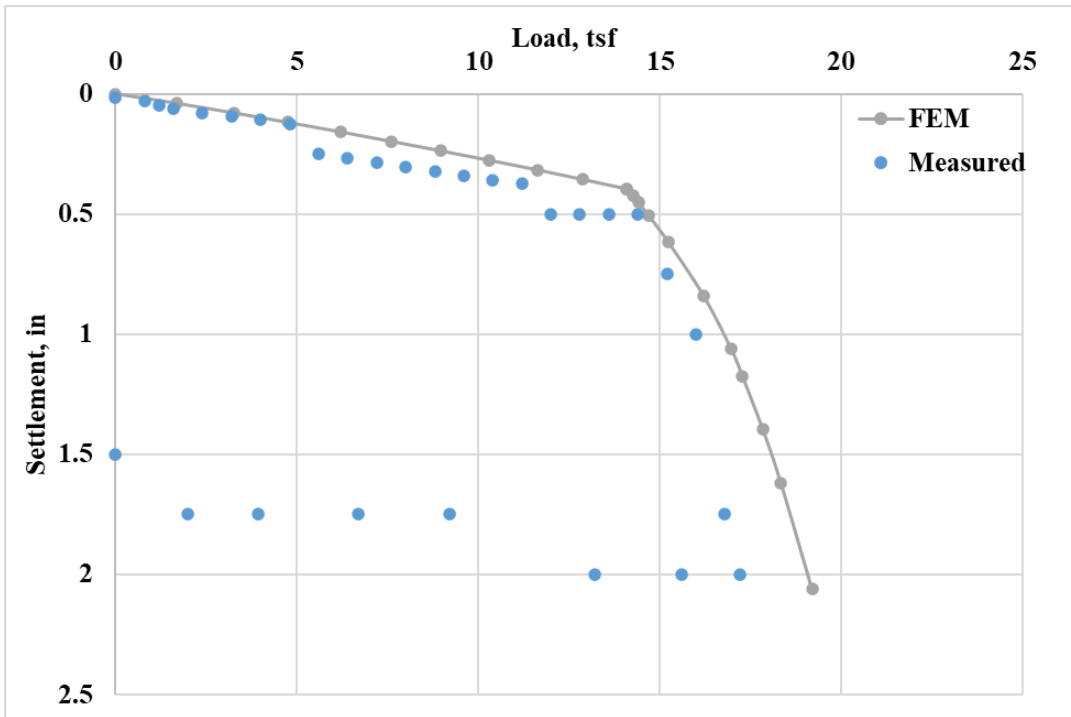


Figure 7-21. Measured vs. predicted load-settlement response

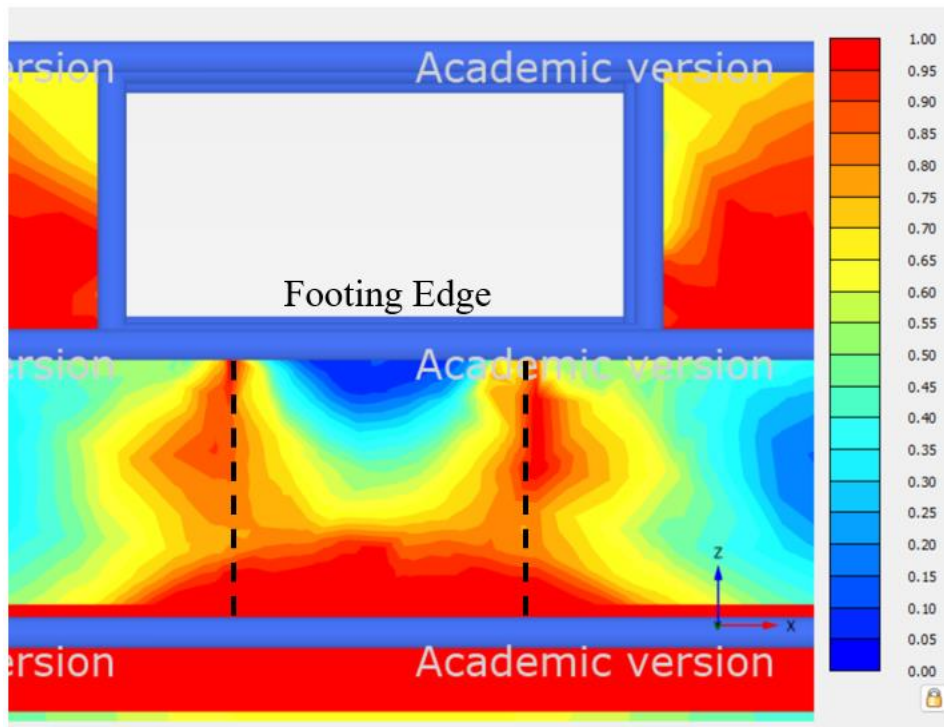


Figure 7-22. Relative shear stress contour at the bearing stress of 14.8 tsf

7.4.2. Burmister Method

For Burmister Method, Eq. 3-10 is used, where δ is the footing settlement, p is the bearing stress, r is half of the footing width, and E_2 is the weak layer modulus. The parameter F is the deflection factor obtained from the modulus ratio: E_1/E_2 (strong/weak) and the ratio of rock thickness to r (half of the footing width) using the chart shown in Figure 3-5. It is evident that as the modulus ratio or the rock layer thickness increases, more of the load is shed to the strong layer and the settlement decreases. However, with a high moduli ratio, the bearing capacity equation (see Eqs. 2-7, 2-12, and 2-13) will result in a reduced bearing stress whereas a thicker rock layer will increase the bearing capacity (10 ft rock thickness - 23 tsf bearing capacity at SR-84 vs. 5 ft rock thickness, 15 tsf bearing capacity at Bell).

Similar to the FEM analysis, the Burmister Method used 36,000 psi as the mass initial modulus of the overlying rock until the bearing capacity was reached and then the modulus of the rock layer was reduced to 9,000 psi to reflect the secant modulus under 2% strain. The Burmister's solution is presented in Table 7-12 and plotted in Figure 7-23, indicates good agreement with the measured load-settlement response, both pre and post bearing failure.

Table 7-12 Burmister’s calculations for rock over sand case (Bell)

	p, contact stress, tsf	Figure 3-5			Settlement, in
	0	$\frac{h}{r} \left(\frac{r}{\frac{B}{2}} \right)$ Table 7-10)	E_2/E_1 (E_{mass}/E_{sand})	F	0
Burmister	16.04 (Bearing stress, Table 7-10)	$\frac{5}{\left(\frac{5}{2}\right)} = 2$	$36000/1950 = 18.5$ (See Table 7-10)	0.25	$\frac{1.18pa}{E_2} F = \frac{1.18 \times 16.04 \times 12 \times 2.5 \times 0.25}{\left(\frac{1950}{13.89 \text{ psi/tsf}}\right)} = 1.01$ (Equation 3-10)
	17.65* (Post bearing stress)	$\frac{5}{\left(\frac{5}{2}\right)} = 2$	$E_{mass, secant}^{**}/E_{sand} = 9000/1950 = 4.6$	0.41	$\frac{1.18pa}{E_2} F = \frac{1.18 \times 17.65 \times 12 \times 2.5 \times 0.41}{\left(\frac{1950}{13.89 \text{ psi/tsf}}\right)} = 1.82$ (Equation 3-10)

* $p = Q_u \times 1.1 = 16.04 \times 1.1 = 17.65$ tsf

** $E_{mass, secant} = E_{mass} \times \text{strain at yield} / \text{strain of interest} = 36000 \times 0.5\% (\text{yielding}) / 2\% = 9000$ psi.

7.4.3. Proposed FB-Multiplier (Winkler Model) Settlement of a Two-layer System

For a two-layer system, the elastic solution developed by Ueshita and Meyerhof (1967; Eq. 3-11) can provide a reliable estimation of mean settlement but an equivalent modulus is required. Fenton and Griffins (2005) indicate that the harmonic mean modulus is more conservative than the geomean modulus or arithmetic modulus in computing elastic settlements. They identify that the harmonic modulus is more reasonable for a strongly layered soil.

The two stage Winkler model (FB-Multiplier) incorporates Eq. 3-11 for load vs. deflection with stress weighted harmonic modulus, E_h , obtained from the rock and underlying soil from Eq. 3-12, where the rock modulus is E_i up to the bearing capacity and then the secant modulus (E_s) after the bearing capacity has been exceeded (same procedure with Section 6.4.3, Table 7-13). The predicted Winkler results vs. the measured value for the third load test is shown in Figure

7-23. When computing the equivalent modulus, the weak layer thickness was set to 10 ft rather than 2 ft. The semi-infinite space was assumed because 3B (B = footing width) is generally considered as the settlement influence zone of a footing (here 5 ft of rock and 10 ft of weak zone). Evident, the model performed well in predicting the full load vs. settlement (Figure 7-23).

Table 7-13 Winkler model calculations for rock-over-sand case (Bell)

FB-M	Bearing Stress, tsf	Figure 3-7		σ_i , tsf	h_i , ft	E_h , psi	Settlement, in
		0		$\frac{\sigma_{sand}}{p}$ (function of h/a and E_1/E_2)	For sand layer, take half of the σ_{sand}		$E_{sand} = 1950$ psi $E_{mass} = 36000$ psi $E_{mass,secant} = 9000$ psi
	16.04 (Bearing stress, Table 6-10)	Use h/a same values as h/r and E_1/E_2 same values as E_2/E_1 in Table 7-12	0.06	Rock**: 8.5	Rock: 5 ft	$E_h = \frac{\sum h_i \sigma_i}{\sum \frac{h_i \sigma_i}{E_i}} = \frac{5 \times 8.5 + 10 \times 0.48}{5 \times \frac{8.5}{36000} + 10 \times \frac{0.48}{1950}} = 12970$ (Equation 3-12)	$\frac{1.5pa}{E_h} = \frac{1.5 \times 16.04 \times 12 \times 2}{12970} = 0.77$ (Equation 3-11)
				Sand***: 0.48	Sand: 10 ft (3B depth)		
	17.65* (Post bearing stress)		0.16	Rock: $(0.16 \times 17.65 + 17.65)/2 = 10.23$	Rock: 5 ft	$E_h = \frac{\sum h_i \sigma_i}{\sum \frac{h_i \sigma_i}{E_{secant}}} = \frac{5 \times 10.23 + 10 \times 0.532}{5 \times \frac{10.23}{9000} + 10 \times \frac{0.532}{1950}} = 5051.3$ (Equation 3-12)	$\frac{1.5pa}{E_h} = \frac{1.5 \times 17.65 \times 12 \times 2}{5051.3} = 2.18$ (Equation 3-11)
				Sand: $0.16 \times 17.65/2 = 1.41$	Sand: 10 ft (3B depth)		

* $p = Q_u \times 1.1 = 16.04 \times 1.1 = 17.65$ tsf

$E_{mass,secant} = E_{mass} \times \text{strain at yield} / \text{strain of interest} = 36000 \times 0.5\% (\text{yielding}) / 2\% = 9000$ psi.

** σ_1 at the center of the rock layer = $(\sigma_{top} + \sigma_{bottom})/2 = (p + \sigma_{sand})/2 = (16.04 + 16.04 \times 0.06)/2 = 8.5$ tsf

*** σ_2 at the center of the sand layer = $(\sigma_{top} + \sigma_{bottom})/2 = (\sigma_{sand} + 0)/2 = (16.04 \times 0.06 + 0)/2 = 0.48$ tsf

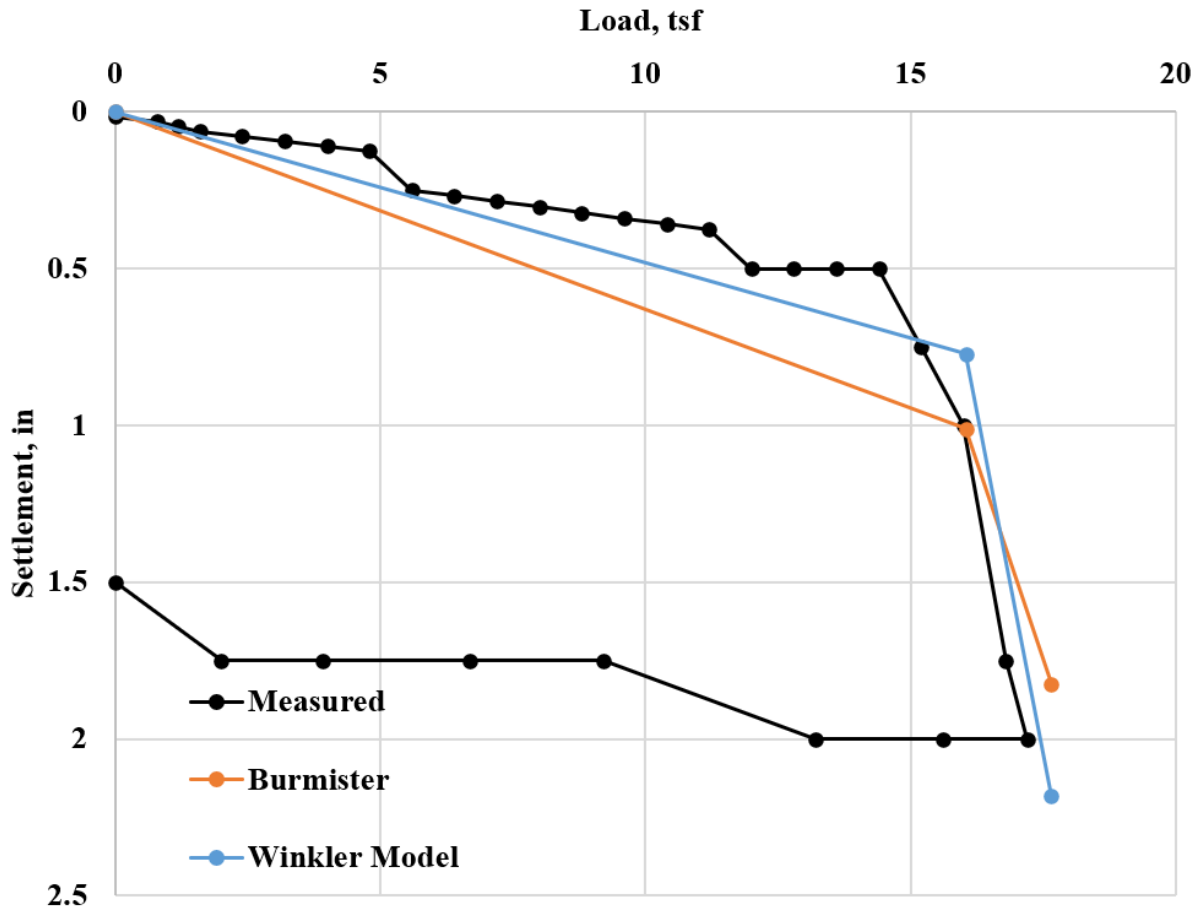


Figure 7-23. Measured vs. Winkler model vs. Burmister's solution: load settlement response (Bell)

Chapter 8

Comparison of FEM, Burmister, and Winkler Model Settlement Predictions for Shallow Foundations in Florida Limestone

8.1. Introduction

Of great interest is load-settlement response of larger footings that would be used under bridge piers. Several shallow foundations (chapter 6) have been designed and constructed under bridge piers (e.g., I-75 and I-595). Typical footing sizes have ranged from 10 ft to 20 ft (B) with L/B ratios between 1 and 2 and embedment from 5 ft to 10 ft. Since, the measured load tests were simulated reasonably well [Cemex – 3.5 ft × 3.5 ft SR-84 – 5ft × 6 ft and Bell – 5 ft × 6 ft], the FEM, Burmister and Winkler will be used in a parametric study of the larger footings.

8.2. Parametric Studies

As discussed in chapters 6 & 7, it is common to see a rock overlying a sand or weak layer. To characterize multiple layers, Burmister (Equation 3-10), Winkler Model, (Equation 3-11 to 3-12) and nonlinear Finite Element Model may be used. For Burmister & Winkler the predictions will be linear up to bearing defined by Equations 2-7 to 2-18 using an initial modulus, E_i , and a secant modulus, E_s (defined at 2% strain) after onslaught of yield. Similarly, the FEM employs a bilinear stress-strain curve for the rock and the sand.

The parametric study (64 simulations in total) used typical values encountered in Phase I & II: footing sizes - 6 ft and 16 ft (width B), L/B ratios = 1 and 2, embedment depth of 0 to 8 ft, rock layer thickness (T) = 3 to 16 ft, rock dry unit weight of 100 pcf and 110 pcf as well as the sand modulus of both loose and dense, Table 8-1. The rock dry unit weight is selected as 100 pcf to 110 pcf based on values from three load tests (97 pcf for Cemex, 110 pcf for SR-84 and 106

pcf for Bell). The strength parameters of the rock are from Table 2-2, along with strength envelope using a $REC_{adjusted} = 80\%$ and moduli from Figure 3-1 a. based on the dry unit weight and are summarized in Table 8-2 As stated earlier, E_i was from the 50 psi confining stress triaxial tests, the Poisson's ratio was 0.1 and E_s , the secant modulus at 2% axial strain. The sand layer modulus is 800 psi for loose and 2,500 psi for dense sand, Table 8-3. Note, as the rock thickness increases, the thickness of sand layer in the finite element model and Equation 3-12 has to increase to account for the larger influence zone in the sand layer, Table 8-4 (T is rock thickness, B is footing width) to minimize the influence of the boundary.

The L/B ratio also has a strong influence on the load-settlement response (i.e., load superposition), as reported by Umashankar and Sekar (2015) from PLAXIS 3D of footings on 2-layer soils with linear elastic perfect plastic model. Their settlement factor [ratio of settlement for $L/B = 2$ to $L/B=1$] is summarized in Table 8-5, for the rock thickness/ half footing width in the range of 1 to 2, and the rock modulus/sand modulus ratio between 10 to 100. Evident, the footing with an $L/B = 2$ has 1.4 to 1.6 times higher settlement than the square footing.

Table 8-1 Variables for parametric study

Embedment Depth (H), ft	0	B/2
Footing Width (B), ft	6	16
L/B	square	2
Rock Thickness (T), ft	B/2	B
Rock Dry Unit Weight, pcf	100	110
Sand Modulus, psi	800	2500

Table 8-2 Rock properties for parametric study: (a) 100 pcf and (b) 110 pcf

(a)

	τ-σ space			p-q space			
	c, psi	φ, °	ω, °	a, psi	α, °	P _p , psi	β, °
Intact properties	47.6	47.75	0.54	32	36.51	308	0.54
Note	Intact properties from Table 2-2						
Mass properties	31.77	36.31	0.43	25.6	30.63	308	0.43
Note	$\frac{a}{\cos\phi} = \frac{25.6}{\cos(36.31)} = 31.77$	asin(tanα)= asin(0.5922)= 36.31°	asin(tanβ)= asin(0.0076)= 0.43°	q×REC _{adjusted}			
E _m , psi	36588 (E _i , Figure 3-1a)×0.55(E _m /E _i , Figure 5-31) = 20123 psi		E _m , secant	20123×0.005/0.02 = 5031 psi			

(b)

	τ-σ space			p-q space			
	c, psi	φ, °	ω, °	a, psi	α, °	P _p , psi	β, °
Intact properties	68.7	47.9	7.7	46	36.6	392	7.6
Note	Intact properties from Table 2-2						
Mass properties	45.7	36.4	6.1	36.8	30.7	392	6.1
Note	$\frac{a}{\cos\phi} = \frac{36.8}{\cos(36.4)} = 45.7$	asin(tanα)= asin(0.5938)= 36.4°	asin(tanβ)= asin(0.1069)= 6.1°	q×REC _{adjusted}			
E _m , psi	64828 (E _i , Figure 3-1a)×0.55(E _m /E _i , Figure 5-31) = 35655 psi		E _m , secant	35655×0.005/0.02 = 8914 psi			

Table 8-3 Sand properties for parametric study

Sand	γ , pcf	E_{sand} , psi	μ	ϕ , °	ψ , °
Loose	100	800	0.25	30	20
Dense	120	2500	0.35	38	28

Table 8-4 Rock thickness versus model depth

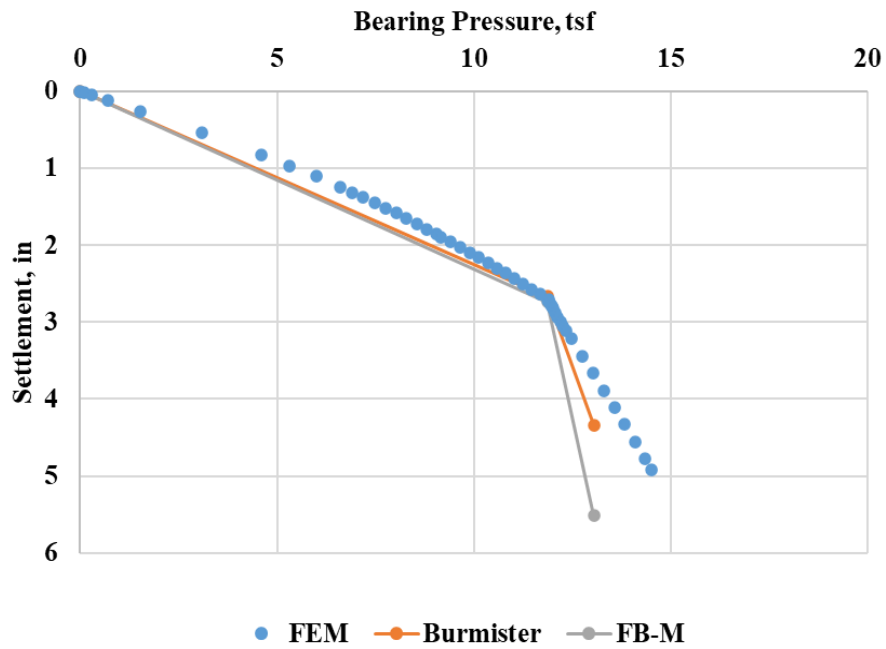
T/(B/2)	Model depth, ft	Note
1	2B	
2	3B	Bell
3	4B	
4	5B	SR84

Table 8-5 The settlement ratio of footings with L/B =2 to 1 (square)

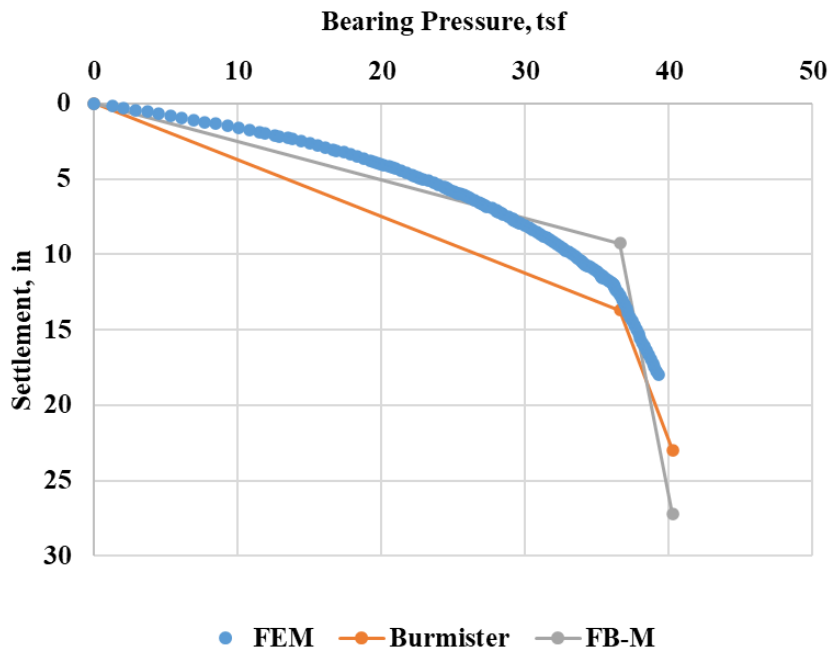
T/(B/2)	E_r/E_{sand}	100	90	80	70	60	50	40	30	20	10
1	Factor	1.61	1.58	1.55	1.53	1.51	1.49	1.48	1.47	1.46	1.45
2		1.61	1.56	1.52	1.49	1.48	1.46	1.45	1.44	1.43	1.42

8.3. Results of Parametric Studies

Figure 8-1 shows the FEM, Burmister, and Winkler predictions for a range of different footing widths and shapes, embedment depths, rock thickness, rock dry unit weights and sand moduli. Note, the influence of rock layer thickness (a vs. b) on bearing capacity, and modulus of the sand (loose - c vs. dense - d) on deformations. Also evident, the secant modulus captures very well the bi-linear FEM response for the two-layer case under multiple geometries and properties. Figure 8-2 presents a comparison of the results of the parametric study (settlement up to punching of the rock); the maximum error between any of the methods (FEM, Burmister, and Winkler) is less than 12%.

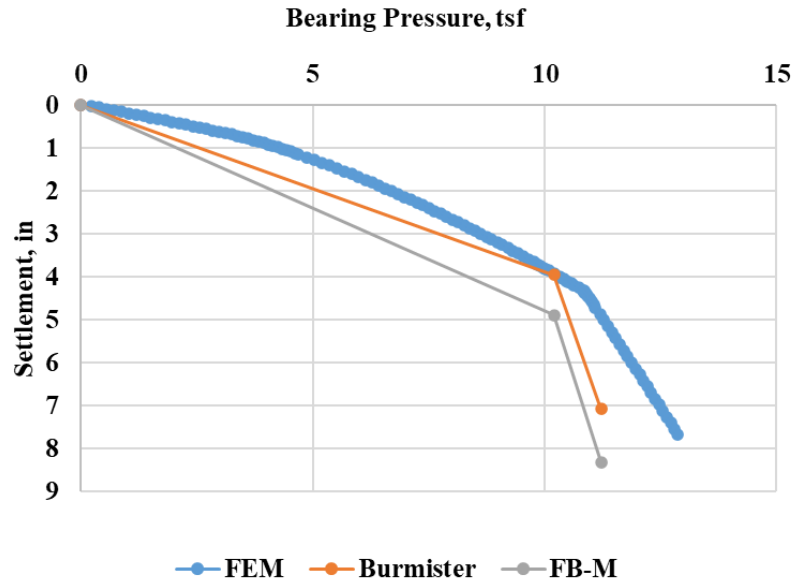


(a)

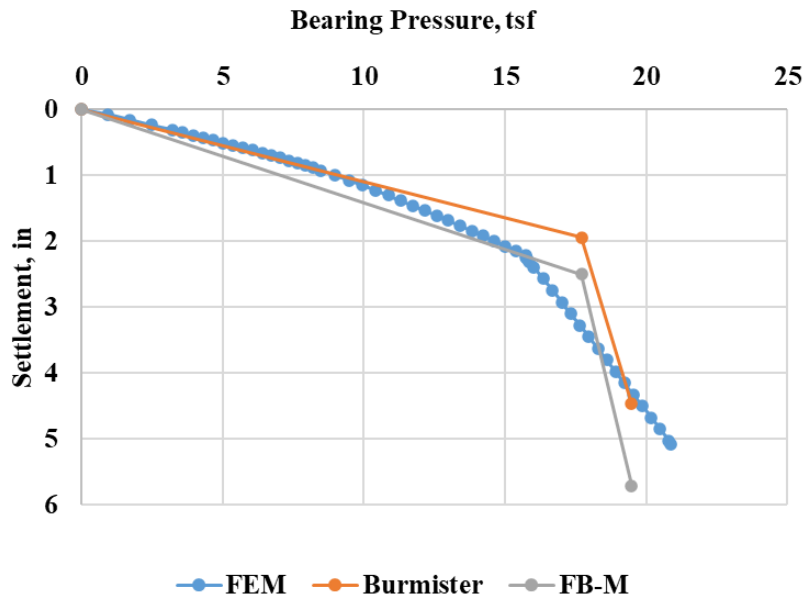


(b)

Figure 8-1 Representative cases: (a) 3 ft rock thickness, 110 pcf, B = 6 ft, square footing, no embedment, loose sand; (b) 16 ft rock thickness, 110 pcf, B = 16 ft, square footing, 8 ft embedment, loose sand

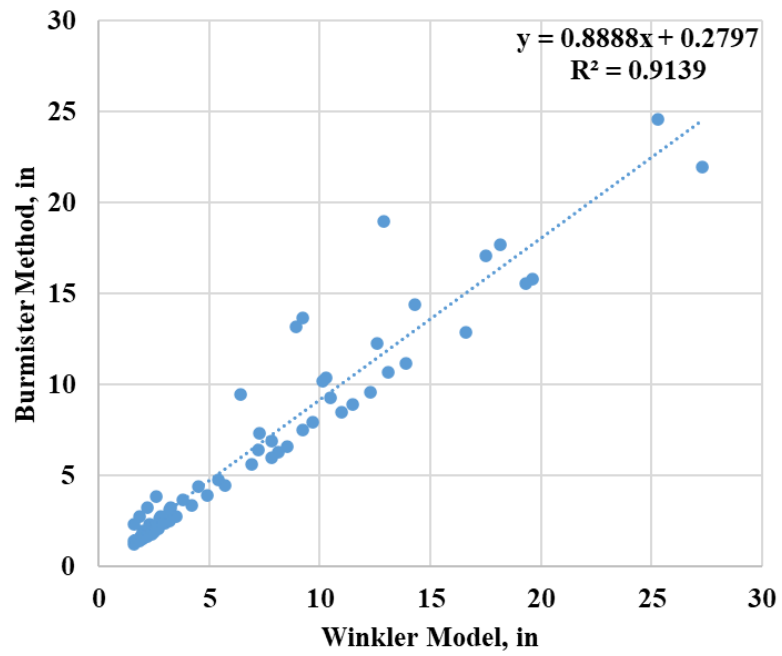


(c)

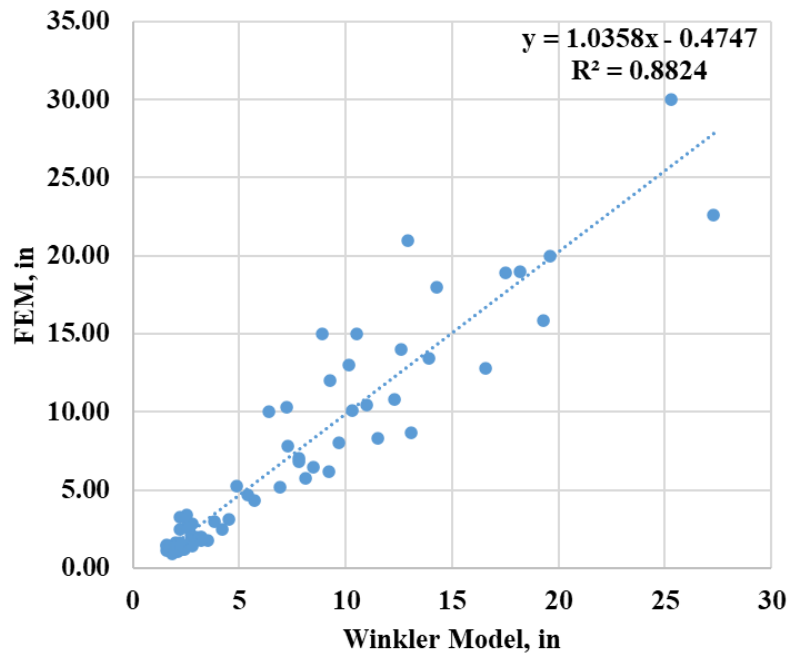


(d)

Figure 8-1 Representative cases: (a) 3 ft rock thickness, 110 pcf, B = 6 ft, square footing, no embedment, loose sand; (b) 16 ft rock thickness, 110 pcf, B = 16 ft, square footing, 8 ft embedment, loose sand; (c) 3 ft rock thickness, 100 pcf, B = 6 ft, L/B = 2, 3 ft embedment, loose sand; (d) 6 ft rock thickness, 100 pcf, B = 6 ft, L/B = 2, 3 ft embedment, dense sand



(a)



(b)

Figure 8-2 Parametric study between Burmister, Winkler, and Finite element models (settlement up to rock failure)

Chapter 9

Worked Examples: Bearing Capacity and Load-settlement response

This chapter provides worked hand solutions for bearing capacities and load vs. settlement for two of Chapter 8 parametric study footings, and two other footings using rock properties near downtown Miami (heterogeneous) and Fort Lauderdale (i.e., rock over sand).

9.1. Two Cases in Parametric Study

Presented in this section is the hand solution to the bearing capacities and settlements for the load-settlement response (Phase III proposed Winkler – FB-MultiPier) for the rock over sand cases in Figure 8-1 (a) and (c). The Florida bearing capacity equations from Chapter 2, shown in Equation 2-3 to 2-18, requires the mass strength parameters (c , p_p , ϕ , ω , Table 8-2). For settlement, the Winkler (bi-linear) model, Equation 3-11 from Ueshita and Meyerhof (1967) is used with the stress-dependent weighted harmonic mean modulus, Equation 3-12 (recommended by Fenton and Griffiths, 2002 and 2005) with the stress-strain response (Figure 3-1a, for E_i and E_s), and thickness of each layer and interface stress from Figure 3-7.

The rock and sand properties used in the examples can be found in Table 8-2 and Table 8-3. For case (a), the footing, 6 ft by 6 ft, resides on 3 ft thick 110 pcf Miami limestone overlying a loose sand layer. The bearing capacity calculation is shown in Table 9-1; note, the initial modulus ($E_i = 35,655$ psi) is used for the bearing capacity of rock layer prior to punching shear and the secant modulus ($E_s = 8,914$ psi) is used after the rock failure. The E_s used here is at 2% strain from 50 psi triaxial tests. For the load-settlement response, based on the rock thickness(T)/half to footing width (B) ($3 \text{ ft}/3 \text{ ft}=1$) and the modulus ratio before and after rock

failure ($35655/800 = 44.57$ and $8914/800 = 11.14$), the ratios interface stress/bearing stress are 0.11 and 0.28, respectively, Table 9-3. Equation 3-11 is employed to estimate settlement by using the equivalent modulus, Equation 3-12 with 3 ft cap rock (h_1) overlying 9 ft loose sand layer (h_2), resulting in 2.74 in of settlement at punching shear failure and 5.51 in settlement after rock failure as shown in Figure 8-1a, for FB-M (FB-MultiPier). Table 9-2 presents the Burmister's solution for case (a) using Equation 3-10 and Figure 3-5, for 2.67 in of settlement at punching shear failure and 4.33 in of settlement for post bearing stress; both showed good agreement with Winkler model results.

For case (c), the footing, 6 ft by 12 ft is embedded 3 ft and resides over 3 ft of 100 pcf Miami limestone underlain by a loose sand layer. Like case (a), the bearing capacity calculation is shown in Table 9-4. For the load-settlement response, based on the rock thickness (T)/half of footing width (B), ($3 \text{ ft}/3 \text{ ft} = 1$) and the modulus ratio before and after rock failure ($20124/800 = 25.15$ and $5031/800 = 6.28$), the ratios of interface stress/bearing stress are 0.18 and 0.35, respectively, Table 9-6. For case of $L/B = 2$, it is recommended to use shape factor of 1.5 based on Table 8-5 (i.e., $1.5 \times$ settlement obtained from Equation 3-11). Using the equivalent modulus from Equation 3-11 with 3 ft cap rock (h_1) overlying 9 ft loose sand layer (h_2), results in 4.89 in settlement at rock punching shear and 8.31 in of settlement after rock failure as shown Figure 8-1c, FB-M (FB-MultiPier). Table 9-5 presents the Burmister's solution for the case (c) using Equation 3-10 and Figure 3-5 for 3.95 in of settlement at punching shear failure and 7.08 in of settlement for post bearing stress; both settlements showed good agreement with Winkler model results.

Table 9-1 Bearing capacities for case a

Footing Geometry	B, ft	6
	L, ft	6
	D _f , ft	0
	T, ft	3
Mass Properties	c, psi	45.7 (Table 8-2b)
	φ, °	36.4 (Table 8-2b)
	P _p , psi	392 (Table 8-2b)
	ω, °	6.1 (Table 8-2b)
	E _{sand} /E _{mass}	E _{sand} /E _{mass} = 800/35655 (Table 8-2b) = 0.0224
Florida Bearing Capacity Equations	N _c	$\frac{1.8 \cos \phi}{0.8 - \sin \phi} = \frac{1.8 \cos (36.4)}{0.8 - \sin (36.4)} = 7.03$ (Equation 2-14)
	N' _c	$\frac{1.8 \cos \phi}{0.8 - \sin \omega} = \frac{1.8 \cos (36.4)}{0.8 - \sin (6.1)} = 2.09$ (Equation 2-15)
	N _γ	$\frac{1.8 [\sin \phi - \sin \omega]}{0.8 - \sin \omega} = \frac{1.8 [\sin (36.4) - \sin (6.1)]}{0.8 - \sin (6.1)} = 1.26$ (Equation 2-16)
	q, psi	0 (Equation 2-17, overburden stress)
	N _q	$(1.5 \frac{p_p}{\sigma_a} - 10)(3 \sin \phi - 1) = (1.5 \times \frac{392}{14.7} - 10) \times (3 \times \sin (36.4) - 1) = 23.5$ (Equation 2-18)
	R	$0.093 T^2 E_{soil} / E_{rock} = 0.093 T^2 E_{sand} / E_{mass} = 0.093 \times 3^2 \times (0.0224) = 0.019$ (Equation 2-13)
	N _R	$0.86 \times R^{-0.25} = 0.86 \times 0.019^{-0.25} = 2.32$ (Equation 2-12)
	n	$\left(\frac{4}{0.3B \text{ in ft}}\right)^{-0.055} = \left(\frac{4}{0.3 \times 6}\right)^{-0.055} = 0.96$ (Equation 2-10)
	ξ	$1 + 0.245 \left(\frac{B}{L}\right)^{0.66} = 1 + 0.245 \left(\frac{6}{6}\right)^{0.66} = 1.245$ (Equation 2-11)
	Qu1, psi	$ncN_c + qN_q = 0.96 \times 45.7 \times 7.03 + 0 = 307.6$ (Equation 2-8)
	Qu2, psi	$n[cN'_c + p_p N_\gamma] + q \cdot N_q = 0.96 \times [45.7 \times 2.09 + 392 \times 1.26] + 0 = 565.8$ (Equation 2-9)
	Qu	$\min(Q_{u1}, Q_{u2}) \times \xi / N_R = \min(307.6, 565.8) \times 1.245 / 2.32 = 164.8 \text{ psi} = 11.9 \text{ tsf}$ (Equation 2-7)

Table 9-2 Burmister solution for case a

	p, contact stress, tsf	Figure 3-5			Settlement, in
	0	$h/r \left(\frac{r}{\frac{B}{2}} \right)$, Table 9-1)	E_2/E_1 (E_{mass}/E_{sand})	F	0
Burmister	11.9 (Bearing stress, Table 9-1)	$\frac{3}{\left(\frac{6}{2}\right)} = 1$	$35655/800 = 44.56$ (See Table 9-1)	0.305	$\frac{1.18pa}{E_2} F = \frac{1.18 \times 11.9 \times 12 \times 3 \times 0.305}{\left(\frac{800}{13.89 \text{ psi/tsf}}\right)} = 2.67$ (Equation 3-10)
	13* (Post bearing stress)	$\frac{3}{\left(\frac{6}{2}\right)} = 1$	$E_{mass, secant}^{**}/E_{sand} = 8914/800 = 11.14$	0.45	$\frac{1.18pa}{E_2} F = \frac{1.18 \times 13 \times 12 \times 3 \times 0.45}{\left(\frac{1100}{13.89 \text{ psi/tsf}}\right)} = 4.33$ (Equation 3-10)

* $p = Q_u \times 1.1 = 11.9 \times 1.1 = 13 \text{ tsf}$

** $E_{mass, secant} = E_i$ (Table 9-1) \times strain at yield/strain of interest = $35655 \times 0.5\%$ (yielding)/ $2\% = 8914 \text{ psi}$.

Table 9-3 Winkler model for case a

FB-M	Bearing Stress, tsf	Figure 3-7		σ_i , tsf	h_i , ft	E_h , psi	Settlement, in
	0			$\frac{\sigma_{sand}}{p}$ (function of h/a and E_1/E_2)		For sand layer, take half of the σ_{sand}	
11.9 (Bearing stress, Table 9-1)	Use h/a same values as h/r and E_1/E_2 same values as E_2/E_1 in Table 9-2	0.11	Rock**:	6.59	Rock: 3 ft	$E_h = \frac{\sum h_i \sigma_i}{\sum \frac{h_i \sigma_i}{E_i}} = \frac{3 \times 6.59 + 9 \times 0.65}{3 \times \frac{6.59}{35655} + 9 \times \frac{0.65}{8914}} = 3246$ (Equation 3-12)	$\frac{1.5pa}{E_h} = \frac{1.5 \times 11.9 \times 12 \times 3}{\left(\frac{3246}{13.89 \text{ psi/tsf}}\right)} = 2.74$ (Equation 3-11)
			Sand***:	0.65	Sand: 9 ft (2B depth)		
13* (Post bearing stress)	Use h/a same values as h/r and E_1/E_2 same values as E_2/E_1 in Table 9-2	0.28	Rock:	$(0.28 \times 13 + 13)/2 = 8.32$	Rock: 3 ft	$E_h = \frac{\sum h_i \sigma_i}{\sum \frac{h_i \sigma_i}{E_{secant}}} = \frac{3 \times 8.32 + 9 \times 1.82}{3 \times \frac{8.32}{35655} + 9 \times \frac{1.82}{8914}} = 1776$ (Equation 3-12)	$\frac{1.5pa}{E_h} = \frac{1.5 \times 13 \times 12 \times 3}{\left(\frac{1776}{13.89 \text{ psi/tsf}}\right)} = 5.51$ (Equation 3-11)
			Sand:	$0.28 \times 13/2 = 1.82$	Sand: 9 ft (2B depth)		

* $p = Q_u \times 1.1 = 11.9 \times 1.1 = 13$ tsf

$E_{mass,secant} = E_i$ (Table 9-1) \times strain at yield/strain of interest = $35655 \times 0.5\%$ (yielding)/2% = 8914psi.

** σ_1 at the center of the rock layer = $(\sigma_{top} + \sigma_{bottom})/2 = (p + \sigma_{sand})/2 = (11.9 + 11.9 \times 0.11)/2 = 6.59$ tsf

*** σ_2 at the center of the sand layer = $(\sigma_{top} + \sigma_{bottom})/2 = (\sigma_{sand} + 0)/2 = (0.11 \times 11.9 + 0)/2 = 0.65$ tsf

Table 9-4 Bearing capacities for case c

Footing Geometry	B, ft	6
	L, ft	12
	D _f , ft	3
	T, ft	3
Mass Properties	c, psi	31.8 (Table 8-2a)
	φ, °	36.3 (Table 8-2a)
	P _p , psi	308 (Table 8-2a)
	ω, °	0.43 (Table 8-2a)
	E _{sand} /E _{mass}	E _{sand} /E _{mass} = 800/20124 (Table 8-2a) = 0.04
Florida Bearing Capacity Equations	N _c	$\frac{1.8 \cos \phi}{0.8 - \sin \phi} = \frac{1.8 \cos (36.3)}{0.8 - \sin (36.3)} = 6.98$ (Equation 2-14)
	N' _c	$\frac{1.8 \cos \phi}{0.8 - \sin \omega} = \frac{1.8 \cos (36.3)}{0.8 - \sin (0.43)} = 1.83$ (Equation 2-15)
	N _γ	$\frac{1.8 [\sin \phi - \sin \omega]}{0.8 - \sin \omega} = \frac{1.8 [\sin (36.3) - \sin (0.43)]}{0.8 - \sin (0.43)} = 1.33$ (Equation 2-16)
	q, psi	3 (D _f) × 100/144 = 2.08 (Equation 2-17, overburden stress)
	N _q	$(1.5 \frac{P_p}{\sigma_a} - 10)(3 \sin \phi_j - 1) = (1.5 \times \frac{308}{14.7} - 10) \times (3 \times \sin (36.3) - 1) = 16.6$ (Equation 2-18)
	R	$0.093T^2 E_{soil} / E_{rock} = 0.093T^2 E_{sand} / E_{mass} = 0.093 \times 3^2 \times (0.04) = 0.033$ (Equation 2-13)
	N _R	$0.86 \times R^{-0.25} = 0.86 \times 0.033^{-0.25} = 2.01$ (Equation 2-12)
	n	$\left(\frac{4}{0.3B \text{ in ft}}\right)^{-0.055} = \left(\frac{4}{0.3 \times 6}\right)^{-0.055} = 0.96$ (Equation 2-10)
	ξ	$1 + 0.245 \left(\frac{B}{L}\right)^{0.66} = 1 + 0.245 \left(\frac{6}{12}\right)^{0.66} = 1.16$ (Equation 2-11)
	Qu1, psi	$ncN_c + qN_q = 0.96 \times 31.8 \times 6.98 + 2.08 \times 16.6 = 246.9$ (Equation 2-8)
	Qu2, psi	$n[cN'_c + p_p N_\gamma] + qN_q = 0.96 \times [31.8 \times 1.83 + 308 \times 1.33] + 2.08 \times 16.6 = 481.8$ (Equation 2-9)
	Qu	$\min(Q_{u1}, Q_{u2}) \xi / N_R = \min(246.9, 481.8) \times 1.16 / 2.01 = 141.63 \text{ psi} = 10.2 \text{ tsf}$ (Equation 2-7)

Table 9-5 Burmister solution for case c

	p, contact stress, tsf	Figure 3-5			Settlement, in
	0	$h/r \left(\frac{r}{\frac{B}{2}} \right)$, Table 9-4)	E_2/E_1 (E_{mass}/E_{sand})	F	0
Burmister	10.2 (Bearing stress, Table 9-4)	$\frac{3}{\left(\frac{6}{2}\right)} = 1$	$20124/800 = 25.15$ (See Table 9-4)	0.35	$\frac{1.18paS_f}{E_2} F = \frac{1.18 \times 10.2 \times 12 \times 3 \times 0.35 \times 1}{\left(\frac{800}{13.89 \text{ psi/tsf}}\right)} = 3.95$ (Equation 3-10)
	11.2* (Post bearing stress)	$\frac{3}{\left(\frac{6}{2}\right)} = 1$	$E_{mass, secant}^{**}/E_{sand} = 5031/800 = 6.28$	0.57	$\frac{1.18paS_f}{E_2} F = \frac{1.18 \times 11.2 \times 12 \times 3 \times 0.57 \times 1}{\left(\frac{800}{13.89 \text{ psi/tsf}}\right)} = 7.08$ (Equation 3-10)

* $p = Q_u \times 1.1 = 10.2 \times 1.1 = 11.2$ tsf

** $E_{mass, secant} = E_i$ (Table 9-4) \times strain at yield/strain of interest = $20124 \times 0.5\%$ (yielding)/ $2\% = 5031$ psi.

Table 9-6 Winkler model for case c

FB-M	Bearing Stress, tsf	Figure 3-7		σ_i , tsf	h_i , ft	E_h , psi	Settlement, in
	0		Use h/a same values as h/r and E_1/E_2 same values as E_2/E_1 in Table 9-5	$\frac{\sigma_{sand}}{p}$ (function of h/a and E_1/E_2)		For sand layer, take half of the σ_{sand}	
10.2 (Bearing stress, Table 9-4)	0.18	Rock**: 6.018		Rock: 3 ft	2344.5 (Equation 3-12)	$E_h = \frac{\sum h_i \sigma_i}{\sum \frac{h_i \sigma_i}{E_i}} = \frac{3 \times 6.02 + 9 \times 0.92}{3 \times \frac{6.02}{20124} + 9 \times \frac{0.92}{5031}} = 2344.5$ (Equation 3-12)	$\frac{1.5paS_f}{E_h} = \frac{1.5 \times 10.2 \times 12 \times 3 \times 1}{\left(\frac{2344.5}{13.89 \text{ psi/tsf}}\right)} = 4.89$ (Equation 3-11)
		Sand***: 0.918		Sand: 9 ft (2B depth)			
11.2* (Post bearing stress)	0.35	Rock: (0.35×11.2 + 11.2)/2 = 7.56	Rock: 3 ft	1518 (Equation 3-12)	$E_h = \frac{\sum h_i \sigma_i}{\sum \frac{h_i \sigma_i}{E_{secant}}} = \frac{3 \times 7.56 + 9 \times 1.96}{3 \times \frac{7.56}{20124} + 9 \times \frac{1.96}{5031}} = 1518$ (Equation 3-12)	$\frac{1.5paS_f}{E_h} = \frac{1.5 \times 11.2 \times 12 \times 3 \times 1}{\left(\frac{1518}{13.89 \text{ psi/tsf}}\right)} = 8.31$ (Equation 3-11)	
		Sand: 0.35×11.2/2 = 1.96	Sand: 9 ft (2B depth)				

* $p = Q_u \times 1.1 = 10.2 \times 1.1 = 11.2$ tsf

$E_{mass,secant} = E_i$ (Table 9-4) \times strain at yield/strain of interest = $20124 \times 0.5\%$ (yielding)/2% = 5031 psi.

** σ_1 at the center of the rock layer = $(\sigma_{top} + \sigma_{bottom})/2 = (p + \sigma_{sand})/2 = (10.2 + 10.2 \times 0.18)/2 = 6.018$ tsf

*** σ_2 at the center of the sand layer = $(\sigma_{top} + \sigma_{bottom})/2 = (\sigma_{sand} + 0)/2 = (10.2 \times 0.18 + 0)/2 = 0.918$ tsf

9.2. Worked Examples: Single Layer and Rock-over-sand Cases

9.2.1. Single Layer Case

In this example, a 10 ft by 15 ft footing (embedded 3ft) is planned for a bridge pier located in downtown Miami. Given its location, Borings RC-1 and RC-2 from Cemex site are used as well as rock data from borings B-1 to B-3 from the SR-84 site which showed similar trends (dry unit

weight versus depth) as depicted in Figure 9-1 (Note: core runs not from same initial depth). Next, using the dry unit weights (Table 9-7), the Young's Modulus as a function of dry unit weight is estimated from Figure 3-1 using the gold trend line. This curve combines the 50-psi confining stress with q_u moduli for dry unit weights less than 90 pcf. Presented in Table 9-8 are the summary statistics of Table 9-7. The CV of dry unit weight (strength) is 0.11 but the CV of modulus is 1.43.

For estimation of bearing capacity of the footing, a representative set of strength parameters is required based on dry unit weight. A 10 ft wide footing generally has a bearing failure 1.5B to 2B below the bottom of footing. However, if a much stronger layer exists deeper, its' penetration may be limited from B to 1.5B (Button, 1953). Therefore, for this example, the rupture surface or bearing zone is limited to 1.5B (depths 3 to 18 ft). Using the dry unit weights within this zone (3-18 ft), a geomean of 97.5 pcf was estimated. Using the closest dry unit specimen strength envelope available (100 pcf -Table 2-2), an adjusted mass strength envelope, Figure 9-2 was developed based on the rock adjusted-recovery (80 %) as discussed.

First the shear values of the specimen strength envelope (100 pcf) in p-q space (q values of 1A, 2B, and 3C) of Figure 9-2 are each multiplied by the $REC_{adjusted}$ (shown in Table 9-9) and plotted in Figure 9-2, as 1a, 2b and 3c. Next, the slopes (α , β) and intercept (a) of mass strength envelope (1a, 2b, and 3c) are assessed, see Table 9-10 with equations. Subsequently, the strength envelope in τ , σ space is found by equations in Table 9-10 (c, psi, ϕ , and ω).

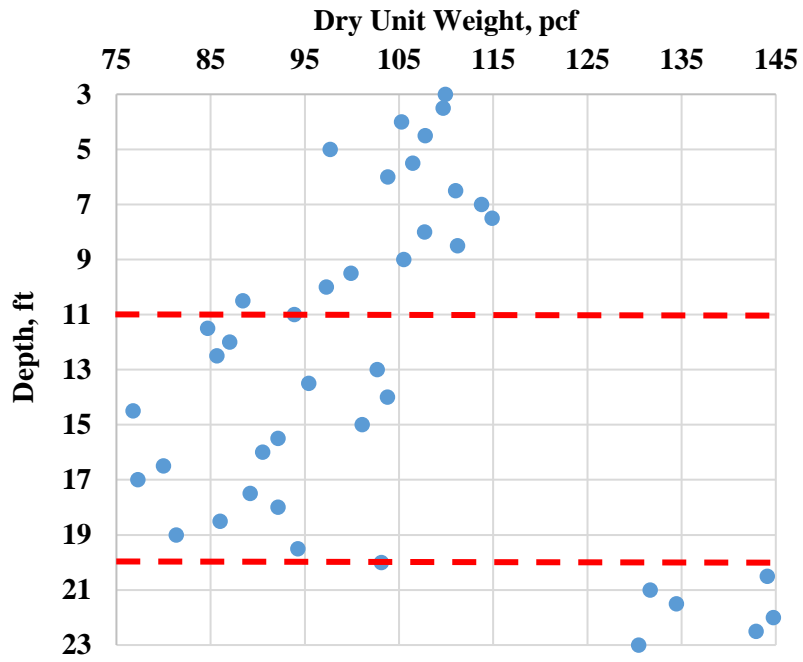


Figure 9-1 Dry unit weight versus depth: single layer case

Table 9-7 Dry unit weight and Modulus profile

Depth, ft	γ_{dt} , pcf	E_i , psi (Figure 3-1a, trendline)	Depth, ft (Continued)	γ_{dt} , pcf	E_i , psi (Figure 3-1a, trendline)
3	109.9	64526.7	13.5	95.4	28132.5
3.5	109.7	63698.1	14	103.8	45430.4
4	105.3	49513.1	14.5	76.8	9681.6
4.5	107.8	57158.5	15	101.1	38922.4
5	97.7	32064.1	15.5	92.2	23369.1
5.5	106.4	52911.9	16	90.5	21298.8
6	103.8	45497.0	16.5	80.0	11655.0
6.5	111.0	68679.2	17	77.3	9985.6
7	113.8	80455.5	17.5	89.2	19714.6
7.5	114.9	85690.2	18 (End of Bearing Layer)	92.2	23369.1
8	107.7	56922.2	18.5	86.0	16427.2
8.5	111.2	69468.0	19	81.4	12591.7
9	105.5	50115.8	19.5	94.3	26365.4
9.5	99.9	36389.5	20	103.1	43743.4
10	97.3	31352.6	20.5	144.1	455892.2
10.5	88.4	18869.8	21	131.7	223959.6
11	93.9	25782.5	21.5	134.5	262681.7
11.5	84.7	15248.0	22	144.8	473204.1
12	87.0	17421.1	22.5	142.9	425740.3
12.5	85.7	16125.3	23	130.4	208682.9
13	102.7	42706.4			

Table 9-8 Summary statistics

	γ_{dt} , pcf	E_i , psi
Count	31	41
Mean	98.2	81986.4
Geomean	97.5	44221.4
Harmonic Mean ($E_h = \frac{n}{\sum \frac{1}{E_i}}$)	96.9	29978.6
Median	99.9	42706.4
Standard Deviation	10.8	117358.8
CV	0.11	1.43

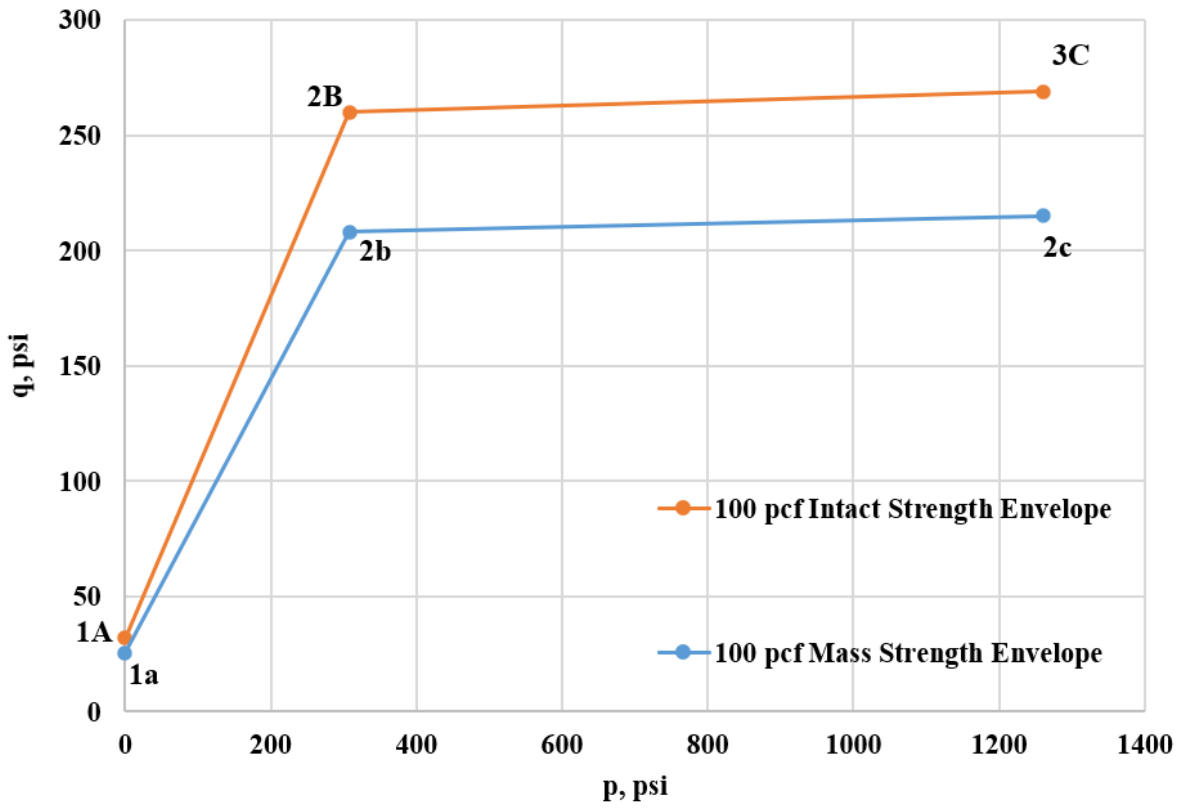


Figure 9-2 100 pcf intact and mass strength envelope

Table 9-9 Intact and mass strength envelope conversion

Point	p, psi	q, psi	Note
1A	0	32	From Table 2-2
2B	308	260	
3C	1260	269	
1a	0	32×0.8=25.6	REC _{adjusted} × q
2b	308	260×0.8=208	
3c	1260	269×0.8=215.2	

Table 9-10 Intact strength versus mass strength properties

	τ-σ space			p-q space			
	c, psi	φ, °	ω, °	a, psi	α, °	P _p , psi	β, °
Intact properties	47.6	47.75	0.54	32	36.51	308, P(2B) from Table 9-9	0.54
Note	Intact properties from Table 2-2						
Mass properties	31.77	36.31	0.43	25.6	30.63	308, P(2b) from Table 9-9	0.43
Note	$\frac{a}{\cos\phi} = \frac{25.6}{\cos(36.31)} = 31.77$	$\text{asin}(\tan\alpha) = \text{asin}(0.5922) = 36.31^\circ$	$\text{asin}(\tan\beta) = \text{asin}(0.0076) = 0.43^\circ$	From Table 9-9: $a = q(1a) = 25.6$, $\tan(\alpha) = \frac{q(2b)-q(1a)}{p(2b)} = \frac{208-25.6}{308} = 0.5922$, $\alpha = \text{atan}(0.5922) = 30.63^\circ$, $\tan(\beta) = \frac{q(3c)-q(2b)}{p(3c)-p(2b)} = \frac{215.2-208}{1260-308} = 0.0076$, $\beta = \text{atan}(0.0076) = 0.43^\circ$			

Next, knowing the mass strength properties of the 100 pcf rock from a depth of 3 ft to 18 ft, the bearing capacity of a 10 ft by 15 ft footing may be estimated, as shown in Table 9-11. First, the bearing capacity factors N_c , N_c' , N_q , and N_γ (see Table 9-11) are determined based on the mass angles of friction (ϕ , ω), along with overburden bearing stress, q (γD_f see Table 9-11). Next, the minimum bearing capacity (smaller of Q_{u1} and Q_{u2}) is found (depends on strength angles ϕ , ω), and shape factor ξ is found and combined ($Q_{u1} \times \xi$) to give the final bearing capacity of 300.4 psi (21.63 tsf) of the 10 ft by 15 ft footing.

Table 9-11 Bearing capacity calculations

Footing Geometry	B, ft	10
	L, ft	15
	D _f , ft	3
Mass Properties	c, psi	31.77 (Table 9-10)
	φ, °	36.31 (Table 9-10)
	P _p , psi	308 (Table 9-10)
	ω, °	0.43 (Table 9-10)
Florida Bearing Capacity Equations	N _c	$\frac{1.8 \cos \phi}{0.8 - \sin \phi} = \frac{1.8 \cos (36.31)}{0.8 - \sin (36.31)} = 6.98$ (Equation 2-14)
	N' _c	$\frac{1.8 \cos \phi}{0.8 - \sin \omega} = \frac{1.8 \cos (36.31)}{0.8 - \sin (0.43)} = 1.83$ (Equation 2-15)
	N _γ	$\frac{1.8 [\sin \phi - \sin \omega]}{0.8 - \sin \omega} = \frac{1.8 [\sin (36.31) - \sin (0.43)]}{0.8 - \sin (0.43)} = 1.33$ (Equation 2-16)
	q, psi	3 (D _f) × 100/144 = 2.08 (Equation 2-17, overburden stress)
	N _q	$(1.5 \times \frac{P_p}{\sigma_a} - 10) \times (3 \times \sin \phi - 1) = (1.5 \times \frac{308}{14.7} - 10) \times (3 \times \sin (36.31) - 1) = 16.64$ (Equation 2-18)
	n	$(\frac{4}{0.3B \text{ in ft}})^{-0.055} = (\frac{4}{0.3 \times 10})^{-0.055} = 0.98$ (Equation 2-10)
	ξ	$1 + 0.245 (\frac{B}{L})^{0.66} = 1 + 0.245 (\frac{10}{15})^{0.66} = 1.19$ (Equation 2-11)
	N _R	1 (Equation 2-12)
	Q _{u1} , psi	$n \times c \times N_c + q \times N_q = 0.98 \times 31.77 \times 6.98 + 2.08 \times 16.64 = 252.95$ (Equation 2-8)
	Q _{u2} , psi	$n \times [c \times N'_c + p_p \times N_\gamma] + q \times N_q = 0.98 \times [31.77 \times 1.83 + 308 \times 1.33] + 2.08 \times 16.64 = 494.51$ (Equation 2-9)
Q _u	$\min (Q_{u1}, Q_{u2}) \times \xi / N_R = \min (252.95, 494.51) \times 1.19 / 1 = 300.4$ psi = 21.63 tsf (Equation 2-7)	

In the case of settlements two approaches maybe considered. One approach is to further subdivide the rock into 3 layers (3 ft to 8 ft, 8 ft to 11 ft and 11 ft to 22 ft), due to the difference in dry unit weights. Then using the weighted (based on stress) harmonic mean modulus (each layer), Table 9-12, the load-settlement response may be predicted. Note, in the harmonic stress weighted modulus (Table 9-12), the ratio of stress/modulus of each sub-layer in the E_h calculation represents the settlement of each sublayer. For the stress in each sublayer, one must interpolate between square and strip, Figure 9-3. Finally, the weighted specimen harmonic

modulus of 35,124 psi is computed (Table 9-12), and the mass weighted harmonic modulus, E_{mass} is found

Table 9-12 Layering, modulus, and additional stress

Depth, ft	γ_{dt} , pcf (average)	h_i , ft	E_i , psi (Figure 3-1a, trendline, based on γ_{dt})	σ_i , psi (Figure 9-3, interpolated between strip and square footings)
3~11	105	8	48580.9	225.3
11~20	90.2	9	20863.3	108.9
20~23	138.1	3	322619.3	63.8
$E_h = \frac{\sum h_i \sigma_i}{\sum \frac{h_i \sigma_i}{E_i}} = \frac{(8 \times 225.3 + 9 \times 108.9 + 3 \times 63.8)}{(8 \times 225.3 / 48580.9 + 9 \times 108.9 / 20863.3 + 3 \times 63.8 / 322619.3)} = 35124.3 \text{ psi}$				

by multiplying specimen modulus, E_h , by mass/specimen ratio (0.55, Figure 5-31 and $REC_{adjusted}$),

$$E_{mass} = 0.55 \times 35,124 \text{ psi} = 19,318 \text{ psi}$$

Subsequently, the settlement of footing may be obtained from elastic theory as

$$\delta = \Delta q_s \frac{B S_f}{E_{mass}} 1.12(1 - \nu^2) = \frac{300.4 \times 10 \times 12 \times 1.12 \times 1.25 \times (1 - 0.01)}{19318.3} = 2.6 \text{ inches}$$

Where Δq_s = bearing stress 300.4 psi

B = footing width 10 ft

ν = Poisson's ratio = 0.1

S_f = shape factor = 1.25 for $L/B = 2$ (Table 8-5)

Even though the above approach does account for layering, it does not account the variability within any layer (see Figure 9-1). Fenton and Griffiths approach (Chapter 3) is the second approach employed for the problem; it uses the Geomean moduli of all rock data, as well as the CV of the moduli (assumed lognormal) to calculate the mean settlement as well as the differential settlement of the footing, as shown in Table 9-13a and b. Again, the mass modulus,

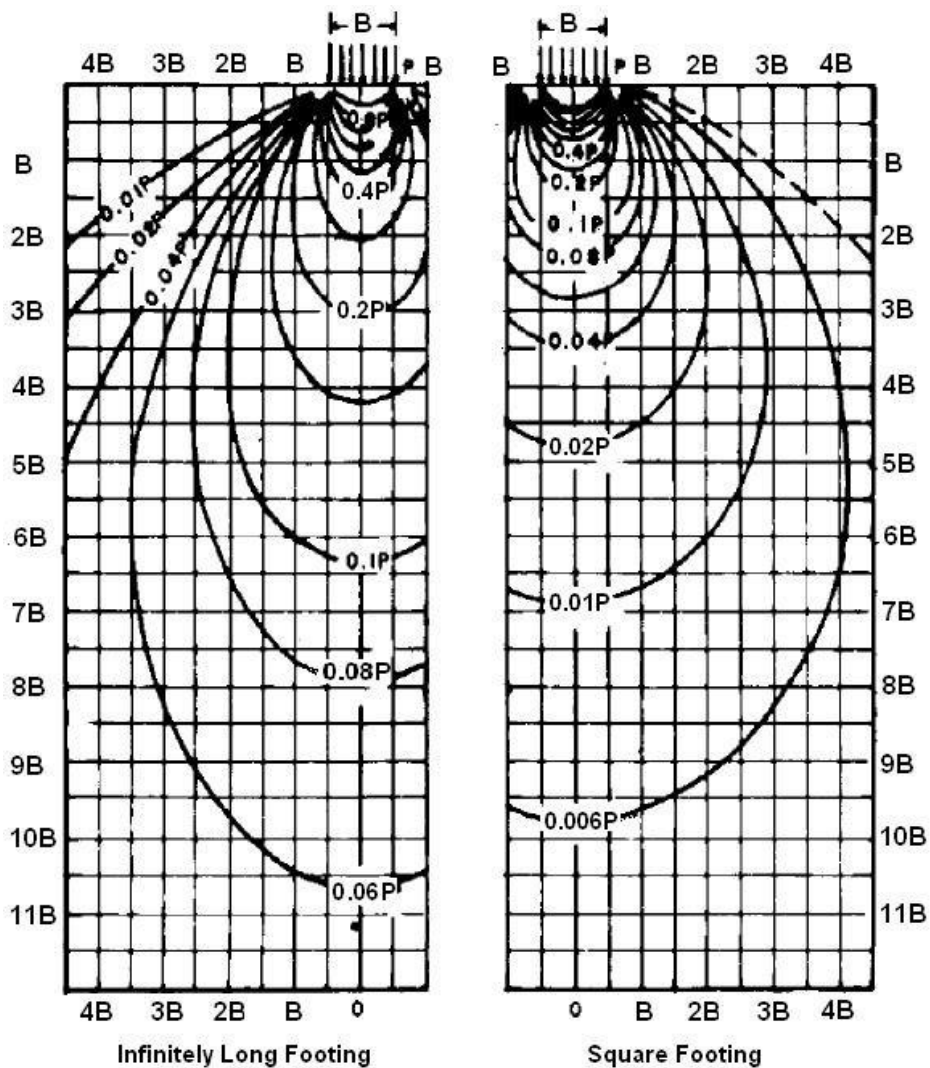


Figure 9-3 Boussinesq stress chart, interpolated between the strip and square footings (Lambe and Whitman, 1969)

Table 9-13b - the Geomean mass modulus, μ_E , is computed from the Geomean specimen modulus, 44221.4 psi (Table 9-8) times mass affects factor (Figure 5-31– 0.55) to give 24,321 psi. Table 9-13a, computes the expected variability ($\sqrt{\gamma(d_1, d_2)}$) of the standard deviation of the settlement, and Table 9-13b finds the both the final mean settlement, 3.74 in, and the standard deviation (differential) settlement, 1.1 in. All equations and values for the calculations are

shown in the tables. Evident, as identified by Fenton and Griffith, the lower estimate of settlement is the mean settlement minus the differential or 3.74 in – 1.1 in= 2.6 in. The latter agrees quite well with the sublayer approach described above, 2.6in. However, due to variability in each sublayer, it is very likely that if the placement of the footing was moved, that larger settlement would occur and mean value of 3.74 in is more representative, Figure 9-4.

Table 9-13 Load-settlement prediction calculation: $\sqrt{\gamma(B, T)}$ calculation

Parameter	Value or Calculation
$\gamma(h)$, ft	3 (Correlation Length)
B, ft	10 (Footing width)
T, ft	15 (Bearing layer thickness)
$\gamma(B)$ ($\gamma(d_1)$ in Equation 3-6)	$\left[1 + \left(\frac{B}{\gamma(h)}\right)^{\frac{3}{2}}\right]^{-\frac{2}{3}} = \left[1 + \left(\frac{10}{3}\right)^{\frac{3}{2}}\right]^{-\frac{2}{3}} = 0.27$ (Equation 3-6)
$\gamma(T)$ ($\gamma(d_2)$ in Equation 3-6)	$\left[1 + \left(\frac{T}{\gamma(h)}\right)^{\frac{3}{2}}\right]^{-\frac{2}{3}} = \left[1 + \left(\frac{15}{3}\right)^{\frac{3}{2}}\right]^{-\frac{2}{3}} = 0.19$ (Equation 3-6)
R_B (R_1 in Equation 3-6)	$\gamma(h) \left[\frac{\pi}{2} + \left(1 - \frac{\pi}{2}\right) \exp \left\{ -\left(\frac{B}{\frac{\pi}{2}\gamma(h)}\right)^2 \right\} \right] = 3 \left[\frac{\pi}{2} + \left(1 - \frac{\pi}{2}\right) \exp \left\{ -\left(\frac{10}{\frac{\pi}{2}3}\right)^2 \right\} \right] = 4.69$ (Equation 27)
R_T (R_2 in Equation 3-6)	$\gamma(h) \left[\frac{\pi}{2} + \left(1 - \frac{\pi}{2}\right) \exp \left\{ -\left(\frac{T}{\frac{\pi}{2}\gamma(h)}\right)^2 \right\} \right] = 3 \left[\frac{\pi}{2} + \left(1 - \frac{\pi}{2}\right) \exp \left\{ -\left(\frac{15}{\frac{\pi}{2}3}\right)^2 \right\} \right] = 4.71$ (Equation 3-6)
$\gamma(B T)$ ($\gamma(d_1 d_2)$ in Equation 3-6)	$\left[1 + \left(\frac{B}{R_T}\right)^{\frac{3}{2}}\right]^{-\frac{2}{3}} = \left[1 + \left(\frac{10}{4.71}\right)^{\frac{3}{2}}\right]^{-\frac{2}{3}} = 0.39$ (Equation 3-6)
$\gamma(T B)$ ($\gamma(d_2 d_1)$ in Equation 3-6)	$\left[1 + \left(\frac{T}{R_B}\right)^{\frac{3}{2}}\right]^{-\frac{2}{3}} = \left[1 + \left(\frac{15}{4.69}\right)^{\frac{3}{2}}\right]^{-\frac{2}{3}} = 0.28$ (Equation 3-6)
$\gamma(B, T)$ ($\gamma(d_1, d_2)$ in Equation 3-6)	$\frac{1}{2} [\gamma(B)\gamma(T B) + \gamma(T)\gamma(B T)] = \frac{1}{2} [0.27 \times 0.28 + 0.19 \times 0.39] = 0.075$ (Equation 3-6)
$\sqrt{\gamma(B, T)}$ ($\sqrt{\gamma(d_1, d_2)}$ in Equation 3-6)	$\sqrt{\gamma(B, T)} = \sqrt{0.075} = 0.27$ (Equation 3-6)

Table 9-9 (Continued) Load-settlement prediction calculation

Mass Properties	μ_E	Mass effect (Figure 5-37) $\times E_i$ (Table 2 Geomean) = $0.55 \times 44221.4 = 24321.8$
	σ_E	CV (Table 9-8) $\times \mu_E = 1.43 \times 24321.8 = 34780$
	ν	0.1 (Poisson's ratio)
	$\gamma(h)$, ft	3 (Correlation length)
Geometry	B, ft	10 (Footing width)
	T, ft	15 (Bearing layer thickness)
Fenton and Griffiths' method	δ_{det} , in	$\Delta q_s \frac{B}{\mu_E} 1.12(1 - \nu^2) = \frac{300.4 \times 10 \times 12 \times 1.12 \times (1 - 0.01)}{24321.8} = 1.64$ (Equation 3-1, $\Delta q_s = Q_u = 300.4$ psi, Table 9-11)
	σ_{lnE}	$\sqrt{\ln(1 + \sigma_E^2(above)/\mu_E^2(above))} =$ $\sqrt{\ln(1 + 34780^2/24321.8^2)} = 1.06$ (Equation 3-4)
	$\sqrt{\gamma(B, T)}$ (Table 7a)	0.27 (Table 9-13a)
	$\sigma_{ln\delta}$	$\sqrt{\gamma(B, T)}\sigma_{lnE}(above) = 0.27 \times 1.06 = 0.29$ (Equation 3-6)
	$\mu_{ln\delta}$	$\ln(\delta_{det}(above)) + \frac{1}{2}\sigma_{lnE}^2(above) = \ln(1.64) + \frac{1}{2}1.06^2 = 1.05$ (Equation 3-5)
	μ_δ , in	$\exp\left\{\mu_{ln\delta}(above) + \frac{1}{2}\sigma_{ln\delta}^2(above)\right\} = \exp(1.05 + \frac{1}{2}0.29^2) =$ 2.99 (Equation 3-7)
	σ_δ , in	$\mu_\delta(above)\sqrt{e^{\sigma_{ln\delta}^2(above)} - 1} = 2.99\sqrt{e^{0.29^2} - 1} = 0.88$ (Equation 3-8)
Settlement shape Factor (L/B= 1.5)		1.25 (Table 8-5)
Final μ_δ , in		Settlement shape factor $\times \mu_\delta = 1.25 \times 2.99 = 3.74$
Final σ_δ , in		Settlement shape factor $\times \sigma_\delta = 1.25 \times 0.88 = 1.1$

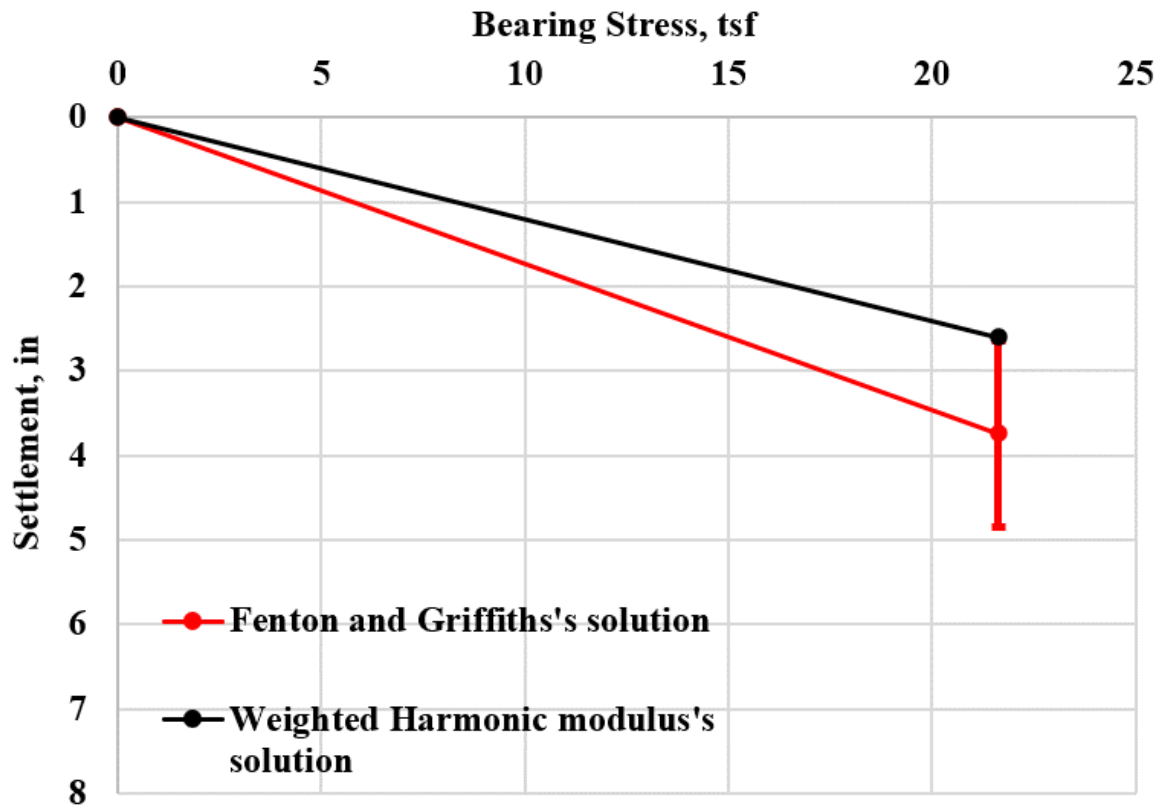


Figure 9-4 Load-settlement prediction of single layer case

9.2.2. Rock-over-sand Case

In this example, a 15 ft by 15 ft footing is planned to be embedded 3 ft in a 13-ft thickness Miami limestone layer overlying a medium dense sand layer. Figure 9-5 is a profile the rock's dry unit weight vs. depth (Fort Lauderdale area - combination of B1 to B3 borings from SR-84 site) with a $REC_{adjusted} = 75\%$ and Figure 9-6 is profile of the sand's SPT Blow count vs. depth. Table 9-14 presents rock dry unit weight (strength) and Young's Moduli within the rock layer. Again, Figure 3-1 was used to estimate the intact specimen Young's Modulus based on dry unit weight. Table 9-15 summarizes the statistics of dry unit weight, and Young's Moduli (E_i and E_{mass}). The mass Young's Modulus was obtained by multiplied the mass correction factor (0.45, Figure 5-31, $REC_{adjusted} = 75\%$) by the intact specimen Young's Modulus. The CV of the dry unit weight is 0.08 and the CV of the rock moduli is 0.66.

In estimating the bearing capacity of the footing, the 2-layer (rock over sand) equations are required. First, the mass strength parameters of the rock must be determined. Since the Geomean and median dry unit weight of the rock is similar (108 pcf, Table 9-15), the closest available intact specimen dry strength envelope, 105 pcf, and will be used to assess mass strength.

To obtain the strength parameter, the shear values of the specimen strength envelope (105 pcf) in p-q space (q values of 1A, 2B, and 3C) of Figure 9-7 are each multiplied by the $REC_{adjusted}$ (0.75 - shown in Table 9-16) and plotted in Figure 9-7, as 1a, 2b and 3c. Next, the slopes (α , β) and intercept (a) of mass strength envelope (1a, 2b, and 3c) are assessed, see Table 9-17 with equations. Subsequently, the strength envelope in τ , σ space is found by equations in Table 9-17 (c, psi, ϕ , and ω).

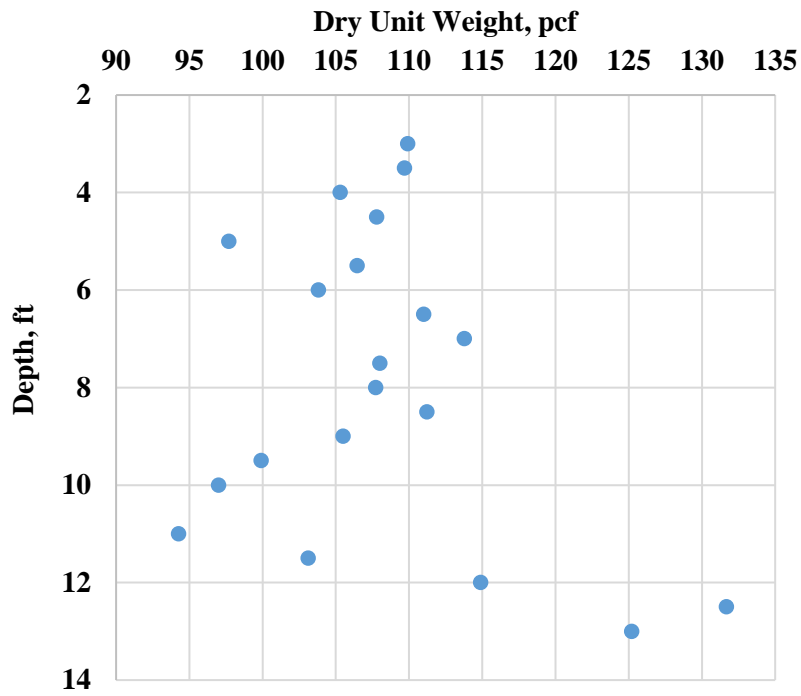


Figure 9-5 Limestone dry unit weight versus depth (3 ft to 13 ft)

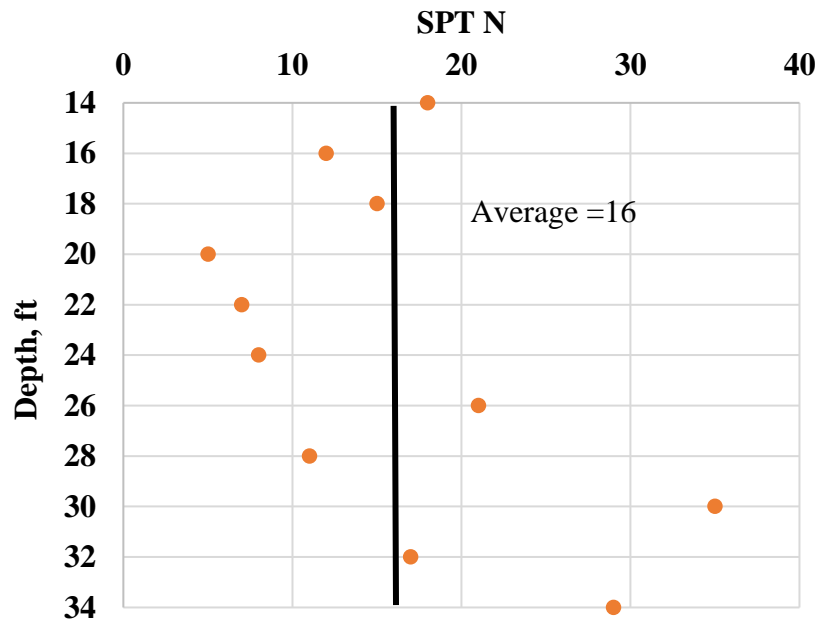


Figure 9-6 Sand layer SPT N versus depth (13 ft to 33 ft)

Table 9-14 Dry unit weight and modulus profile

Depth, ft	γ_{dt} , pcf	E_i , psi (Figure 3-1a, trendline)
3	109.9	64526.7
3.5	109.7	63698.1
4	105.3	49513.1
4.5	107.8	57158.5
5	97.7	32064.1
5.5	106.4	52911.9
6	103.8	45497.0
6.5	111.0	68679.2
7	113.8	80455.5
7.5	108.0	57820.1
8	107.7	56922.2
8.5	111.2	69468.0
9	105.5	50115.8
9.5	99.9	36389.5
10	97.0	30819.2
11	94.3	26365.4
11.5	103.1	43743.4
12	114.9	85799.8
12.5	131.7	223959.6
13	125.2	154651.9

Table 9-15 Summary statistics: rock-over-sand case

	γ_{dt} , pcf	E_i , psi	E_m , psi (Mass effect – 0.45, Figure 5-37)
Count	20	20	20
Mean	108.2	67527.9	$0.45 \times E_i = 30387.6$
Geomean	107.9	58475.5	$0.45 \times E_i = 26314$
Harmonic Mean ($E_h = \frac{n}{\sum \frac{1}{E_i}}$)	107.5	52568.0	$0.45 \times E_i = 23656$
Median	107.8	57040.3	$0.45 \times E_i = 25668$
Standard Deviation	8.7	44758.8	$0.45 \times E_i = 20141.5$
CV	0.08	0.66	0.66
SPT N average value = 16 (Figure 9-6), $E_{sand} = 250(N+15) = 250 \times (16+15) = 7750 \text{ kPa} = 1100 \text{ psi}$ (Equation 30)			

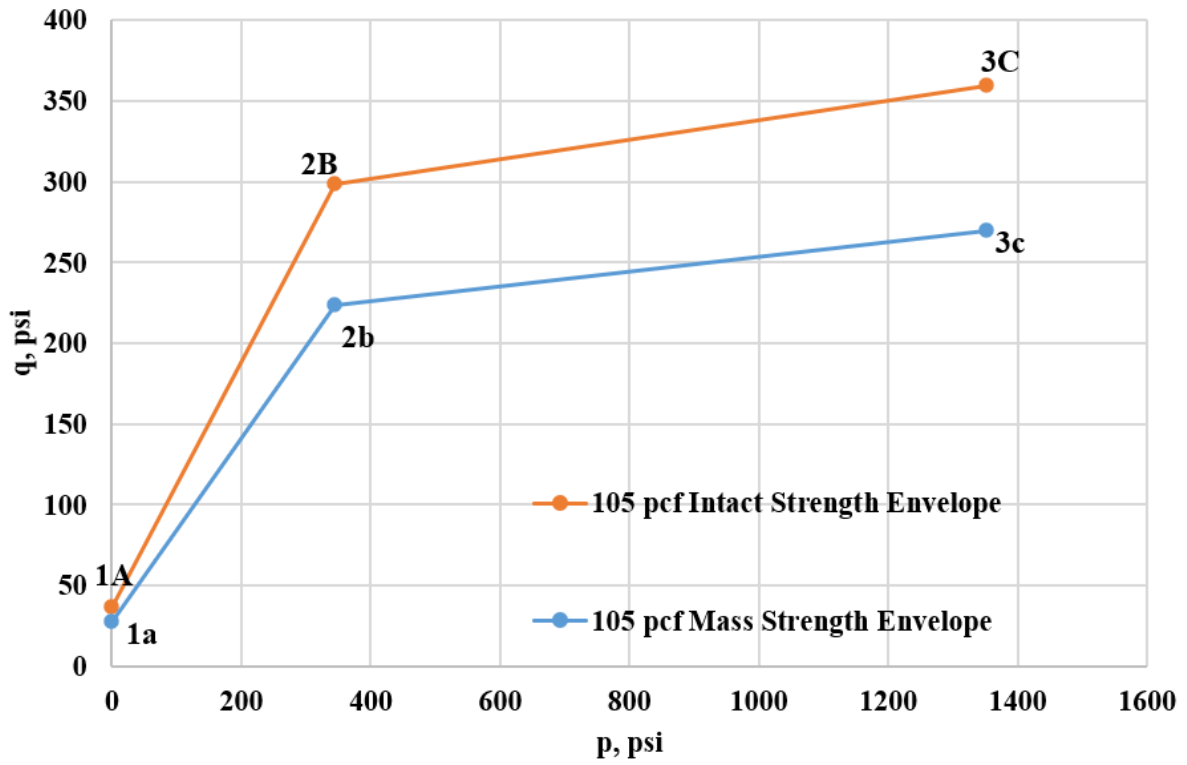


Figure 9-7 105 pcf intact strength envelope and mass strength envelope

Table 9-16 Intact and mass strength envelope conversion

Point	p, psi	q, psi	Note
1A	0	37	From Table 2-2
2B	344	298.44	
3C	1352	359.62	
1a	0	$37 \times 0.75 = 27.75$	$REC_{adjusted} \times q$
2b	344	$298.44 \times 0.75 = 223.83$	
3c	1352	$359.62 \times 0.75 = 269.72$	

Table 9-17 Intact strength versus mass strength properties

	τ-σ space			p-q space			
	c, psi	φ, °	ω, °	a, psi	α, °	P _p , psi	β, °
Intact properties	56.93	49.46	3.48	37	37.23	344, P(2B) from Table 9-16	3.47
Note	Intact properties from Table 2-2						
Mass properties	33.77	34.75	2.61	27.75	29.68	344, P(2b) from Table 9-16	2.6
Note	$\frac{a}{\cos\phi} = \frac{27.75}{\cos(34.75)} = 33.77$	$a\sin(\tan\alpha) = a\sin(0.57) = 34.75^\circ$	$a\sin(\tan\beta) = a\sin(0.046) = 2.61^\circ$	From Table 9-16: $a = q(1a) = 27.75$, $\tan(\alpha) = \frac{q(2b)-q(1a)}{p(2b)} = \frac{223.83-27.75}{344} = 0.57$, $\alpha = \text{atan}(0.57) = 29.68^\circ$, $\tan(\beta) = \frac{q(3c)-q(2b)}{p(3c)-p(2b)} = \frac{269.72-223.83}{1352-344} = 0.04651$, $\beta = \text{atan}(0.046) = 2.6^\circ$			

Knowing the mass strength properties of the 105 pcf rock, the bearing capacity of a 15 ft by 15ft footing may be estimated, as shown in Table 9-18. First, the bearing capacity factors N_c , N_c' , N_q , N_R and N_γ (see Table 9-18) are determined based on the mass angles of friction (ϕ , ω), along with overburden bearing stress, q (γD_f see Table 9-18 – note, γ of 100 pcf was used because of sand over rock). Next, the reduction of rock bearing due to the sand layer is found N_R , which requires R , or an estimate of ratio of sand modulus to rock mass modulus ($E_{\text{sand}}/E_{\text{rock}}$) and distance below footing to rock (T) (see Table 9-18). Since the median (25,668 psi) and geomean (26, 316 psi) mass moduli are similar, the lower (median) is employed (discussed in Chapter 6). Using R , the value of N_R (bearing capacity reduction) is found, 1.16, along with the footing shape factor ξ (1.245). Finally, the footing bearing capacity, Q_u (274.4 psi = 19.8 tsf) was found, Table 9-18. Note, the bearing capacity of a strong over weak layer ($E_{\text{rock}}/E_{\text{soil}} \sim 25$) will be associated with a punching shear type failure of the upper rock layer.

Table 9-18 Bearing capacity for rock-over-sand case

Footing Geometry	B, ft	15
	L, ft	15
	D _f , ft	3
	T, ft	10 (Figure 9-5)
Mass Properties	c, psi	33.77 (Table 9-17)
	φ, °	34.75 (Table 9-17)
	P _p , psi	344 (Table 9-17)
	ω, °	2.61 (Table 9-17)
	E _{sand} /E _{mass}	E _{sand} /E _{mass} (Table 9-15) = 1100/25668 (median) = 0.04285
Florida Bearing Capacity Equations	N _c	$\frac{1.8 \cos \phi}{0.8 - \sin \phi} = \frac{1.8 \cos (34.75)}{0.8 - \sin (34.75)} = 6.43$ (Equation 2-14)
	N' _c	$\frac{1.8 \cos \phi}{0.8 - \sin \omega} = \frac{1.8 \cos (34.75)}{0.8 - \sin (2.61)} = 1.96$ (Equation 2-15)
	N _γ	$\frac{1.8 [\sin \phi - \sin \omega]}{0.8 - \sin \omega} = \frac{1.8 [\sin (34.75) - \sin (2.61)]}{0.8 - \sin (2.61)} = 1.25$ (Equation 2-16)
	q, psi	3 (D _f) × 100/144 = 2.08 (Equation 2-17, overburden stress)
	N _q	$(1.5 \frac{p_p}{\sigma_a} - 10)(3 \sin \phi - 1) = (1.5 \times \frac{344}{14.7} - 10) \times (3 \times \sin (34.75) - 1) = 17.82$ (Equation 2-18)
	R	$0.093T^2 E_{soil} / E_{rock} = 0.093T^2 E_{sand} / E_{mass} = 0.093 \times 10^2 \times (0.04285) = 0.4$ (Equation 2-13)
	N _R	1.2 - 0.1 × R = 1.2 - 0.1 × 0.4 = 1.16 (Equation 2-12)
	n	$\left(\frac{4}{0.3B \text{ in ft}}\right)^{-0.055} = \left(\frac{4}{0.3 \times 15}\right)^{-0.055} = 1$ (Equation 2-10)
	ξ	$1 + 0.245 \left(\frac{B}{L}\right)^{0.66} = 1 + 0.245 \left(\frac{15}{15}\right)^{0.66} = 1.245$ (Equation 2-11)
	Qu1, psi	ncN _c + qN _q = 1 × 33.77 × 6.43 + 2.08 × 17.82 = 255.72 (Equation 2-8)
	Qu2, psi	n[cN' _c + p _p N _γ] + qN _q = 1 × [33.77 × 1.96 + 344 × 1.25] + 2.08 × 17.82 = 537 (Equation 2-9)
	Qu	min (Q _{u1} , Q _{u2}) × ξ/N _R = min(255.72, 537) × 1.245/1.16 = 274.4 psi = 19.8 tsf (Equation 2-7)

Next, the settlement of the 15 ft x 15 ft footing on rock of sand is estimated. Since, the rock will undergo punching or crushing of the rock with shedding of the load to the underlying sand, the initial median mass modulus of the rock (25,668 psi, Table 9-18) is used up to the bearing and then a secant mass modulus based on 2% strain in the rock, post peak.

As identified in Chapter 3, there are two methods of estimating settlement using secant linear elastic theory: Burmister and Winkler (modified Ueshita and Meyerhof). Presented in Table 9-19 is Burmister's approach which uses Eq. 31 (function of F - Figure 3-5). The settlement factor F determined (Figure 3-5) knowing the ratio of rock thickness to the half of footing width and modulus ratio ($E_{\text{mass}}/E_{\text{sand}}$). In the case of pre-bearing capacity, $E_{\text{mass}} = 25,668$ psi and $E_{\text{soil}} = 1100$ psi. Post bearing, the E_{mass} of the rock is obtained by taking 25,668 psi and multiplying by strain ratio (0.5% / 2% - $E_{\text{mass}} = 25,668 \times 0.005/0.02 = 6,417$ psi) which is strain ratio of rock at failure to post peak – 2%. Table 9-19 shows the F factors at bearing and approximately 10% beyond. Settlements of 7.95 in. at bearing and 15.3 in. at 22 tsf and are plotted in Figure 9-8.

In the case of the Winkler model, Ueshita and Meyerhof settlement Equation 32 is employed along with the stress weighted harmonic mean modulus $E_h = \frac{\sum h_i \sigma_i}{\sum \frac{h_i \sigma_i}{E_i}}$. Note, the latter was the sublayer approach employed in Section 9.2.1 for estimating settlements of the 10 ft x 15 ft footing. Table 9-20, shows the estimation of stress at center of each layer as well as the calculation of E_h at both bearing capacity and stresses 10% beyond. Again, in the latter case, the secant mass modulus of the rock at 2% ($E_{\text{mass}} = 6,417$ psi) was used). The Winkler model (Table 9-20) gives settlement of 8.11 in. at bearing (19.8 tsf) and 16.2 in. at 22 tsf and are plotted in Figure 9-8 with the Burmister's settlements. Evident, both approaches yield similar settlement estimates.

Table 9-19 Burmister calculations for rock-over-sand case

	p, contact stress, tsf	Figure 3-5			Settlement, in
	0	$h/r \left(\frac{r}{\frac{B}{2}} \right)$ Table 9-18)	E_2/E_1 (E_{mass}/E_{sand})	F	0
Burmister	19.8 (Bearing stress, Table 9-18)	$\frac{10}{\left(\frac{15}{2}\right)} = 1.33$	$25668/1100 = 23.33$ (See Table 9-15)	0.3	$\frac{1.18pa}{E_2} F = \frac{1.18 \times 19.8 \times 12 \times 7.5 \times 0.3}{\left(\frac{1100}{13.89 \text{ psi/tsf}}\right)} = 7.95$ (Equation 3-10, Point A in Figure 9-9)
	22* (Post bearing stress)	$\frac{10}{\left(\frac{15}{2}\right)} = 1.33$	$E_{mass, secant}^{**}/E_{sand} = 6417/1100 = 5.83$	0.52	$\frac{1.18pa}{E_2} F = \frac{1.18 \times 22 \times 12 \times 7.5 \times 0.52}{\left(\frac{1100}{13.89 \text{ psi/tsf}}\right)} = 15.34$ (Equation 3-10, Point B in Figure 9-9)

* $p = Q_u \times 1.1 = 19.8 \times 1.1 = 22 \text{ tsf}$

** $E_{mass, secant} = E_i(\text{Table 9-15}) \times \text{strain at yield/strain of interest} = 25668 \times 0.5\% (\text{yielding}) / 2\% = 6417 \text{ psi}$.

Table 9-20 Winkler model calculations for rock-over-sand case

FB-M	Bearing Stress, tsf	Figure 3-7		σ_i , tsf	h_i , ft	E_h , psi	Settlement, in
	0			$\frac{\sigma_{sand}}{p}$ (function of h/a and E_1/E_2)		For sand layer, take half of the ϵ_{sand}	
19.8 (Bearing stress, Table 9-18)	Use h/a same values as h/r and E_1/E_2 same values as E_2/E_1 in Table 9-19	0.15	Rock**:	11.39	Rock:	$E_h = \frac{\sum h_i \sigma_i}{\sum \frac{h_i \sigma_i}{E_i}} = \frac{10 \times 11.39 + 20 \times 1.485}{10 \times \frac{11.39}{25668} + 20 \times \frac{1.485}{1100}} = 4567$ (Equation 3-12)	$\frac{1.5pa}{E_h} = \frac{1.5 \times 19.8 \times 12 \times 7.5}{4567}$ (Equation 3-11, Point a in Figure 9-9) = 8.11
			Sand***:	1.485	Sand:		
22* (Post bearing stress)		0.3	Rock:	$(0.3 \times 23 + 23)/2 = 14.95$	Rock:	$E_h = \frac{\sum h_i \sigma_i}{\sum \frac{h_i \sigma_i}{E_{secant}}} = \frac{10 \times 14.95 + 20 \times 3.45}{10 \times \frac{14.95}{6417} + 20 \times \frac{3.45}{1100}} = 2540$ (Equation 3-12)	$\frac{1.5pa}{E_h} = \frac{1.5 \times 23 \times 12 \times 7.5}{2540}$ (Equation 3-11, Point b in Figure 9-9) = 16.24
			Sand:	$0.3 \times 23/2 = 3.45$	Sand:		

* $p = Q_u \times 1.1 = 19.8 \times 1.1 = 22$ tsf

$E_{mass,secant} = E_i$ (Table 9-15) \times strain at yield/strain of interest = $25668 \times 0.5\%$ (yielding)/ 2% = 6417 psi.

** σ_1 at the center of the rock layer = $(\sigma_{top} + \sigma_{bottom})/2 = (p + \sigma_{sand})/2 = (19.8 + 19.8 \times 0.15)/2 = 11.39$ tsf

*** σ_2 at the center of the sand layer = $(\sigma_{top} + \sigma_{bottom})/2 = (\sigma_{sand} + 0)/2 = (0.15 \times 19.8 + 0)/2 = 1.485$ tsf

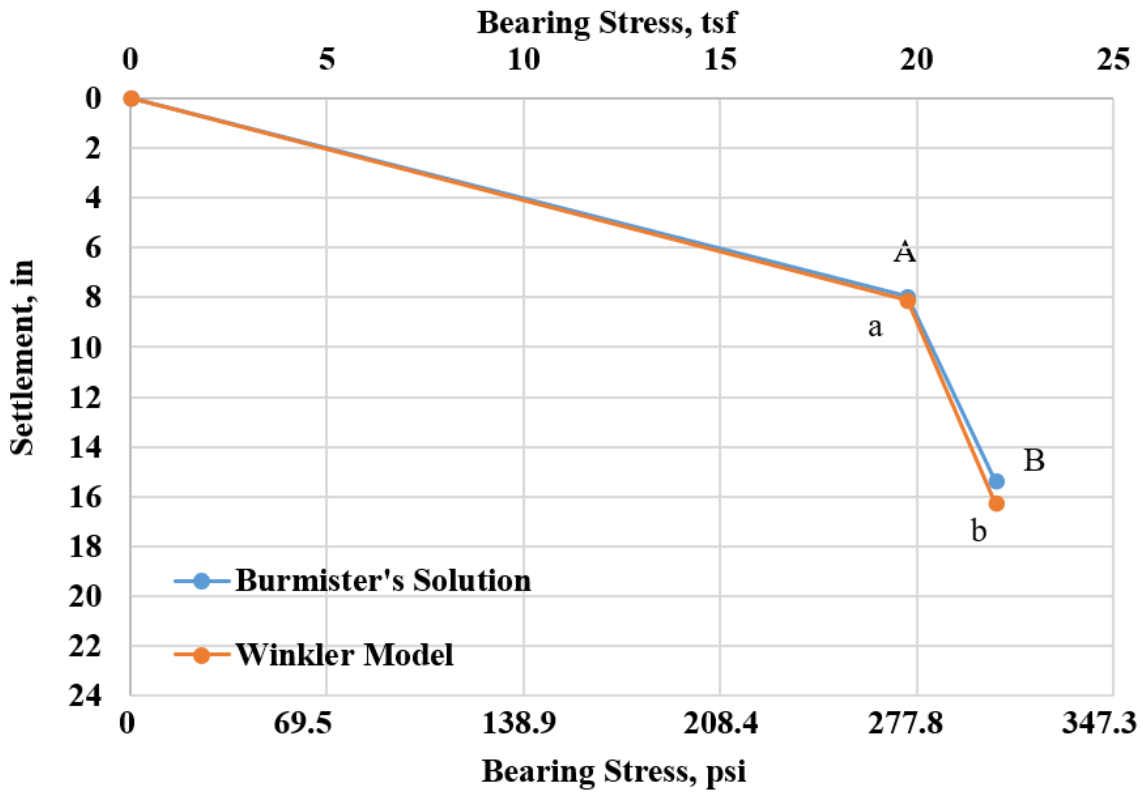


Figure 9-8 Load-settlement prediction for rock over sand case

Chapter 10

Conclusions and Recommendations

Large shallow limestone formations exist on the Florida peninsula, e.g., South, and East Coast of Florida as well as North Central Florida. The FDOT is interested in pursuing the use of shallow foundations resting on limestone to replace deep foundation elements that need drilling (e.g., piles) through the shallow limestone to support bridge piers. The design of a shallow foundation requires both strength limit and serviceability limit designs, i.e., bearing capacity and load-settlement response.

In Phase I, researchers investigated the strength of Florida carbonate rocks and/or intermediate geomaterials (IGM) under different confining stresses, developed the bi-linear strength envelope (concave downward) and the bearing capacity equations, which is a function of the formation and dry unit weight. In general, Florida rock strengths are low and undergo crushing at low to medium confining pressures (10 to 600 psi); most of the splitting tension strength q_t values are less than 250 psi, and most of the unconfined compression strength q_u values are less than 1,300 psi, with a median q_u of only 435 psi. The carbonate rocks in other regions reported in literature are typically much stronger with $q_u = 10,000$ psi to 50,000 psi (Hoek and Brown, 1980, 1988, 2018 and Johnston, 1985). The low strength of Florida limestone and the crushing phenomena may be attributed to its natural high porosity. For instance, Fereidooni and Khajevand (2018) indicated travertine samples with $n=7\%$ were porous; Schwartz (1964) considered the Pottsville sandstone and Indiana limestone as porous rocks, with porosities of $n = 14\%$ to 20% , respectively. Gowd and Rummel (1980) considered $n = 15\%$ as porous. In Mogi (1966), rocks with $n = 1\%$ to 10% were grouped as porous, and $n > 10\%$ as very porous, with a highest porosity cited as $n = 21.6\%$. In comparison, 90% of Florida carbonate

rocks have porosities greater than 20% and only 10% of Florida carbonate rocks have porosities between 5% and 20%. In general, the rocks that are typically considered porous in literature are considered “dense” and “outlier” data for Florida.

Due to the porosity, most of Florida limestone exhibits ductile behavior. The stress-strain response of Florida limestone can be simplified to a bi-linear relationship, linear up to yield then flat, and a function of the dry unit weight and the confining pressure of the test. The flat portion of the stress-strain curve is associated with crushing (ductile behavior the rock). As the confining pressure of the test increases (triaxial) or if the density the rock is higher, then a stiffer stress-strain response and higher modulus are obtained. The Young’s Modulus of initial linear slope of stress-strain curve is called initial modulus (E_i) and the secant modulus from the origin to any point on the flat line portion of the curve is called secant modulus (E_s , function of strain level).

Given the stratigraphy of Florida limestone, any footing design will usually consider a thick single homogeneous/heterogeneous rock layer or a thin (5 ft to 10 ft) stiff rock layer over a softer soil/rock layer. In the case of the single layer problem, the load-settlement response up to bearing can be predicted by linear elastic theory (based on linear stress-strain response of the rock up to yield/failure). In addition, because of the heterogeneity, a geomean E_i should be employed within the zone of influence (Fenton and Griffins, 2002). Also, if the rock has significant layering with strong over a weak layer (e.g., weathered layer), then the case of a 2-layer approach should be employed. In the case of a strong layer over weaker layer (e.g., rock over soil), the likelihood of punching shear will be high, and a large amount of settlement will occur in the weaker underlying layer. Here, the median of the E_i of the overlying rock is employed until shear failure/yield and then a secant modulus of rock is employed based on the strain level.

The moduli of the rock should be assessed from triaxial tests at 50 psi confining stress and underlying weak layer from in-situ methods (e.g., Bowles based on SPT).

Assisting with defining the properties and layering are improved methods of field sampling (e.g., MWD) and NDT testing. For example, the seismic shear testing results in a much larger volume of rock tested at much smaller cell size (1 ft x 1 ft x 1ft) which provides more information on rock/soil layering as well as mass properties (i.e., dry unit weight vs. intact specimens), and associated variability as well as correlation lengths.

In the case of 2-layer problems, Burmister (1958) was shown capable of predicting settlement up to punching shear and after (chapters 2, 5 and 7). Ueshida and Meyerhof (1973) are also capable of predicting 2-layer settlements; if more layers, then the harmonic mean modulus (chapter 2) may be employed (Winkler model – chapter 3), and it has been shown to predict settlement (chapters 5, 6, and 7) up to punching shear (top rock layer yielding) and afterward. Moduli of non-rock layers (e.g., sand, gravel, etc.) may be obtained by various in-situ methods (e.g., SPT, CPT, PMD, DMT).

For validation of bearing capacity and load-settlement equations, three full scale in-situ load tests were conducted in downtown Miami, Davie (SR-84-Fort Lauderdale), and Bell, Florida. The Miami test involved a 42 in x 42 in footing overlying a highly variable Miami limestone layer (Chapter 5). The Davie test was a 60 in x 72 in footing residing on 10 ft thick Miami limestone underlain by sand (Chapter 6). The Bell test involved a 60 in x 60 in footing residing on 5 ft layer of stiff Ocala limestone, underlain by a weathered rock/sand/clay mixed layer (Chapter 7). The seismic results (Chapter 4) for Cemex site shows the density varied from 1400 kg/m³ (87 pcf) to 2200 kg/m³ (137 pcf) vertically (10 ft) and from 1400 kg/m³ (87 pcf) to 1800 kg/m³ (112 pcf), horizontally (7 ft). For the SR-84 site, the top of rock ranged from ½ ft to 5 ft

depth, with rock thickness ranging from 9 to 12 ft and rock density varied 1650 kg/m^3 (103 pcf) to 1800 kg/m^3 (112 pcf) based on seismic results. At Bell site, the top of rock starts from the ground surface down to 10 ft. At the Bell site the rock surface varied from 5 ft to 10 ft with dry unit weights varying from 100 pcf to 112 pcf (Ocala limestone); at the test location, the rock layer was 5 ft thick and was underlain by a weathered layer of rock, sand, and clay.

The bearing capacity of all three sites were estimated based on Phase I Bearing Capacity Equations (Chapter 2) using the mass dry unit weights determined from either the seismic shear density tests or with the geomean or median dry unit weight from cores recovered in the footprints. Bearing capacities ranged from 14 tsf to 28 tsf at the three sites and the predicted agreed very favorably with the measured results. For load vs. settlement, both the mean and differential settlements at the general shear failure (Cemex) was predicted favorably with Fenton and Griffiths (2002) elastic model using the geomean E_i of the rock ($CV = 1.37$). In the case of SR-84 and Bell Sites which had 2 layers, both the settlement at punching shear/yield of the rock, as well as the settlement afterward were predicted favorably using the median E_i ($CV > 1$) of the rock until rock shear/yield and then secant E_s based on 2% strain within the rock; both cases also used Bowles to estimate the 2nd layer modulus based on SPT N value (Chapter 6 & 7).

Since the mass vs. intact specimen properties has a strong influence (due to rock's high porosity), on both bearing capacity and load-settlement response of the footing, it is recommended to use a REC-adjusted strength envelope for the bearing capacity, as well as the Young's Moduli for settlement. However, the REC needs to be adjusted (adjusted-recovery) based on the actual length of tested specimens for q_u , q_t , and triaxial cores (need to neglect the rubble portion in core box). The significance of this is reflected in that an 80% REC (vs. 100%) will reduce the bearing capacity (Chapter 2) by 40%.

Also, it is strongly recommended that recovered cores from below the water table be stored in a moisture room or a tank (filled with water) within 1 day after the rock is cored. In general, rock cores contain both voids and vugs providing pathways for drainage (1 to 2 days); note lower moisture content will result in much higher dry unit weights and in unrealistic (higher) bearing capacity predictions. Besides typical (dry unit weight from moisture content and wet unit weight), the dry unit weights of the rock may be obtained from AASHTO T-100 (2015)/ ASTM D-854 (2014), and specific gravity or non-invasively by seismic shear tests.

Due to Florida rock variability, it is recommended that 20 to 25 samples (tested cores) be obtained within the footing's influence zone (3B) to assess strength, moduli, layering and summary statistics for both bearing and settlement analyses. Other field measuring techniques like seismic shear and Measuring While Drilling (MWD) should be considered for obtaining higher resolution (less than 1 ft) assessment of properties (dry unit weight, and strength), and identifying potential thin layers (e.g., Bell site) which will impact both bearing (punching shear) and settlement of the footing. Finally, in determining the mass Young's Modulus, it is recommended to use the E_m/E_i vs $REC_{adjusted}$ developed by Ko (2010) to account for the voids existing in porous Florida limestone formations.

LIST OF REFERENCES

- AASHTO. (2017). AASHTO LRFD Bridge Design Specification. American Association of State Highway and Transportation Officials, Washington, D.C.
- AASHTO Standard T-100. (2015). Standard Specifications for Transportation Materials and Methods of Sampling and Testing, and AASHTO Provisional Standards, American Association of State Highway and Transportation Officials, Thirty-Fifth Edition. Part 1B: Specifications, Washington, D.C.
- ASTM Standard D854. (2014). Standard Test Methods for Specific Gravity of Soil Solids by Water Pycnometer, ASTM International, West Conshohocken, PA.
- Bowles, J. E. (1996). Foundation Analysis and Design, McGraw-Hill, New York.
- Button S.J. (1953). The Bearing Capacity of Footings on a Two-Layer Cohesive Subsoil, 3rd ICSMFE, Vol. 1, pp. 332–335.
- Burmister, D. M., (1958), Evaluation of Pavement Systems of the WASHO Road Test by Layered Systems Methods, Highway Research Board Bulletin 177, 26-54.
- Canadian Geotechnical Society. (2006). Canadian Foundation Engineering Manual, Canadian Geotechnical Society, Richmond, B.C.
- Carter, J. P. & Kulhawy, F. H. (1988). “Analysis and Design of Foundations Socketed into Rock”. Report No. EL-5918. Empire State Electric Engineering Research Corporation and Electric Power Research Institute, New York, pp. 158.
- Consoli, N.C.; Dalla Rosa, F. & Fonini, A. (2009). Plate load tests on cemented soil layers overlying weaker soil. *Journal of Geotechnical and Geoenvironmental Engineering*, 135(12):1846-1856.
- Fenton, G. A., & Griffiths, D. V. (2005). Three-dimensional probabilistic foundation settlement. *Journal of Geotechnical and Geoenvironmental Engineering*, 131(2), 232–239.
- Fenton, G.A., & Griffiths, D.V. (2002) “Probabilistic Foundation Settlement on Spatially Random Soil.” *Journal of Geotechnical and Geoenvironmental Engineering*, 128(5), 381-390.
- Fereidooni, D. and Khajevand, R. (2018). “Determining the Geotechnical Characteristics of Some Sedimentary Rocks from Iran with an Emphasis on the Correlations between Physical, Index, and Mechanical Properties.”: *Geotechnical Testing Journal*, Vol 41(3), pp. 555-573.
- Fox, L. (1948). Computation of traffic stresses in a simple road structure. H.M. Stationery Off., London.
- Gorbunov-Possadov M. & Malikova TA. (1973) Calculation of structures on elastic foundation [in Russian]. Moscow: Stroiizdat

- Gowd, T. N., & Rummel, F. (1980). Effect of confining pressure on the fracture behavior of a porous rock. *International Journal of Rock Mechanics and Mining Sciences & Geomechanics Abstracts*, Vol. 17, No. 4, pp. 225-229.
- Harro, D., & Kiflu, H. (2018). Imaging of deep sinkholes using the multi-electrode resistivity implant technique (merit) case studies in Florida. *Proceedings of the 15th Multidisciplinary Conference on Sinkholes and the Engineering and Environmental Impacts of Karst and the 3rd Appalachian Karst Symposium*, 341–346, National Cave and Karst Research Institute, Shepherdstown, West Virginia.
- Hassan, K. M., O'Neill, M. W., Sheikh, S. A., & Ealy, C.D. (1997). "Design method for drilled shafts in soft argillaceous rock." *J. Geotech. Eng. Div., Am. Soc. Civ. Eng.*, 123(3), 272-280.
- Hoek, E. & Brown, E. T. (1980). "Empirical strength criterion for rock masses", in *Journal of the Geotechnical Engineering Division*, Vol 106-9, pp. 1013-1035.
- Hoek, E. & Brown, E. T. (1988). "The Hoek-Brown Failure Criterion - a 1988 Update." in "Proceedings of the 15th Canadian Rock Mechanics Symposium", editor Curran, J. H., Toronto, Civil Engineering Department, University of Toronto, pp 31–38.
- Hoek, E. & Brown, E. T. (2018). "The Hoek-Brown failure criterion and GSI – 2018 edition", in: *Journal of Rock Mechanics and Geotechnical Engineering*, in press, accepted manuscript. doi.org/10.1016/j.jrmge.2018.08.001
- Johnston I. (1985). "Strength of Intact Geomechanical Materials", in: *ASCE Journal of Geotechnical Engineering* 111, pp. 730-749.
- Kenny, M. J., & Andrawes, K. Z. (1997). "The bearing capacity of footing on sand layer overlying soft clay." *Geotechnique*, 47(2), 339– 345.
- Ko, J. (2010) "Evaluation of Tip Behavior of Drilled Shaft in Florida Limestone." University of Florida, Print.
- Kuo, Y. L., Jaksa, M. B., Kaggwa, G. S., Fenton, G. A., Griffiths, D. V., & Goldsworthy, J. S. (2004). Probabilistic analysis of multi-layered soil effects on shallow foundation settlement. *Australia-New Zealand Conference on Geomechanics (9th: 2004: Auckland, NZ)*.
- Lambe, T.W., & Whitman, R.V. (1969). *Soil mechanics*. John Wiley & Sons, New York.
- Mogi K. (1966). "Pressure dependence of rock strength and transition from brittle to ductile flow", in *Bulletin of Earthquake Research Institution*, Vol 44, pp. 215-232.
- Pantelidis, L. (2019). The equivalent modulus of elasticity of layered soil mediums for designing shallow foundations with the Winkler Spring Hypothesis: A critical review. *Engineering Structures*, 201, 109452. <https://doi.org/10.1016/j.engstruct.2019.109452>
- Peck, R. B., Hanson, W. E. & Thornburn, T. H. (1974). *Foundation Engineering*. John Wiley, London, 514 pp.

Perras, M. A., & Diederichs, M. S. (2014). A review of the tensile strength of Rock: Concepts and testing. *Geotechnical and Geological Engineering*, 32(2), 525–546.
<https://doi.org/10.1007/s10706-014-9732-0>

Schwartz, A.E. (1964). “Failure of rock in the triaxial shear test”, in: “Proceedings of the 6th U.S Symposium on Rock Mechanics”, American Rock Mechanics Association. Rolla, MI; pp. 109-51

Florida Department of Transportation (FDOT) (2018). “Soils and Foundations Handbook”, State Materials Office, Florida.

Ueshita, K., & Meyerhof, G.G. (1967). Deflection of Multilayer Soil Systems. *Journal of the Soil Mechanics and Foundations Division*, 93(5), 257–282. <https://doi.org/10.1061/jsfeaq.0001023>

Umashankar, B., & Sekar, P. (2015). Settlements of Rigid Rectangular Footings on Layered Soils. 50th Indian Geotechnical Conference, 17-19 Dec, 2015, Pune, India.

Appendix A
Load Test Design

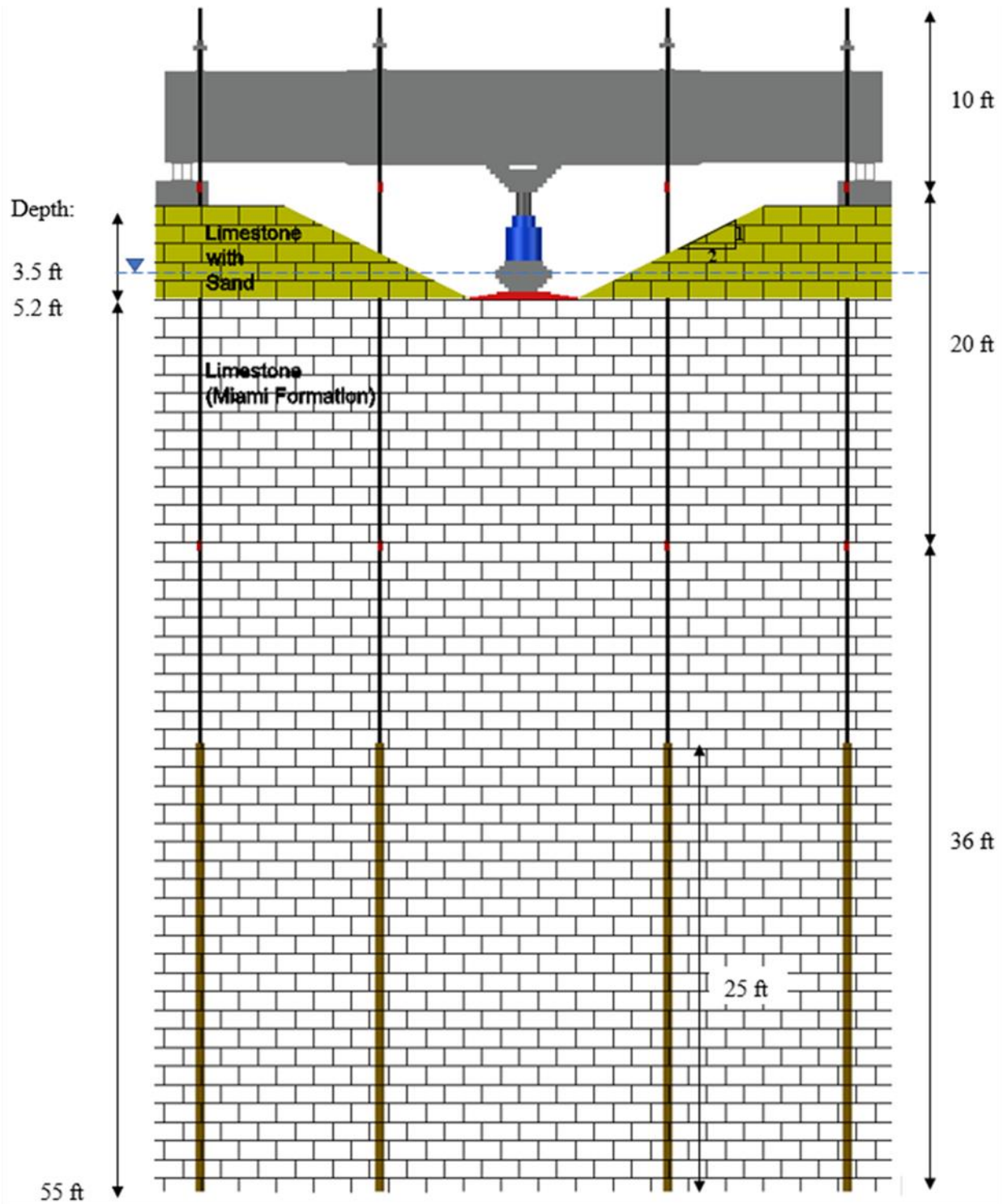


Figure A-1 Load test design for Cemex site

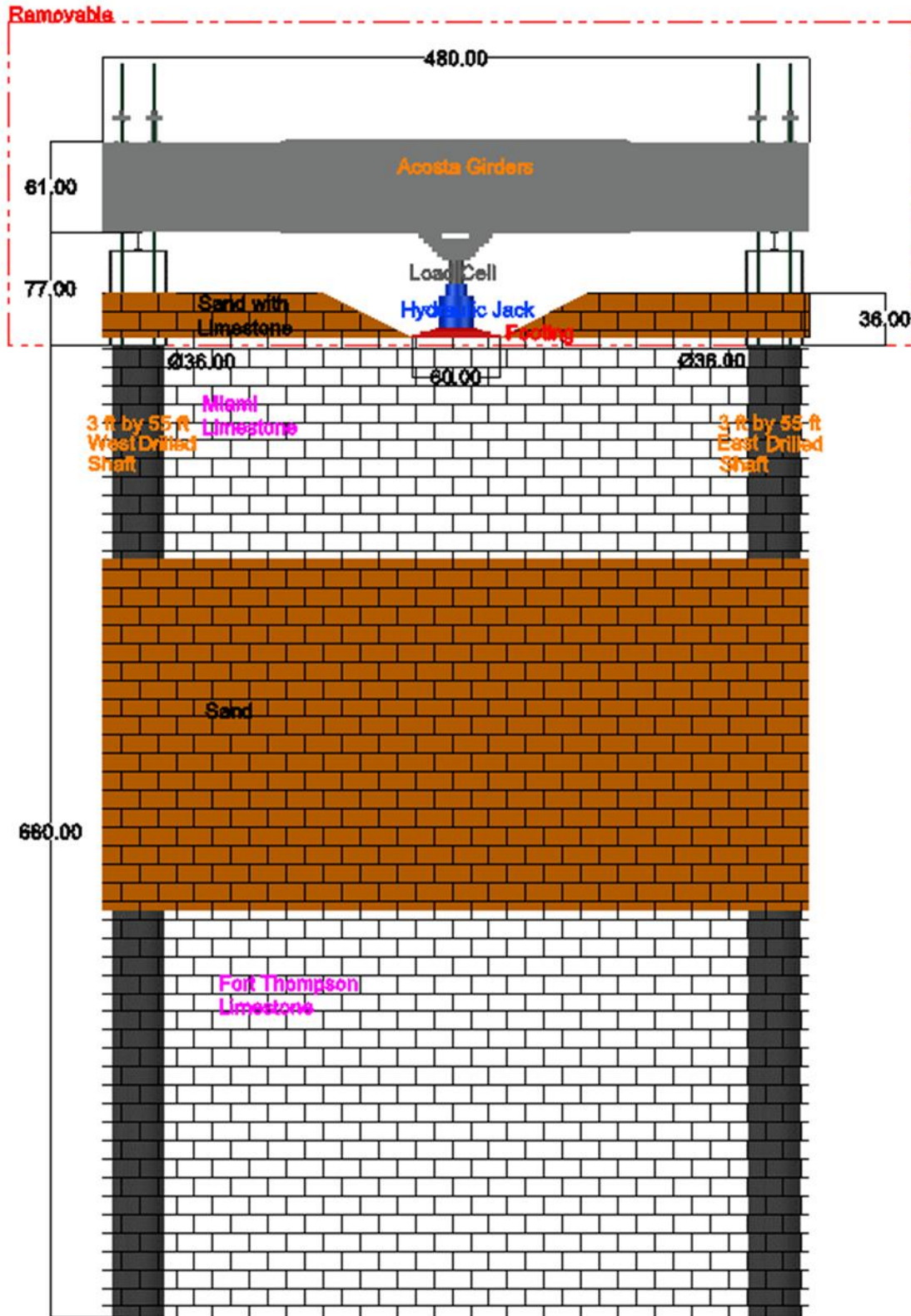


Figure A-2 Load test design at SR-84 site

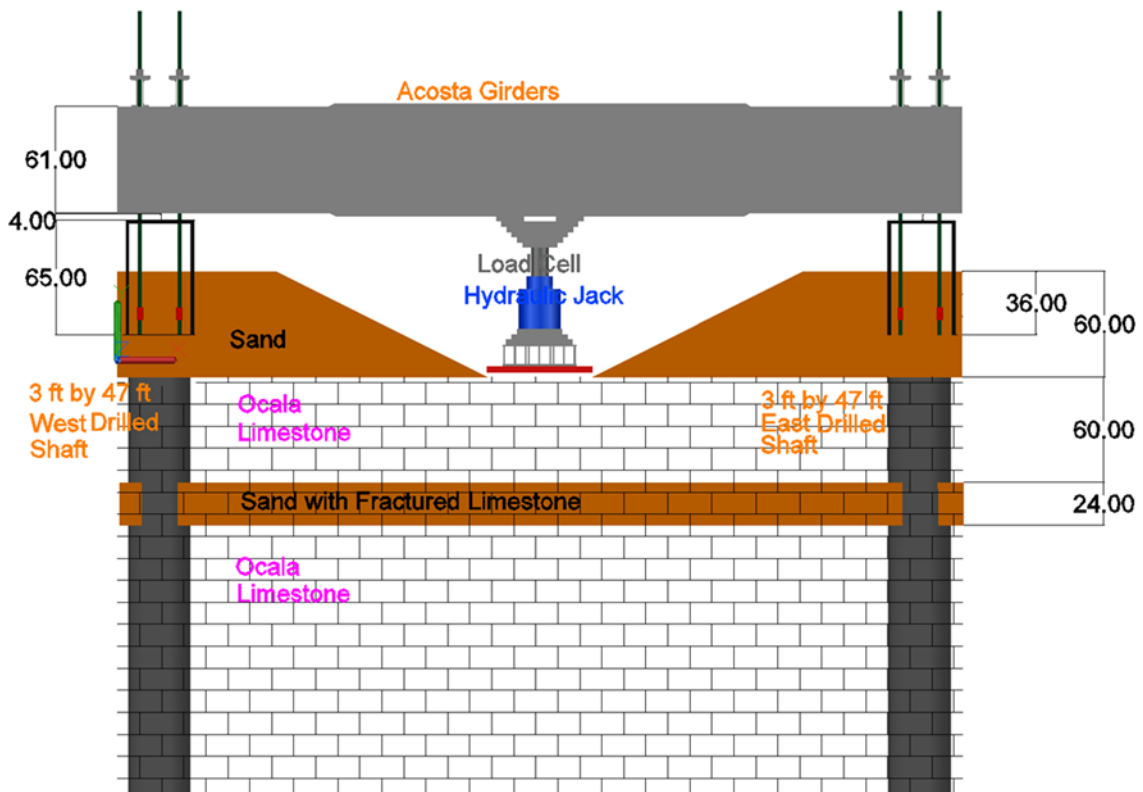


Figure A-3 Load test design at Bell site

Appendix B
SPT and Rock Cores for Miami Limestone

CORE: RC-1

Date: 4/29/2020

Run 1 (5' to 10')



Run 2 (10' to 15')

Core Run / (Depth Interval)	REC (In)	REC (%)	RQD (%)	Time (sec)
Run 1 / (5' to 10')	60	100	36	310
Run 2 / (1' to 6')	60	100	60	955

Project Manager: HS	Project No: HS195028	Terracon	PHOTOGRAPHS OF ROCK CORES	Exhibit
Drawn by: SQF	Title: N.T.S.		FDOT D6 Geotechnical Services Contract Task 21 - Districtwide Material Testing Miami-Dade County, Florida	A
Checked by: HS	File Name: HS195028			
Approved by: HS	Date: 5/6/2020			

Figure B-1 RC 1 run 1 and run 2

CORE: RC-1

Date: 4/29/2020

Run 3 (20' to 25')



Run 4 (30' to 35')

Core Run / (Depth Interval)	REC (In)	REC (%)	RQD (%)	Time (sec)
Run 3 / (20' to 25')	57	95	20	195
Run 4 / (30' to 35')	60	100	60	365

Project Manager: HS	Project No: HE185028		PHOTOGRAPHS OF ROCK CORES	Exhibit
Drawn by: SCF	Scale: N.T.S.		FDOT D6 Geotechnical Services Contract	A
Checked by: HS	File Name: HE185028		Task 21 - Districtwide Material Testing	
Approved by: HS	Date: 5/6/2020		Miami-Dade County, Florida	

Figure B-2 RC 1 run 3 and run 4

CORE: RC-1

Date: 4/29/2020

Run 5 (40' to 45')



Run 6 (50' to 55')

Core Run / (Depth Interval)	REC (In)	REC (%)	RQD (%)	Time (sec)
Run 5 / (40' to 45')	60	100	11	605
Run 6 / (50' to 55')	60	100	47	310

<table border="1"> <tr> <td>Project Manager:</td> <td>HS</td> </tr> <tr> <td>Drawn by:</td> <td>SDF</td> </tr> <tr> <td>Checked by:</td> <td>HS</td> </tr> <tr> <td>Approved by:</td> <td>HS</td> </tr> </table>	Project Manager:	HS	Drawn by:	SDF	Checked by:	HS	Approved by:	HS	<table border="1"> <tr> <td>Project No:</td> <td>HR165020</td> </tr> <tr> <td>Scale:</td> <td>N.T.S.</td> </tr> <tr> <td>File Name:</td> <td>HR165020</td> </tr> <tr> <td>Date:</td> <td>4/29/2020</td> </tr> </table>	Project No:	HR165020	Scale:	N.T.S.	File Name:	HR165020	Date:	4/29/2020	<p style="text-align: center;">Terracon</p> <p style="font-size: small;">1625 S.W. 37th Ave., Suite 100 Miami Lakes, Florida 33103 (772) 321-1000 Fax: (772) 321-1000</p>	<p style="text-align: center;">PHOTOGRAPHS OF ROCK CORES</p> <p style="text-align: center;">FDOT D6 Geotechnical Services Contract Task 21 - Districtwide Material Testing Miami-Dade County, Florida</p>	<table border="1"> <tr> <td>Exhibit</td> </tr> <tr> <td style="text-align: center;">A</td> </tr> </table>	Exhibit	A
Project Manager:	HS																					
Drawn by:	SDF																					
Checked by:	HS																					
Approved by:	HS																					
Project No:	HR165020																					
Scale:	N.T.S.																					
File Name:	HR165020																					
Date:	4/29/2020																					
Exhibit																						
A																						

Figure B-3 RC 1 run 5 and run 6

CORE: RC-2

Date: 4/29/2020

Run 1 (5' to 10')



Run 2 (10' to 15')

Core Run / (Depth Interval)	REC (In)	REC (%)	RQD (%)	Time (sec)
Run 1 / (5' to 10')	57	95	73	730
Run 2 / (1' to 6')	58	96	77	830

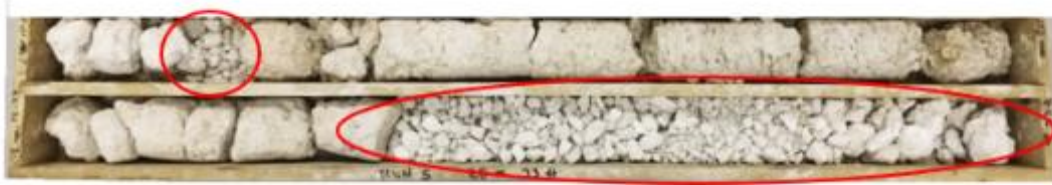
Project Manager: HS	Project No: F8195528	Terracon	PHOTOGRAPHS OF ROCK CORES	Exhibit
Drawn By: SCF	Title: N.T.S.		FDOT D6 Geotechnical Services Contract Task 21 - Districtwide Material Testing Miami-Dade County, Florida	A
Checked By: HS	File Name: F8195528			
Approved by: HS	Date: 5/8/2020			

Figure B-4 RC 2 run 1 and run 2

CORE: RC-2

Date: 4/29/2020

Run 3 (15' to 20')



Run 5 (28' to 33')

Core Run / (Depth Interval)	REC (In)	REC (%)	RQD (%)	Time (sec)
Run 3 / (15' to 20')	60	100	55	420
Run 4 / (23' to 28')	No Recovery			155
Run 5 / (28' to 33')	58	97	13	255

Project Manager: HS	Project No: H6195020	 <small>2000 SW 10th Ave, Suite 100 Miami, Florida 33135 Tel: 305 420-1000 Fax: 305 420-1000</small>	PHOTOGRAPHS OF ROCK CORES	Exhibit
Drawn by: SCF	Scale: N.T.S.		FDOT D6 Geotechnical Services Contract	A
Checked by: HS	File Name: H6195020		Task 21 - Districtwide Material Testing	
Approved by: JTC	Date: 4/29/2020		Miami-Dade County, Florida	

Figure B-5 RC 2 run 3 and run 4

CORE: RC-2

Date: 4/29/2020

Run 6 (33' to 38')



Run 7 (45' to 48')

Core Run / (Depth Interval)	REC (In)	REC (%)	RQD (%)	Time (sec)
Run 6 / (33' to 38')	60	100	10	715
Run 7 / (45' to 48')	60	100	40	840

Project Manager: HS	Project No: HS185028		PHOTOGRAPHS OF ROCK CORES	Exhibit
Drawn by: SCIF	Date: N.T.S		FDOT D6 Geotechnical Services Contract Task 21 - Districtwide Material Testing Miami-Dade County, Florida	A
Checked by: HS	File Name: HS185028			
Approved by: HS	Date: 5/6/2020			

Figure B-6 RC 2 run 5 and run 6

For the rubbles in the recovered core runs, where they do not retain the cylindrical shape for strength tests: researchers decided to ignore this rubble portion and counted it as unrecovered material, and the Recovery was adjusted to 72% for the Cemex Site, as shown in Table B-1.

Table B-1 Adjusted-recovery at the Cemex site

RC-1	Run 1	Run 2	Run 3	Run 4	Run 5	Run 6
REC, %	60	78	48	94	47	71
RC-2	Run 1	Run 2	Run 3	Run 5	Run 6	Run 7
REC, %	95	96	94	32	86	63
Average, %	72					



Figure B-7 Pictures of rock cores for B-1. (a): 3 ft – 13 ft; (b): 33 ft – 43 ft; (c): 68 ft – 73 ft



Figure B-8 Pictures of rock cores for B-2. (a):3 ft – 13 ft; (b): 33 ft – 43 ft; (c): 43 ft – 53 ft



(a)



(b)



(c)

Figure B-9 Pictures of rock cores for B-3. (a): 3 ft – 13 ft; (b): 33 ft – 43 ft; (c): 43 ft – 53 ft

Ignoring the rubber portion gives an adjusted-recovery for Miami Limestone Layer: 78 %
and an adjusted-recovery for Fort Thompson Layer: 70%.

Table B-2 B-1 SPT log for Cemex site

Elev.		Depth (ft)		SPT Blows (per 6")				N	Material Description
0.00	-2.00	0.00	2.00	50/3				REFUSAL	Limestone with fine sand
-2.00	-4.00	2.00	4.00	18	13	10	10	23	Limestone with fine sand
-4.00	-6.00	4.00	6.00	5	3	7	9	10	Limestone with fine sand
-6.00	-8.00	6.00	8.00	16	23	32	28	55	Limestone with fine sand
-8.00	-10.00	8.00	10.00	18	20	23	50/3	43	Limestone with fine sand
-10.00	-12.00	10.00	12.00	50/2				REFUSAL	Limestone with fine sand
-12.00	-14.00	12.00	14.00	50/2				REFUSAL	Limestone with fine sand
-14.00	-16.00	14.00	16.00	50/3				REFUSAL	Limestone with fine sand
-18.50	-20.00	18.50	20.00	9	3	5		8	Limestone with fine sand
-21.00	-22.50	21.00	22.50	7	5	8		13	Limestone with fine sand
-23.50	-25.00	23.50	25.00	10	7	9		16	Limestone with fine sand
-26.00	-27.50	26.00	27.50	3	5	5		10	Limestone with fine sand
-28.50	-30.00	28.50	30.00	14	6	50/3		REFUSAL	Limestone with fine sand
-31.00	-32.50	31.00	32.50	5	3	5		8	Limestone with fine sand
-33.50	-35.00	33.50	35.00	19	7	10		17	Limestone with fine sand
-36.00	-37.50	36.00	37.50	3	2	3		5	Limestone with fine sand
-38.50	-40.00	38.50	40.00	3	4	50/3		REFUSAL	Limestone with fine sand
-41.00	-42.50	41.00	42.50	5	8	5		13	Limestone with fine sand
-43.50	-45.00	43.50	45.00	40	4	4		8	Limestone with fine sand
-46.00	-47.50	46.00	47.50	5	5	7		12	Limestone with fine sand
-48.50	-50.00	48.50	50.00	14	7	20		27	Limestone with fine sand
-51.00	-52.50	51.00	52.50	3	5	8		13	Limestone with fine sand
-53.50	-55.00	53.50	55.00	10	4	15		19	Limestone with fine sand
-56.00	-57.50	56.00	57.50	9	5	10		15	Limestone with fine sand
-58.50	-60.00	58.50	60.00	16	50/3			REFUSAL	Limestone with fine sand

Table B-3 B-2 SPT log for Cemex site

Elev.		Depth (ft)		SPT Blows (per 6")				N	Material Description
0.00	-2.00	0.00	2.00	50/3				REFUSAL	Limestone with fine sand
-2.00	-4.00	2.00	4.00	18	13	10	10	23	Limestone with fine sand
-4.00	-6.00	4.00	6.00	5	3	7	9	10	Limestone with fine sand
-6.00	-8.00	6.00	8.00	16	23	32	28	55	Limestone with fine sand
-8.00	-10.00	8.00	10.00	18	20	23	50/3	43	Limestone with fine sand
-10.00	-12.00	10.00	12.00	50/2				REFUSAL	Limestone with fine sand
-12.00	-14.00	12.00	14.00	50/2				REFUSAL	Limestone with fine sand
-14.00	-16.00	14.00	16.00	50/3				REFUSAL	Limestone with fine sand
-18.50	-20.00	18.50	20.00	9	3	5		8	Limestone with fine sand
-21.00	-22.50	21.00	22.50	7	5	8		13	Limestone with fine sand
-23.50	-25.00	23.50	25.00	10	7	9		16	Limestone with fine sand
-26.00	-27.50	26.00	27.50	3	5	5		10	Limestone with fine sand
-28.50	-30.00	28.50	30.00	14	6	50/3		REFUSAL	Limestone with fine sand
-31.00	-32.50	31.00	32.50	5	3	5		8	Limestone with fine sand
-33.50	-35.00	33.50	35.00	19	7	10		17	Limestone with fine sand
-36.00	-37.50	36.00	37.50	3	2	3		5	Limestone with fine sand
-38.50	-40.00	38.50	40.00	3	4	50/3		REFUSAL	Limestone with fine sand
-41.00	-42.50	41.00	42.50	5	8	5		13	Limestone with fine sand
-43.50	-45.00	43.50	45.00	40	4	4		8	Limestone with fine sand
-46.00	-47.50	46.00	47.50	5	5	7		12	Limestone with fine sand
-48.50	-50.00	48.50	50.00	14	7	20		27	Limestone with fine sand
-51.00	-52.50	51.00	52.50	3	5	8		13	Limestone with fine sand
-53.50	-55.00	53.50	55.00	10	4	15		19	Limestone with fine sand
-56.00	-57.50	56.00	57.50	9	5	10		15	Limestone with fine sand
-58.50	-60.00	58.50	60.00	16	50/3			REFUSAL	Limestone with fine sand

Table B-4 SPT log for SR-84 site

Depth (ft)		SPT Blows (per 6")				N	Material Description
Top	Bottom						
0.0	2	5	7	7	6	14	Light Brown LIMEROCK with Fine to Medium Grained Sand
2.0	4	10	22	39	38	61	Light Brown Weathered Oolitic LIMESTONE (Miami Formation)
4.0	6	21	19	20	19	39	
6.0	8	17	20	29	25	49	
8.0	10	50/2"				REFUSAL	
10.0	12	50/4"				REFUSAL	
12.0	14	50/5"				REFUSAL	
14.0	16	50/5"				REFUSAL	Light Brown Medium Dense Sand with Limestone and Cemented Sand Fragments (Fort Thompson Formation)
17.0	18.5	15	11	10		21	
18.5	20	10	9	12		21	Light Gray LIMESTONE and Cemented Sand (Fort Thompson Formation)
22.0	23.5	50/3"				REFUSAL	
23.5	25	50/2"				REFUSAL	Light Brown Medium Dense Sand with Limestone and Cemented Sand Fragments (Fort Thompson Formation)
27.0	28.5	8	6	7		13	
28.5	30	4	6	6		12	
32.0	33.5	6	10	10		20	
33.5	35	7	8	10		18	
37.0	38.5	14	38	48		86	
38.5	40	50/4"				REFUSAL	Light Gray LIMESTONE and Cemented Sand (Fort Thompson Formation)
42.0	43.5	50/2"				REFUSAL	
43.5	45	50/2"				REFUSAL	
47.0	48.5	6	10	10		20	
48.5	50	8	14	21		35	
52.0	53.5	8	10	19		29	
53.5	55	24	32	11		43	
57.0	58.5	38	50/4"			REFUSAL	
58.5	60	50/2"				REFUSAL	
62.0	63.5	38	41	35		76	
63.5	65	30	29	33		82	

Appendix C
Resistivity Test, MWD Profile and SPT Log at Bell Site

The resistivity test was conducted by SMO drilling crew, the location can be found in Figure 7-1. The result is shown in Figure C-1, the interpretation is made by summarizing the work of Harro and Kiflu, 2018. Harro and Kiflu did multiple resistivity test across the Florida: Tampa, Orlando and Lake County, the data was validated by various methods: SPT, CPT and GPR and is summarized in Table C-1. It is evident that the geomaterial cannot be differentiated since the overlapping between the resistivity of sand, clay, and weathered limestone. Such that no layering information is obtained.

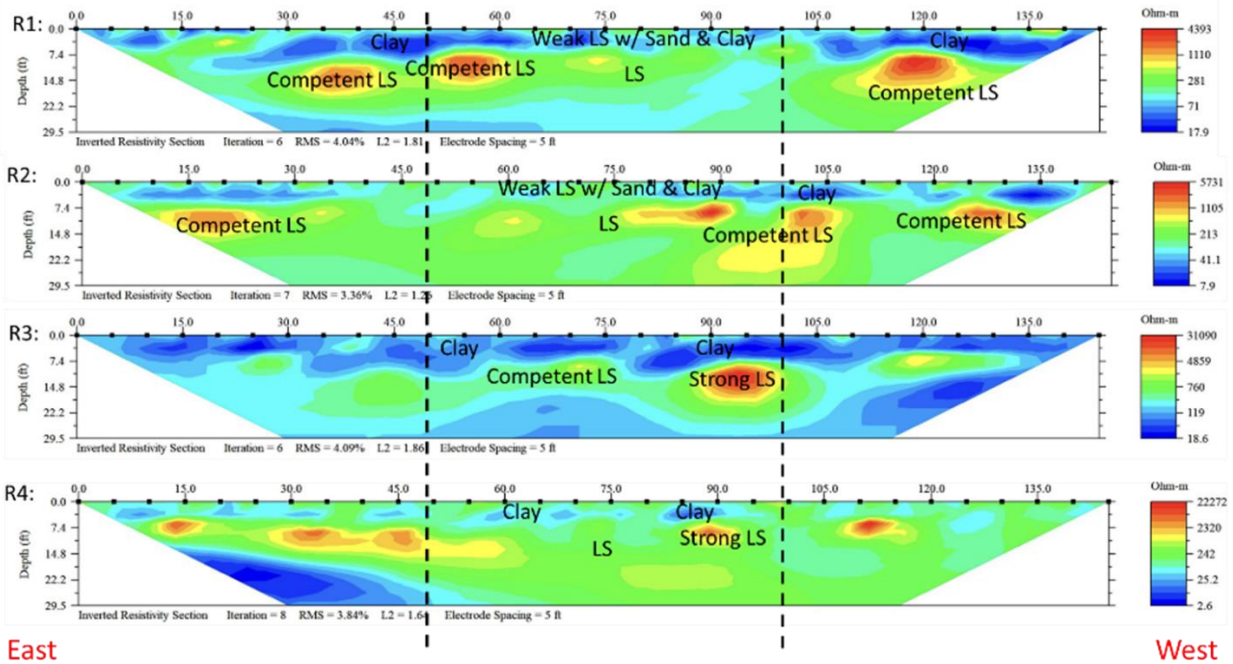


Figure C-1 Resistivity test

Table C-1 Resistivity of different soil types

Soil Type	Resistivity, Ohm-m
Sand	70 ~ 500
Clay	1 ~ 150
Weathered Limestone	50 ~ 200
Competent Limestone	> 700

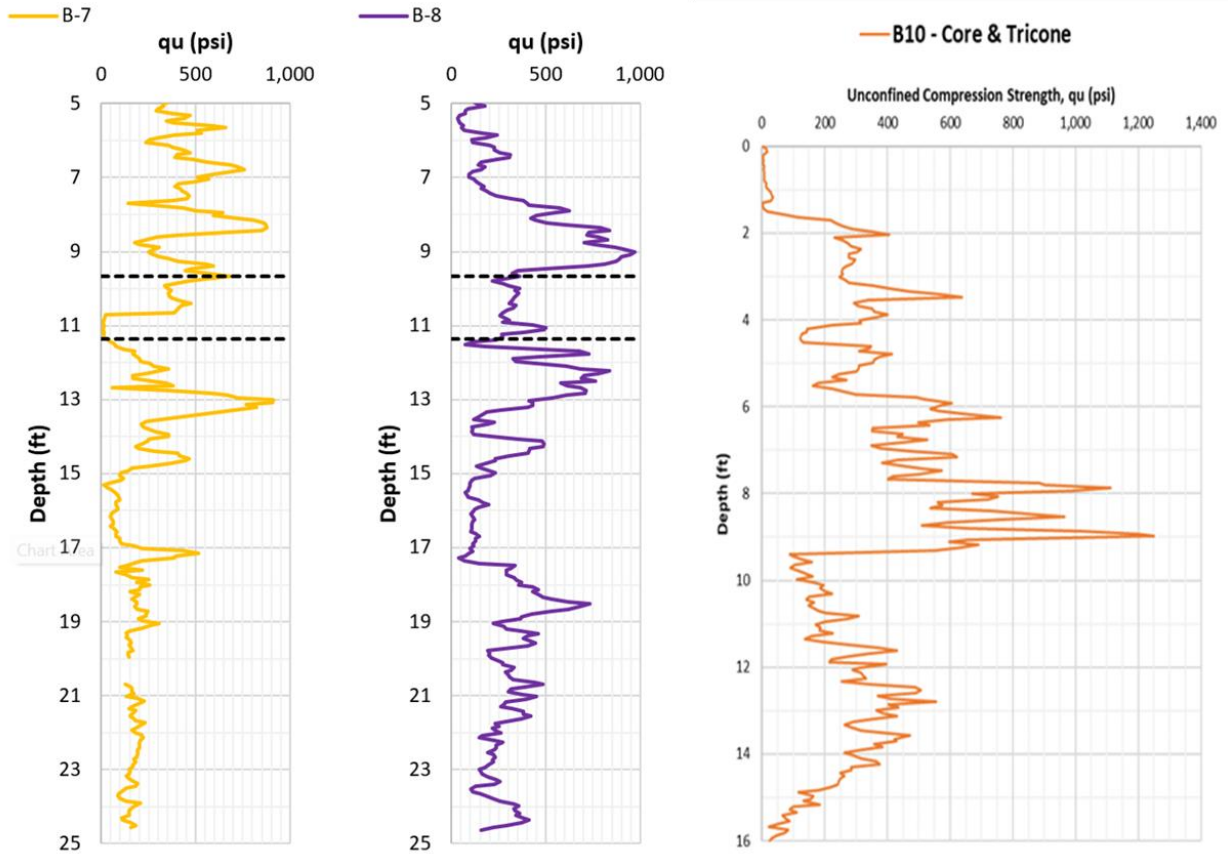


Figure C-2 MWD profile: q_u versus depth

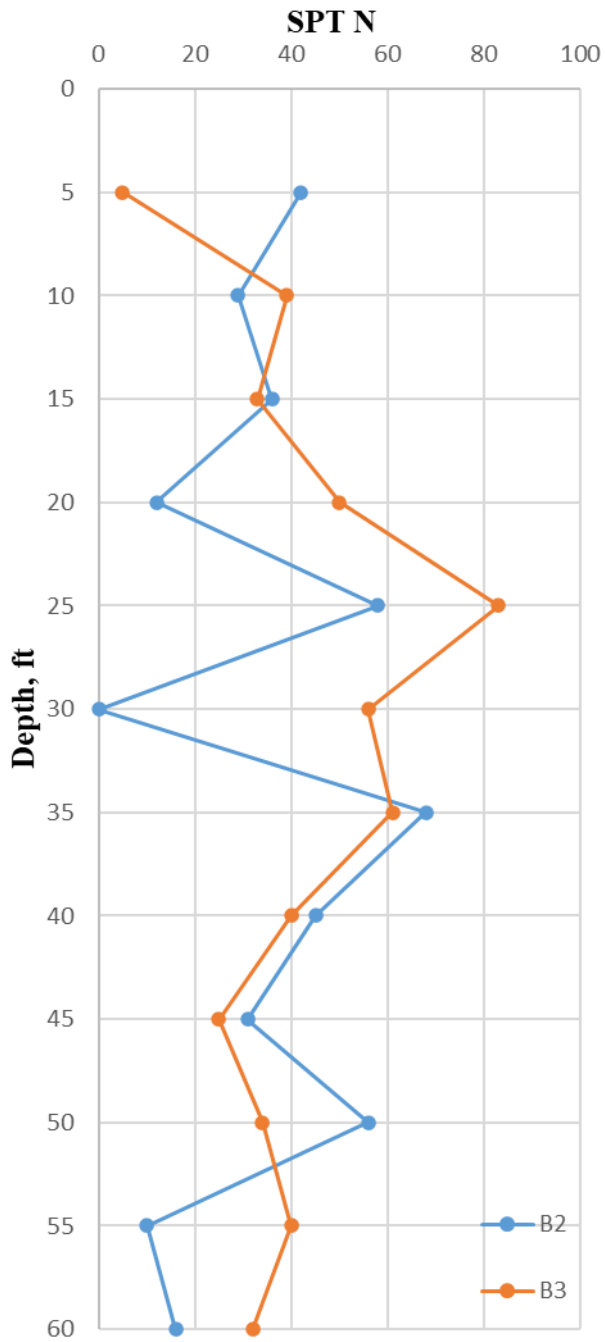


Figure C-3 SPT log of boring B2 and B3